LITHIUM ION BATTERY PERFORMANCE IN LOW EARTH ORBIT SATELLITE APPLICATIONS

by

Riley William Cook

Submitted in Partial fulfillment of the requirements
for the degree of Master of Applied Science

at

Dalhousie University
Halifax, Nova Scotia
August 2020

Table of Contents

List of Tables

List of Figures

Abstract

CubeSats powered by lithium-ion batteries (LIB) are increasingly being used as a cost-effective alternative to conventional large satellite missions. CubeSat mission lengths of 18+ months (8,760 + cycles) are being proposed, necessitating the need for high cycle life batteries. The objective of this work is to establish a LIB technology that is best suited for lengthier CubeSat missions by means of experimental degradation battery cycling. If successful, future CubeSat missions will benefit from lower battery energy storage mass and volume, ultimately reducing the cost of launching to space at no sacrifice to performance. To support the main objective, secondary experiments include cell dissection, scanning electron microscopy (SEM), energy dispersive X-ray spectroscopy (EDS), a comprehensive heat transfer analysis of the experimental setup, the effect of manufacturer sleeves and performance differences in ~0.2 kPa vacuum pressure as opposed to the true low Earth orbit (LEO) ambient pressure (~10^{-9} kPa).

This research investigates performance of three groups of 18-65 cylindrical lithium-ion cells with different positive active materials (NCA – nickel cobalt aluminium, NMC – nickel manganese cobalt, LFP – lithium iron phosphate), negative active material (NAM) graphite average particle sizes (2 – 30 μm) and electrode designs (high power, high energy). Each was tested using an accelerated LEO CubeSat cycle in a 3P group configuration in ambient *laboratory* (~101 kPa, 20 °C), enhanced with low *temperature* (~101 kPa, 10 °C) and enhanced with *vacuum* (~0.2 kPa, 10 °C) conditions. With identical energy demand on each cycle, cell groups were continuously operated unless failure was achieved.

The NCA cell type failed from both IR growth and excessive internal gas buildup disconnecting the current interrupt device (CID) whereas NMC cell groups failed purely from IR growth. In all three conditions the LFP cell type outperformed the NCA and NMC cell type with regards to total discharge energy throughout and energy efficiency. This finding proves that the LFP cell type shows high potential in battery design for longer CubeSat missions, while also reducing the total required photovoltaic array size due to improved energy efficiency.

List of Abbreviations and Symbols Used

Acronyms

BoL	Beginning of Life
CAD	Computer-Aided Design
CC	Constant Current
CC-CV	Constant Current Constant Voltage
CID	Current Interrupt Device
CP	Constant Power
CV	Constant Voltage
DC	Direct Current
DEC	Diethyl Carbonate
DMC	Dimethyl Carbonate
dV/dQ	Differential Voltage Analysis
EC	Ethyl Carbonate
EDS	Energy Dispersive X-ray Spectroscopy
EMC	Ethyl Methyl Carbonate
EoL	End of Life
IR	Internal Resistance
LAM	Loss of Active Material
LCO	Lithium Cobalt Oxide (Chemical Abbreviation: $LiCoO_2$)
LEO	Low Earth Orbit
LFP	Lithium Iron Phosphate (Chemical Abbreviation: $LiFePO_4$)
LIB	Lithium-ion Battery
LLI	Loss of Lithium Inventory
LMO	Lithium Manganese Oxygen (Chemical Abbreviation: $LiMn_2O_4$)
LNMO	Lithium Nickel Manganese Oxygen (Chemical Abbreviation: $LiNi_{0.5}Mn_{1.5}O_4$)
MA	Methyl Acetate
MoL	Middle of Life
NAM	Negative Active Material
NCA	Nickel Cobalt Aluminum (Chemical Abbreviation: $LiNiCoAlO_2$)
NMC	Nickel Manganese Cobalt (Chemical Abbreviation: $LiNiMnCoO_2$)
OCV	Open Circuit Voltage
PAM	Positive Active Material
PC	Propylene Carbonate
PTC	Positive Temperature Coefficient
SEI	Solid Electrolyte Interface
SEM	Scanning Electron Microscopy
SoC	State of Charge
SoE	State of Energy

Symbols and Constants (Units)

$\boldsymbol{A_{cond}}$	Area for conductive heat transfer (m^2)
A_{conv}	Area for convective heat transfer (m^2)
A_{rad}	Area for radiative heat transfer (m^2)
E_{chg}	Charge energy (Wh)

E_{dis}	Discharge energy (Wh)
h	Convective heat transfer coefficient $\left(\frac{\mathrm{W}}{\mathrm{m}^2 K}\right)$
H_o	Null hypothesis
H_1	Alternative hypothesis
i	Charge or discharge current (A)
k	Conductive heat transfer thermal conductivity $\left(\frac{\mathrm{W}}{\mathrm{m\ K}}\right)$
k_B	Boltzmann constant = $1.380622 * 10^{-23}\left(\frac{\mathrm{N\ m}}{\mathrm{K}}\right)$
L_{cond}	Conductive heat transfer length
$L_{k,9}$	Kinetic temperature to altitude ratio for 120 – 1000 km = 12.0 $\left(\frac{\mathrm{K}}{\mathrm{km}}\right)$
M	Molecular mass (g/mol)
m_f	Mass fraction (g/g)
n_f	Mol fraction (mol/mol)
n_A, n_B	Sample size of cell group 'A' and 'B' respectively
n_i	Altitude dependent number density of atmospheric gasses (m^{-3})
P	Power (W)
P_{avg}	Average Power (W)
Pr	Pressure (Pa)
$Pr_{chamber}$	Pressure in the vacuum chamber (Pa)
Pr_{gauge}	Pressure at the vacuum gauge (Pa)
Pr_{400}	Pressure at 400 km altitude LEO
Pr_{700}	Pressure at 700 km altitude LEO
Q	Capacity (Ah)
$q_{avg,loss}$	Average power loss throughout a cycle (W)
q_{cond}	Heat transfer from conduction (W)
q_{conv}	Heat transfer from convection (W)
q_{gen}	Heat generation (W)
q_{loss}	Total heat transfer from convection, conduction, and radiation (W)
q_{ohmic}	Ohmic heat generation (W)
q_{rad}	Heat transfer from radiation (W)
R_g	Radius of gyration (Angstroms)
R_{ohmic}	Ohmic resistance (Ω)
r_0	Radius of earth = 6,357 (km)
S^2	Data variance
S_p^2	Paired data variance of cell group 'A' and 'B'
T	Temperature (K)
T_{Al}	Aluminum plate temperature for heat transfer model (K)
T_{10}	Temperature at Z_{10} = 360 (K)
T_∞	Kinetic temperature as per Figure 2.12 (K)
T_s	Surface temperature (K)
T_i	Surface temperature on inside of sleeve (K)
T_o	Surface temperature on outside of sleeve (K)
T_{sur}	Ambient surrounding temperature used for heat transfer equations (K)
t_{crit}	Critical t-value determined using the t-distribution tables
t_0	Null hypothesis t-value
t_p	PAM thickness on one side of current collector (mm)

t_n	NAM thickness on one side of current collector (mm)
t_s	Separator material thickness (mm)
t_{Al}	Aluminum positive current collector thickness (mm)
t_{Cu}	Copper negative current collector thickness (mm)
t_{stack}	Complete jelly roll thickness (mm)
t_{chg}	Charge time (s)
t_{dis}	Discharge time (s)
V_{cell}	Cell voltage throughout cycle (V)
v	Degrees of freedom
$\bar{X}$	Mean of sample data
Z	Altitude (km)
Z_{10}	Lower limit altitude = 120 (km)

Greek Letters (Units)

Ω	Resistance (Ω)
λ	A quantified fraction of the temperature between equation limits (K)
ξ	A quantified fraction of the altitude between equation limits (km)
ε	Surface emissivity constant for radiative heat transfer
σ	Stefan-Boltzmann constant = $5.67 * 10^{-8}\left(\frac{W}{m^2K^4}\right)$
η	Real time energy efficiency (%)
η_{LEO}	Average LEO cycle energy efficiency (%)
η_{factor}	Efficiency factor – Adjusts power losses using real time energy efficiency
μ	Population mean
α	Significance level
Δ	"Change in". Example: Change in temperature → ΔT

Chemical Nomenclature

Al	Aluminum
C	Carbon
Co	Cobalt
F	Fluorine
Fe	Iron
Li	Lithium
Mn	Manganese
Ni	Nickel
O	Oxygen
P	Phosphorous

Acknowledgements

First and foremost, I would like to thank Dr. Lukas Swan for his guidance and support throughout this research project. Thanks to Lukas' unwavering optimism and leadership, this research project gave me the opportunity to grow as an engineer and a person. Lukas truly is a special supervisor and will go to great lengths to pick you up when you fall down no matter how busy he may be. Lukas is one of the hardest working individuals I have ever met, and he is certainly an asset to Dalhousie University and to those who are fortunate enough to work by his side.

Some pivotal individuals throughout my MASc experience include Dr. Ted Hubbard for his mentorship and belief in my teaching ability. Mark MacDonald and Albert Murphy for their machine shop skills and humour.

A big thank you to all the scholarships and grants awarded to me for this research which include the Roland E. Gagne Scholarship (2018, 2019), Nova Scotia Department of Energy and Mines Pengrowth Scholarship (2019), FGS Scholarship (2019), and my Graduate Stipend funded by the Canadian Space Agency which was awarded to Kevin Plucknett. In addition to providing funding, Kevin was instrumental in the success of this research project through provision of equipment and guidance.

I'd like to thank everyone that was a part of the Renewable Energy Storage Lab during my time there. The RESL team is extraordinary in many regards, making every week something to look forward to. From the thought-provoking conversations on a Monday morning with a nice cup of coffee in hand, to the Friday afternoon get togethers for everyone to share their triumphs and tragedies of the week. My Masters studies have given me the experience of a lifetime and I will always look back fondly at my research days as a student at RESL.

Finally, I'd like to give a special thanks to my good friend Mark Elliot who I met by joining RESL. Without Mark, my time at RESL would never have been as fun and exciting. I believe the two of us mutually bettered our graduate student experience, as well as our futures.

Chapter 1 : Introduction

The space industry is increasingly adopting nano-satellites as a means of cost-effective services and exploration, with CubeSats (10x10x10 cm) being a popular nano-satellite class. The low cost of CubeSats ($200,000 to $2 million) relative to conventional medium and larger satellites ($50 million to $2 billion) establishes a clear cost benefit [1], which has led to significant deployment growth on a global scale over the last 10 years [2]. Parallel to the growth of CubeSat technology, there has been tremendous development and production ramp of lithium-ion batteries (LIB). The first rechargeable LIB was made commercially available by Sony in 1991 and contained a lithium cobalt oxide (LCO) positive electrode material [3], [4]. Since then, a range of other positive active materials (PAM) have been developed such as nickel cobalt aluminium (NCA), nickel manganese cobalt (NMC), and lithium iron phosphate (LFP). Each PAM variant offers trade-offs which include power capability, energy density, specific energy, cycle life and cost. At present, there is a gap in the literature regarding performance comparison of these variants for low Earth orbit (LEO) CubeSat applications which have unique cycling profiles in vacuum at relatively low temperatures. To address this, my research analyzes three different LIB cells with varying PAM chemistries (NCA, NMC, LFP), negative active material (NAM) graphite average particle sizes (2 – 30 μm) and electrode designs (high energy, high power) for LEO CubeSat applications.

1.1 Research Objectives

This experimental research tests industry leading, commercial off-the-shelf lithium-ion cells from both conventional (i.e. high energy density) and unexploited (i.e. high power density) PAM variants for the CubeSat technology. By utilizing present and alternative state of the art cells available for CubeSat design, this work will influence the design of CubeSats battery systems being launched over the coming years, ultimately transforming the trajectory of satellite energy storage design and mission capability. This experimental research provides the opportunity for disruption in traditional nano-satellite battery technology, as LFP is relatively unutilized in both academic and industrial CubeSat projects. The research objectives of this work are listed below.

I. As NCA and NMC cells have much greater energy density than LFP, their ΔSoE (change in state of energy) and ΔSoC (change in state of charge) operating window is much less. Combined with their ability to degrade substantially in capacity while still completing the LEO discharge-charge cycle has lead CubeSat battery system designers to overlook the LFP technology. The primary

objective of this work is to determine if high cycle life, high power and low energy density cells (i.e. LFP) have potential to improve battery design in LEO CubeSat missions compared to traditional low cycle life, low power and high energy density cells (i.e. NCA and NMC).

II. Contrast the performance of each cell type in ambient *laboratory*, *temperature*, and *vacuum* conditions. Results from this comparison will determine if degradation cell testing for future CubeSat projects should be done in a low cost setting (i.e. *laboratory* condition), medium cost setting (i.e. *temperature* condition) or a high cost setting (i.e. *vacuum* condition).

III. Analyze the failure mode from each cell type to further quantify degradation. This gives insight into which degradation mechanisms are causing end of life (EoL) conditions and shortlists the focus on which components should be improved for the next generation of LIB for CubeSats applications.

IV. Differentiate how cells are degrading in terms of loss of active material (LAM) and loss of lithium inventory (LLI) using differential voltage analysis (dV/dQ) techniques. Potential degradation mechanisms include excessive SEI growth or lithium plating. Results will distinguish if the PAM or NAM are the leading cause of cell failure and help guide future experimental design.

V. Provide an alternative method of viewing and analyzing cell performance from beginning of life (BoL) to EoL for partial ΔSoE applications such as LEO CubeSats. This methodology will characterize how power capability improves available energy and plays a critical role in continued cell operation.

VI. Analyze the thermal model of each condition and cell group and determine their respective heat transfer contributions. Results are related to LEO CubeSat design and provide insight to how heat is rejected from each 3P grouping.

VII. Determine the effect on cell operating temperature and performance with and without the manufacturer sleeve in the *vacuum* condition. Results will determine if it is necessary to remove sleeves in order to reasonably compare performance across different cell types in the vacuum setting. Results will also suggest if flight cells which are required to have their manufacturer sleeve replaced due to outgassing regulations are affected by this change.

VIII. Determine the effect of cell operating temperature between the *vacuum* condition and true LEO pressure. Results will indicate if operating cells in the *vacuum* condition pressure is viable for validating performance in the true LEO pressure.

Chapter 2 : Background

CubeSats rely on LIB. Chapter 2 reviews the fundamentals of LIB function, materials, degradation mechanisms and the 18-65 cell format. Background of LEO satellite orbital theory and LEO conditions (pressure, temperature) are discussed with the intent to justify research experiment design parameters.

Lithium-ion cells are commercially available in different formats (cylindrical, pouch and prismatic), electrode designs (high power, low power), with options for electrolytes, separators, and active materials. All lithium-ion cells work using the same principle of storing chemical potential energy using lithium ions. Single cell voltage varies depending on the active materials in a lithium-ion cell, with typical nominal voltages of 3.3 or 3.6 V. In order to achieve greater voltages, capacity and power capability, lithium-ion cells are assembled in series and parallel configurations to form modules (a configuration of cells) and packs (a configuration of modules). Battery modules and packs use the notation "xSyP" to describe cell configuration, where 'xS' indicates 'x' cells or cell groups (if >1P) in series and 'yP' indicates 'y' cells in parallel.

A lithium-ion cell stores chemical potential energy by transporting lithium ions across the separator by means of electrolyte from the PAM into the NAM during charge; the reverse occurring during discharge. For every lithium-ion transported, one electron leaves the NAM and goes to the PAM by way of an external electrically conductive circuit. As electrons and lithium ions flow between PAM and NAM, they respectively experience ohmic and ionic resistance, which generate heat. A diagram representing the movement of electrons and lithium ions is presented by Deng [5] in Figure 2.1.

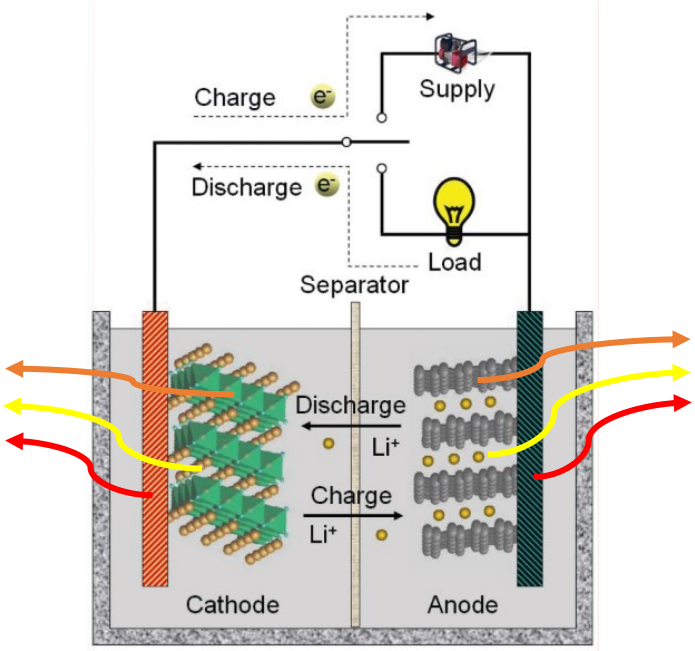

Figure 2.1 LIB electrochemical process showing charge and discharge. Resistive heat generated by ohmic (red), ionic (yellow) and both (orange) depicted by arrows [5]

The flow of electrons (A) depicted in Figure 2.1 can be maintained for a duration proportional to the coulombic capacity (Ah) of the cell. Cycling rates for lithium-ion cells are often characterized by the term "C rate". The C rate is the current at which a battery is cycled relative to its full coulombic capacity. For example, a 1 Ah cell cycled at 2 A undergoes a 2C rate.

Both SoC and SoE are metrics used to respectively quantify the remaining coulombic and energy capacity in a LIB. When a 1 Ah cell is at 100% SoC, there is 1 Ah of coulombic capacity remaining. If that same 1 Ah cell discharges at a nominal 3.6 V, there is 3.6 Wh of energy capacity at 100% SoE. However, as LIB discharges, the voltage changes non-linearly during cycling. Consequently, when cycling a LIB, the rate of change in SoE is different than that of SoC. For example, a 1 Ah cell discharged at 1 A for 30 minutes would finish discharge at 50% SoC. However, for the first half of discharge the cell had an average voltage of 3.8 V, resulting in a 1.9 Wh discharge over the same 30 minutes, thus the cell is at 47% SoE. Although minimal, the distinction between SoC and SoE is critical to understand when discussing battery operation. From an applications engineering perspective, SoE is most important as it describes how much energy remains in a LIB to do work. From an electrochemistry perspective, SoC is useful as it best describes lithium inventory and

movement in both PAM and NAM which aids in identification of electrochemical degradation mechanisms.

In a lithium-ion cell, active materials are mixed in a slurry which contains a binder (polyvinylidene fluoride) and conductive diluent (carbon black or graphite) which are adhered to the positive current collector (aluminium foil) [4]. The binder and carbon black account for ~2% each by weight of the PAM and NAM blend [4].

2.1.1 Positive Active Material

When a LIB is fully discharged, the PAM has fully intercalated lithium into all available lithium sites. The first successfully commercialized lithium-ion cell that could reversibly intercalate lithium ions contained an LCO PAM and was fabricated by Sony in 1991 [3], [4]. Since then, many other popular active materials have emerged with the attempt to lower cost, increase energy density, power capability, and improve cycle life. The various popular PAM and their crystalline structures include:

- NCA – Ordered rock salt
- NMC – Ordered rock salt
- LFP – Olivine
- LMO (lithium manganese oxide) – Spinel
- LCO – Ordered rock salt

The market share of each PAM as of 2016 is presented by Pillot [6] in Figure 2.2.

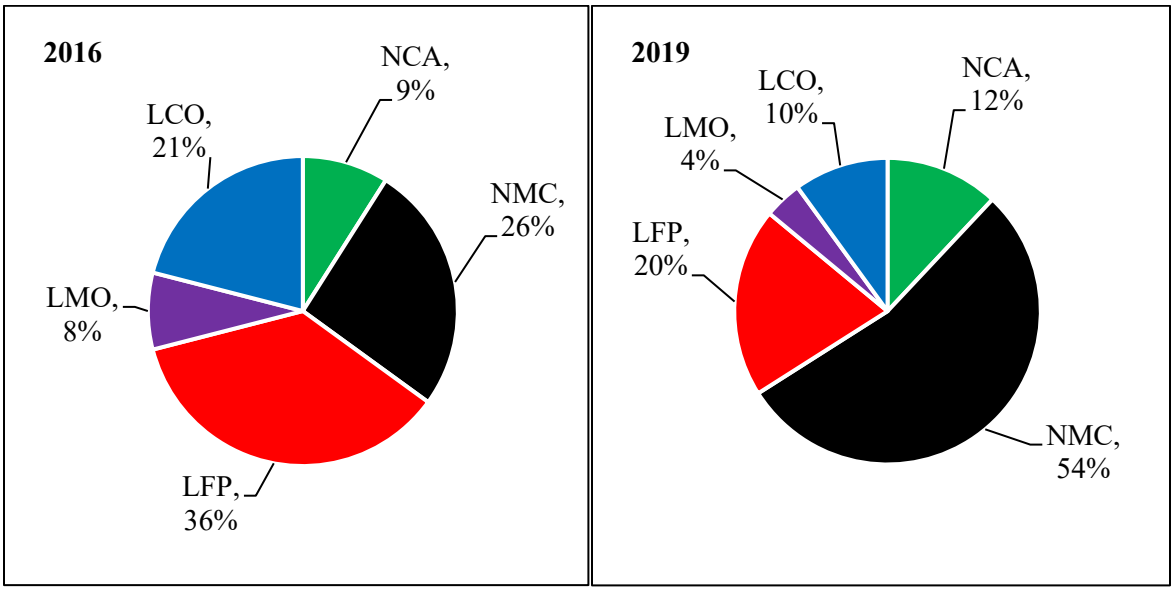

Figure 2.2 Use of PAM in commercialized LIB as of 2016 [6] and 2019 [7]

As shown in Figure 2.2, the most popular PAM as of 2016 was LFP, however with growing EV markets, both NCA and NMC have grown substantially while phasing out LCO and LMO. While LFP still remains relevant in LIB technology, its market share has decreased substantially due to an exponentially increasing electric vehicle market [8], which predominantly uses NCA and NMC due to its high energy density with the exception of LFP in China [9], [10]. From Figure 2.2 it is evident that PAM market share is evolving quickly due to growing markets and technological advances of the nascent stage LIB technology.

High specific energy PAM chemistries such as NCA and NMC, yield specific capacities respectively of 220 and 190 mAh/g [4] with nominal operating potentials at 3.6 volts [11], [12]. Whereas the LFP chemistry offers a specific capacity of 160 mAh/g [4] and a nominal operating potential of 3.3 volts [13]. The performance difference in each PAM can be partially attributed to the difference in how these materials intercalate lithium ions. The NCA, NMC and LCO lithium ions move along layers (2D lithium movement), whereas LFP they move in 1D tunnels. NCA, NMC, LCO and LFP each intercalate lithium ions into octahedral sites [4], [14]. Alternatively, lithium manganese oxygen (LMO) has the spinel structure which uses 3D tunnelling and intercalates lithium into tetrahedral sites [4].

Ionic conductivity is improved with increased dimensions of tunnelling, decreased particle size and increased electrode surface area. The performance difference between the three different crystalline

structures (ordered rock-salt, olivine, and spinel) translates into power density, energy density and cycle life. In industry, high energy density cells contain NCA or NMC active materials that achieve their higher capacities with the ordered rock-salt structure (2D tunneling) at the cost of poor power capability and cycle life which is dominated by the olivine structured (1D tunneling) LFP. Initially it was thought that LFP would only support low power LIB designs due to low ionic conductivity as a result of 1D tunnelling [10], [15]. However, LFP achieves its high power capability from its smaller "nanoparticle" size relative to the "microparticle" sized NCA and NMC materials [4]. Nanoparticles increase the power capability of a given PAM by reducing the lithium solid state diffusion distance by up to 3 orders of magnitude, however it comes at the cost of increased degradation resulting from an increased surface area for oxidation and electrolyte decomposition as the high voltage limit is increased. LFP has a 3.6 V high voltage limit which is lower than that of NCA and NMC (4.2 V). As result of the reduced high voltage limit in LFP relative to NCA and NMC, it utilizes nanoparticle technology without the negative effect of increased degradation.

2.1.2 Negative Active Material

When a LIB is fully charged, the NAM has completely intercalated lithium ions into all available lithium sites and is in the fully lithiated state. The earliest rechargeable lithium-ion cells contained a lithium-metal NAM. There have been attempts to make safe lithium metal NAM for rechargeable batteries due to its high capacity potential, however no successful commercialized products have been made [4]. The issue with lithium-metal anode resides in its change in surface morphology throughout cycling, this is known as dendritic growth which eventually penetrate the separator material and make contact with the PAM creating an electrical short in the cell which may result in thermal runaway [4], [16]. As a lower capacity alternative to the lithium-metal anode, carbon anodes are used and make up a total 89% of all commercialized lithium-ion batteries as of 2016 [6], see Figure 2.3.

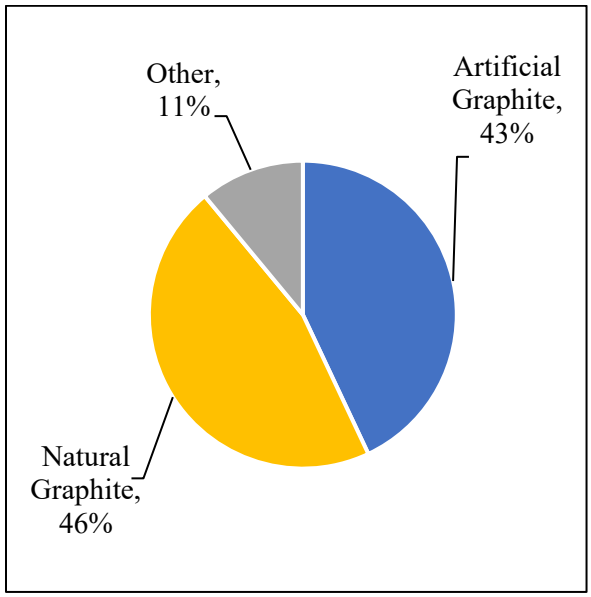

Figure 2.3 Anode material share of commercial LIB in 2016 [6]

Carbon anodes use synthetic or natural graphite which have a relatively low cost compared to alternatives, while maintaining high lithium cyclability and safety [4]. In order for carbon anodes to reversibly intercalate lithium ions well, they must be heated to form ordered graphene planar sheets; a process that is well described by Dahn's Falling Cards Model [17]. To form ordered graphene sheets, heat treatment temperatures range from 2000 to 3000 °C for soft carbons and above 3000 °C for hard carbons [4]. The two ordered graphite structures are 2H graphite (ABABAB stacking) and 3R graphite (ABCABC stacking) [4], see Figure 2.4.

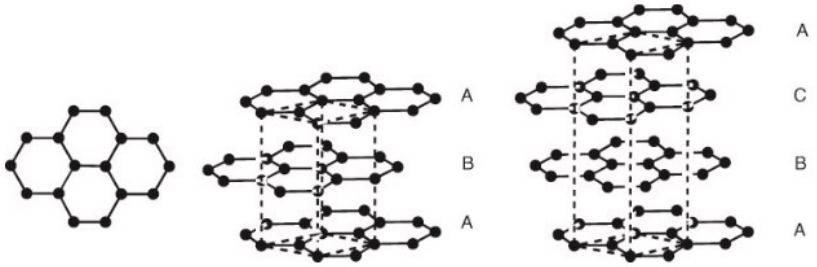

Figure 2.4 Graphene planar sheets (A, B, C) in both hexagonal 2H and rhombohedral (3R) structure of graphite [4]

An ordered graphite structure is required to intercalate lithium ions. Fully lithiated (i.e. all potential sites filled with lithium) graphite takes the molecular form LiC_6 and intercalates between two parallel

sheets (A, B or C) [4]. When lithium ions intercalate between specific parallel graphene sheets, this is known as lithium staging and creates a voltage plateau on charge or discharge.

Prior to heat treatment, carbon materials contain some ordered parallel carbon sheets, however they are mostly considered "turbostratically misaligned" [4]. The turbostratically misaligned sheets cannot intercalate lithium ions, thus the capacity of a graphite anode material can be calculated by multiplying the theoretical capacity (~372 mAh/g) by the fraction of graphene sheets that are parallel [4].

2.1.3 Electrolyte

The purpose of electrolyte is to transport lithium ions between PAM and NAM through the separator material. There are many types of electrolytes, with the most common electrolyte salt being $LiPF_6$ (lithium hexafluorophosphate), due to its high ionic conductivity [4]. Electrolyte ionic conductivity varies with viscosity, dielectric constant, and molarity. Viscosity of a fluid is related to temperature; hence at different temperatures, lithium-ion cells will have different ionic conductivities. In electrolytes, viscosity is inversely propositional to ionic conductivity, hence as viscosity increases, ionic conductivity decreases.

Increasing electrolyte molarity from 0 M to 1 M provides an increase in the dielectric constant which directly increases ionic conductivity due to an increased concentration of PF_6^- to transport lithium ions. However, after 1.0 to 1.5 M concentrations, the ionic conductivity decreases due to what is known as ion pairing [18], [19]. Ion pairing reduces the ionic conductivity of the electrolyte as PF_6^- ions pair to each other, ultimately reducing the concentration of available PF_6^- ions available to transport lithium ions. A plot by Valøen [18] of a $LiPF_6$ electrolyte reveals how ionic conductivity peaks between 1.0 to 1.5 M and increases with temperature, see Figure 2.5.

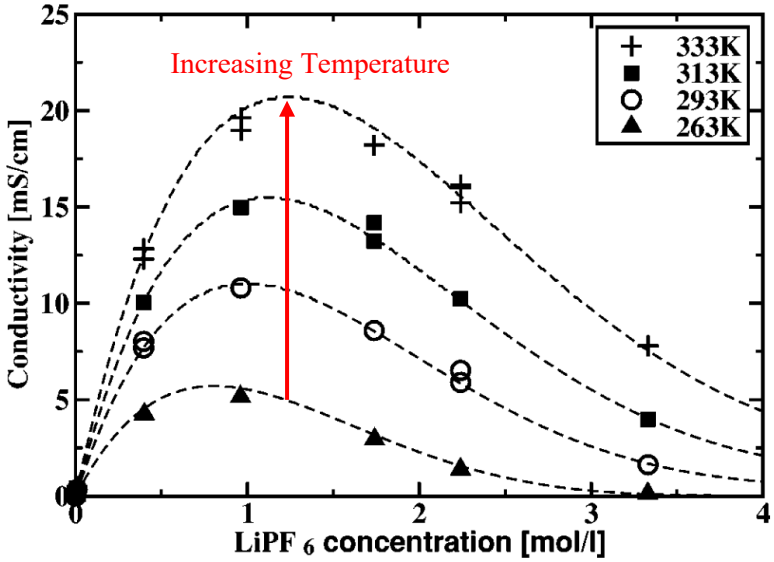

Figure 2.5 Electrolyte conductivity versus concentration at various temperatures [19]

To modify electrolyte conductivity, various carbonates, esters and acetate solvent additives are used forming approximately 2% of the total electrolyte [4]. Electrolytes typically use anywhere between 3–5 solvents in one mixtures to achieve their desired conductivity at a given temperature range [4]. Acetates such as methyl acetate (MA) typically give an order of magnitude increase in an electrolyte ionic conductivity when added in conjunction with a ethylene carbonate (EC) at low temperatures (-40 °C), making them ideal for high power cells in cold operating conditions, see Figure 2.6.

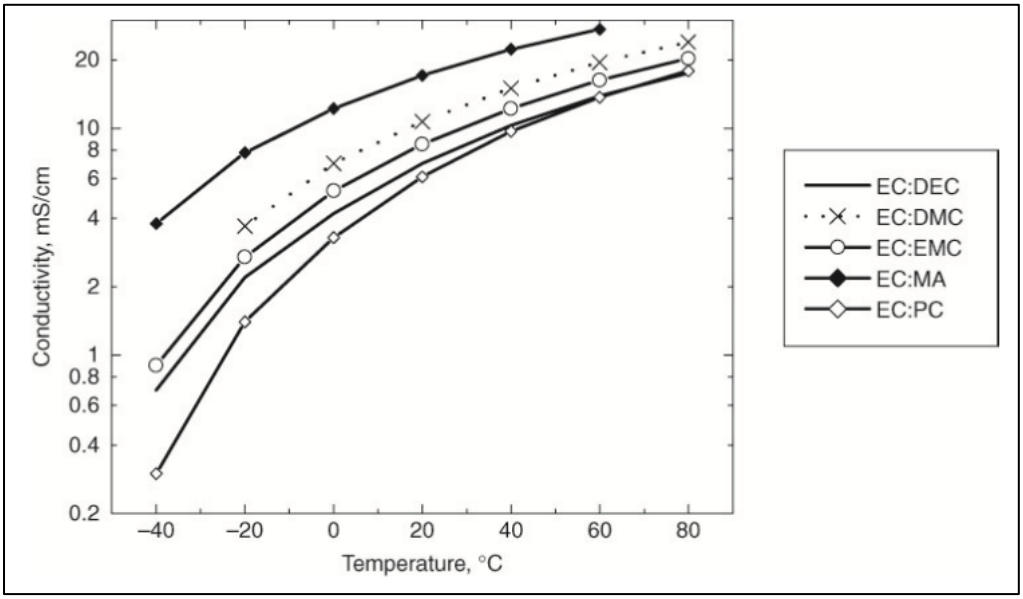

Figure 2.6 Conductivity versus temperature of 1 M $LiPF_6$ electrolyte with EC mixed with various other solvents [4]

By altering the electrolyte additives scientists and engineers make design trade-offs which include safety, performance (i.e. power at various temperatures) and cycle life (i.e. electrolyte degradation).

2.1.4 Separator Material

As lithium ions are transported from PAM to NAM during cycling, they pass through an ionically conductive yet electrically insulative layer known as the separator. Typical commercially available LIB use a 10 to 25 μm thick microporous polyolefin separator [4]. As the separator is inactive material, it provides no additional capacity to the LIB, making it ideal to have the thinnest separator possible. However, making the separator material excessively thin runs the risk of electrical shorting across the PAM and NAM, as demonstrated by Samsung's Galaxy Note 7 fire [20]. As the thickness of a separator decreases, this increases the risk of an internal short due to small electrode deformations caused by a mechanical stress (drop, impact, etc…). Separators in commercial use today include either a single layer polyethylene or polypropylene, or a tri-layer PP/PE/PP [4]. These microporous polyolefins have approximately 30 to 55% porosity with 0.03 to 0.1 μm pores [4]. The pores in the separator material act as a corridor for lithium ions to traverse from PAM to NAM. The microporous polyolefins polyethylene and polypropylene have respective melting temperatures of 135 °C and 155 °C [4]. If the separator melting temperature is achieved, the pores close preventing the transport of lithium ions, improving the safety of the LIB. However, once the melting point of the separator

materials is achieved, resulting in a decreased porosity, the separator may shrink and ultimately introduce an internal short. To prevent the shrinking of separator materials the tri-layer polypropylene/polyethylene/polypropylene separator material is utilized where the polyethylene melts, closing off its pores, whilst the polypropylene maintains its mechanical integrity and porous state. In the case of an external short where the cells temperature rises to the polyethylene melting temperature, the tri-layer separator closes all ionic pathways, eliminating electrochemical activity, consequently stopping electrical current flow.

2.1 Degradation Mechanisms

Degradation mechanisms in lithium-ion batteries reduce performance (i.e. discharge capacity, power and energy efficiency) and can ultimately cause the cell to fail entirely. Degradation is continuous but typically non-linear and occurs in all lithium-ion cells with each cycle. Cycle aging is minimized by operating the cell within the specified voltage range and cycling rates (i.e. power, current). Degradation can also occur through calendar aging which is minimized by storing cells at 50% SoC [21]. Given the variety of active materials, separators and electrolytes used to make lithium-ion cells there are a multitude of models and software packages (e.g. GT-AutoLion [22]) developed to simulate LIB performance using various electrodes sizes and cell formats. Model accuracy relies on five main degradation elements, which according to Smith [23] are mechanical, chemical, electrochemical, electrochemo-mechanical and thermal coupling. Mechanical degradation corresponds to the cell structure including packaging failure as a result of a physical load compromising cell integrity [23]. Chemical failure includes undesirable side-reactions occurring throughout calendar aging and is accelerated at elevated temperatures. Electrochemical degradation occurs as a result of cycle aging and is temperature and rate-dependant. Coulombic inefficiencies represent electrical current flow that contribute to unwanted side reactions, as a result, cycle aging is related to its coulombic efficiency. With increased electrochemical failure, unwarranted swelling and expansion of the cell originates causing internal mechanical stress on cell material which induces additional degradation, this is known as electrochemo-mechanical degradation. Thermal coupling is the aggregate element of chemical and electrochemical failure, as it accounts for increased chemical failure at elevated temperatures and increased electrochemical failure at decreased temperatures. There are numerous sub-categories of degradation mechanisms which lead to loss of cell capacity (e.g. current collector corrosion, microcracking and binder degradation [24]), however the two most predominant forms are excessive solid electrolyte interface (SEI) growth [23] and lithium plating [25] which are both products of cell LAM and LLI.

Modes of degradation such as lithium plating become contributors to degradation when the negative electrode voltage, with respect to lithium metal approaches 0 V near 100% SoC [25], [26]. Charging at slower rates reduces the probability of lithium plating as it raises the negative electrode voltage relative to lithium metal. Although the average potential versus lithium metal on the negative electrode may exceed 0 V, there can be a localized sections of the negative electrode that achieve 0 V relative to lithium metal due to a potential gradient across the electrode-electrolyte surface interface which is enhanced with increased charging rates [27]. Consequently, it is standard protocol that all lithium-ion cells are charged slower near the fully charged state to prevent the occurrence of lithium plating as this is when the negative electrode is closest to 0 V versus lithium metal. Lithium plating can also occur when the LAM on the negative electrode reaches a point where there is less capacity for lithium storage in the NAM than the PAM [4], [26]. Both SEI growth and lithium plating occur on the negative electrode and consequently consume lithium inventory and NAM. In order to account for the early stages of SEI growth and prevent the occurrence of lithium plating, a 10 – 20% additional NAM capacity preload is added to each LIB [4], [26].

The formation of the SEI layer requires an electron, electrolyte molecule and lithium-ion [24], [28]. The SEI layer is ionically conductive allowing lithium ions to pass freely, however once fully formed, the SEI layer is electrically insulative preventing additional electrolyte decomposition and further SEI growth [3], [4], [23], [26], [29]. SEI is formed on the negative electrode during initial cycling however can continuously grow due to mechanisms such as microcracking which compromise the electrical insulation allowing for electrons to re-contribute to SEI growth [3], [24], [28].

Evolution of electrolyte (gassing) occurs when either electrode achieves a voltage potential outside of the stability range for a given electrolyte [30]. As SEI growth is caused by decomposition of the electrolyte, when severe gassing occurs in a cell it is suspected that SEI growth is causing internal resistance (IR) growth as opposed to lithium plating. SEI growth and lithium plating can also be distinguished by the rate of capacity degradation as it is found that exponential capacity degradation is caused by lithium plating where linear capacity degradation suggests SEI growth [27]. As a majority of SEI growth occurs on the first cycle, the majority of gas generation is also formed on the first cycle, see Figure 2.7.

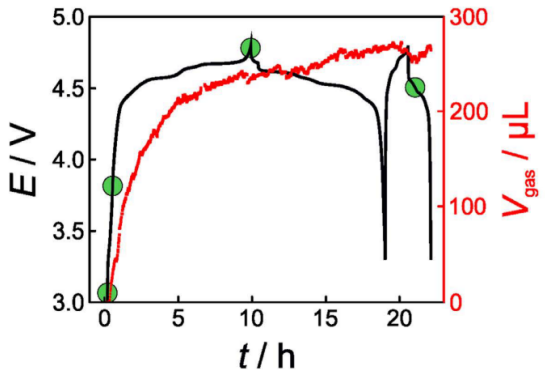

Figure 2.7 Graphite||LNMO (lithium nickel manganese oxygen) cell voltage and gassing response of first two cycles versus time - cycle 1 (C/10), cycle 2 (C/2) [30]

It is documented that gassing does not stop after cycles 1 and 2 and will continue to occur with increased cell degradation [31]. Galushkin et al. quantify the different gassing mechanisms and the molecular constituents of the gas with respect to cycling for a graphite||NMC 111 lithium-ion battery (LIB) [31]. Gasses inside the cell include CO_2, CO, H_2, C_2H_4 and O_2 [31]. CO and H_2 gasses are directly released as a result of electrolyte decomposition, whereas the CO_2 is formed as a result of combining O_2 and CO [31]. O_2 and CO are released from the PAM while H_2 and C_2H_4 are released from the NAM [31]. The gassing rate is dependant on temperature, electrolyte, active materials, cycling rates and operating voltage range of the cell. Holding all parameters constant other than operating voltage, will affect gassing, see Figure 2.8.

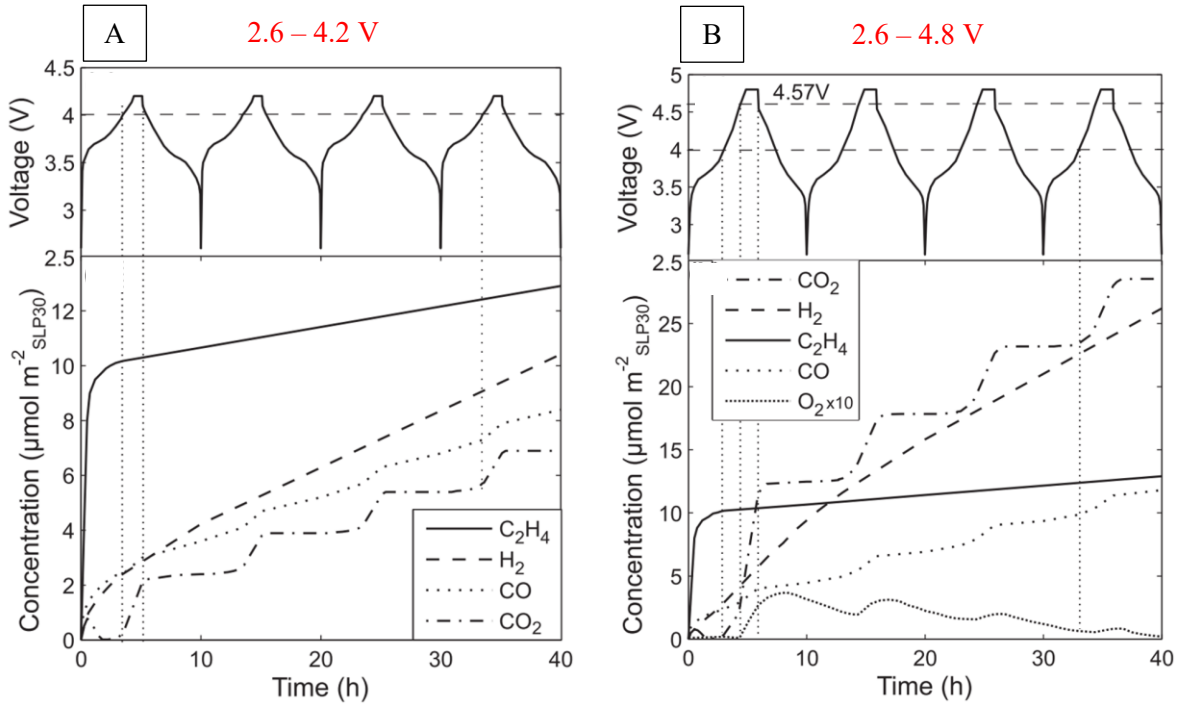

Figure 2.8 Gas generation as a result of operating voltage range A: 2.6 to 4.2 Volts, B: 2.6 to 4.8 Volts for SLP_{30} graphite||NMC cells [31]

The rate of C_2H_4 evolution appears to be constant for each voltage range whereas H_2, CO, and CO_2 have increased in generation on the larger voltage range. Figure 2.8 shows that increasing the operating voltage beyond the stable potential range of the electrolyte greatly accelerates gassing rates. In addition to the gassing study by Galushkin et al. [31], Metzger et al. [32] obtained similar results using an NMC cell, see Figure 2.9.

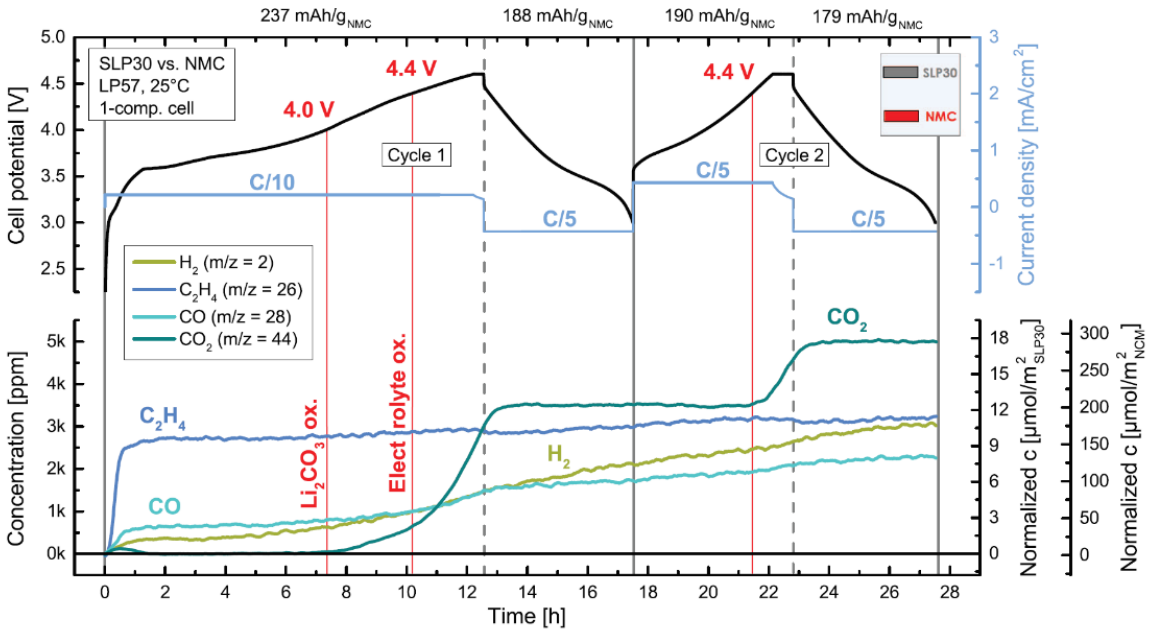

Figure 2.9 First 2 cycles of NMC cell gas generation results for SLP_{30} graphite||NMC cells [32]

The results from Galushkin [31] and Metzger [32] both agree that C_2H_4, CO_2, CO and H_2 make up the generated gas in a graphite||NMC lithium-ion cell. As the high voltage limit is increased, only H_2 and CO_2 gas generation is significantly increased, while CO and C_2H_4 gas production remain relatively constant. There is no evidence suggesting that the gas constituents would change for any other PAM oxide other than NMC as each gas contains no trace of nickel, manganese or cobalt and NMC is not considered to be to be a catalyst by both Galushkin [31] and Metzger [32].

Thus far, capacity loss has been attributed to LLI as a result of SEI growth and lithium plating. However, in addition to LLI, LAM can occur as a result of various mechanisms such as transition metal dissolution into the electrolyte and active material decomposition due to changes in crystal structure and oxidation [26]. While LLI reduces the available lithium ions for intercalation, LAM reduces the available lithium intercalation sites. Using dV/dQ techniques, the distinction between LLI and LAM can be made for degraded cells at EoL.

2.2 Cylindrical 18-65 Design Review

Three typical cell formats are pouch, prismatic and cylindrical. This research is focused on the 18-65 cylindrical cell design. The “18” and “65” respectively represent the diameter and length of the cell in millimetres. Cylindrical cells consist of what is known as a “jelly roll”. The jelly roll is a wound length of stacked positive current collector, PAM, separator, NAM, and negative current collector, all soaked in electrolyte. The cell dissection performed in this research experiment showed that 18-65 cells that have high energy densities utilize jelly roll lengths of ~550 mm whereas high-power ratings use 840 mm lengths. A longer jelly roll offers higher power due to the increased available surface area for improved lithium conductivity. A shorter jelly roll has a thicker active material which ultimately yields higher energy density for the same 18-65 cell cannister. The jelly roll is wound and inserted into a metal cannister with the negative and positive current collector tabs welded at the base and button top of the cannister respectively, see Figure 2.10.

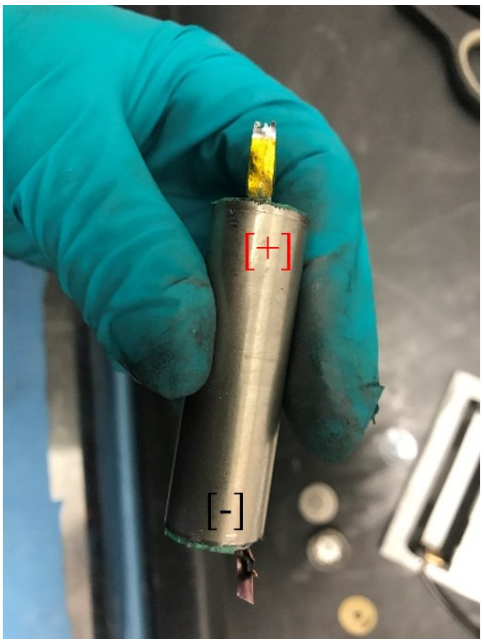

Figure 2.10 18-65 Base and top removed showing negative copper and positive aluminium current collector tabbing

The button top in a cylindrical cell contains several protective devices used to improve the safety of the cell [33]–[35]. Protective devices include a positive temperature coefficient (PTC) material, current interrupt device (CID) and scored disk vent, Figure 2.11.

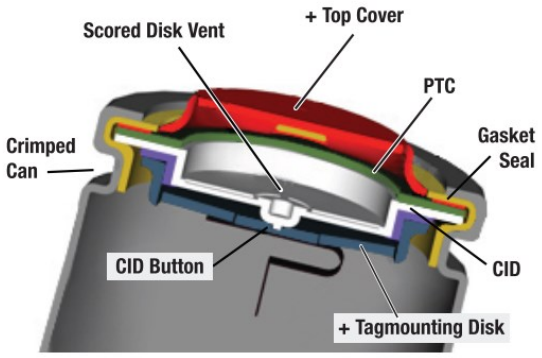

Figure 2.11 Cylindrical cell positive terminal cross-section showing protective devices [36]

Protective devices reduce the risk of thermal runaway or uncontrolled venting. Thermal runaway is the phenomenon of lithium-ion cell self igniting its own chemical constituents until all remaining flammable constituents have been consumed. The PTC operates by increasing its resistance with temperature. As the cell temperature increases and nears thermal runaway conditions, the PTC will become electrically resistive to the point that current will no longer be able to pass through the PTC to the button top positive terminal [33]. The CID is normally closed allowing for current to flow as shown in Figure 2.11, however if the pressure inside the cell exceeds 1000 kPa, the CID top will deflect upwards causing an electrical disconnect [33]–[35], [37]. Pressure increase inside a lithium-ion cell is caused by side-reactions producing gas inside the cell (Section 2.1). As shown in Figure 2.11, the PTC and CID are in a series configuration, thus if either are actuated, electrical current is stopped. On the CID top there are scored disk vents which will permanently rupture before the pressure inside the cell causes the metal cannister to burst in an uncontrolled manner [33].

2.3 Low Earth Orbit Conditions

The LEO CubeSat application offers unique cycling profiles and conditions which will affect performance and degradation of a LIB. The majority of LEO CubeSats use rechargeable LIB [38]. LEO satellites maintain circular or elliptical orbit altitude of 250–2000 km [39]. Depending on the altitude, the orbit period varies from 90-120 minutes with velocities ranging from 6-10 km/s [39], [40]. Consequently, LEO satellites experience 12-16 solar exposure / eclipse cycles per Earth day with the ratio of time spent in solar exposure and eclipse affected by inclination. Satellite inclination is the orbital angle relative to the equatorial plane measured in degrees. For a polar orbit (i.e. inclination of 90°) during summer and winter periods, there are month long periods of solar exposure occurring without eclipse [39]. According to the NanoSats Database [2], LEO CubeSats achieve

inclinations up to 100° with altitudes ranging up to 700 km. With a variety of inclination and altitude combinations, time spent during solar exposure and eclipse is by no means consistent between various LEO satellites. For example, with the same inclination, a 400 km altitude LEO with a 90 minute orbital period will experience a maximum eclipse period of 35 minutes whereas a 700 km LEO will experience a maximum eclipse period of 32 minutes (Note: this can be calculated using the radius of earth, the sun and their center-to-center distance). From this example it is clear that the benefit of being closer to earth to improve satellite imagery resolution is at the cost of extending eclipse time. Furthermore, changing the inclination will alter the ratio of solar exposure to eclipse time throughout the seasons. Orbital planes / inclinations are chosen based on the desired frequency for communication to the ground station and performing tasks such as infrared imaging over certain regions of the globe [39]. A satellite inclined at 90° may have the added benefit of monthlong periods with no solar exposure, however it will have less frequent communication to a specific ground station and repeated visits to specific surface locations on Earth [39]. A satellite inclined at 0° demands more from its energy storage than that of a polar orbit satellite due to a higher average eclipse period, however it will pass over the ground station to upload data and survey specific landscapes more frequently. Depending on the mission requirements (e.g. Survey location and frequency of data reporting), altitude and inclination play an important role in LEO satellite design and drastically affect how a satellite performs. According to Woellert [41], typical LEO CubeSats experience solar exposure for 66% of their mission whereas the remaining time the CubeSat is eclipsed by Earth.

The latest US Standard Atmosphere 1976 [42] explains how to compute the ambient pressure for elevations up to 1000 km above sea level. Depending on the range of altitude a specific formula must be applied. Typical LEO satellites maintain an altitude from 400 to 700 km, thus the formula used to calculate 120 to 1000 km altitude ambient pressure is used [43], [44], see equation (1).

$$Pr = \sum n_i * k_B(T_\infty - (T_\infty - T_{10}) * e^{-\lambda\xi}) \quad (1)$$

Where the kinetic temperature $'T_\infty'$ is defined by Figure 2.12 using the latest "1976" curve.

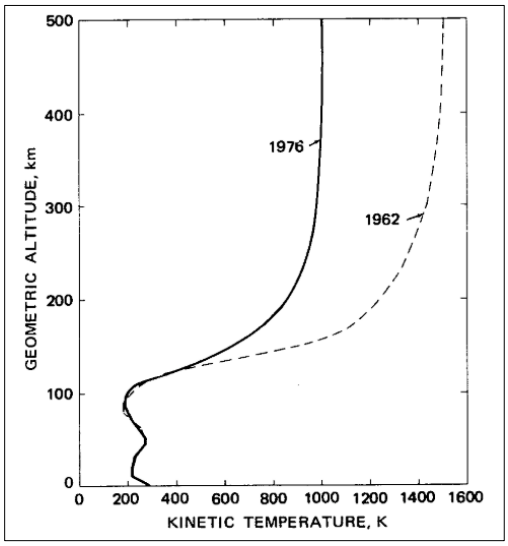

Figure 2.12 Kinetic temperature as a function of geometric altitude [42]

Beyond 150 km, the kinetic temperature varies significantly between the 1962 and 1976 model. The difference between each model is attributed to various altitude density measurements performed at various points across the solar cycle between the 1962 and 1966 [45].

The Greek constants 'λ' and 'ξ' are defined by equations (2) and (3).

$$\lambda = \frac{L_{K,9}}{T_\infty - T_{10}} = 0.022\ km^{-1} \tag{2}$$

$$\xi = \frac{(Z - Z_{10})(r_0 + Z_{10})}{r_0 + Z} \tag{3}$$

$$\xi = 268 \text{ km at } Z = 400 \text{ km}$$

$$\xi = 532 \text{ km at } Z = 700 \text{ km}$$

The variable $'\sum n_i'$ represents the gaseous species number density present at a given altitude can be approximated with negligible losses by calculating the density of each gaseous species individually [42]. The sum of the several gaseous species (N_2, O, O_2, Ar, He, H) number density is approximated using Figure 2.13 [42].

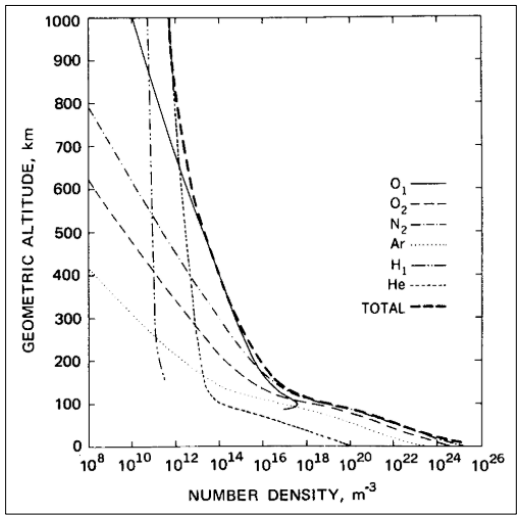

Figure 2.13 Number density of individual and total species as a function of geometric altitude [42]

From Figure 2.13 the total number densities at 400 and 700 km altitude are respectively 10^{14} and $5\text{x}\ 10^{13}\ \text{m}^{-3}$. Substituting the findings from equation (2), (3) and Figure 2.13 into equation (1) respectively yields an ambient pressure at 400 and 700 km, of $Pr_{400} = 1.24\ x\ 10^{-9}$ kPa and $Pr_{700} = 6.2\ x\ 10^{-10}$ kPa using the 1976 kinetic temperature model. Using kinetic temperature values from the 1962 model leads to overestimating the ambient pressure by up to 40%. An approximation for pressure can also be retrieved from Figure 2.14 which agrees with the calculated findings above for the 1976 model and with literature sources [46]–[49].

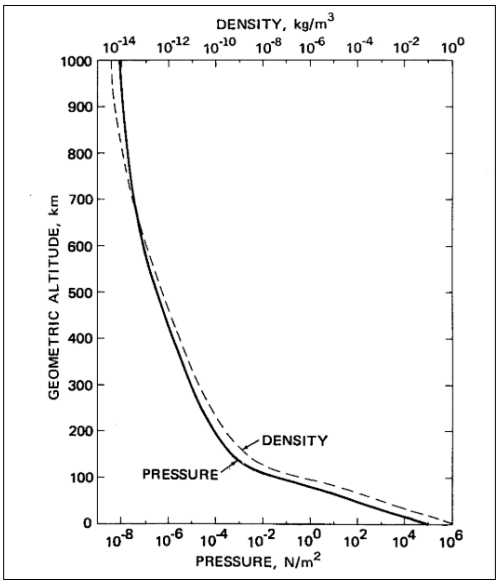

Figure 2.14 Total pressure and mass density as a function of geometric altitude [42]

The ambient temperature drastically fluctuates throughout the 90-minute LEO and is well documented by Harvey and Kinard's [50] international space station payload carrier data. Harvey and Kinard's findings [50] show temperature fluctuations from -50 to 150 °C with other published works [40], [48] reporting similar temperature ranges. However, because a battery is concealed inside the satellite, it is insulated from the majority of radiative solar effects. Additionally, the battery and satellite frame have thermal masses and are connected in a thermally conductive pathway to distribute heat. Both the thermal insulation, thermal mass and conductive network of the satellite stabilize battery temperature relative to the ambient LEO temperature. In the literature, the experimental ambient temperature used to test LIB for LEO range from 0 to 40 °C [51]–[53]. The intent of testing batteries in a range of temperatures for LEO applications highlights the necessity to represent battery operation and performance for the variety of satellite designs and power requirements. For example, some satellites with higher power demand operate cells warmer than a lower power demand. Additionally, satellites with the battery thermally affixed to the CubeSat chassis would be able to conduct heat to and from the frame at higher rates compared to a thermally insulated battery. Due to the insulated nature and thermal mass of a LEO CubeSat combined with the high frequency ambient temperature cycling in LEO (~90 minutes), experimental work can simulate the LEO condition using the average LEO temperature at steady state. The average temperature near the mean of Harvey and Kinard's [50] data was found to be approximately +10 °C.

Chapter 3 : Literature Review

The literature review summarizes experimental research performed on LIB for space applications. LIB experimental research in the electrical grid is also reviewed and contrasted with experimental research for CubeSat applications. A review of commercially available lithium-ion cells by format is presented which highlights cell availability and applicability to the CubeSat application. A review of how temperature, cycling rate, storage, ΔSoC and cycling equipment affect LIB discharge capacity and cycle life is included. Finally, a prediction model and EoL analysis technique that are both directly related to the findings of this research experiment are reviewed.

3.1 LIB Research for Satellite Applications

In 2005, Wang et al. [54] experimentally investigated the use of LCO chemistry for LEO satellite applications. They examined the effect of charge rate and voltage taper cut-off with respect to cell performance and impedance growth. It was found that increased charge rates induced more impedance growth while lowering the cut-off taper voltage from 4.20 to 4.10 provided significant advantages in reducing impedance growth at the cost of lowering discharge capacity. At the time, LCO was the highest produced lithium-ion chemistry. More recent work by Navarathinam et al. [47] investigates various LIB and lithium-polymer cells for CubeSat applications showing 25% capacity degradation in standard temperature and pressure (101 kPa, 0 °C) after 700 LEO cycles. However, Navarathinam et al. [47] did not repeat the 700 LEO cycles in a vacuum condition to fully prove their cells ability in the LEO vacuum environment. Additionally, they did not differentiate each LIB by their respective PAM, NAM, or electrode design. Work by Clark [51], Jeevarajan [52], [53], [55], [56] and Su [57] experimentally tested LIB in the pouch cell format for LEO small satellite applications. The motivation to validate pouch cells for LEO is driven by the future potential for a 5-10% increase in specific energy (Wh/kg) the mylar wrapped pouch cell has compared to the steel cylindrical can cell. It should be noted that to date, no pouch cell can withstand the vacuum in LEO without the addition of external restraints; ultimately negating any gains in specific energy. Although a 5-10% increase in battery specific energy is beneficial to CubeSats, it is my hypothesis that choosing the proper cell design (PAM, NAM, electrode sizing) has the potential to minimize the required mass and volume of energy storage onboard a CubeSat by more than 5-10%.

In 2019, Bugga et al. [58] completed a workshop presenting 18-65 (18 mm diameter and 65 mm height) LIB research for space applications. Test cells include the LG Chem MJ1, LG Chem M36, Samsung 35E, Panasonic GA and Sony VC7. These cells have high specific energy (259-276 Wh/kg)

and energy density (704-735 Wh/L) utilizing graphite NAM in combination with PAM made from NCA or NMC. Their work included a teardown, cycle life analysis, impedance growth analysis and resistance to radiation exposure for each cell. Radiation exposure was found to have had negligible effects on cell performance. Cycle life testing was completed at C/5 with 100% ΔSoC yielding 87 – 92% capacity retention from their initial capacity. LEO cycle life testing was completed at 20 °C for 20% and 40% ΔSoC cycles, however charge-discharge rates were not made clear. Bugga et al. [58] provided details on PAM, NAM and electrode design for each cell and comprehensively examined each cell for generic space applications, however, as their C/5 constant current (CC) cycling is not similar to a LEO CubeSat cycle it is unclear how these cells would perform in such conditions.

Presently, CubeSat missions typically utilize commercial off-the-shelf LIB such as the 18-65 Panasonic NCR18650B. CubeSat teams typically choose this cell based on its flight heritage [59], [60]. Jet Propulsion Laboratory in California [61] considers the Panasonic NCR18650B to be the current state of practice with future "state of the art" cells having a higher initial energy density. Krause et al. [62] investigated the performance of the Panasonic NCR18650B on both MarCO-A (6U) and MarCO-B (6U) CubeSat missions with the intent to utilize this battery in future missions as a result of its success in the MarCO missions. The strict mass and volume requirements of a CubeSat mission generally only accommodate two 18-65 cells per unit size (i.e. a 1U CubeSat houses two 18-65 cells), hence, cells with the highest energy density provide the largest initial energy capacity for the CubeSat. With CubeSats ranging in size from 1U to 16U [2], the modularity of a single 18-65 cell allows for battery packs to be scaled accordingly. An increase in initial energy capacity reduces the ΔSoE while cycling, and consequently the ΔSoC required from the cell. As presented by Dubarry and Devie [63], a decrease in operating ΔSoC increases cycle life. The advantage of a low ΔSoC on cycle life is one reason why the CubeSat industry continues to utilize cells with high initial energy density such as the Panasonic NCR18650B. However, high initial energy density is typically traded for power density and cycle life. The Panasonic NCR18650B has lower cycle life in comparison to the Lithium Werks APR18650M1B cell which has a relatively low initial capacity, high power rating and high cyclability as a result of its nanoscale LFP PAM. Few CubeSats utilize the LFP chemistry in their design. A conference paper by Drieger et al. [64] reveals a 3U CubeSat design that uses the LFP chemistry for LIB energy storage, however this LFP design choice is presented without any engineering justification. Having a lower initial capacity requires the cell to operate at a larger ΔSoE and ΔSoC in order to perform the same task, which lowers cycle life. However, if a low initial capacity cell can achieve greater total discharge energy throughput and LEO cycles, regardless of its increase

in ΔSoC, the questions remains whether a short life chemistry with high initial capacity provides the minimal battery mass and volume for a CubeSat. With CubeSat missions extending to 18 months (8,640 LEO cycles / orbits) or longer, there should be more emphasis placed on cell cycle life and total discharge energy throughput, as opposed to its initial capacity, energy density and specific energy. This may lead to minimized mass and volume of a CubeSat battery storage system for extended mission lengths.

3.2 Positive Active Material Selection by Application

As many industries utilize the LFP PAM technology, it begs the question why LFP has yet to be considered a point of research in the CubeSat application. Choi et al. [65], Crawford et al. [66] and Omar et al. [67] have investigated LIB PAM variants for a variety of other applications, notably for peak shaving, frequency regulation, and electric vehicle services. Their findings are summarized in Table 3.1.

Table 3.1 Frequency regulation, peak shaving and electric vehicle battery literature summary

Author		Findings Summary
Choi et al. [65]	i.	LFP has the lowest capacity degradation and IR growth under frequency regulation cycling.
	ii.	Electric vehicle capacity degradation between NCA and LFP cells are similar.
	iii.	Cycling ability varies with cell engineering/design while keeping PAM constant.
Crawford et al. [66]	i.	NCA and LFP have similar degradation rates under frequency regulation cycling.
	ii.	LFP has better capacity, energy, and round-trip energy efficiency retention than NCA cells under electric vehicle and peak shaving service cycling.
	iii.	NCA cells show continuous IR growth whereas LFP cells displayed initial growth that plateaued after 100 cycles for all services.
Omar et al. [67]	i.	LFP has advantages in power capability, capacity retention, energy efficiency and low temperature operation compared to NCA and NMC.
	ii.	LFP cells experience better cycling capability under the ISO 12405-1 battery cycling standard for electric vehicles compared to NCA and NMC.

The findings presented in Table 3.1 give the impression that NCA and NMC cells will perform better in short term CubeSat applications at low power and high temperature where LFP cells will perform

better in long term CubeSat applications at high power and low temperature. However, there is no CubeSat specific experimental testing to prove this hypothesis prior to this research.

3.3 Commercially Available Lithium-ion Cell Selection by Format

CubeSats are cube shaped satellites. In order to optimize the batteries volumetric footprint a square shaped cell inherently offers design advantages. The disadvantage of placing a cylindrical cell into a square object is quantified by the hexagonal stacking factor of roughly 0.907 by wolfram alpha [68]. In other words, cylindrical cells have a volumetric packing factor efficiency of 90.7% and subsequently require at most 10% higher energy densities than square format cells (prismatic/pouch). Of course, when comparing cylindrical and pouch cell formats, there are differences beyond the stacking factor. One unique advantage of the pouch cell is its potential for a higher specific energy by using soft case mylar bag instead of a steel can, however its energy density is hindered due to the volume required for electrode tabbing. Prismatic cells are a rectangular shaped cell with a metal cannister, which offers a hybridized format between pouch and cylindrical format. Comparing the most volumetric and gravimetric energy dense lithium-ion 18-65 cylindrical cells made by Panasonic [12] and LG Chem [11] with similarly sized commercially available pouch cells [69] and Panasonic's high energy density prismatic cells [70] it is clear that the 18-65 cylindrical format is currently superior with regards to energy density and specific energy, see Figure 3.1.

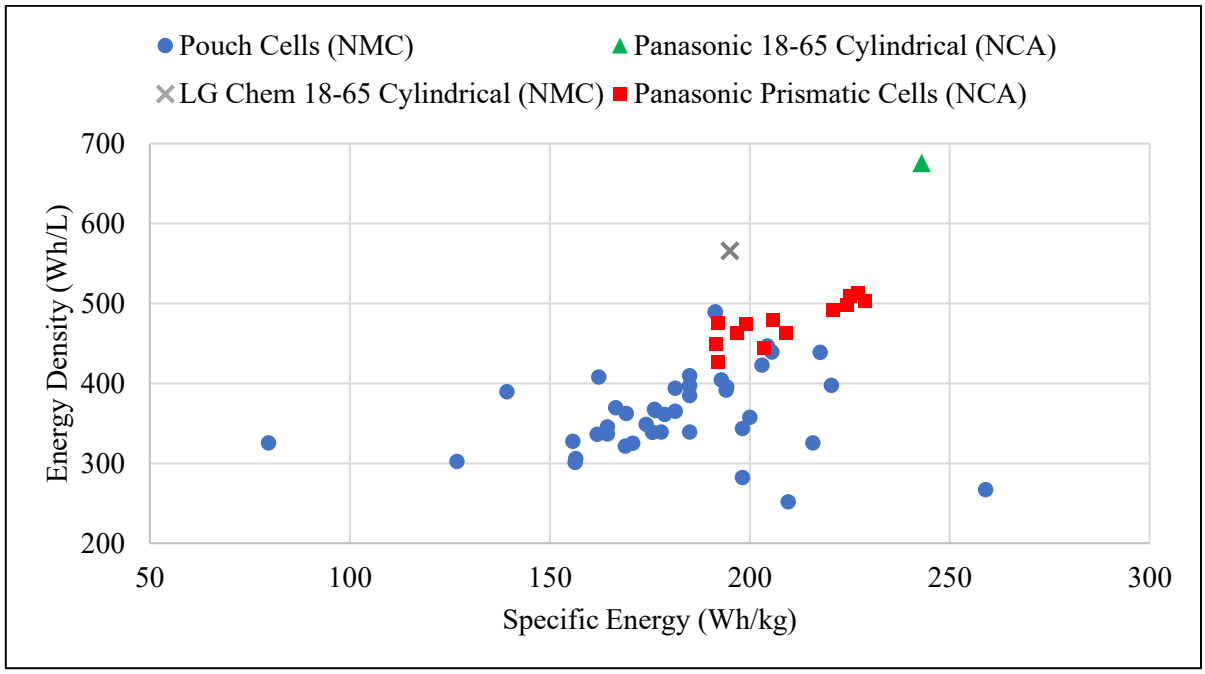

Figure 3.1 Energy density versus specific energy of commercially available cylindrical and pouch cells [11], [12], [69], [70]

In Figure 3.1 there is a clear advantage in energy density and specific energy with the Panasonic cells. This is due the Panasonic cell PAM chemistry (NCA) being the more energy dense than the LG Chem PAM chemistry (NMC). Regardless, both NCA and NMC 18-65 cells offer a gravimetric and volumetric energy density combination that is unparalleled by the pouch or prismatic format of similar energy capacities.

As cells become larger, it is typical for energy density to increase as the ratio of active material to inactive material (e.g. metallic casing, protective devices) decreases. However, even larger scale pouch cells by top tier manufacturers have energy densities and specific energies of 355 Wh/L and 180 Wh/kg respectively (example from A123's 26 Ah NMC cell [71]). These metrics are less than appealing compared to the Panasonic NCA and LG Chem NMC cylindrical cells previously presented in Figure 3.1. Its clear that both chemistries (NCA and NMC) have the highest combined energy density and specific energy in the cylindrical format that make up the aforementioned 10% stacking efficiency loss.

For CubeSat applications, having a relatively high gravimetric and volumetric energy density is desirable, however the cells must also be able to operate at vacuum. There has been extensive work

on pouch cells for space applications with the intention that there will eventually be a more volumetric and gravimetric energy dense pouch cell than the currently available 18-65 cells. However, the collective work by various researchers such as Clark [51], Jeevarajan [52], [53], [55], [56] and Su [57] indicate that pouch cells cannot maintain their capacity throughout cycling in vacuum conditions due to LIB side reactions generating gas (electrochemical degradation) which causes their thin mylar outer jacket to expand significantly. Expansion of the mylar jacket causes separation between electrode layers and ultimately accelerating side reactions (electrochemo-mechanical degradation) causing an exponential release of gas leading to rapid cell failure. Jeevarajan [56] clearly demonstrates how pouch cell degradation in vacuum can be mitigated by the use of restraints. Additionally, the use of restraints on pouch cells is mandated by NanoRack's regulation [72]. However, by introducing restraints on pouch cells, any specific energy advantage associated with the pouch cell format is abandoned. It is clear that the use of pouch cells without the use of restraints in vacuum environments should not be considered until electrochemical degradation side reactions can be entirely eliminated. In order to achieve zero side reactions in lithium-ion cells, the coulombic efficiency will need to be 100%. A recent paper by Yang et al. [73] quantified the coulombic efficiency of commercially available lithium-ion cells to be from 99.58–99.99%, highlighting that even such high coulombic efficiencies, degradation and gas generation is still excessive. In addition, cylindrical cells offer safety mechanisms which are not present in pouch cells. Considering the findings of this subsection, the LIB cylindrical cell format technology is the most promising for CubeSat applications and explains why cylindrical cells are dominant in the CubeSat industry.

3.4 Effect of Temperature, Cycling Rate, Storage / Cycling State of Charge and Test Equipment on Performance

Dubarry and Devie [74] show that for a given cell design (format, chemistry), cycle life is impacted in a non-linear fashion at different ambient temperatures (+25, +35, +45 °C), discharge rates (1, 2 , 3C) and ΔSoC per cycle (5, 40, 70%). Each change contributes to a variety of degradation mechanisms (e.g. lithium plating, current collector corrosion, SEI formation, micro-cracking, gas evolution). Ma et al. [75] summarize that as the LIB temperature decreases, the viscosity of the electrolyte increases, consequently decreasing the rate in which active materials can intercalate lithium ions due to a reduction in ionic conductivity. This decrease in ionic conductivity can result in lithium plating during charge. As the LIB temperature increases, degradation mechanisms predominantly take the form of electrolyte decomposition, PAM breakdown in crystallographic

structure, binder migration to the NAM surface and SEI growth, all of which irreversibly reduce capacity and impede lithium-ion transfer due to an increased IR [75]–[77].

Krause et. al [62] completed performance testing of the NCR18650B cells for the MarCO A & B CubeSat missions at 0, 20 and 30 °C. Cells were cycled at C/5 (0.58 A) CC rates, in 8S groupings, over the full 100% ΔSoC range, with a 60 mA terminating taper current during constant voltage (CV) charge. Cycle life testing showed that initial discharge capacity was reduced by 16%, and the capacity degradation rate was doubled at 0 °C relative to 30 °C. IR measurements were completed at 20% SoC increments on cells at 0 and 20 °C, revealing that cells cycled at 0 °C had a 70% higher initial IR, achieving three times the IR growth rates compared to cells in the 20 °C condition. Cells were also assembled into 3S4P groups, to represent the 6U MarCO CubeSat battery size, and cycled at various CC discharge rates (C/20, C/10, C/5, C/3, C/2, 1C) and a C/10 charge rate at 0 °C. Results indicated an initial 31% reduction in total discharge energy at 1C relative to the C/20 discharge rate. Bugga et al. [58] tested five different 18-65 cells (LG Chem M36, LG Chem MJ1, Panasonic BJ, Samsung 35E, Sony VC7) for space applications that varied in PAM (NCA or NMC) and electrode sizing. Cells were cycled over 100% ΔSoC at C/5 at 20 °C and showed that the LG Chem MJ1 achieved the best capacity retention after 500 cycles (92%), whereas the Sony VC7 achieved the worst capacity retention (87%). The results by Krause [62] and Bugga [58] exemplify the variance in measured cell performance at various rates, temperatures and cell types.

Variation in cell performance is also significantly affected by testing equipment, experimental setup and storage SoC prior to cycling [21], [78]. Taylor et al. [78] indicate a variation in cell performance measurements of up to 4% occurring between experimental results for the same cell type, ambient conditions and cycling rates due to different experimental setup (e.g. voltage connections) or testing equipment (e.g. battery cyclers). Ashwin et al. [21] performed a calendar aging study on the same 18-65 NCA cells, at 20%, 50% and 90% SoC at 25 °C, in triplicate groups. Capacity measurements were taken prior to calendar aging at ~65-day increments. Results indicated that storing cells at 50% SoC achieved 1.4% and 3.4% better capacity retention than 20% and 90% SoC conditions. Findings such as this show that cell performance can be significantly affected by storage SoC. With the wide variation in battery testing equipment, cycling rates and manufacturer storage SoC, the importance of testing cells with the same equipment, experimental apparatus and from the same cell batch is critical in avoiding any inherent error in comparing results.

3.5 Prediction Models and Experimental Validation

Due to the non-linearity of LIB degradation, data-driven models that use end of discharge voltage to estimate spacecraft EoL have been proposed by Song et. al [79]. By utilizing end of discharge voltage, the spacecraft does not need to undergo 100% ΔSoC capacity reference cycles in order to estimate EoL failure. This technique allows continual mission operation while giving insights to EoL beyond that of generic reference cycling.

The non-linearity of LIB degradation inspired Fermín-Cueto et al. [80] to integrate machine learning in order to quantify EoL conditions. Utilizing machine learning, Fermín-Cueto et al. [80] can predict the point at which non-linear degradation initiates (the knee-onset) and when accelerated degradation begins (i.e. the knee-point) with a 12.0% and 9.4% error, respectively, using information from the first 50 cycles. The machine learning prediction model dataset was taken from Severson et al. [81] which utilizes 124 commercialized APR18650M1A graphite||LFP cells cycled over a 100% ΔSoC range from 1C to 20C. The data reveals that in all cases, linear degradation occurs at BoL until the knee-onset, after which degradation rates increase until EoL.

Song et. al [79] and Fermín-Cueto et al. [80] methodologies for battery performance analysis provide different forms of insight to battery performance as a part of the experimental work completed in this thesis. Where degradation rates are similar, the end of discharge voltage analysis presented by Song et al. [79] will be applied to estimate which cell groups will achieve the greatest EoL energy throughput. As Fermín-Cueto et al. [80] have utilized similar high power LFP cells to this experimental research, a contrast between their results on degradation trends, knee-onset and knee-point can be applied to the experiments results in this thesis.

Chapter 4 : Experimental Methods

In these subsections, lithium-ion cell selection, groupings and test equipment are presented. Cycling procedures to simulate LEO conditions and measure performance (i.e. discharge capacity, energy efficiency, IR, LAM and LLI) are also presented.

4.1 Lithium-ion Cells

The cells used in this study are shown at 1:1 scale in Figure 4.1 and summarized in point form below.

Figure 4.1 Panasonic NCR18650B (graphite||NCA), LG Chem ICR18650B4 (graphite||NMC) and Lithium Werks APR18650M1B (graphite||LFP). Scale 1:1

- Panasonic NCR18650B with graphitic NAM and a PAM composed of nickel cobalt aluminium (subsequently referred to as "NCA")
- LG Chem ICR18650B4 with graphitic NAM and a PAM composed of nickel manganese cobalt (subsequently referred to as "NMC")
- Lithium Werks APR18650M1B with graphitic NAM and a PAM composed of lithium iron phosphate (subsequently referred to as "LFP")

Each cell type has a unique PAM, NAM graphite particle size and electrode size (length, thickness), but are packaged in the same 18-65 cylindrical format. These cell types range significantly in design for energy and power, with the NCA type having almost 3 times as much energy capacity as the LFP type, and the LFP type having approximately 5 times the power density of the NCA and NMC type. Operating parameters from manufacturer datasheets are presented in Table 4.1.

Table 4.1 Single 18-65 cylindrical cell manufacturer data sheet specifications

Parameter	**NCA** [12]	**NMC** [11]	**LFP** [13]
Low Voltage Limit (V)	2.50	2.75	2.0
Nominal Voltage (V)	3.6	3.6	3.3
High Voltage Limit (V)	4.2	4.2	3.6
Max Continuous Discharge Current (C rate)	2.0	2.0	27.3
Max Continuous Charge Current (C rate)	0.5	1.0	3.63
CC-CV Charge Taper Current (mA)	65	50	50
Discharge Temperature Range (°C)	-20 to +60	-20 to +60	-30 to +55
Charge Temperature Range (°C)	0 to +45	0 to +45	0 to +55
Capacity (Ah)	3.35	2.6	1.1
Capacity (Wh)	12.1	9.3	3.6
Maximum Discharge Power (W)	24.1	18.8	99.0
Energy Density (Wh/L)	731	561	217
Specific Energy (Wh/kg)	265	214	93
Discharge Power Density (W/L)	1442	1121	5919
100% ΔSoE Cycles to 80% Capacity	250	300	4000

A batch of 30 cells were procured for each cell type and labelled A01 through A30. A Fluke BT-510 battery analyser (Section 4.2) was used for initial IR and OCV measurements, while mass measurements were taken with a Sartorius ELT103 milligram scale (Section 4.2), see Figure 4.2.

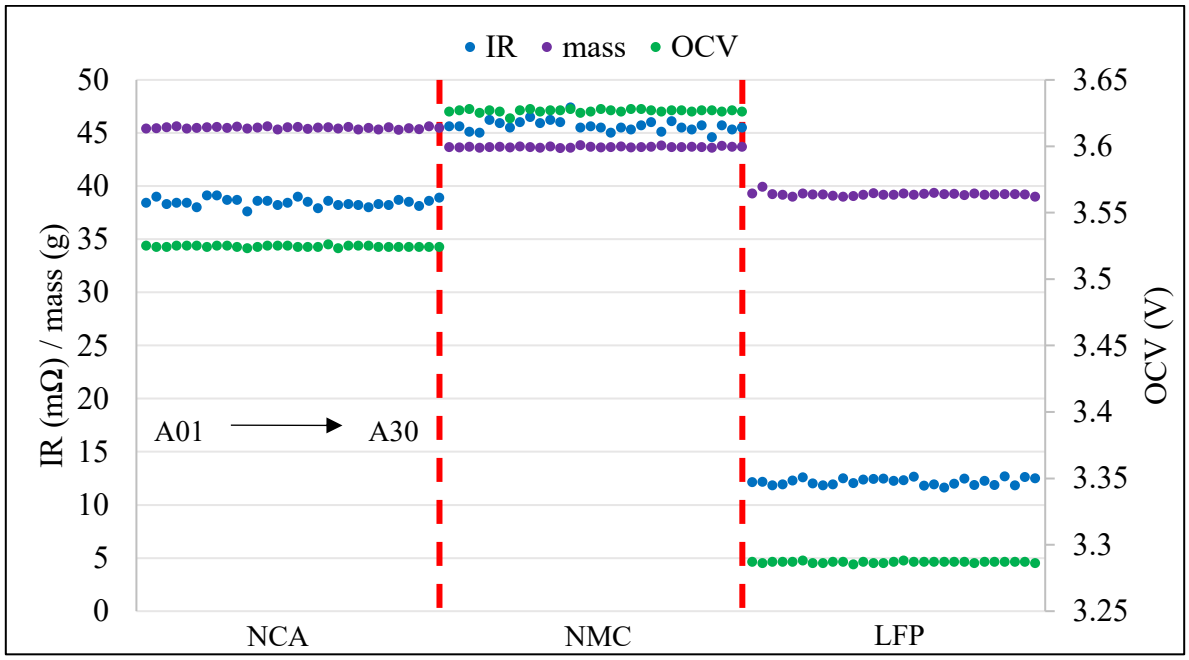

Figure 4.2 As received IR, mass and storage OCV measurements for cells A01 through A30 (left to right) for each batch of cells (NCA, NMC, LFP)

Manufacturing quality was assessed based on consistency between cells from a similar group. Since the viability of this research relies on these cells being state of the art lithium-ion 18-65 cells with no manufacturer flaws, it is not only important that they have adequate performance characteristics but that they are manufactured consistently to ensure performance repeatability. To assess the manufacturing quality of these three cells, the extremes (min/max) to the median is presented for the three cell types (NCA, NMC, LFP) and contrasted with a fourth low quality cell (brand 'X') as a control, see Figure 4.3.

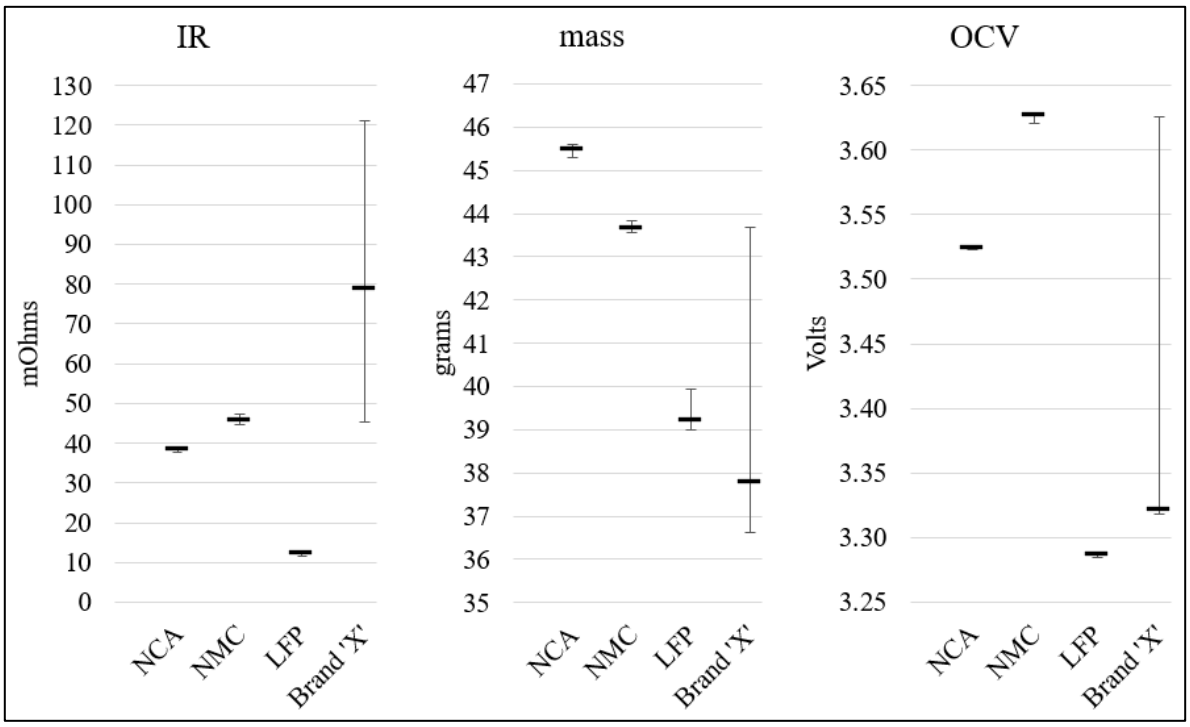

Figure 4.3 Median ± range bar (min/max) of as received IR, mass and storage OCV of four cell types (NCA, NMC, LFP, Brand 'X')

Figure 4.3 reveals that the three cells chosen for this research (NCA, NMC, LFP) are of much higher manufacturing precision than a low-quality brand 'X' cell by simply comparing the range in values for a batch.

From each batch of 30 cells, nine test cells were selected for experimental degradation cycling, verifying that they were well within the norm of each cell batch population in terms of mass, IR, and as-received OCV. Additionally, the initial discharge capacity of each of the test cells were validated to be within 1% of each other.

4.2 Equipment

Two types of battery cyclers, the Arbin BT2000 (Figure 4.4) and Neware BTS-5V50A (Section 4.2.1), were used to accommodate experimental design and desired cycling rates. The battery cyclers, thermal chamber and additional equipment used throughout this experimental study are summarized in Table 4.2.

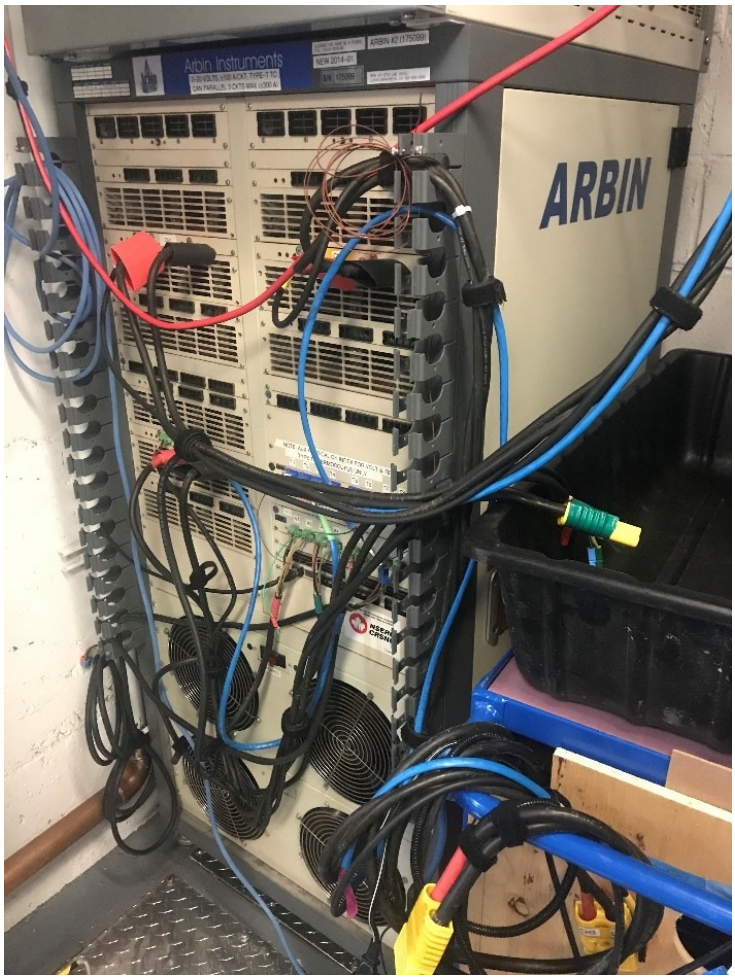

Figure 4.4 Arbin BT2000 power cycler

Table 4.2 Instrument summary (experimental design)

Instrument	Description
Fluke 289 multimeter [82]	Voltage range 0.05 to 50 VDC ± 0.025% accuracy, current range 500 µA to 10 A ± 0.15% accuracy.
Arbin BT2000 battery cycler [83]	3 channels each rated for ± 20 V and ± 100 A with type T thermocouple sensors. Medium current setting used (±2 A). Accuracy on medium current setting: ± 20 mV, ± 2 mA.
Neware BTS-5V50A battery cycler [84]	8 channels each rated for ± 5 V and ± 50 A with type T thermocouple sensors. Accuracy: ± 5 mV, ± 15 mA (as per in lab calibration verification). Minimum current ±250 mA.
CSZ-32 thermal chamber [85]	1 chamber, -73 °C to +190 °C, Accuracy of ± 0.1 °C, interior volume: 0.9 m^3, floor area: 0.93 m^2.
Sartorius ELT103 milligram scale [86]	Max weight 100 grams at ± 0.003 g accuracy.
Fluke BT-510 battery analyser [87]	Voltage range ± 6 VDC at ± 0.09% accuracy, IR range 3 to 3000 mOhms at ± 0.8% accuracy.
Hitachi S-4700 scanning electron microscope [88]	Device used to perform scanning electron microscopy (SEM) imaging.

4.2.1 Neware BTS-5V50A

The Neware power cycler (Figure 4.5) completed all accelerated LEO cycling, discharge capacity, energy efficiency and IR reference cycling, resulting in excess of 99% of all cycling that correspond with this research.

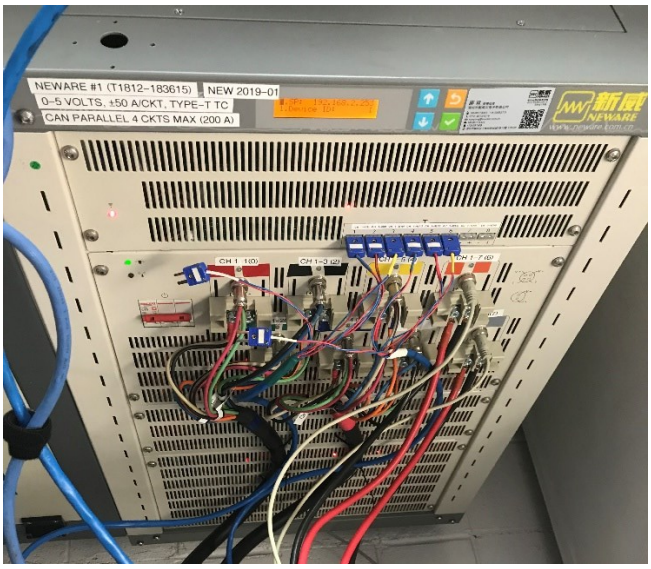

Figure 4.5 Neware BTS-5V50A (8 Channel) power cycler

The accuracy of the Neware power cycler for both voltage and current is specified to be ± 0.1% of full-scale output (5 V, 50 A), thus the accuracy is ± 5 mV and ± 50 mA. It is critical to understand the accuracy of this machine and its operating range when designing a test. For instance, the manufacturer data sheet for the NCA, NMC and LFP cells being tested as a part of this research specify a standard constant current constant voltage (CC-CV) charge taper current of 65 mA [12], 50 mA [11] and 15 mA [13] respectively. These taper currents according to the specified accuracy would yield large measurement inaccuracies.

In order to determine the minimum current used in the experimental design, a calibration verification of the Neware was completed on both its voltage and current using the Fluke 289 multimeter. The Fluke 289 was recently calibrated (2018) and is one order of magnitude more accurate than the Neware. In order to confirm voltage measurements a test was performed which consisted of connecting a LIB to each channel while measuring the voltage with the Fluke 289 and the Neware simultaneously, see results for each channel in Figure 4.6.

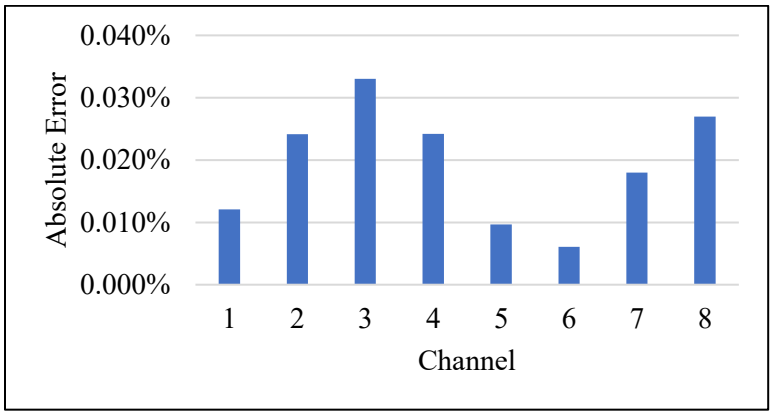

Figure 4.6 Neware BTS-5V50A voltage calibration verification

The results from Figure 4.6 indicate a max inaccuracy of ± 0.033% (at 3.3 V) on channel 3 which is more accurate than the manufacturer specified voltage accuracy of ± 0.1% (at 5 V).

To perform a calibration verification on current, a shunt is placed in the electrical loop between a battery and Neware. For currents up to 10 A the Fluke 289 multimeter (current mode) inbuilt shunt resistor is used, see Figure 4.7A. For currents ranging from 10 A to 50 A an external shunt resistor with a known resistance was used in conjunction with the Fluke 289 multimeter (voltage mode) to measure the voltage across the shunt and directly calculate the current travelling across the shunt using Ohm's law, see Figure 4.7B.

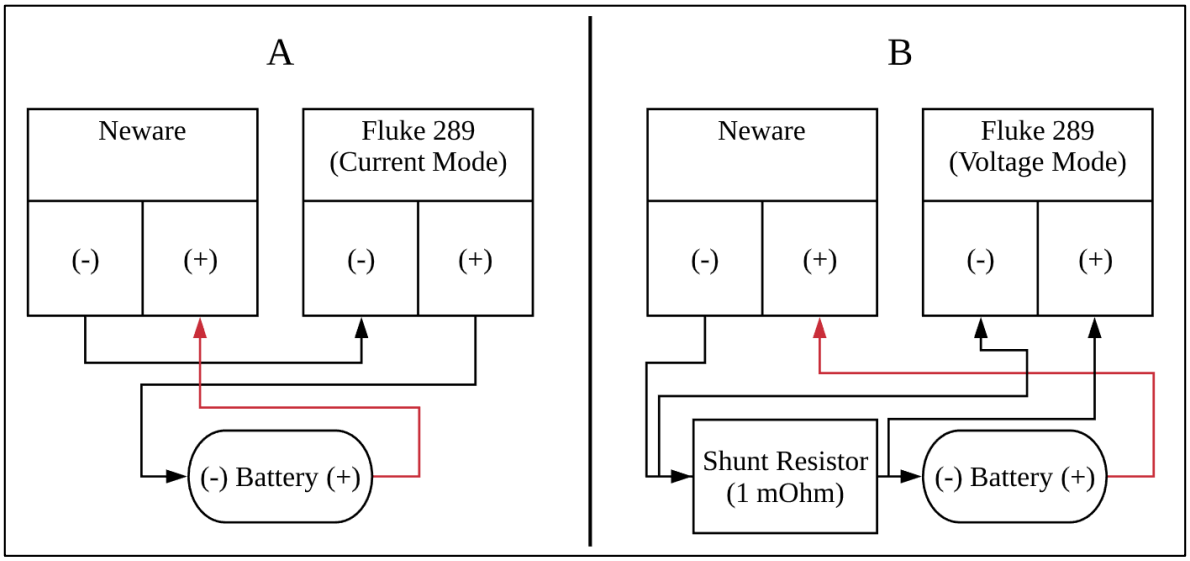

Figure 4.7 Calibration verification setup schematic. A: Fluke using internal shunt (current mode), B: Fluke measuring external shunt (voltage mode)

Currents tested on each channel range from 10 mA to 50 A for both charge (positive current) and discharge (negative current) with the absolute error between the Fluke and Neware represented for all currents, see Figure 4.8.

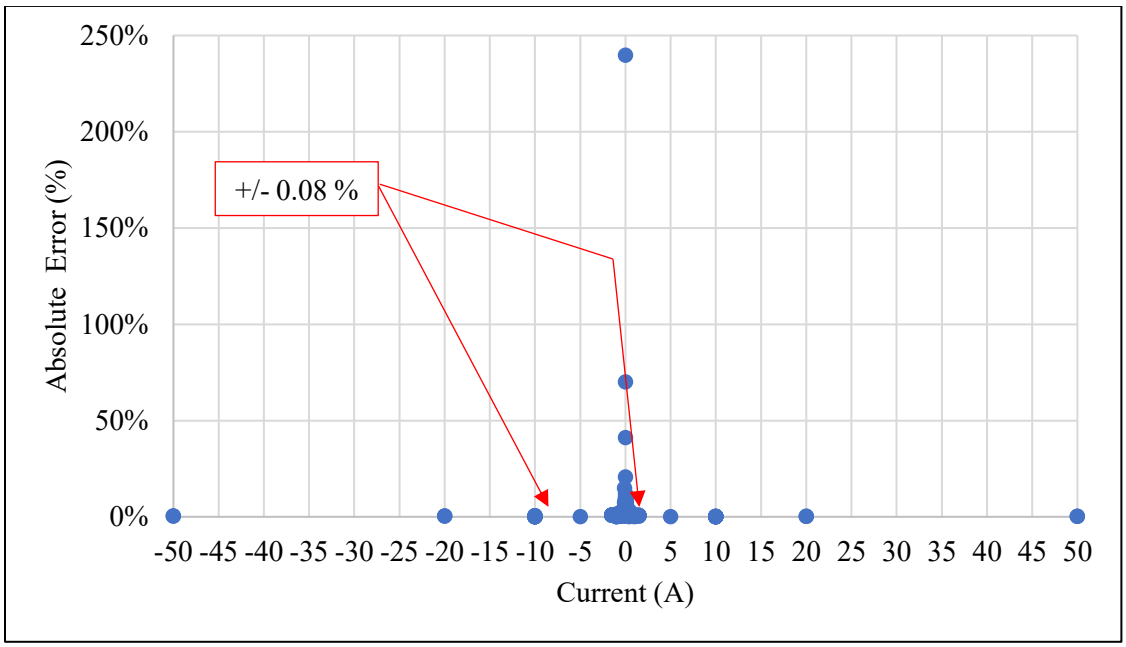

Figure 4.8 Neware absolute error with respect to the Fluke 289 (%) versus current (-50 to +50 A)

It is clear from Figure 4.8 that the current measurement error increases exponentially as the current approaches zero on both charge and discharge. Figure 4.8 indicates that that currents greater than 5 A can be achieved with negligible error using the Neware power cycler.

Focusing on the 10 mA to 1 A range reveals that there is no significant difference in accuracy between charge and discharge and also highlights where CC-CV taper currents should be set for reference cycles, see Figure 4.9.

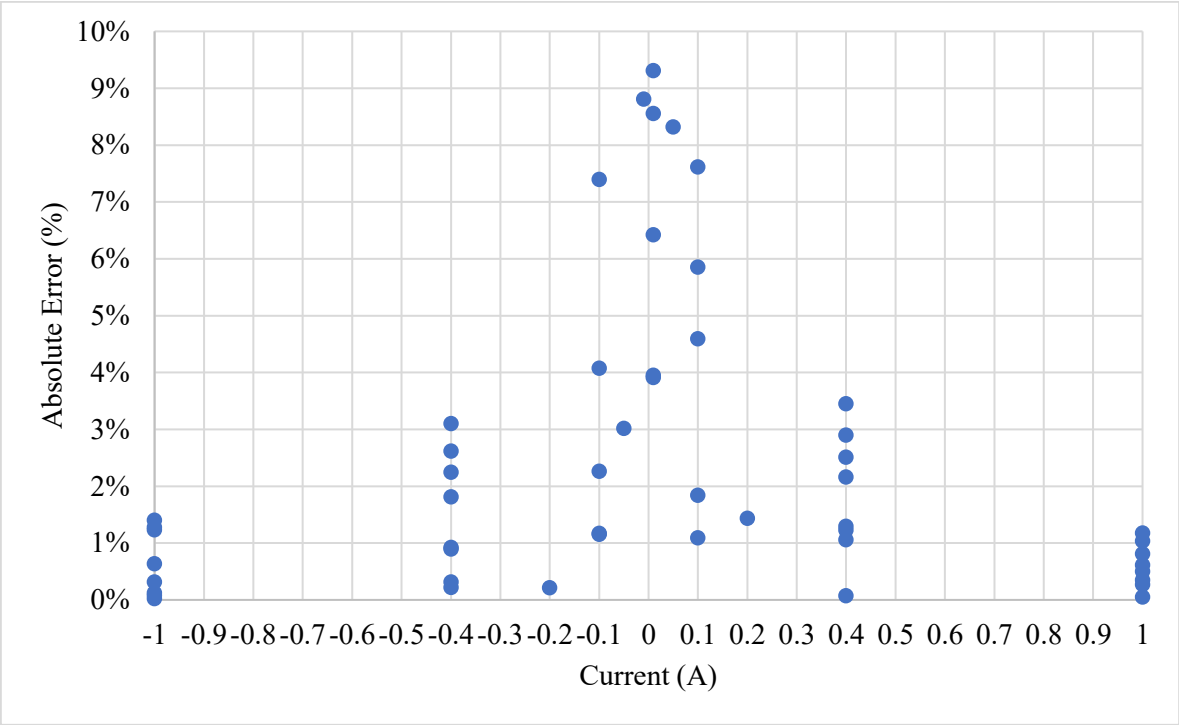

Figure 4.9 Neware absolute error with respect to the Fluke 289 (%) versus current (10 mA to 1 A) for all eight channels

Reference cycling is dependent on the capacity obtained from CC-CV to be consistently measured, thus the final CC-CV taper should not enter an exceedingly high level of absolute measurement error. Considering the results from Figure 4.9, it was deemed that the Neware should not be used for currents below 250 mA. However, for a 24-hour cycling required to perform dV/dQ cycling (Section 4.5.3), constant currents as low as 140, 109 and 46 mA are required for the NCA, NMC and LFP cell types, respectively. These currents are too low for the Neware to accurately perform as per this calibration verification. Thus, the Arbin BT2000 power cycler was utilized for 24-hour cycling due to its ±2 mA accuracy (Table 4.2).

4.2.2 Vacuum System

The vacuum pump, plumbing, chamber, and electronic vacuum gauge used to achieve the 0.2 kPa pressure for the vacuum condition are presented ins this subsection. A summary of each component is presented in Table 4.3.

Table 4.3 Instrument summary (vacuum system)

Instrument	Description
Oil Filter	Flanged vacuum oil-mist-eliminating exhaust filter. Reduces atomized oil particulate to lab environment.
Oil Tray	Plastic yellow case for when oil mist filter drips oil.
Tubing	Flexible vacuum tubing (4 m in length), Approximate inner diameter of 6.6 mm.
Vacuum Chamber (Appendix A)	Interior volume: 0.0077 m^3, 16 current/voltage lines via two 304 SS ISO-KF-16 flanged couplings, 4 type T thermocouple lines via one 304 SS ISO-KF-40 flanged coupling, 1 vacuum line via a 304 SS ISO-KF-16 flanged coupling. 304 SS plate and leg material. Clear top is made of cast acrylic. Outer dimension: 610 mm x 305 mm x 30.5 mm. Minimum pressure of 0.2 kPa using the Leybold D4B Vacuum Pump.
Vacuum Gauge	Elitech VGW 760 vacuum gauge used to view and vacuum pressure inside chamber with a range of 0 to 2533 Pascals absolute. Data was recorded and logged using a remote sensing Samsung Galaxy S5 smart phone with Elitech Gauge application. Accuracy: ± 20 Pa for 53-263 Pa range Resolution: 0.7 Pa for 53-263 Pa range
Leybold D4B Vacuum Pump [89]	Oil based vacuum pump, max flowrate/vacuum: 2 m^3/hr / 1 kPa, max specification vacuum with/without gas ballast: 0.1 kPa / 0.061 kPa at zero flow. Achievable vacuum with/without gas ballast: 0.3 kPa / 0.2 kPa using this experimental setup.

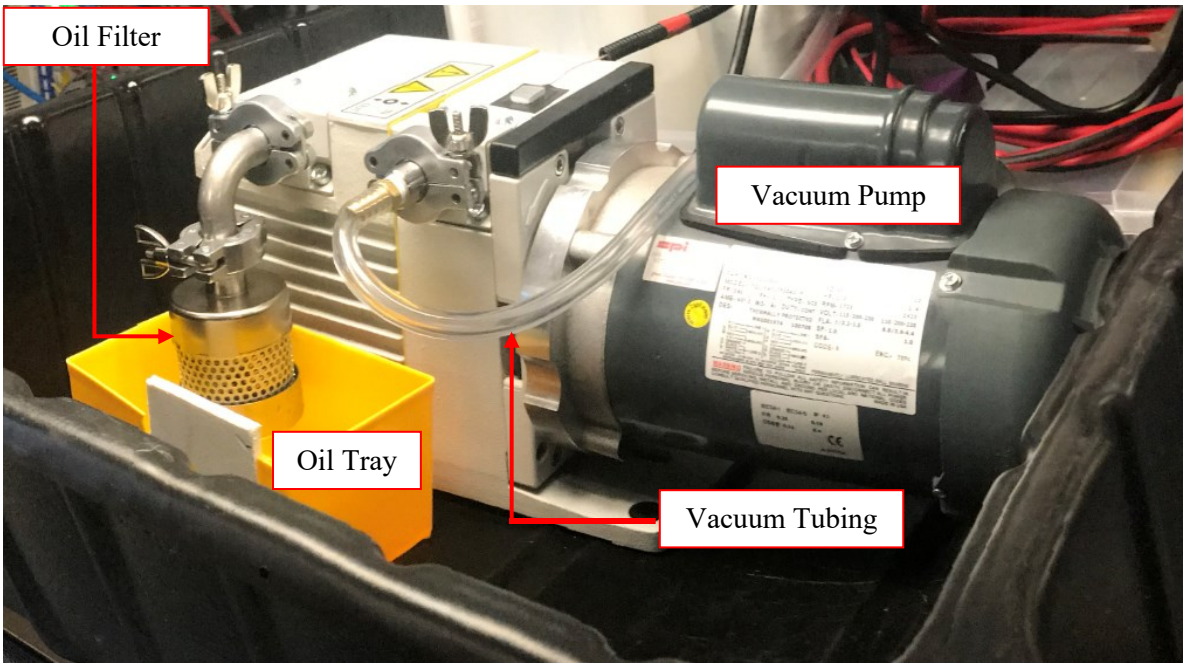

Figure 4.10 Vacuum pump in black plastic tote on top of thermal chamber

The vacuum chamber was custom designed and built to meet the needs of this research project, see Figure 4.11.

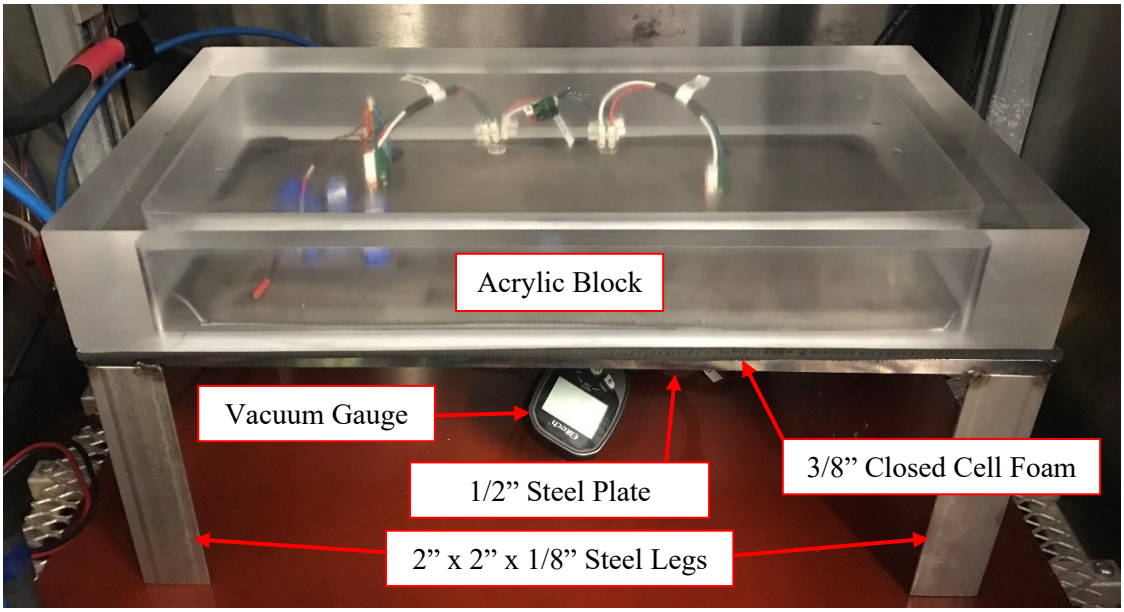

Figure 4.11 Vacuum chamber inside thermal chamber

The vacuum chamber consists of 304 SS angle for the legs and plate for the surface inside the chamber. The top of the chamber is made from a milled acrylic block which compresses a closed cell foam gasket to form a vacuum seal. The acrylic block was milled from an original 610 mm x 305 mm x 89 mm block yielding an interior dimension of 534 mm x 229 mm x 63.5 mm which provides adequate enclosure volume for the 3-cell battery holster apparatus. To ensure the milled acrylic block could withstand full vacuum (~101 kPa) distributed load, analytical calculations were completed to show stress along the longest length (i.e. 610 mm) of the acrylic block, see stress-deflection curves in Figure 4.12.

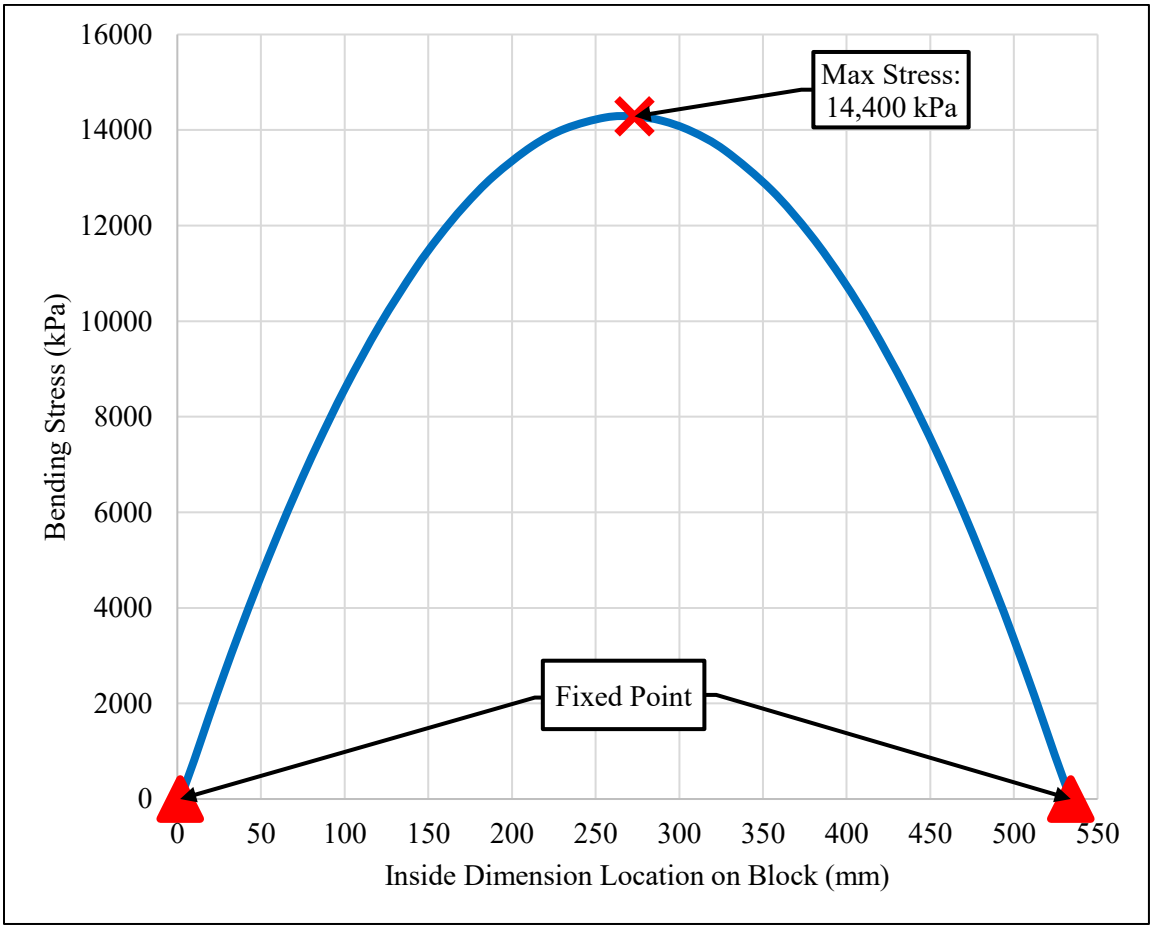

Figure 4.12 Analytical bending stress and deflection present along 534 mm inside length of acrylic block using BeamBoy v2.2 analytical beam bending stress and deflection software.

The modulus of elasticity and yield stress used for this analysis are 3.1 GPa and 69,000 kPa as per the physical properties for cast acrylic on MatWeb's [90] online database. The maximum stress was calculated to be 14,400 kPa which yields a safety factor of 5. The maximum deflection was calculated

to be 11 mm which is greater than desired but will not contact the test samples. However, as the analytical approach does not account for the wall support along the 610 mm length, the analysis is conservative meaning the deflection and bending stress and deflection should be less in reality. Upon fabricating the vacuum chamber, the actual deflection was measured and found to be approximately 1 mm, reassuring how conservative these calculations are and that the acrylic block can successfully tolerate a full vacuum load for the duration of the experiment.

The vacuum chamber has three hermetically sealed flanged couplings that are butt welded to the bottom side of the 304 stainless steel plate which are used for current, voltage and temperature connections, see Figure 4.13.

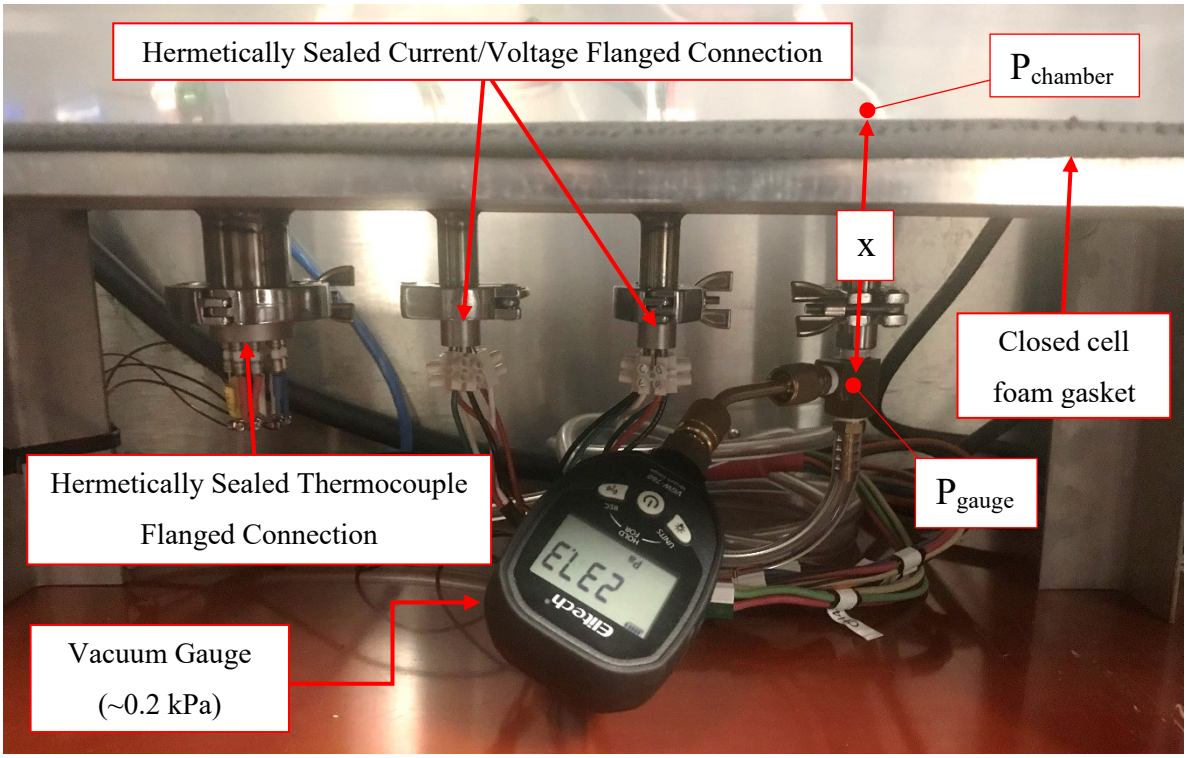

Figure 4.13 Underside of vacuum chamber showing Elitech digital vacuum gauge plumbed directly below base of the vacuum chamber

The fourth flange shown in Figure 4.13 support the vacuum tubing and gauge. Having the vacuum gauge outside of the chamber is ideal for resetting the gauge, changing batteries, or direct wiring without the need of additional vacuum tight electrical connections. As the flow rate of the vacuum pump is unknown, the vacuum gauge was plumbed as closely as possible to the vacuum chamber to

minimize any pressure difference along pipe length ‘x’ between the gauge measurement and the vacuum present in the chamber, as shown in Figure 4.13.

In Figure 4.13 the pressure in the chamber and at the gauge are respectively $Pr_{chamber}$ and Pr_{gauge}, while the distance between these pressures is represented by the length ‘x’. To verify that the pressure drop along the length of plumbing length ‘x’ was negligible, the vacuum gauge was placed inside the chamber to record vacuum pressure for a 3-hour period as shown in Figure 4.14.

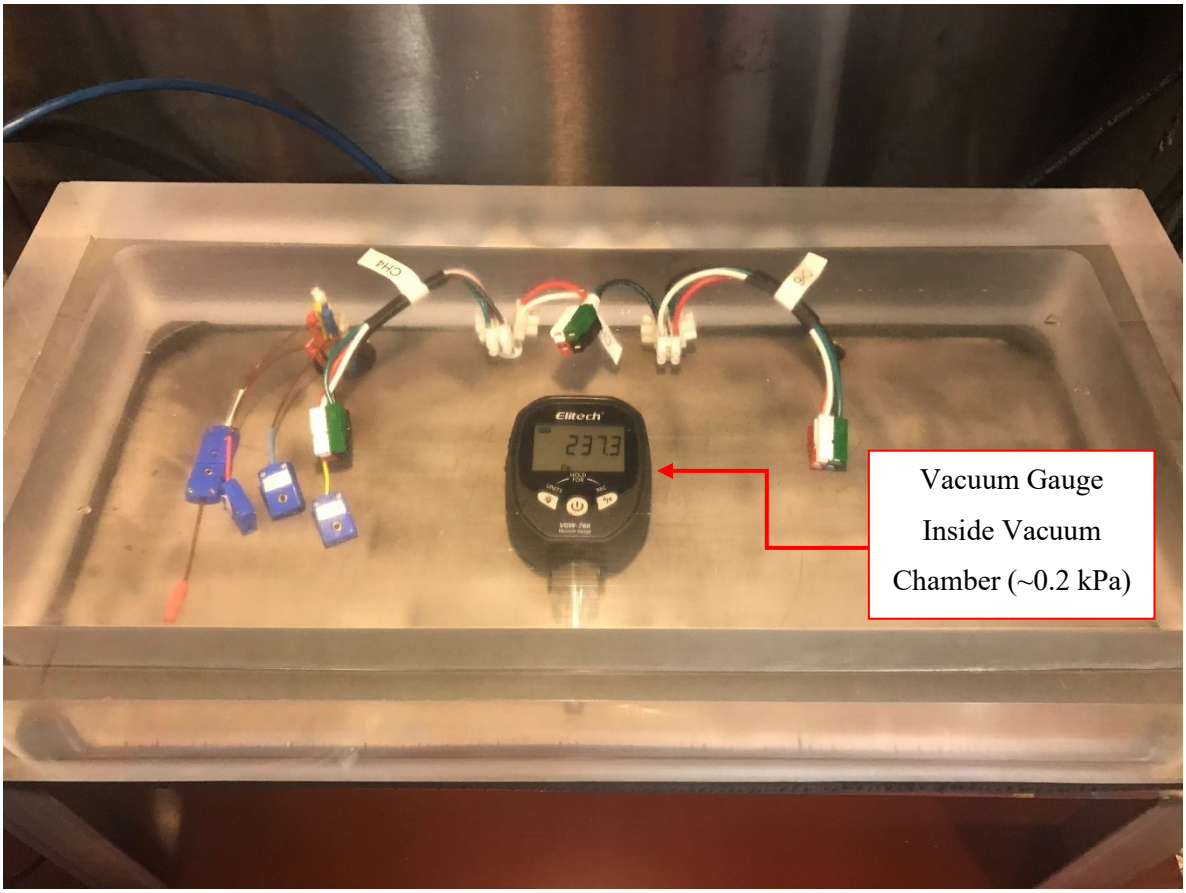

Figure 4.14 Vacuum gauge inside vacuum chamber to verify pressure difference between Pr_{gauge} and $Pr_{chamber}$

Upon comparing the vacuum pressure results obtained from the setup in Figure 4.13 to those in Figure 4.14, after 3-hours the pressure difference between Pr_{gauge} and $Pr_{chamber}$ was found to stabilize on identical pressure of 237.3 Pa with a instrument accuracy of ±20 Pa, concluding that the difference in pressure between both locations is negligible.

It was found through a technical investigation, that the Elitech vacuum gauge uses the Pirani principle to measure vacuum. In short, this finding was critical to perform the vacuum measurement shown in Figure 4.14 as the Pirani principle measures pressure using a heated wire with known thermophysical properties. Doms et al. [91] discuss the fundamental principles of the Pirani principle and show the heat loss from the wire is dependent on all forms of heat transfer (convection, conduction, radiation). As the vacuum gauge uses heat transfer to measure the pressure, the full gauge can be placed inside the vacuum chamber and accurately read the pressure. It should be noted that if a Bourdon tube gauge were placed in the vacuum chamber as shown in Figure 4.14, it would incorrectly measure the vacuum as it uses pressure differential between its surroundings and the desired point of measure. Consequently, a Bourdon tube gauge would read 0 kPa-gauge / 101 kPa-abs pressure if placed in the vacuum chamber.

4.3 Cell Groupings

Cells of a given type were grouped three-in-parallel (3P) for LEO CubeSat cycling, which represents a typical 2U sized CubeSat battery pack. From each cell type, one 3P group was cycled in the *laboratory* condition (101 kPa, 20 °C), one group in a *temperature* condition (101 kPa, 10 °C) and the other group in the *vacuum* condition (0.2 kPa, 10 °C). Cells were tested individually during reference cycling to identify inter-cell deviations of a group. This gives a minimum, median, and maximum value of each cell group for any metric of interest. This is intended to give confidence to the findings if inter-cell deviations are small relative to group differences and precludes a single good or bad cell from influencing conclusions.

The experimental setup diagram is shown in Figure 4.15. The three test conditions are described below:

1. ***Laboratory* condition (101±1 kPa, 20±1 °C).** The *laboratory* condition provides new information on LIB performance and capacity degradation while subject to a CubeSat power profile. Such testing requires only a programmable commercial battery power cycler. The laboratory is served by a dedicated tight-tolerance heating/cooling system. Cells are connected to a Neware BTS-5V50A power cycler that applies a varying power LEO cycle that discharges and charges the cell. The cycler has 8 channels each rated 0-5 V and ± 50 A with type T thermocouple temperature sensors. Accuracy: ± 5 mV, ± 15 mA, ±1 °C.
2. **Enhanced with low *temperature* condition (101±1 kPa, 10±0.1 °C)**. A temperature of 10 °C coincides well with the observed average temperature in LEO [50]. This low

temperature condition requires both a programmable thermal chamber (cooling mode) and battery power cycler. The thermal chamber is a Cincinnati Sub-Zero CSZ-32 (0.9 m^3) rated -73 °C to +190 °C with accuracy of ±0.1 °C.

3. **Enhanced with *vacuum* condition (0.2±0.05 kPa, 10±0.1 °C)**. The vacuum present in LEO is approximately 10^{-9} kPa [42]. This *vacuum* condition at low temperature is the most complicated, requiring 3 separate pieces of equipment, but best emulates the LEO conditions experienced by CubeSat batteries. A custom clear vacuum chamber was constructed, as shown in Figure 4.11. The vacuum pump achieves 0.2 kPa which is 99.8% of the vacuum in LEO. Other researchers have also opted for near 0.2 kPa for testing [51]–[53], [55].

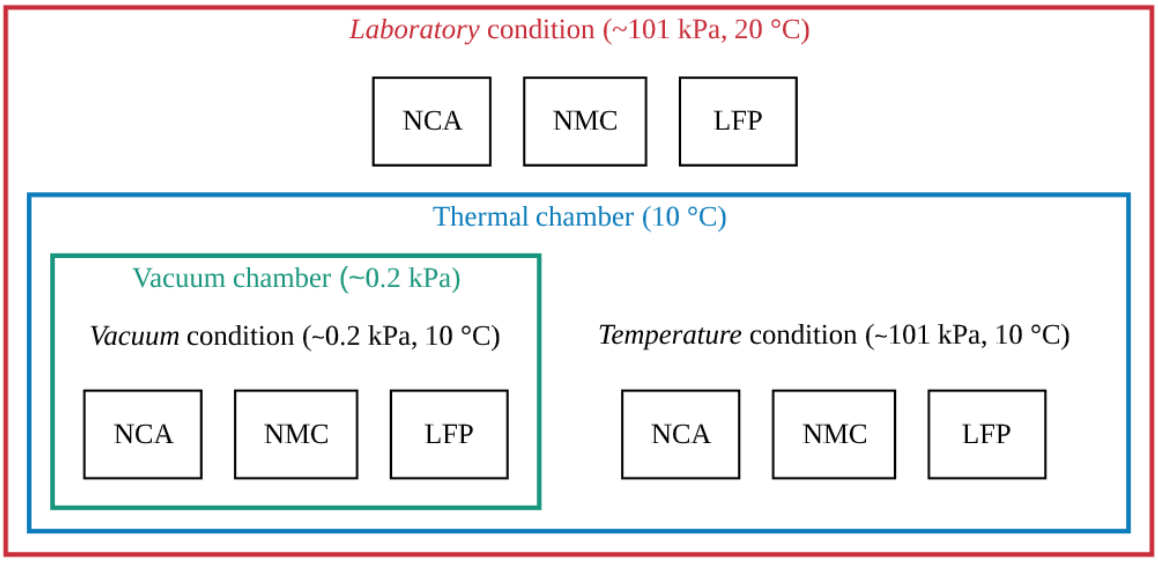

Figure 4.15 Experimental test configuration showing the temperature and pressure values for each of the three test conditions

A photo of the *laboratory* condition which is on top of the thermal chamber is shown in Figure 4.16, and the *temperature* and *vacuum* conditions which are inside the thermal chamber are shown in Figure 4.17.

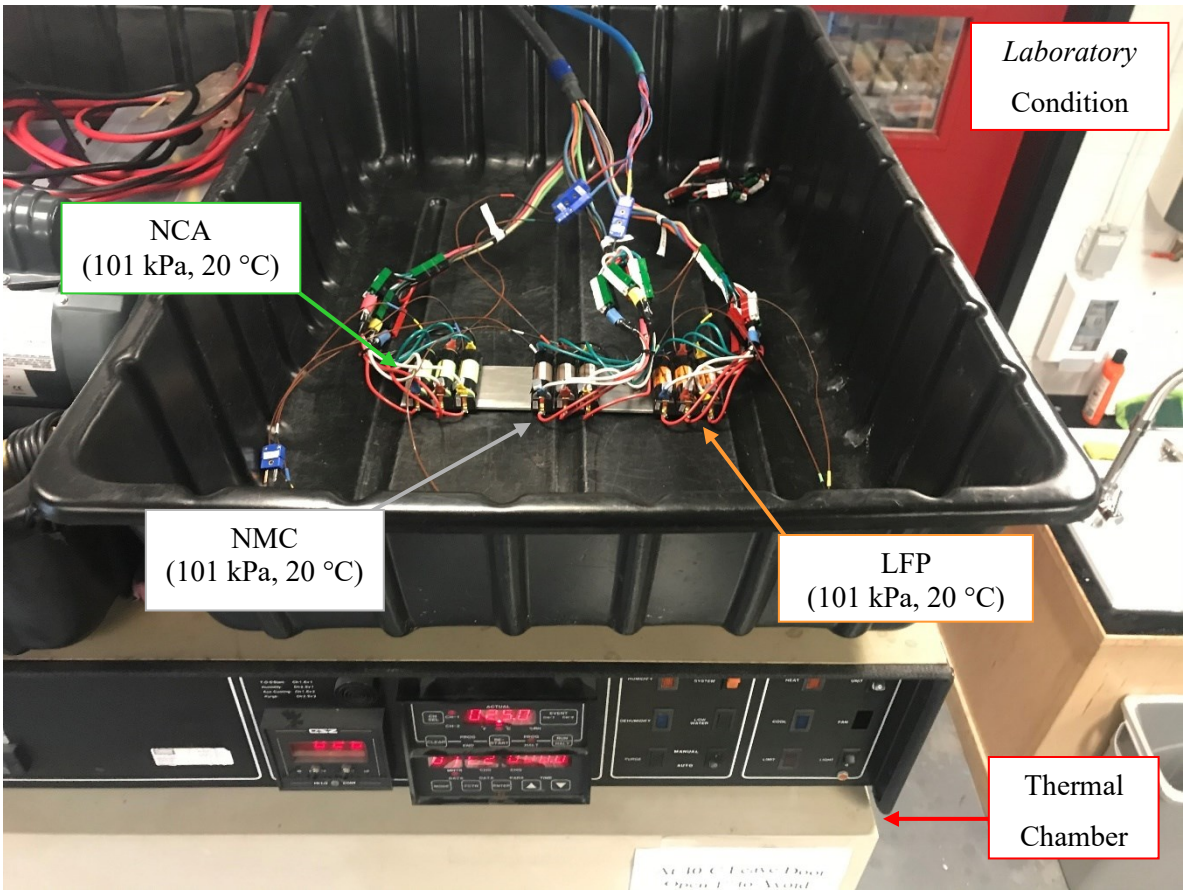

Figure 4.16 Experimental setup photograph of the laboratory condition test cells (101 kPa, 20 °C) in 3P groupings with current, voltage, and temperature connections on top of thermal chamber

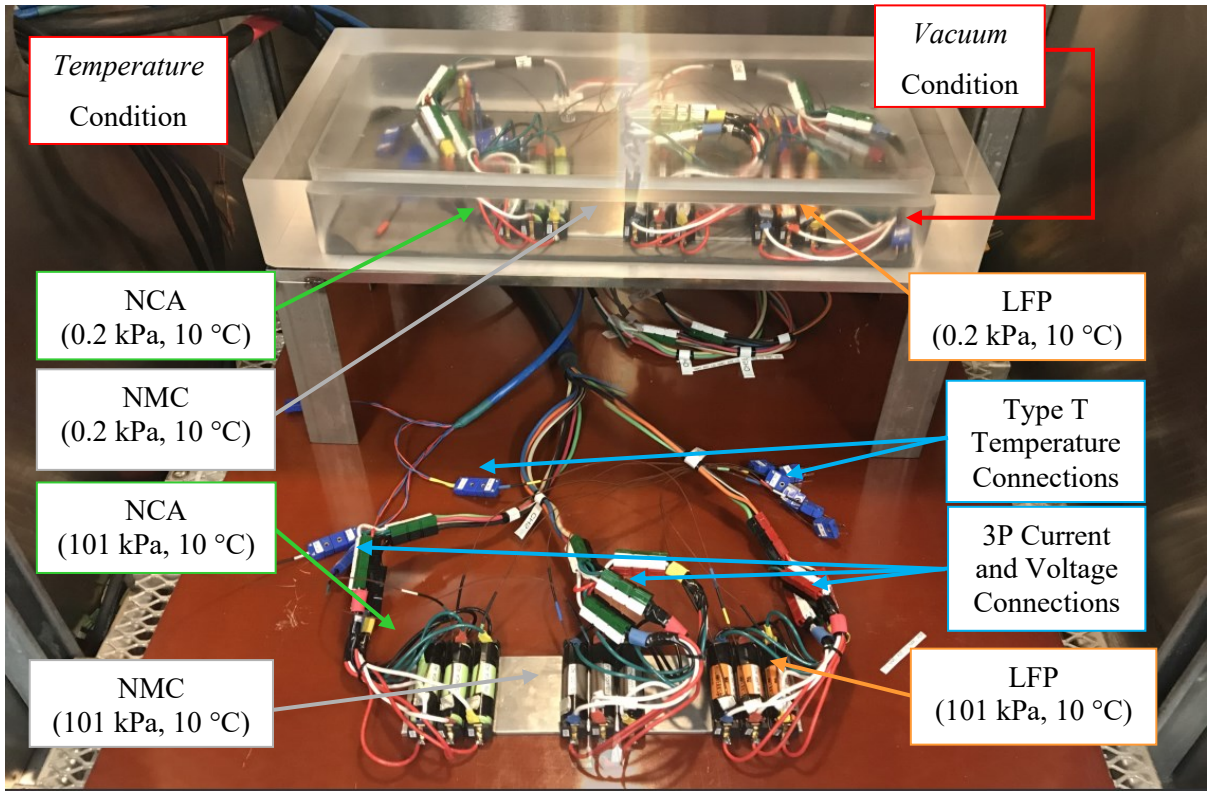

Figure 4.17 Experimental setup photograph of the interior of thermal chamber with temperature condition test cells (101 kPa, 10 °C) and vacuum condition test cells (0.2 kPa, 10 °C) in 3P groupings with current, voltage, and temperature connections. Note that the test cells in laboratory condition (101 kPa, 20 °C) are not shown

The cell groups were subjected to a representative LEO cycle consisting of constant power (CP) discharge and sinusoidal power charge in their respective conditions. Initially it was of concern that the vacuum chamber ambient temperature would not remain at 10 °C during LEO cycling due to its small volume and lack of air. However, each condition (*laboratory*, *temperature*, *vacuum*) temperature was found to remain at the desired steady state temperature (10 or 20 °C) condition regardless of the heat rejection during LEO cycling.

Tests used independent current taps and voltage sense taps for each 3P grouping. A 24 gauge type T thermocouple was adhered to the side of each cell, with a small piece of insulating tape placed over it (5 x 5 mm), as shown in Figure 4.18.

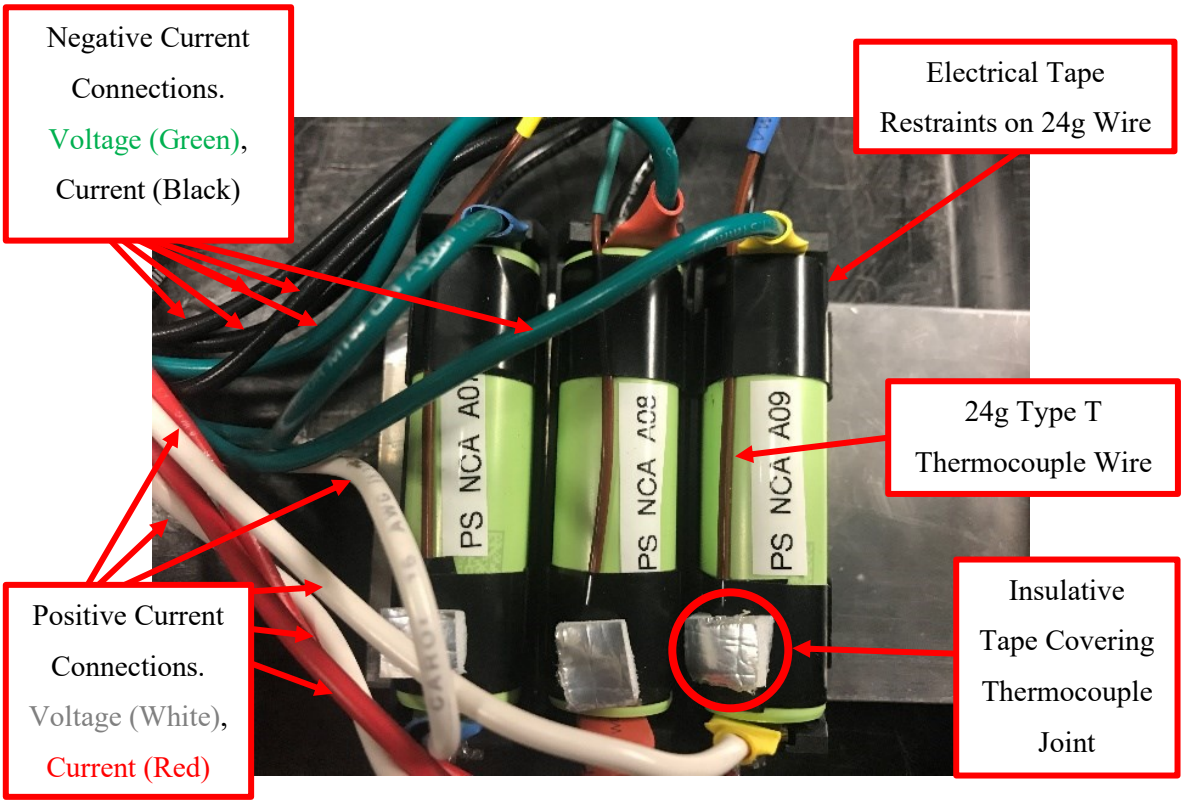

Figure 4.18 Grouping of three NCA cells with type T thermocouples permanently adhered to all cells in group for duration of experimental testing. Only middle type T thermocouple connected to power cycler for LEO cycling. The group holder construction assembly is given in Appendix A

Cells are kept in the same holder for the duration of testing. In Figure 4.18 the three cells can be modified from 3P groupings to three single cells without being removed from respective holders by simply disconnecting the "3P current and voltage connections" shown in Figure 4.17. Cell electrical connections are modified from a 3P configuration to a single cell configuration according to the needs of the test schedule.

4.4 Accelerated Low Earth Orbit CubeSat Cycling

During the accelerated LEO cycling, measurements were taken on a 5 s timestep. Insulated type T thermocouples were adhered to the middle cell of the 3P group (Figure 4.18), the inside of the laboratory, thermal chamber and vacuum chamber for measurement and safety purposes.

As discussed in Section 2.3, the altitude and inclination should be used to determine the change in power profile throughout the 365 day period of Earth's orbit about the Sun. However, for experimental battery testing, simulating inclinations near 90° would create month long periods of little to no discharge due to the lack of eclipse. Cycling batteries in this way would lengthen experimental battery testing time at no benefit due to long periods of rest. When testing battery energy

storage with the intent to expedite degradation results, it is ideal to use the maximum eclipse time to model battery discharge (i.e. simulating a 0 degree inclination) as it provides the largest amount of discharge energy throughput for a given rate.

One normal LEO typically requires 90 minutes, resulting in 16 orbits per 24-hour Earth day period. Orbit time varies with altitude and velocity with a maximum eclipse time of 35 minutes [39], [92]. During this 35-minute (2100 s) eclipse, the battery is discharged with a remaining 55 minute (3300 s) solar exposure charge period. In order to expedite cycling in this experiment, the LEO cycle was accelerated by a factor of 3, with 700 s discharge periods and 1100 s charge periods for a total LEO cycle period of 1800 s. During the eclipse period, a constant discharge power of 33.6 W is applied for 700 s to a 3P cell group, resulting in 2.178 Wh discharged per cell. During solar exposure, charge follows a sinusoid profile to represent fixed photovoltaic orientation. The charge profile provides sufficient energy to support a cell with 74% LEO cycle energy efficiency or greater. Since the test cells (NCA, NMC, LFP) have energy efficiencies above 74%, they complete charge early. The full 30 minute accelerated LEO cycle discharge-charge profile is shown in Figure 4.19.

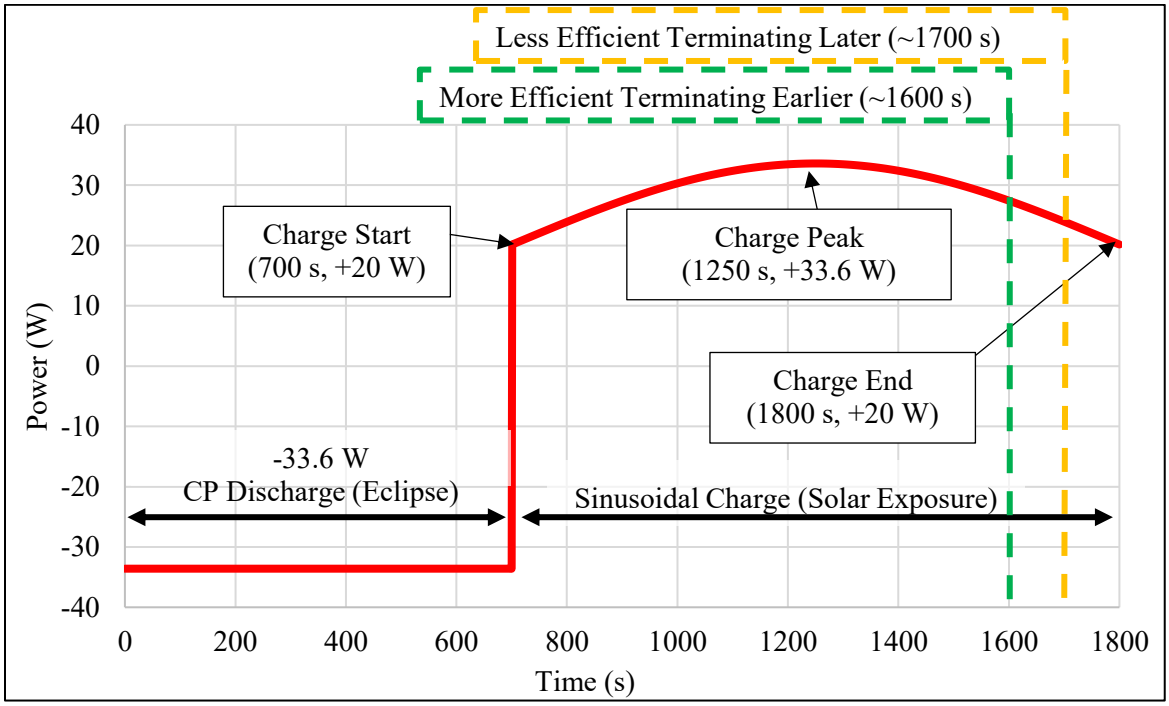

Figure 4.19 One accelerated LEO cycle. CP discharge (-33.6 W) with sinusoidal charge profile (start: 20 W, peak: 33.6 W, end 20 W)

To emulate use in a CubeSat application, all cell groups experience the same LEO cycle discharge and charge profile shown in Figure 4.19. Consequently, the lowest rated capacity cell group was used to define the LEO cycling parameters. At BoL a maximum SoE of 90% was selected to extend the operating life and a minimum SoE of 30% was selected to provide sufficient reserve to account for capacity degradation and IR growth before a failure to complete the accelerated LEO cycle occurs. This leads to a ΔSoE of 60%, which when using the rated energy capacity of LFP given in Table 4.1 in 3P configuration is 6.53 Wh. Maximizing the ΔSoE during cycling will increase the rate of degradation and is ideal for expediting the experiment. All cell groups, regardless of chemistry, had exactly 6.53 Wh discharged on each LEO discharge, leading to unique ΔSoE and C-rates for each cell group because of their varied rated energy capacities, see Table 4.4.

Table 4.4 ΔSoE and approximate cycling rates for each cell type during accelerated LEO cycling

Cell	BoL ΔSoE	CP Discharge Rate	Peak Charge Rate	Minimum Charge Rate
NCA	18%	0.93C	0.93C	0.55C
NMC	23%	1.20C	1.20C	0.71C
LFP	60%	3.09C	3.09C	1.84C

Each accelerated LEO cycle takes 30 minutes and thus 48 cycles are completed each 24-hour Earth day. After 10 days of continuous accelerated LEO cycling (480 cycles), each cell in a group has experienced significant discharge energy throughput (1045 Wh per cell). Because the accelerated LEO cycle is a partial SoC operation (Table 4.4), a reference cycle that operates over the full 100% ΔSoC range is necessary to contrast capacity degradation, energy efficiency and IR growth between different cell types and conditions. After the reference cycles are conducted, another 10 days of accelerated LEO cycles are initiated.

4.5 Reference Cycles

During LEO cycling outlined in Section 4.3, the capacity degradation, energy efficiency, IR growth and dV/dQ measurements cannot be obtained. These measurements are obtained through what is known as a reference cycle. Thus, LEO cycling must be stopped in order to complete reference cycles. Reference cycles were completed individually on each cell. During reference cycling, the ambient temperature was 25 °C as this is the ideal temperature given in each cell manufacturer data sheet

[11]–[13]. During reference cycling, each cell is in a single cell electrical configuration with a dedicated insulated type T thermocouple adhered to its side. A combination of CC and CC-CV cycling techniques were used. Three forms of reference cycles are completed to obtain performance and material degradation metrics such as discharge capacity, energy efficiency, IR growth, LAM and LLI. For consistency purposes, the charge and discharge C-rates for each cell type are identical while remaining within manufacturer data sheet specifications.

4.5.1 Discharge Capacity and Energy Efficiency Reference Cycling

Three 100% ΔSoC discharge cycles were completed with the third cycle used to represent the remaining capacity and efficiency of the cell. The purpose of the three cycles is as follows: cycle 1 recovers from previous LEO cycling test; cycle 2 thermally acclimates the cell to the new reference cycling; and cycle 3 provides consistent test cycle for obtaining results. The role this reference cycling is to measure the remaining discharge capacity and calculate the energy efficiency (ratio of discharge energy to charge energy) for each cell. Capacity and energy efficiency reference cycling was completed using the cycle schedule shown in Table 4.5.

Table 4.5 Capacity and energy efficiency reference cycle schedule (1 s timestep). Screenshot of full script in Appendix B

Step #	Mode	Rate	End Condition	Description
1	Rest	n/a	Time > 30 s Temp < 28 °C	Lab protocol
2	CC Discharge	1 C	Voltage < Low voltage limit	100% discharge
3	Rest	n/a	Time > 30 s Temp < 28 °C	Allow cells to cool
4	CC Charge	C/2	Voltage > High voltage limit	100% charge
5	CC-CV Charge	C/2	Current < 250 mA	Finish with CV charging
6	Rest	n/a	Time > 30 s Temp < 28 °C	Allow cells to cool
7	Loop to Step 2	n/a	3 Cycles	Cycle 1 and 2 – Condition cell Cycle 3 – Capacity and energy efficiency data for analysis
8	Rest	n/a	Time > 30 s Temp < 28 °C	Lab protocol

4.5.2 Internal Resistance Cycling

The fourth reference cycle was to determine IR and was completed using 30 second current pulses that recur every 300 s. IR was calculated by dividing the change in voltage by the change in current that occurs 1 s before the pulse and the end of the pulse.

During experimental cycling, it is not feasible to complete IR measurements manually at a specific SoC for each battery with consistency (as done in Section 4.1). Thus, a more automated form of measuring IR of a cell is required. Crawford et al. [66] utilized a pulse test with a baseline discharge of C/2 and with pulses occurring at 100% SoC for 10 s at 10% SoC increments. Crawford tested both NCA and LFP chemistries with this pulse methodology at pulse ratings of 1.45C and 2.7C respectively [66].

At RESL, it was determined that pulsing for only 10 s did not provide sufficient time for voltage to asymptotically plateau. Thus, it was determined that pulsing would be completed in 30 s intervals to obtain a cell voltage near the end of pulse that has reasonably approached its voltage asymptote. This pulse test method was applied to both charging and discharging portions of the cycle for contrasting IR at similar states of charge. For consistency purposes, each cell was charged at C/2 normally and charge pulsed at 1 C, discharged at 1C normally and discharge pulsed at 2 C. The IR reference cycle schedule is shown in Table 4.6.

Table 4.6 DC pulsing IR reference cycle schedule (1 s timestep). Screenshot of full script in Appendix B

Step #	Mode	Rate	End Condition	Description
1	CC Discharge	1C	Voltage < Low voltage limit	Discharge IR measurements
	Pulse CC Discharge (recurs each 300 s)	2C for 30 s		
2	Rest	n/a	Time > 30 s Temp < 28 °C	Allow cells to cool
3	CC Charge	C/2	Voltage > High voltage limit	Charge IR measurements
	Pulse CC Charge (recurs each 300 s)	1C for 30 s		
4	CC-CV Charge	C/2	Current < 250 mA	100% charge
5	Rest	n/a	Time > 30 s Temp < 28 °C	Lab protocol

4.5.3 Differential Voltage Analysis Cycling

Prior to LEO cycling, a C/24 charge-discharge cycling was completed on one cell from each 3P group at BoL to obtain a reference dV/dQ curve. The dV/dQ reference curve will then be compared to the final dV/dQ curve at EoL to differentiate between LAM and LLI contributions to total capacity loss. The Arbin power cycler was utilized for dV/dQ cycling due to its high accuracy and precision at the low currents (45 to 140 mA) required for such cycling (C/24). Cells were charged using their respective reference cycling script outlined in Sections 4.5.1 and 4.5.2 on the Neware power cycler prior to undergoing dV/dQ cycling.

Cycling at a C/24 rate inherently requires more time than cycling at 1C as performed in the capacity and energy efficiency reference cycling. However, the slow C/24 rate allows the discharge in cycle 1 (step 2) to both recover the cell from previous reference cycling at higher rates and thermally acclimate the cell to its steady state cell temperature. A charge-discharge cycle 2 (step 4 and 6) then provides a consistent test cycle for obtaining results, see Table 4.7.

Table 4.7 dV/dQ reference cycle schedule (1 s timestep). Screenshot of full script in Appendix B

Step #	Mode	Rate	End Condition	Description
1	Rest	n/a	Time > 30 s Temp < 28 °C	Lab protocol
2	CC Discharge (Cycle 1)	C/24	Voltage < Low voltage limit	100% discharge to condition cell
3	Rest	n/a	Time > 30 s Temp < 28 °C	Lab protocol
4	CC Charge (Cycle 2)	C/24	Voltage > High voltage limit	100% charge for dV/dQ
5	Rest	n/a	Time > 30 s Temp < 28 °C	Allow cells to cool
6	CC Discharge (Cycle 2)	C/24	Voltage < Low voltage limit	100% discharge for dV/dQ
7	Rest	n/a	Time > 30 s Temp < 28 °C	Allow cells to cool
8	CC-CV Charge	C/2	Current < 250 mA	100% charge
9	Rest	n/a	Time > 30 s Temp < 28 °C	Allow cells to cool

Due to the dV/dQ reference cycling extensive time (3 days per cell) and laboratory resource consumption (Arbin cycler with 3 independent channels) which respectively delay LEO cycling and other research experiments at RESL, dV/dQ reference cycling was only completed at the BoL and EoL on one of the three cells in each 3P grouping.

4.6 Complete Low Earth Orbit and Reference Cycling

The combined reference cycles (discharge capacity and energy efficiency, IR, dV/dQ) and the accelerated LEO cycle form the full experimental test performed on each cell and group. During reference cycling, cells are in a single cell configuration whereas when in LEO cycling, they are in 3P groupings. To clarify this process, the entire cycling schedule single cell power and current with voltage response is presented in Figure 4.20.

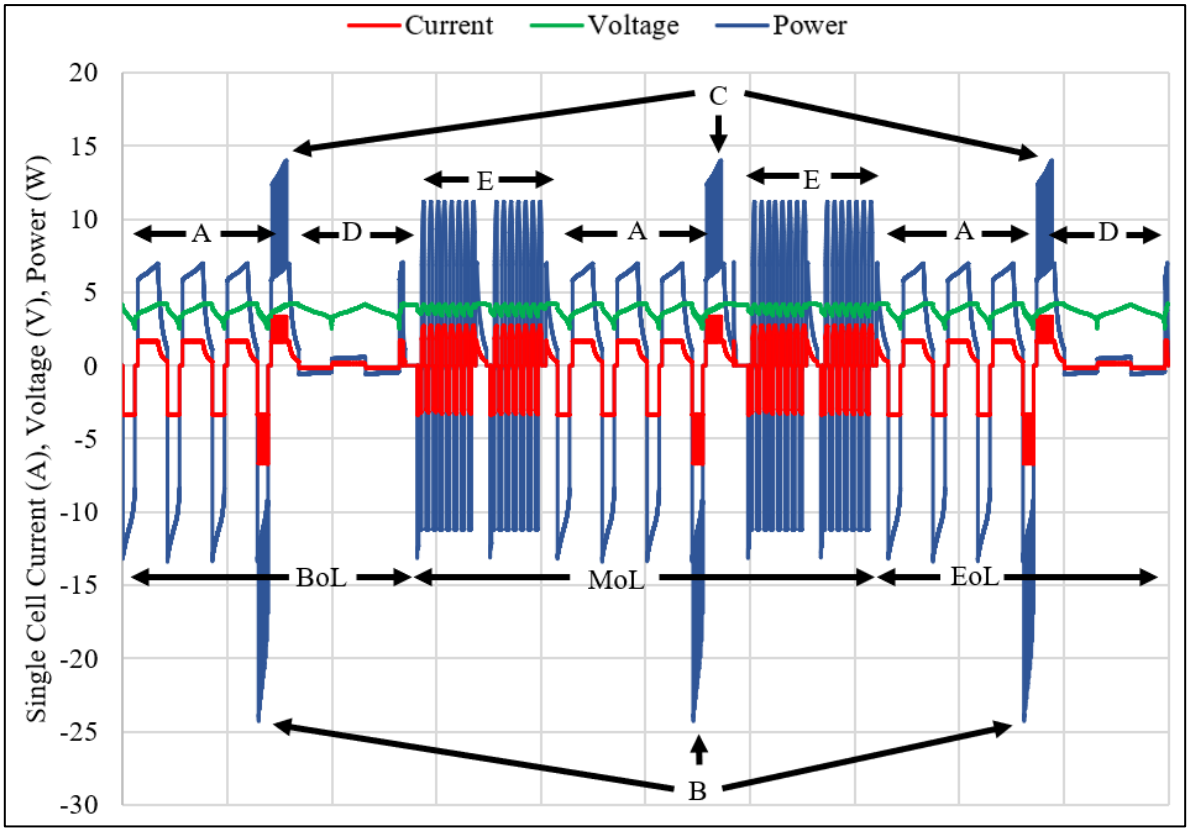

Figure 4.20 Collective LEO and reference cycling single cell power, current and voltage versus truncated time domain for the NCA cell type. A: Discharge capacity and energy efficiency reference cycling, B: Discharge IR cycling, C: Charge IR cycling, D: dV/dQ reference cycling, E: Accelerated LEO cycling partial view representing 480 cycles

Figure 4.20 shows that each cell prior to LEO cycling undergoes three discharge capacity and energy efficiency cycles (A), one direct current pulse IR cycle (B+C) and differential voltage cycling (D). Upon completing A through D, the 3P cell group is electrically assembled and undergoes LEO cycling (E). As LEO cycling was completed in 3P groupings, power and current measurements for LEO

cycling were divided by three in Figure 4.20 to allow for 1:1 comparison of power and current amplitude to reference cycling. Upon successful execution of 480 LEO cycles, cell groups are dissembled into a single cell configuration repeating reference cycles A through C prior to the next round of LEO cycles. Once LEO cycling commences, sections A, B, C and E are repeated until the 3P group fails to execute the LEO cycle. This repetition of LEO cycles, capacity and IR reference cycles is denoted as MoL (middle of life) in Figure 4.20. Upon failure, a final reference cycle procedure identical to the BoL is completed which includes dV/dQ reference cycling. In order to show the cyclic nature of LEO cycling, only 14 of 480 LEO cycles are shown, consequently the horizontal axis which represents time is truncated for clarity. The break in the middle of LEO cycling occurs subsequent to the completion of the 240th LEO cycle and represents the point in which one complete CC-CV charge is executed to reset any coulombic counting errors that occurred during the last 240 LEO cycles. By doing this reset, the drift in ΔSoC is minimized as a result of coulombic counting error while not overly cycling the 3P group in a non-LEO type cycle. As a result of this reset, the 480 LEO cycles are broken into two sets of 240 LEO cycles. Figure 4.20 shows that the highest charge and discharge rates occur during direct current (DC) pulses during IR cycling (B and C) while the lowest occurs during dV/dQ cycling (D). A better resolution of voltage response is shown in Figure 4.21.

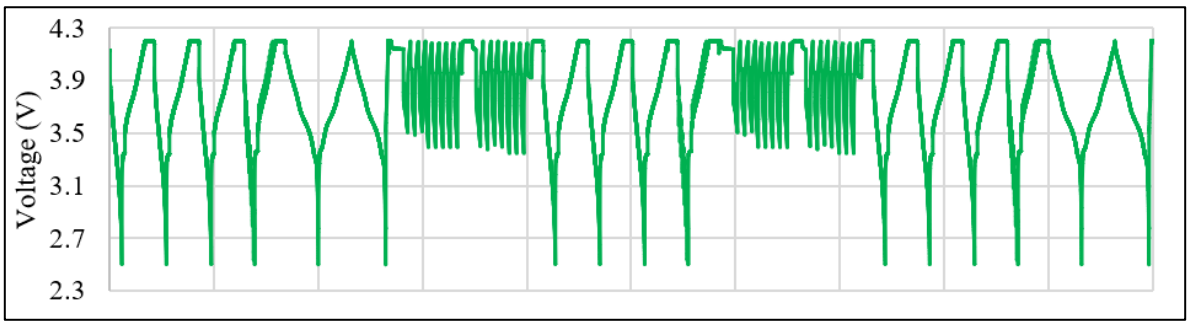

Figure 4.21 Collective LEO and reference cycling voltage versus truncated time domain for the NCA cell type

As a result of the partial ΔSoC achieved in LEO cycling, the operating voltage range is less than that of reference cycling. It should be noted that at BoL, the LEO cycling voltage range will be the lowest, and increases to the full range at EoL.

4.7 Differential Voltage Analysis Techniques

dV/dQ cycling is used to measure the differential voltage with respect to differential capacity during both charge and discharge which is calculated using equation (4).

$$\frac{dV}{dQ} = \frac{\Delta Voltage}{\Delta Capacity} = \frac{V_2 - V_1}{Q_2 - Q_1} \tag{4}$$

dV/dQ cycling requires low rates (e.g. C/20, C/24 and C/40). By cycling full cells (i.e. the original experimental cell) slowly, changes in voltage with respect to capacity reveal features in both the NAM and PAM simultaneously. Thus, it is necessary to fabricate and cycle half-cells, each with either the NAM or PAM acting as the positive electrode and lithium metal as the negative electrode. Lithium metal employs lithium plating in order to store lithium, consequently lithium metal has a flat voltage curve while cycling and presents no peak features in the differential voltage analysis process, making it ideal for dV/dQ half-cells. Details on the half-cell fabrication process is described by Elliot [93].

The experimental full cell and both lithium metal half-cells are each cycled using slow rates described in Table 4.7 in order to observe changes in lithium staging (i.e. lithium intercalation sites) in the NAM and PAM. The full cell utilizes intercalation as a means of storing lithium in the respective active materials, hence, they contain what is known as lithium staging which causes peak and valley features used in the differential voltage analysis. With respect to the graphite NAM in each cell, lithium staging represents moments during charge or discharge when lithium is specifically intercalating between A-B, B-C, or C-A graphene sheets (Figure 2.4), resulting in three lithium intercalation stages.

After cycling both NAM and PAM half-cells, and the full cell, active material contributions to the full cell features can be made using dV/dQ plots. Aggregating the dV/dQ NAM half-cell curve on discharge with the PAM half-cell curve on charge forms the artificial full cell dV/dQ curve. The reason for the use of "artificial" is that the dV/dQ curve formed from both half-cell curves was developed using small samples of the full cell active materials which are summed at a 1:1 capacity ratio. The artificial cell does not account for NAM preloading which is present in the full cell. As a result, the true full cell NAM features will shift right due to an excess in NAM lithium-ion intercalation sites.

The dV/dQ peaks and valley features present in half-cells can be correlated to the full cell, consequently labelling which peaks are from lithium staging occurring in the NAM and PAM. Finally, the BoL and EoL dV/dQ versus normalized capacity curve can be contrasted to quantify cell

degradation into LAM and LLI of both the PAM and NAM using the dV/dQ prognostic article techniques by Dubarry et. al [26], which are summarized in Table 4.8.

Table 4.8 Differential voltage peak shift observation technique with associated cause

Peak shift observation	**Cause**
dV/dQ peaks shift but distance between peaks remain constant	LLI in full cell
dV/dQ distance between peaks decreases	LAM on respective electrode
dV/dQ valley intensity decreases	Unable to lithiate active material at respective stage as a result of LAM, LLI or both
dV/dQ peak intensity decreases	Unable to lithiate active material at respective stage as a result of LAM, LLI or both

Chapter 5 : Experimental Results

The experimental results are presented in subsections in order to answer the research objectives described in Section 1.1. Subsections are summarized below with a short description.

Section 5.1: The experimental results are presented on discharge capacity, energy efficiency, IR, thermal response, failure mode analysis, differential voltage analysis, operational ΔSoE and end of discharge voltage analysis. These results encapsulate the majority of work and the crux of this research experiment.

Section 5.2: A dissection of all three cell types (NCA, NMC, LFP) to determine jelly roll thickness and length parameters. Samples are taken from the dissection process and underwent SEM and energy dispersive X-ray spectroscopy (EDS) of active materials to determine elemental composition and morphology in order to associate cell performance by PAM elemental composition and graphite NAM particle sizing.

Section 5.3: A heat transfer analysis is completed to achieve a better understanding of how each test condition (*laboratory*, *temperature*, *vacuum*) manage heat rejection from the 3P group with respect to convective, conductive, and radiative heat transfer contributions.

Section 5.4: Manufacturer sleeves are mandated to be removed prior to boarding the international space station [72]. The sleeve adds safety; hence it is ideal to leave them on for experimental testing. In order to determine if cell sleeves affect test performance, experimental analysis of the impact on cell operating temperature with and without the manufacturer sleeves was completed to determine if cell sleeves effect long-term degradation testing.

Section 5.5: The LEO pressure (1.24×10^{-9} kPa) is 8 magnitudes less than what is achievable in the vacuum system (~0.2 kPa) used in this research. To understand if the additional 0.2 kPa pressure inside the vacuum chamber affects cell performance, cells were operated at 0.2 kPa and 2 kPa under the accelerated LEO cycle while measuring cell operating temperatures as a proxy for determining the difference between 0.2 kPa and the actual LEO pressure.

5.1 Experimental Cycling Results

The results and findings from Section 5.1 are partially published in the Journal of Energy Storage [94]. *Riley Cook was the primary researcher responsible for the experimental design, fabrication, execution, and data analysis as part of this thesis research. Riley Cook is first author of the journal article and wrote the majority of the manuscript.*

Using an accelerated LEO CubeSat cycle, the three cell types (NCA, NMC, LFP) in this experiment were cycled to monitor capacity fade, decrease in energy efficiency and IR growth as metrics to represent degradation. The energy and coulombic capacity degradation for each cell type and condition (*laboratory*, *temperature*, *vacuum*) are contrasted on a discharge energy throughput, LEO cycles completed and equivalent cycles of initial measured coulombic capacity basis. Data points marked with a cross 'X' indicate the point in which the cell group failed during LEO cycling. Absence of an 'X' indicates the cells are still operational at the time this thesis was written. Range bars are added to each data point to represent the minimum and maximum cell with respect to the median cell for each 3P cell group. Each data point was obtained from a reference cycle. The span between data points is 480 accelerated LEO cycles. A statistical t-test was completed to verify the significance between cell groups that performed similarly and is given in Appendix E.

In addition, the temperature response of cells in both reference cycles and accelerated LEO cycles are presented and related to IR and energy efficiency measurements. Cell failure from IR growth and a disconnected CID are discussed and contrasted. Differential voltage analysis is used to identify LAM and LLI between BoL and EoL in each cell type. Finally, a perspective on how operational SoE shifts throughout LEO cycling is presented to enhance the understanding of how cells performed throughout LEO cycling and reveal how increases in IR reduce the available energy during LEO cycling.

5.1.1 Energy and Coulombic Capacity Degradation

The median cell discharge energy is plotted for each cell type (NCA, NMC, LFP) in each condition (*laboratory*, *temperature*, *vacuum*) with respect to the completed LEO cycles and discharge energy throughput in Figure 5.1.

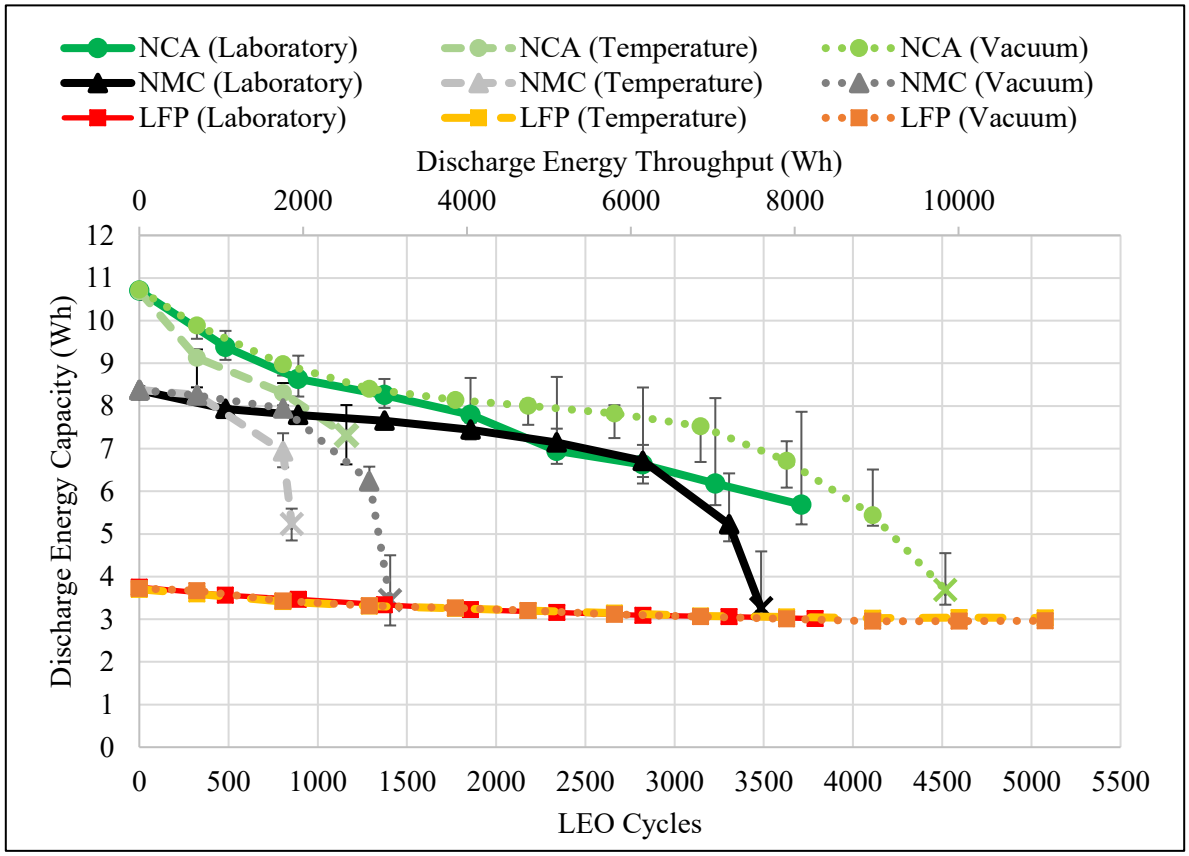

Figure 5.1 Discharge energy capacity measured at reference cycles versus completed LEO cycles and discharge energy throughput for each cell type (NCA, NMC, LFP) and LEO cycling condition (laboratory, temperature, vacuum)

Figure 5.1 shows that all cells experience continuous energy capacity decline due to the wear of LEO cycles. NCA cells experience a substantial initial decline in capacity over the first 250 LEO cycles that is not apparent with the other chemistries. After this, NCA cells in the *laboratory* condition continue degrading at a reduced linear rate and have yet to fail operation, having attained 3700 LEO cycles. NCA cells in the *temperature* condition show the greatest degradation rate of the NCA cell type and fail at 1161 LEO cycles. NCA cells in *vacuum* experience reduced degradation rate, until 3000 LEO cycles, after which they begin to degrade rapidly and fail.

NMC cells have relatively little degradation until 500 LEO cycles, after which they rapidly degrade to failure in all three conditions. This suggests the NMC cells experience a different failure mode mechanism than the NCA cell. The NMC cell type respectively achieves the lowest and highest

discharge energy throughput in the *temperature* and *laboratory* condition. This finding indicates the NMC cell type dependency on warmer operational temperatures to achieve competitive cycle life to the NCA cell type.

Both NCA and NMC cells in the *vacuum* condition experience failure at approximately half of their original energy capacity. In a CubeSat application, significant initial capacity oversizing would be required to allow for such substantial degradation, especially considering the relatively small ΔSoC of each LEO cycle (Table 4.4). It is noted that the cell energy capacity at failure is 3.5 Wh or greater, which is substantially more capacity than is discharged during the LEO cycle eclipse (2.178 Wh per cell). This means that failures are not due to insufficient energy capacity, but instead the ability of the cell to maintain working voltage at the eclipse CP discharge rate. The low degradation rate of LFP cells suggests that CubeSats employing this cell type would not be required to oversize the initial capacity by a substantial amount. Additionally, this finding suggests that significant oversizing of the CubeSat battery pack is not necessarily beneficial to maintaining operation due to the inability to deliver the desired power rate.

The range bars in Figure 5.1, showing minimum and maximum cell capacity for a given group are indistinguishable for all cell types at the BoL. This gives confidence that all cells within a group are consistent at the beginning of test. As cycling progresses, the range bars become larger as individual NCA and NMC cells degrade at slightly different rates. It is noted the LFP cells have indistinguishable capacity differences (the range bars are hidden by the median cell marker). This suggests that inter-cell energy capacity differences are a function of degradation, rather than number of LEO cycles, discharge energy throughput, or even degradation rate itself. Consequently, less capacity oversizing and lower degradation rates allow the battery management system to balance battery packs more easily. While inter-cell differences for NCA and NMC groups are identified, they are relatively small compared to the larger differences that exist between cell types and LEO cycle operating pressure lending confidence to the overall findings.

Figure 5.1 shows the LFP cells experience only small and reducing degradation rate with LEO cycles relative to the NCA and NMC cell types. Due to the lesser degradation rate in the LFP cell type, the discharge energy capacity data is reproduced in Figure 5.2 for improved resolution.

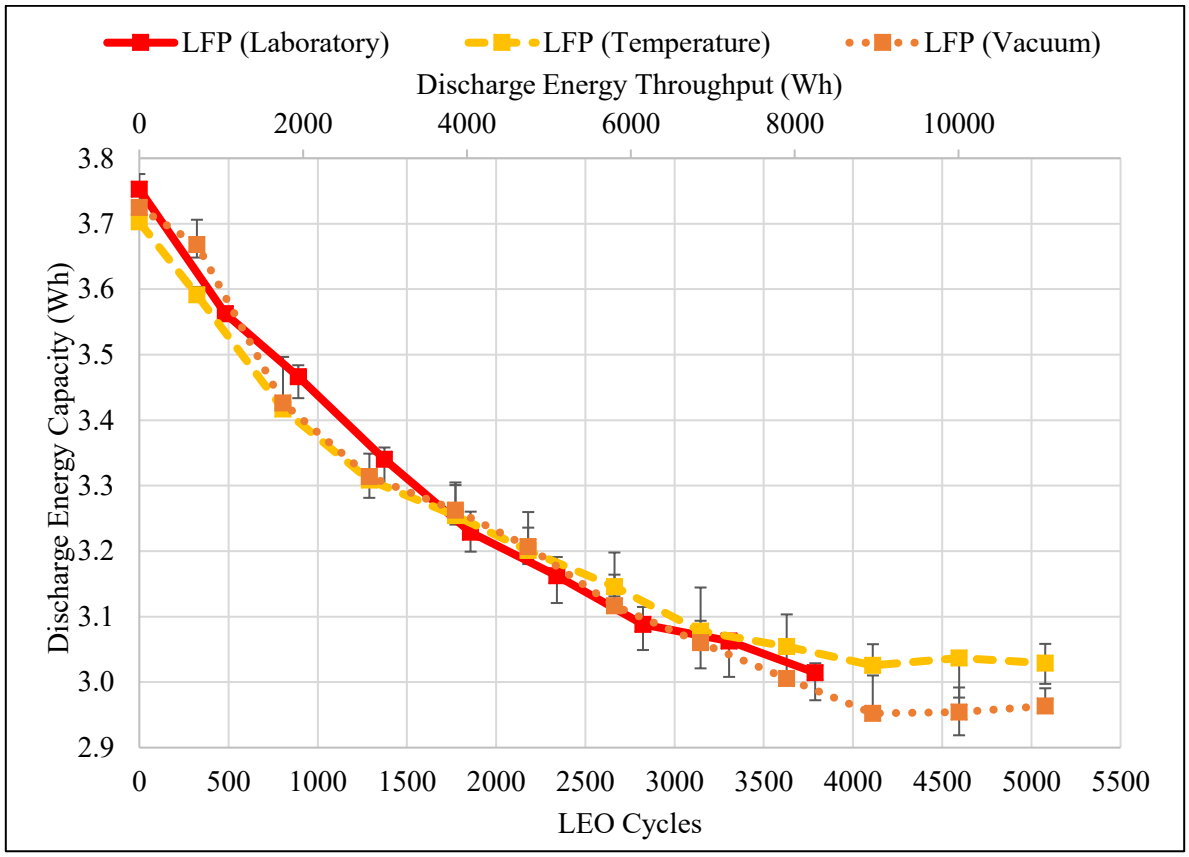

Figure 5.2 Discharge energy capacity measured at reference cycles versus completed LEO cycles and discharge energy throughput for the LFP cell type in each LEO cycling condition (laboratory, temperature, vacuum)

Figure 5.2 reveals that the LFP cells have insignificant discharge capacity differences between those in *laboratory* and *vacuum* condition throughout the entirety of cycling. The *laboratory* LFP condition (3,789 LEO cycles) is trending between both the *vacuum* (5,078 LEO cycles) and *temperature* (5,078 LEO cycles) condition with regards to discharge energy capacity, thus a plateau of capacity degradation is expected to occur near 4000 LEO cycles similar to the more cycled *temperature* and *vacuum* condition. Although both *temperature* and *vacuum* LFP groups show similar remaining discharge energy capacity at EoL, there is a statistically significant difference between the *temperature* and *vacuum* discharge energy capacity after the 4112th LEO cycle. Meaning, the LFP cell degrades less in the *temperature* condition with a cooler operating cell temperature than in the *vacuum* condition. The finding that LFP performed better with regard to capacity degradation with a lower cell temperature is opposite to both the NCA and NMC cell type. This suggests that implementing LFP cells in CubeSats reduce the need for heating compared to traditional NCA and

NMC cell chemistries. Additionally, all LFP cells are still operational as denoted by the lack of an 'X' on the final reference curve. With such close performance proximity, no true conclusion on which condition provides the best cycle life can confidently be determined from Figure 5.2.

Contrasting all three cell types in their respective conditions as a function of equivalent cycles of initial measured coulombic capacity and normalized discharge coulombic capacity demonstrates the high cyclic ability of the LFP relative to both NCA and NMC cell groups, see Figure 5.3.

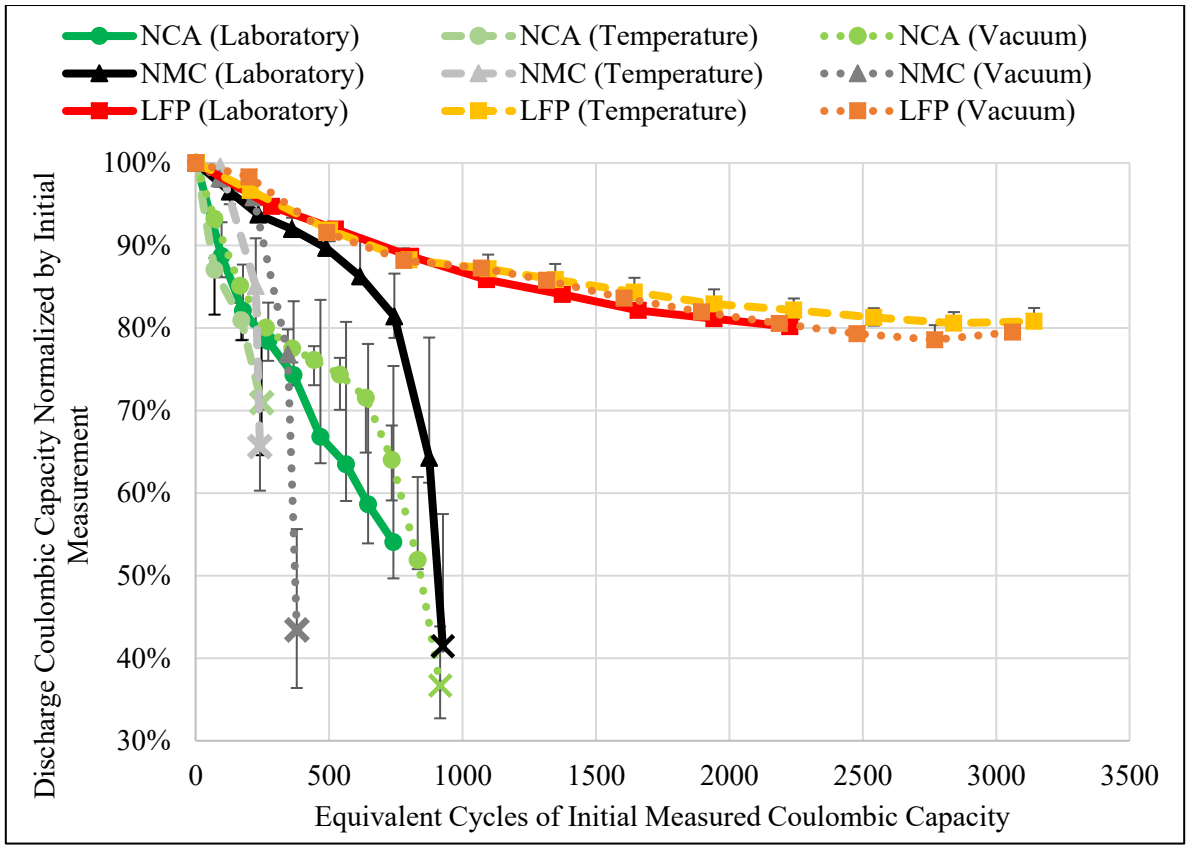

Figure 5.3 Normalized discharge energy capacity measured at reference cycles versus number of equivalent cycles of initial measured coulombic capacity for each cell type (NCA, NMC, LFP) and LEO cycling condition (laboratory, temperature, vacuum)

Similar to Figure 5.1, the LFP data in Figure 5.3 show little capacity degradation relative to the NCA and NMC cell types in all conditions. Figure 5.3 shows degradation for each LFP cell at BoL degrades at a relatively linear rate until 1000 equivalent cycles (~90% capacity remaining) and subsequently decelerates in degradation until the end of test at ~80% capacity remaining. This finding is contrary to that of Severson et al. [81] which only showed cases of accelerated degradation until ~88% capacity

remaining. Interestingly, the graphite||LFP (graphite PAM, LFP NAM) cells used by Severson et al. [81] (APR18650M1**A**) is the predecessor model of the LFP cell used in this study (APR18650M1**B**). This finding once again highlights the importance of testing cells in their partial ΔSoC application as opposed to a 100% ΔSoC in order to reflect performance in the actual application.

5.1.2 End of Discharge Voltage Analysis

As shown in Figure 5.2, LFP cells in all three conditions have similar capacity degradation (±1%), with the same total discharge energy throughput and are still operational at the time of writing this thesis (July 2020). However, the capacity degradation curves in Figure 5.2 suggests that the LFP cell type in the colder *temperature* condition will yield better LEO cycle count compared to the increasingly warmer *vacuum* and *laboratory* conditions. By examining LFP cycle life using the alternative end of discharge voltage approach proposed by Song et al. [79], further insights to EoL conditions are revealed, see Figure 5.4.

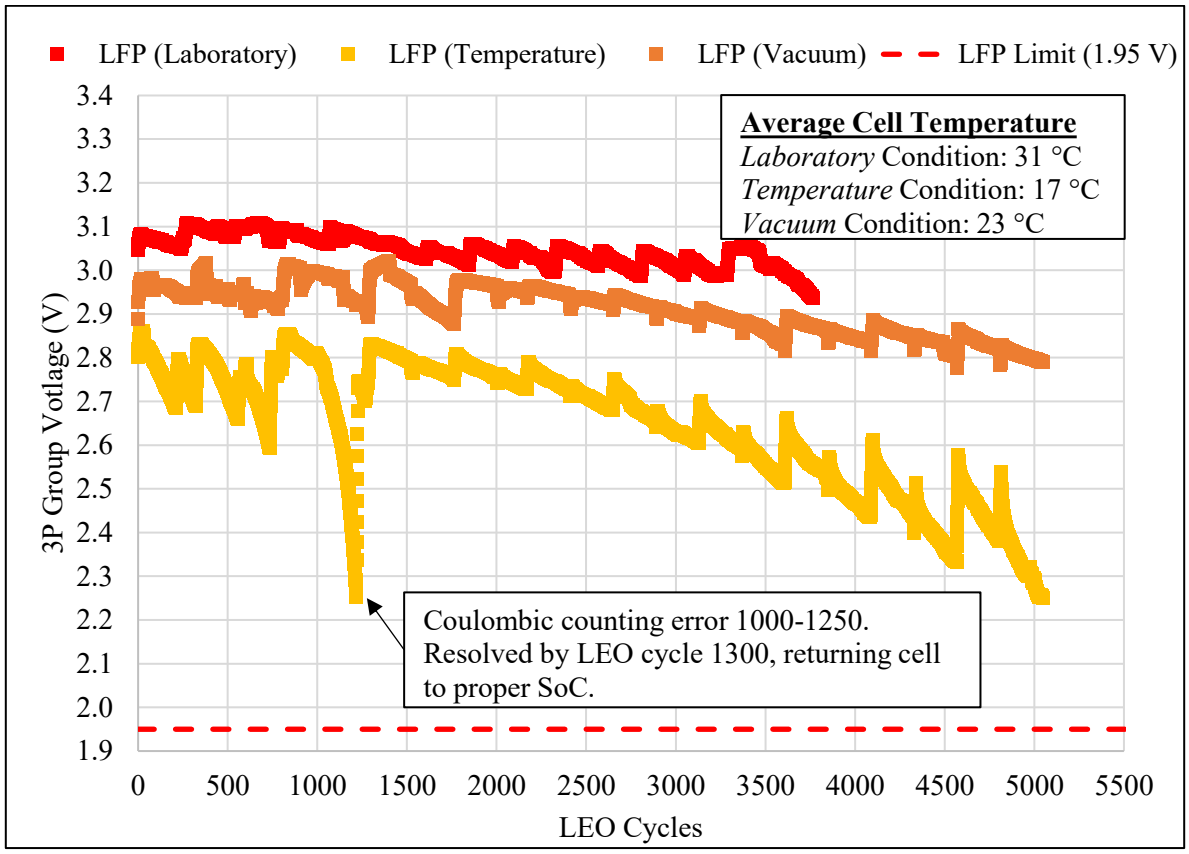

Figure 5.4 *LEO cycling end of discharge voltage versus completed LEO cycles for LFP cells in all three conditions*

From BoL to EoL, Figure 5.4 reveals that the operating temperature effects the end of discharge voltage, with the warmest condition (i.e. *laboratory*) having the highest end of discharge voltage. The rate at which the end of discharge voltage decreases is different for each condition. Both the *laboratory* and *vacuum* conditions end of discharge voltage decreases linearly at different rates for the entirety of the testing, whereas the *temperature* condition experiences an exponential decrease in end of discharge voltage. As a result of different starting positions and trend rates, the end of discharge voltage range increases between cell groups in different conditions throughout LEO cycling. The results in Figure 5.4 suggest that the *laboratory* LFP group will achieve the greatest LEO cycle count, second will be the *vacuum* condition, and third will be the *temperature* condition. This indicates that although colder operating temperature reduced degradation in the LFP cell type, EoL is still likely to occur prior to cells with warmer operating temperatures. This suggests that a dynamic thermal management system which operates LFP cells colder at BoL and heating them towards EoL will provide the best cycle life and discharge energy throughput.

5.1.3 IR and Energy Efficiency

The minimum IR during discharge for each cell group in all three conditions versus LEO cycles is shown in Figure 5.5.

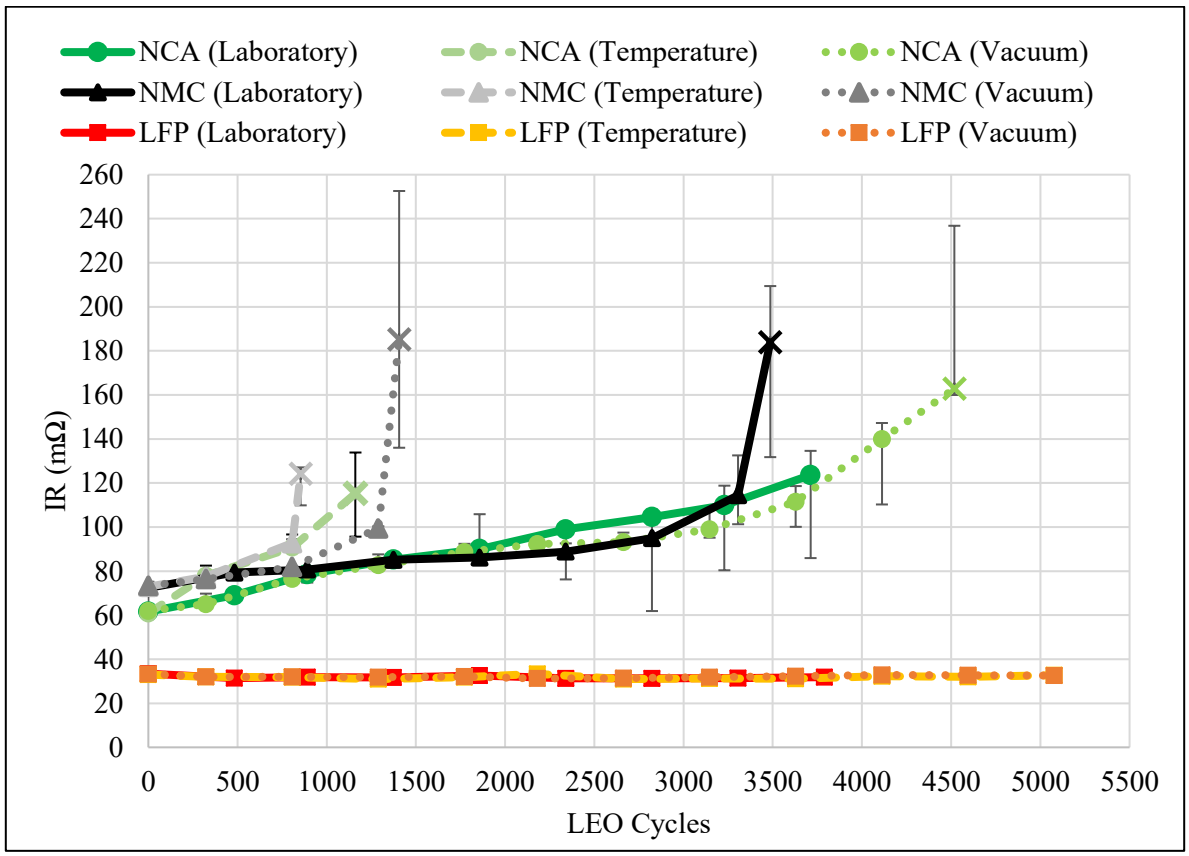

Figure 5.5 Minimum IR during discharge measured at reference cycles versus completed LEO cycles for each cell type (NCA, NMC, LFP) and LEO pressure condition (laboratory, temperature, vacuum)

Figure 5.5 shows the continuous IR growth for both NCA and NMC cells in all three conditions. The *laboratory* NCA group experiences a low steady state linear increase in IR for the first 3700 LEO cycles. The IR growth is greater in the *temperature* setting due to the lower operating temperature. The *temperature* NCA group experiences a sharp steady state linear increase in IR at approximately three times the rate of the *laboratory* and *vacuum* condition. The *vacuum* NCA group shows a continuous IR growth which plateaus after approximately 2000 LEO cycles, increasing again after 3000 cycles, peaking prior to cell group failure. All three NMC groups experience a sharp increase in IR prior to failure which correlates to the sharp decrease in discharge capacity found in Figure 5.1.

These sharp increases in IR in all three NMC groups are the cause of failure during LEO cycling. Although both NCA and NMC cell groups have significant capacity degradation (Figure 5.1), the NCA group does not experience as abrupt an increase in IR as the NMC group (Figure 5.5). This is believed to be attributed to different degradation contributions. LFP experiences no discernable IR growth in the first 5000 LEO cycles. The changes in IR are reflected in each group reference cycle energy efficiency as shown in Figure 5.6.

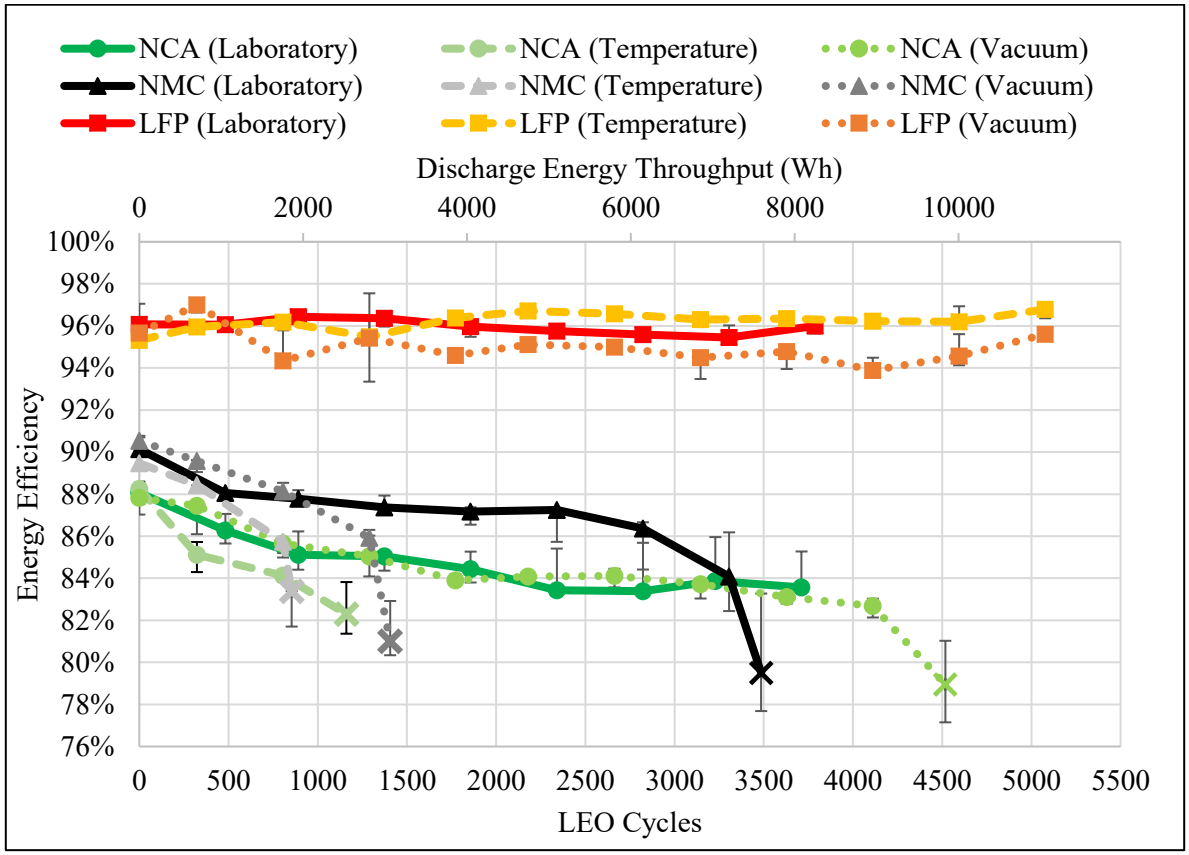

Figure 5.6 Energy efficiency measured at reference cycles versus completed LEO cycles and discharge energy throughput for each cell type (NCA, NMC, LFP) and LEO condition (laboratory, temperature, vacuum)

The NCA and NMC energy efficiency begins at approximately 90% and degrades with LEO cycles. By the point of failure, these cells achieve less than 84% round trip energy efficiency. In contrast, the LFP cells show efficiencies of approximately 96% from BoL to EoL.

Similar trends between IR growth and energy efficiency decrease are observed in both NCA and NMC cell types. This negative correlation between IR and energy efficiency is expected and brings confidence to the method used to measure IR described in Section 4.5.2.

After approximately 1500 LEO cycles, the *temperature* LFP group maintains a 2% greater energy efficiency than the *vacuum* LFP group. The 2% difference in energy efficiency correlates to the difference in retained initial capacity between the *temperature* and *vacuum* LFP groups presented in Figure 5.3. Compared to the NCA and NMC cell types, LFP shows minor differences in energy efficiency between each condition. This finding suggests that CubeSat designs employing NCA and NMC cell types should consider thermal management (i.e. heat transfer analysis and heating) more carefully that those utilizing the LFP cell type in order to improve energy efficiency.

The energy efficiency data presented in Figure 5.6 was measured during a reference cycle (100% ΔSoC, 101 kPa, 25 °C, 1C discharge, 0.5C charge). However, energy efficiency in the *vacuum* condition LEO cycle (partial ΔSoC, 0.2 kPa, 10 °C, CP discharge, sinusoidal charge) is more relevant to a LEO CubeSat design, see Figure 5.7.

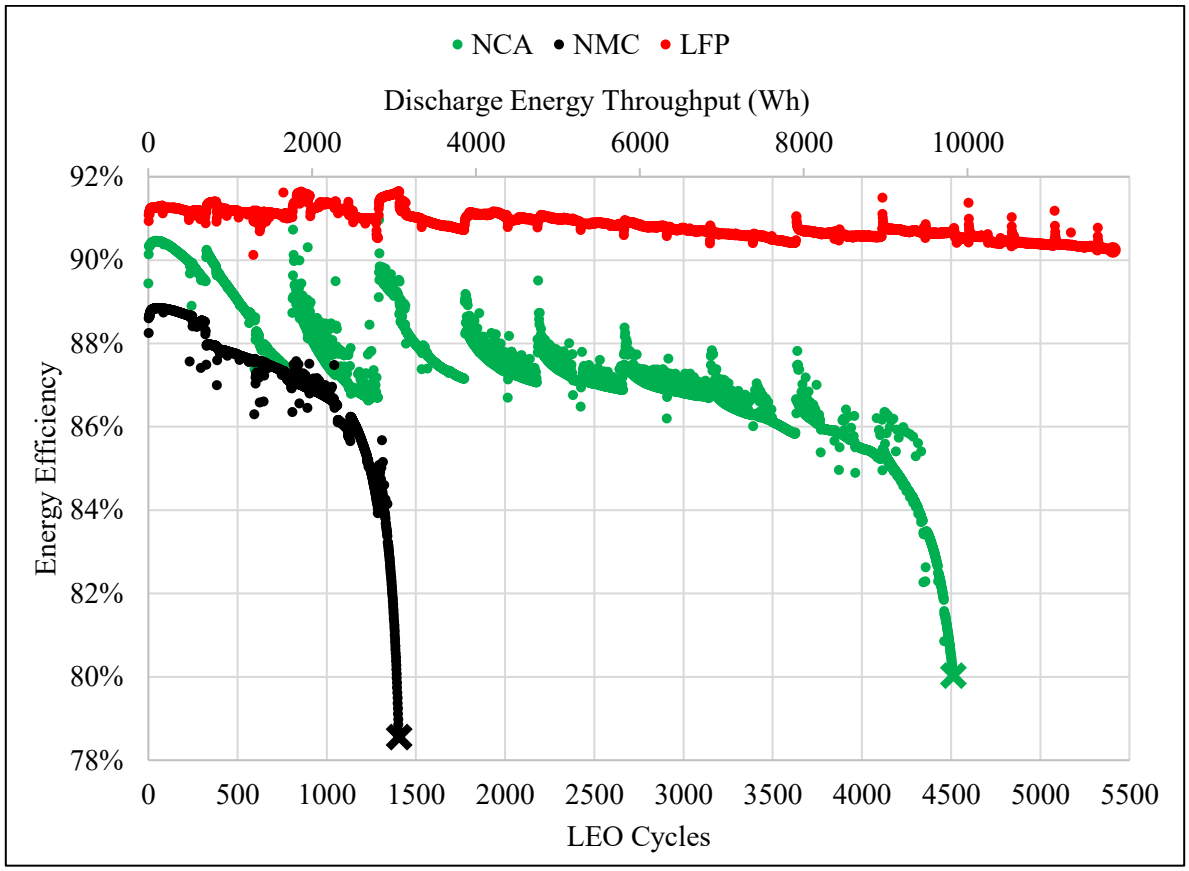

Figure 5.7: Energy efficiency measured at LEO cycles versus completed LEO cycles and discharge energy throughput for each cell type (NCA, NMC, LFP) in the vacuum condition

Contrasting Figure 5.6 and Figure 5.7 reveal that the LEO energy efficiencies for both *vacuum* NCA and NMC cell groups in the LEO cycle are similar (i.e. ±1%) to the reference cycle single cell energy efficiency (Figure 5.6), showing similar exponential decay near EoL. In Figure 5.7, the NCA group experiences discontinuous and decaying energy efficiency between each set of 480 LEO cycles which is believed to be attributed to periods of gas evolution and absorption into the electrolyte causing temporary increased energy efficiency due to a reduction is electrode separation. Gas absorption occurring in the LIB is supported by Self et al. [95] and findings later in this thesis (Section 5.1.5.1) support that the NCA cell type is prone to gas generation whereas the NMC and LFP are not.

The *vacuum* LFP cell during the reference cycle achieved a constant ~96% energy efficiency (Figure 5.6) whereas in the LEO cycle a constant ~91% energy efficiency (Figure 5.7) was observed. The difference in energy efficiency is mostly attributed to cycling rates being increased 3 to 6 fold from reference to the LEO cycle outweighing the benefit of a partial ΔSoE operation. Regardless of the

decrease in energy efficiency observed during the LEO cycle, the LFP cell type remained advantageous with regards to energy efficiency from BoL to EoL compared to the NCA and NMC cell types. Energy efficiency is important in CubeSat design because it impacts the quantity of photovoltaic cells. Designers must take into consideration that energy efficiency of some cells degrade with use and that additional charge energy generation will be required as the CubeSat approaches EoL. Consequently, the LFP cell type should be considered for LEO CubeSat missions in order to reduce the quantity of photovoltaic cells installed on a CubeSat.

5.1.4 Thermal Response

The thermal response of a cell is dependent on several things, including: electrochemical operating voltage; the combination of IR and operating power (discharge or charge); the cell shape and heat transfer characteristics. The cycle energy efficiency is inversely related but not proportional to the IR and cycle power. As IR increases, heat generation increases, consequently the thermal response correlates well with cell IR throughout a reference cycle, as shown in Figure 5.8.

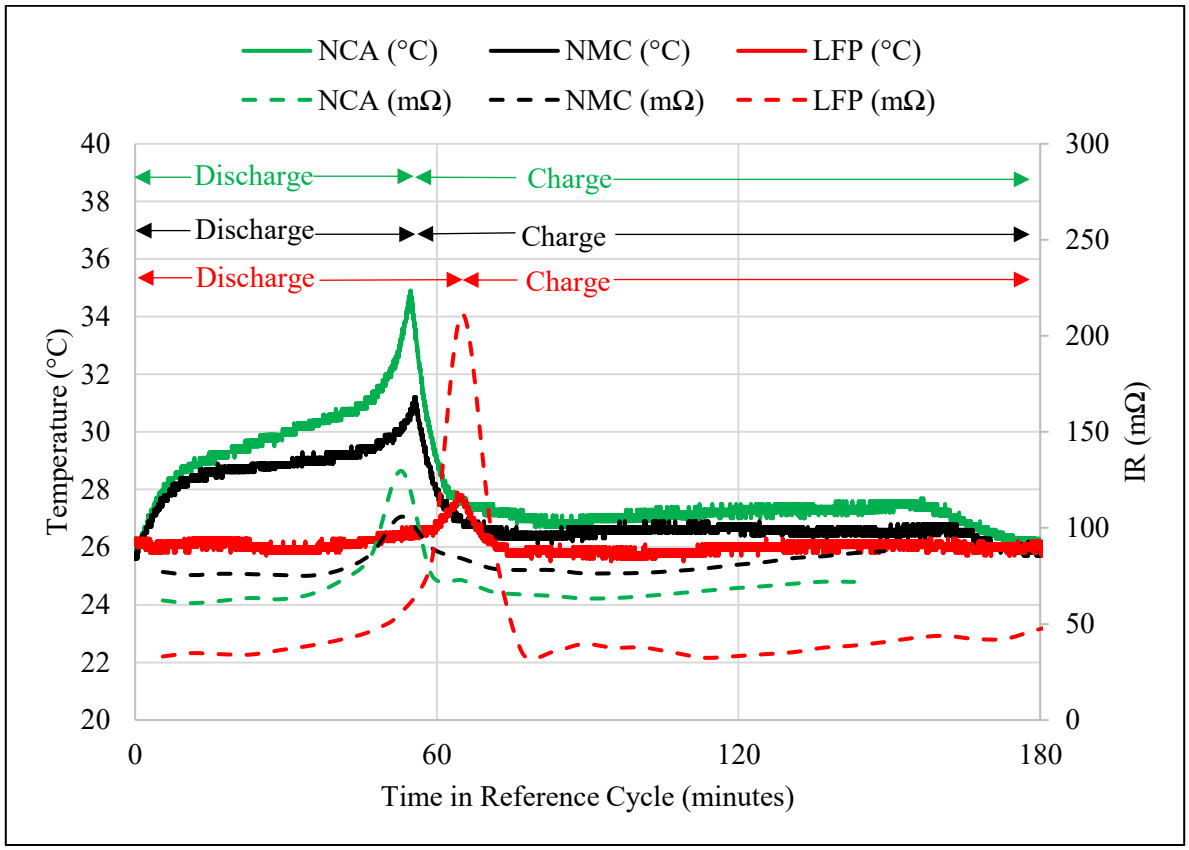

Figure 5.8 Temperature and IR throughout the reference cycle (C/1 discharge, C/2 charge) at BoL for each cell type (NCA, NMC, LFP)

The NCA cell operates at the highest temperature with the greatest temperature peak. The NMC cell temperature peak is slightly less than the NCA cell and the LFP cell operates significantly cooler than both NCA and NMC. The IR plot of both NCA and NMC cells terminate discharge early due to the charge and discharge cut-off voltage limits being reached prematurely during DC pulses required to obtain IR measurements. The peak IR for each cell occurs at the end of discharge and correlates with the peak temperature achieved. Interestingly, if the cell temperature were tightly controlled to a specific value via thermal management, the IR peak would increase further. As each cell was cycled at different rates, the magnitude of the IR peak is not proportional to the thermal response.

Reference cycles are completed at 101 kPa and 25 °C every 480 LEO cycles, thus the majority of cycling (greater than 99%) is completed under the accelerated LEO cycle conditions. The convective heat transfer properties between 101 kPa and 0.2 kPa absolute pressure differ substantially. This was well quantified by Saidi and Abardeh [96], showing that a decrease in pressure caused a decrease in

the convective heat transfer coefficient. The various convective properties result in different temperature profiles directly affecting cell performance. As a result of higher cell temperatures, a lower IR is achieved due to increased ionic conductivity. The increased degradation rate in NCA and NMC cells in the *temperature* condition is due to the greater convective heat transfer coefficient keeping cells cooler than those operating in the *vacuum* and *laboratory* condition. Cells in *vacuum* achieved more desirable operating temperatures (23 to 27 °C) while cells in the *temperature* condition operated on average 6 to 9 °C cooler than their *vacuum* condition counterpart. Cells in the *laboratory* condition achieve the highest average operating cell temperature operating an additional 8 to 10 °C warmer than the *vacuum* condition counterpart. The temperature profile for cells operating inside the *laboratory*, *temperature* and *vacuum* conditions are shown in Figure 5.9 for the 10th LEO cycle completed.

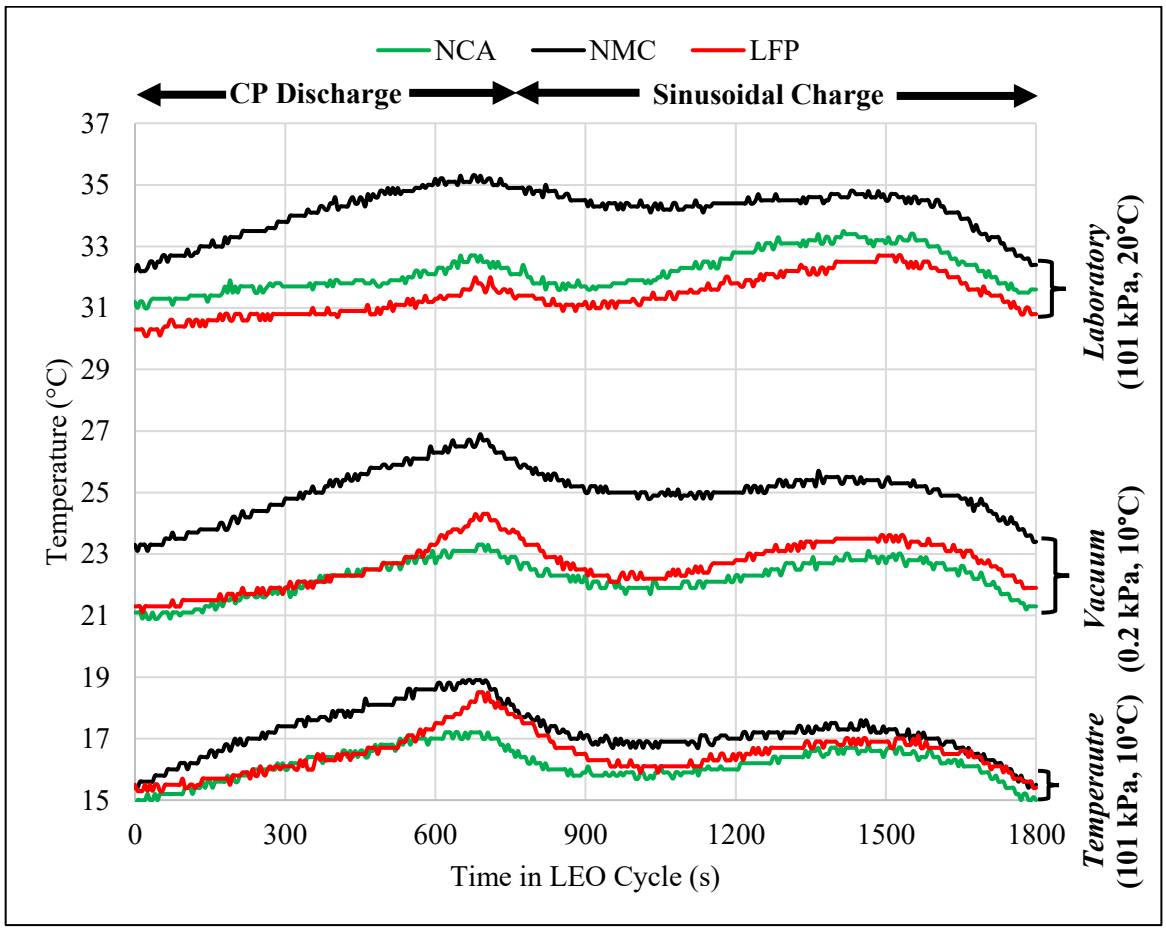

Figure 5.9 Temperature throughout the 10th accelerated LEO cycle for each cell type (NCA, NMC, LFP) and LEO condition (laboratory, temperature, vacuum)

Figure 5.9 shows how each cell group has a global peak temperature at the end of the CP discharge and local peak at the middle of sinusoidal charge. The thermal profiles in the *temperature* condition are most similar, while in in the *laboratory* and *vacuum* condition the NMC cell group appears to operate 2 °C warmer than the NCA and LFP cell groups. By contrasting Figure 5.8 and Figure 5.9 it is clear that warmest cell during LEO cycling is not the warmest during reference cycling as each cell chemistry is cycled at identical power rates and in a ΔSoC operating window that avoids the large IR peak at the end of discharge. As operating temperature affects performance (Section 3.4), this highlights the necessity to operate cells in the partial ΔSoC application to properly reflect performance.

Cell IR increases throughout LEO cycling, as shown by Figure 5.5. With this increase in IR, the thermal profile of each cell shifts upward, see Figure 5.10.

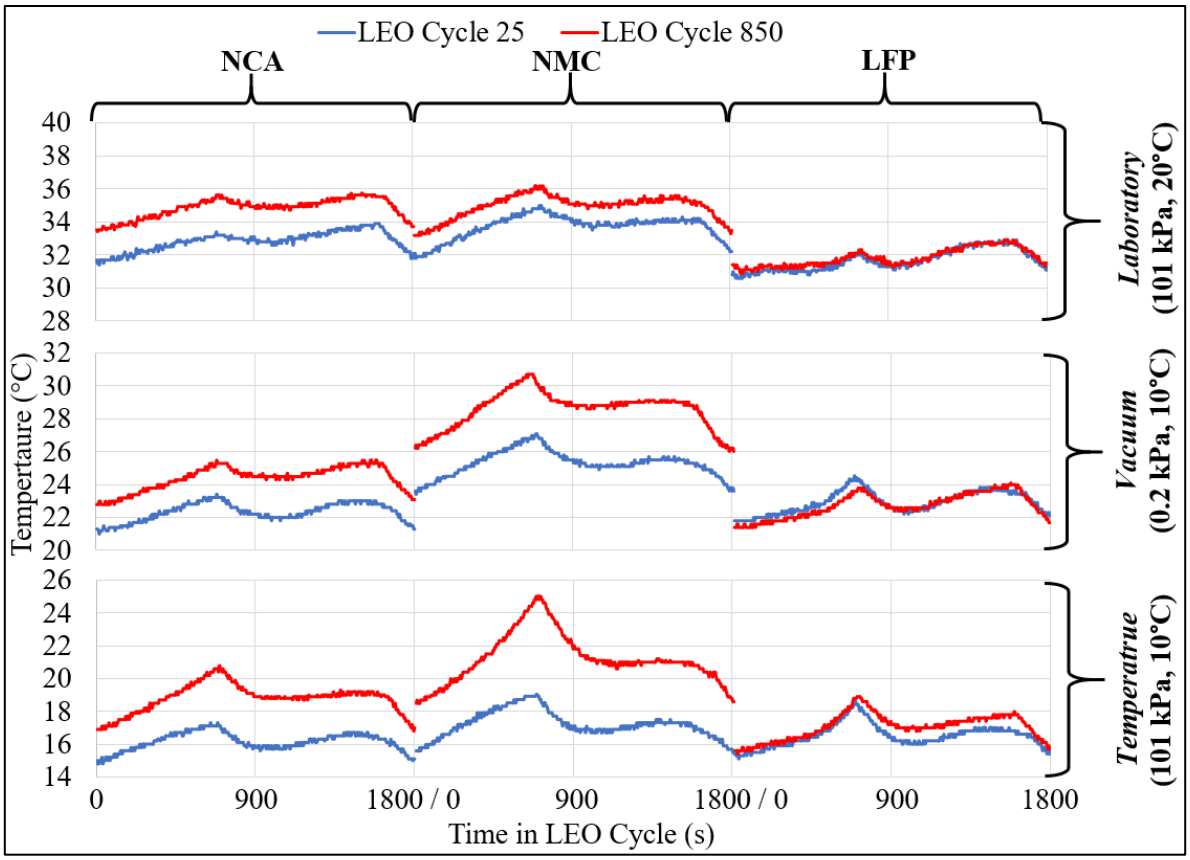

Figure 5.10 Temperature throughout the 25th and 850th accelerated LEO cycle for each cell type (NCA, NMC, LFP) and LEO condition (laboratory, temperature, vacuum)

Figure 5.10 shows there is an upwards shift in temperature profile from the 25th to 850th LEO cycle. This increase in temperature is a result of increasing IR as the cell group degrades. Cell groups with lesser capacity degradation (i.e. LFP) in the first 850 LEO cycles experienced a lesser upwards shift in temperature profile compared to cells with a greater degradation (i.e. NCA and NMC). By the 850th LEO cycle there is a noticeable increase in the operating temperature of both NCA and NMC cells in all three conditions. In contrast to the NCA and NMC cell groups, there is a small change in the LFP temperature profile between the 25th and 850th LEO cycle. This small change in the LFP temperature profile correlates well with the very minor IR growth all three conditions. The largest increase in temperature profile was that of the NMC cell group operating in the *temperature* condition.

As the temperature profile for each cell group is constantly shifting upwards from BoL to EoL, the average operating temperature throughout the entire lifetime of the cell group was used to distinguish between cell temperatures in different groups, see Table 5.1.

Table 5.1 Average LEO operating cell temperature (+/- 1 °C) for each cell type (NCA, NMC, LFP) and experimental condition (laboratory, temperature, vacuum)

Cell Type	***Laboratory***	***Temperature***	***Vacuum***
NCA	36 °C	18 °C	27 °C
NMC	37 °C	18 °C	27 °C
LFP	31 °C	17 °C	23 °C

As shown in Table 5.1, the temperature profile for a given cell type varies significantly between conditions due to the change in heat transfer properties that are later quantified in Section 5.3. The increased degradation rate in NCA and NMC cells in the *temperature* condition is due to the greater convective heat transfer coefficient keeping the cells cooler than cells operating in the *laboratory* and *vacuum* condition. Although the thermal profile of the LFP cell type varies with each condition, performance is less affected by operating temperature relative to the NCA and NMC cell types.

5.1.5 Failure Mode Analysis

Failure mode analysis for of both *temperature* and *vacuum* NCA cells and NMC cells in all three conditions are considered. Failure mode conditions include both excessive IR growth and electrically disconnected CIDs. At the time of writing this thesis (July 2020), all three LFP groups and the

laboratory NCA group continue to successfully execute the accelerated LEO cycle, consequently no failure mode analysis was performed on cells from these four groups.

5.1.5.1 NCA

On the 1161st LEO cycle, the *temperature* NCA cell group failed to execute the accelerated LEO cycle. Analysis of the NCA 3P group voltage profile shown in Figure 5.11 reveals a clear and sudden voltage drop from 2.80 to 2.45 Volts during CP discharge.

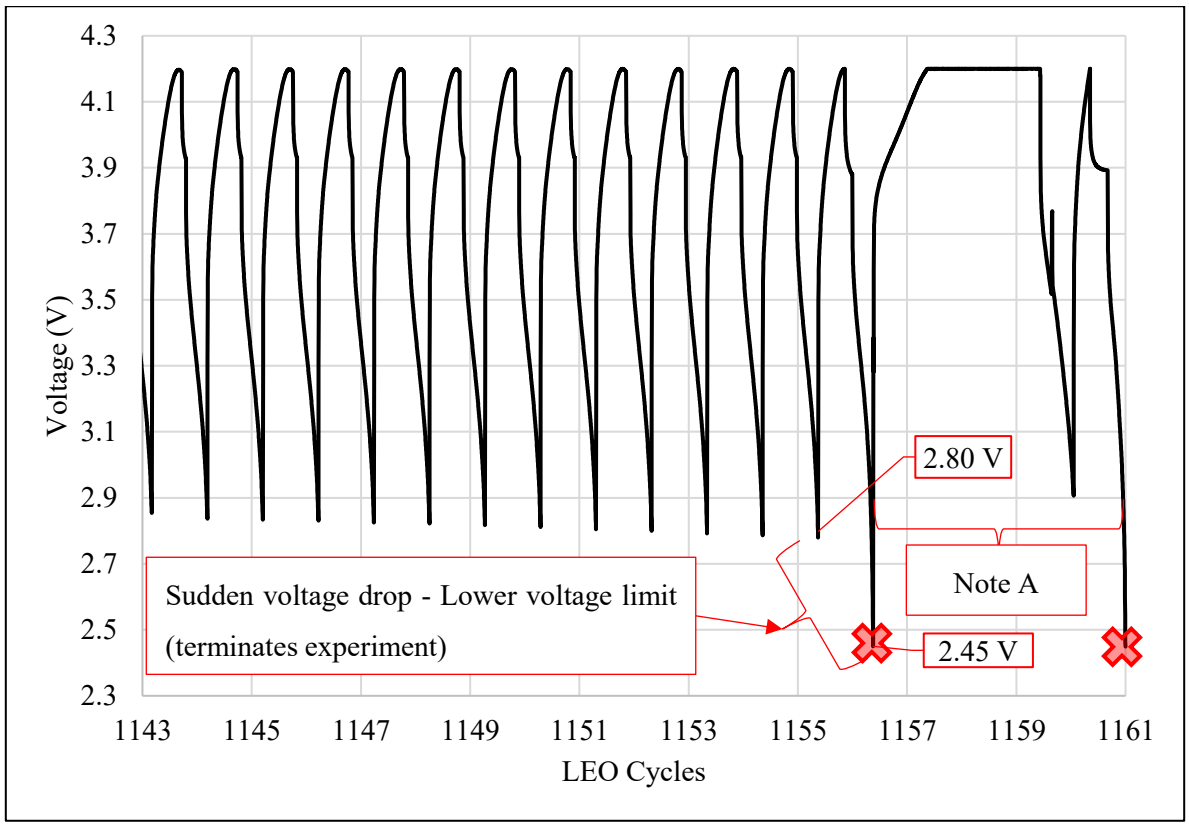

Figure 5.11 Voltage response of the temperature condition NCA cell group (101 kPa, 10 °C) during accelerated LEO cycles immediately preceding failure. Failure points marked by red 'X'

The sudden drop in voltage resulted from one cell in the NCA 3P group causing its CID to electrically disconnect, causing the cell to enter open circuit mode. A CID is disconnected from excessive interior gas generation on the inside of the sealed cell resulting in a pressure increase above the rated pressure of the CID. The cell was confirmed as having a disconnected CID as the OCV was zero upon removal from the 3P group. The CID prevents the cell from operating as the positive current terminal is electrically disconnected, causing the 3P group to now act as a 2P group. When this occurs, the

remaining accelerated LEO discharge load of 33.6 W is applied to the other two cells in the 3P configuration, resulting in a 50% increase in discharge power from the remaining two cells in operation. As the remaining 2 cells cannot manage the additional load, there is a sudden voltage drop below the lower voltage alarm limit (2.45 V). Subsequent to the first *temperature* NCA cell CID failure during LEO cycling, reference cycles were conducted on the remaining two cells in the 3P grouping. During reference cycling, the CID from a second cell in the same 3P group disconnected. The occurrence of a second CID being disconnected gives confidence that neither failure was from a manufacturer defect causing a prematurely disconnected CID. Therefore, a CID disconnect causing cell group failure is representative of the NCA cell type operated in the *temperature* condition.

Note "A" in Figure 5.11 highlights the additional CC-CV charge and CC discharge completed to re-attempt one more LEO Cycle. The intent of the additional CC-CV charge and CC discharge is to bring the cell capacity to 90% SoC and reinitiate the LEO cycle in order to perform a verification that the first failure was not due to coulombic counting miscalculation or some other machine error. Immediately upon completion of the CV hold and a CC discharge to 90% SoC, a LEO cycle was commenced, and the cell group failed for a second time on the CP discharge due to hitting the lower voltage limit (2.45 V), confirming the cell group could not execute the accelerated LEO cycle.

The *vacuum* NCA group experienced accelerated capacity loss after the 3000th LEO cycle, resulting in only 37% of remaining initial discharge coulombic capacity at EoL on the 4518th LEO cycle. As 37% remaining initial capacity is sufficient capacity to complete a LEO cycle (18% ΔSoE) while accounting for the initial 10% decrease in SoC prior to a set of 480 LEO cycles, this confirms that the NCA cell did not fail from capacity loss. Rather, the *vacuum* NCA group had substantial IR growth causing the cell to gradually reach the lower voltage limit during the LEO cycle CP discharge (i.e. eclipse), see Figure 5.12.

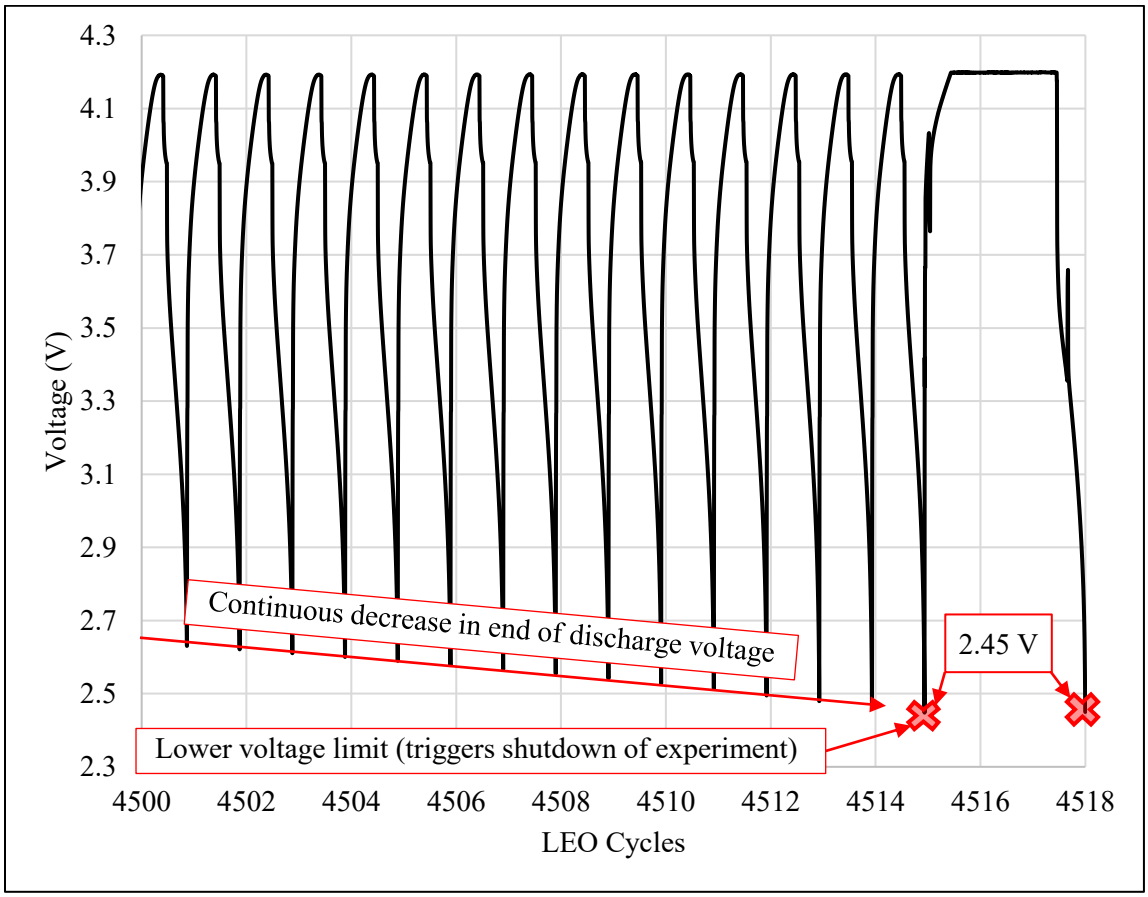

Figure 5.12 Voltage response of the vacuum condition NCA cell group (0.2 kPa, 10 °C) during accelerated LEO cycles immediately preceding failure. Failure points marked by red 'X'

The exponential IR increase shown in Figure 5.5 correlates well with the exponential trend of the end of discharge voltage towards the lower voltage limit, see Figure 5.13.

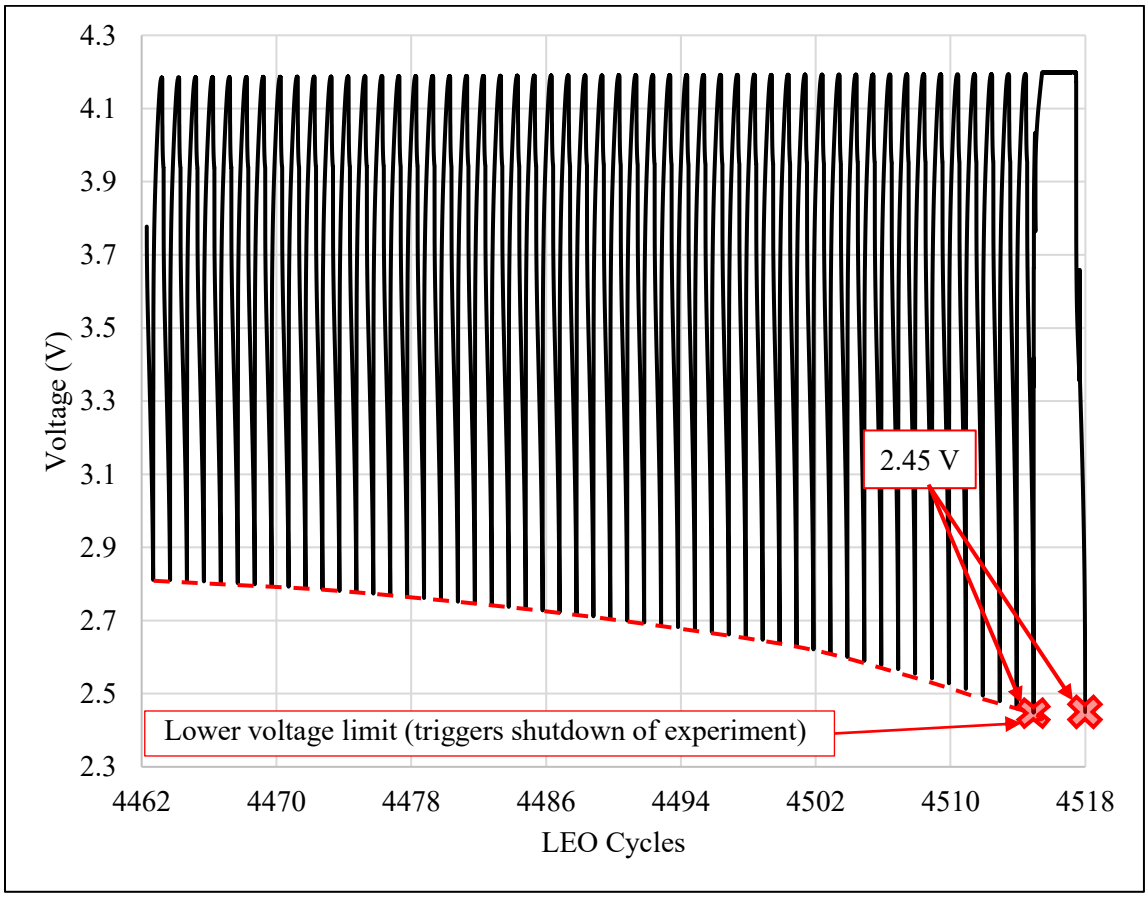

Figure 5.13 Voltage response of the vacuum condition NCA cell group (0.2 kPa, 10 °C) during accelerated LEO cycles immediately preceding failure. Failure points marked by red 'X'. Dashed red line showing lower voltage limit exponential trend toward termination

5.1.5.2 NMC

Similar to the continuous IR growth failure in the *vacuum* NCA group, all NMC cell groups failed as a result of continuous IR growth resulting in a steady decline in end of CP discharge voltage during the LEO cycle. The *laboratory* NMC group completed the most discharge energy throughput and LEO cycles of all other NMC groups, completing a total of 3486 LEO cycles. The final 20 LEO cycles reveal the cause of failure being IR growth resulting in the lower voltage limit (2.70 V) being attained during CP discharge of its final accelerated LEO cycle, see Figure 5.14.

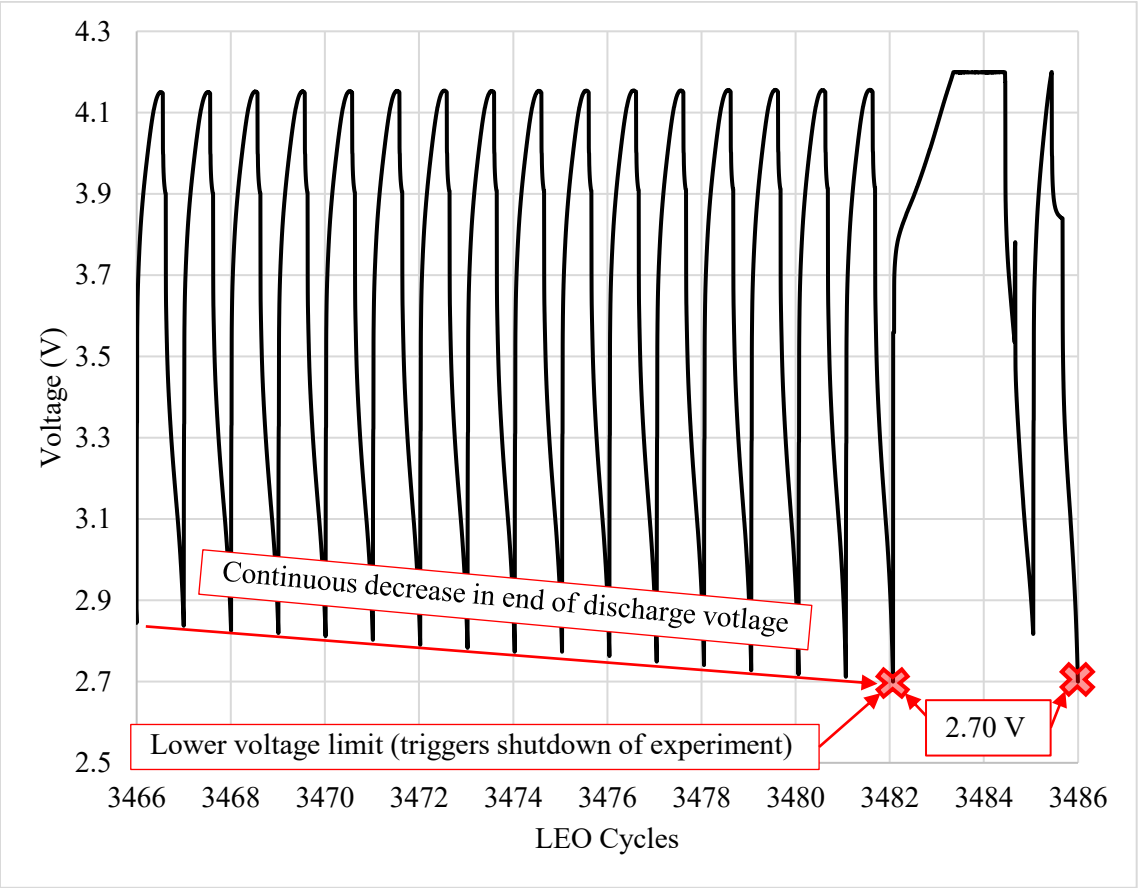

Figure 5.14 Voltage response of the laboratory condition NMC cell group (101 kPa, 20 °C) during accelerated LEO cycles immediately preceding failure. Failure points marked by red 'X'

The *temperature* condition NMC group energy efficiency decreases significantly after the 800th LEO cycle and failed to continue operation on the 854th LEO cycle due to a sharp increase in IR (Figure 5.5). By analyzing the end of discharge voltage curve of the *temperature* condition NMC group during the last 20 LEO cycles, the effect of a continuous increase in IR is apparent prior to failure, see Figure 5.15.

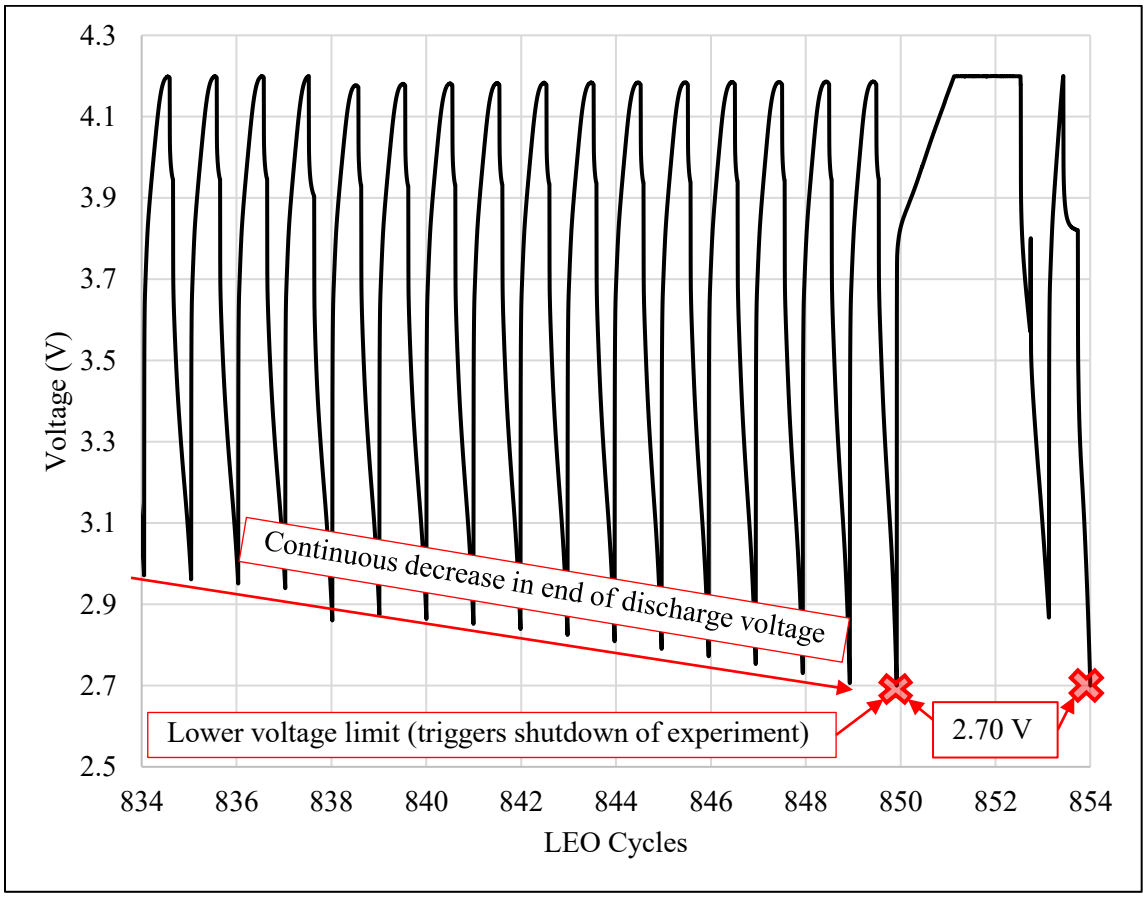

Figure 5.15 Voltage response of the temperature pressure NMC cell group (101 kPa, 10 °C) during accelerated LEO cycles immediately preceding failure

Similar to the *laboratory* and *temperature* condition NMC groups, the *vacuum* NMC group failed from increased IR growth resulting in excessive voltage drop during the CP discharge. The additional LEO cycles completed by the *vacuum* NMC group (1406 LEO cycles) compared to the *temperature* NMC group (854 LEO cycles) are due to the warmer operating cell temperature of the NMC group in *vacuum* (average 27 °C) versus *temperature* (average 18 °C), lowering the IR and increasing ionic conductivity in both PAM and NAM. The *vacuum* condition achieved far less LEO cycles compared to that of the *laboratory* condition (average 37 °C, 3486 LEO cycles), due to its relatively lower operating temperature. The NMC cell type clearly operates best at warmer temperatures as the increase in ionic conductivity significantly improves the ability of a lithium-ion to intercalate into both PAM and NAM. Hence, NMC is likely dominated by cold temperature side reactions such as lithium metal plating.

The IR of a cell, for both charge and discharge, increase as the cell capacity degrades and is dependant on SoC. Because the accelerated LEO cycle is a partial SoC operation, only certain SoC IR points are reached during cycling. As the cell degrades, a broader spectrum of ΔSoC is used, and consequently the impact from IR growth become more pronounced. Figure 5.16 shows these trends by plotting IR, individually for charge and discharge, over the range of SoC, from the BoL to the EoL of a cell.

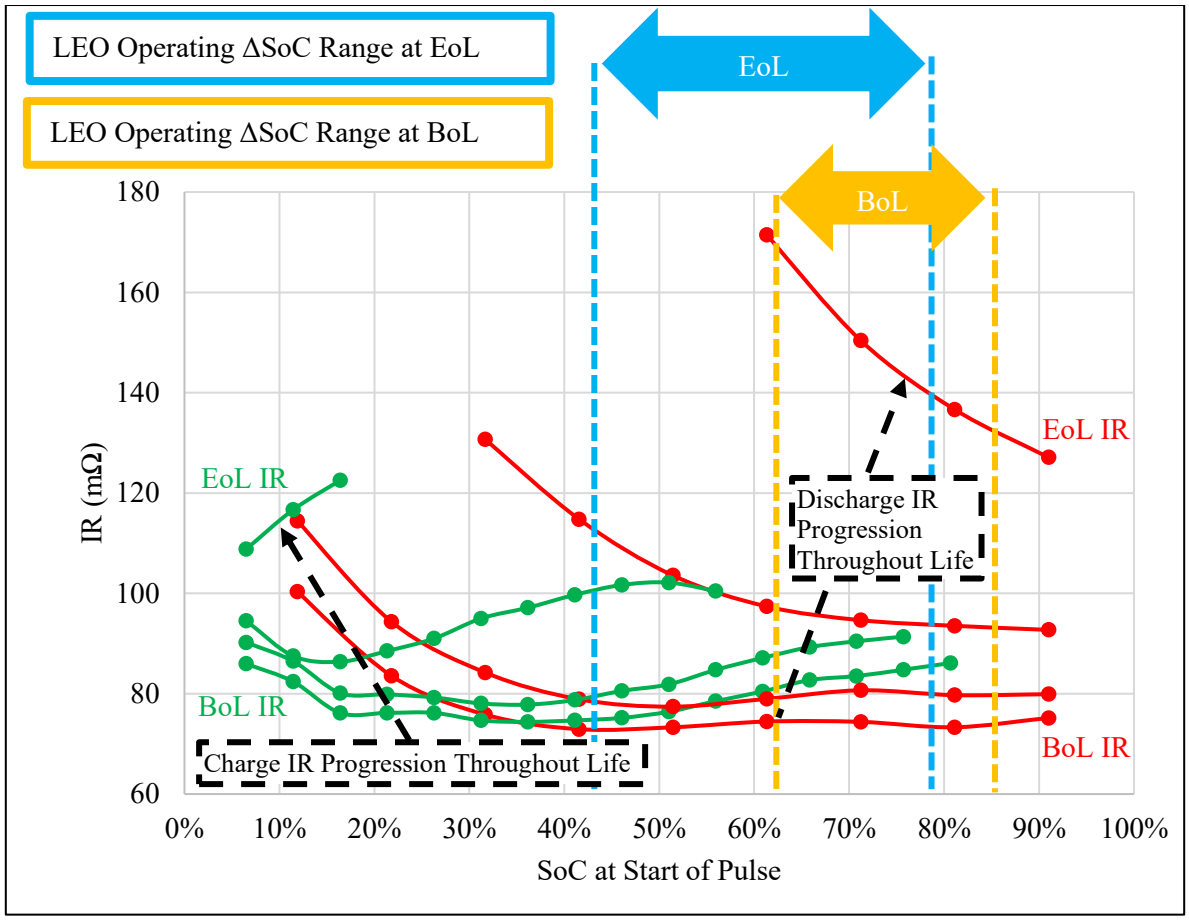

Figure 5.16 IR of the median cell from the temperature condition NMC cell group (101 kPa, 10 °C) during reference cycles showing progression from BoL to EoL for discharge (red) and charge (green) as a function of SoC. The accelerated LEO operating ΔSoC ranges are shown for BoL (yellow) and EoL (blue) to aid in identifying critical IR points

The LEO cycle ΔSoC range at BoL and EoL highlights the IR points which affect LEO cycling. The various charge (green) and discharge (red) IR curves in Figure 5.16 show IR growth progression from

BoL to EoL. IR during discharge is greater than charge. As the cell group capacity continues to degrade, the ΔSoC increases from 23% at BoL (62%-85% SoC) to 35% at EoL. This increase in ΔSoC combined with IR growth and the shift towards a lower SoC causes the cell group lower voltage to exponentially trend towards the lower voltage limit with each cycle.

The differences in each condition caused both CID and IR growth failures in the NCA cell type while the NMC cell type failed purely from IR growth. These failure modes although different, both terminate the 3P cell group while in the LEO cycle. The CID is disconnected as a result of gas generation which can occur from electrolyte degradation throughout cycling and from initial and ongoing SEI growth. IR growth occurs from a number of degradation mechanisms and are predominantly lithium plating and SEI growth, which are dependant on LLI and LAM. To further quantify LLI and LAM leading to IR growth, loss in discharge capacity and cell group failure, dV/dQ techniques were utilized.

5.1.6 Differential Voltage Analysis

The following differential voltage analysis results were developed using theory related to degradation mechanisms discussed in Section 2.1, cycling methods from Section 4.5.3 and analysis methodology in Section 4.6. Differential voltage analysis cycling was completed at BoL and EoL. It should be noted that LFP groups in each condition, *laboratory* NCA and NMC groups were excluded from this section due to the 4-month shutdown as a response to the COVID-19 pandemic. This 4-month shutdown resulted in shelf life capacity degradation in these highly degraded cells before a true EoL differential voltage analysis cycle could be completed.

Each cell has unique PAM whereas the NAM is graphite in all three cells. Lithium staging results for the lithium metal||graphite half-cells are presented, followed by the dV/dQ results for each of the three cell types (NCA, NMC, LFP).

5.1.6.1 Lithium Metal||Graphite Half-cell Staging

The lithium metal||graphite half-cell use graphite as the PAM, hence the graphite acts as the cathode and lithium metal acts as the anode. The lithium metal||graphite half-cell voltage versus normalized discharge capacity for each cell type (NCA, NMC, LFP) is presented in Figure 5.17.

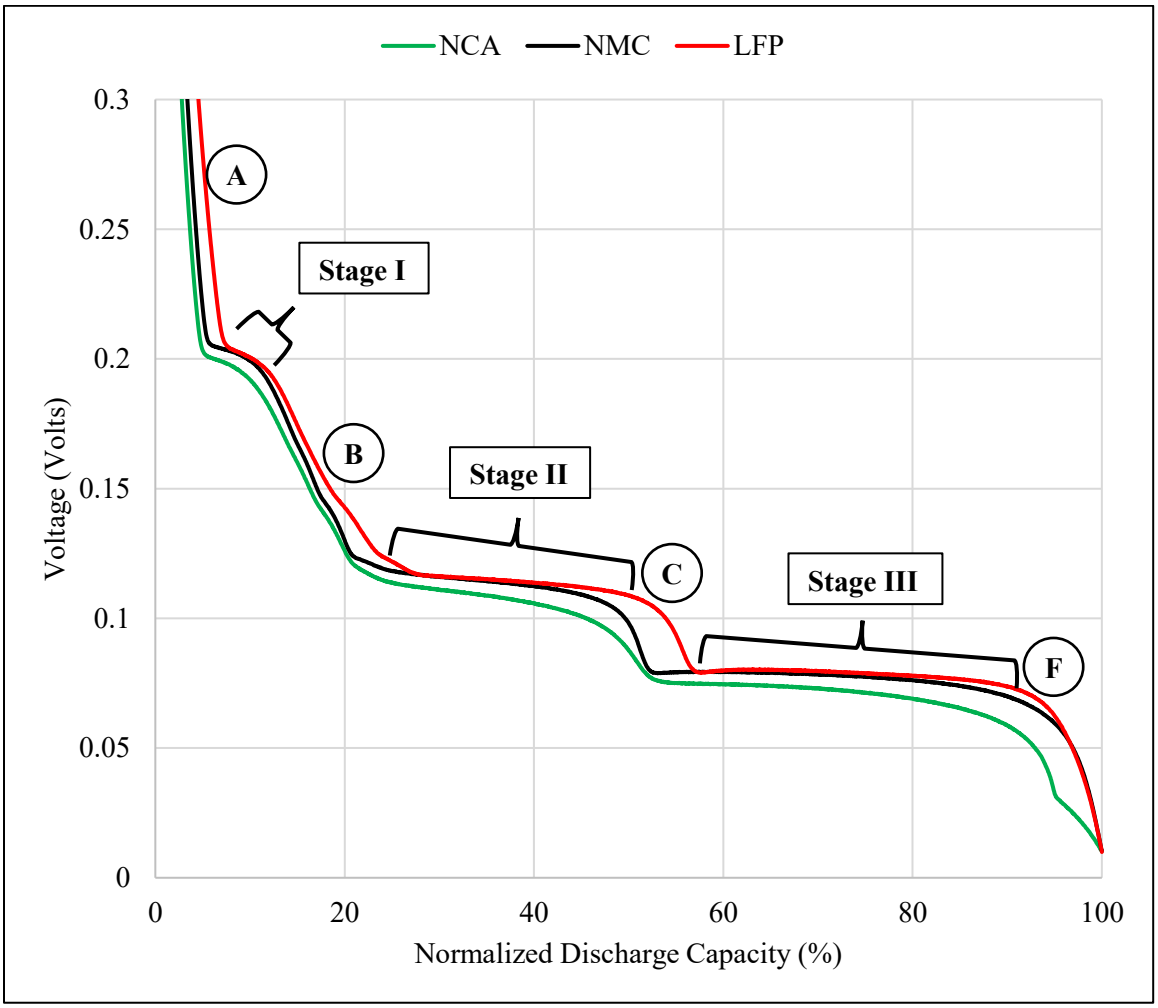

Figure 5.17 Lithium staging in lithium metal||graphite half-cell voltage versus normalized discharge capacity (%) at C/40 discharge for all three cell types. Graphite materials represented by their full cell PAM

As expected, results presented in Figure 5.17 reveal a change in lithium staging occurring at similar SoC in all three graphite materials. However, the differences between graphite can be attributed to each graphite having a different fraction of parallel sheets causing variation in available lithium intercalation sites at the different stages. The changes in lithium staging features are labelled A, B, C and F (features D and E will be presented later in the PAM dV/dQ results) in Figure 5.17 and correlate to the peaks occurring in dV/dQ plots subsequent to this Section. Ehrlich and Dahn [4] show that lithium ions cannot intercalate between graphene sheets that are turbostratically misaligned, rather they must be parallel. Consequently, graphite with less turbostratically misaligned sheets allows for more lithium intercalation in each lithium intercalation stage. For example, Figure 5.17 reveals how

the graphite found in the NMC cell intercalates more lithium into Stage III compared to the NCA and LFP cell types.

5.1.6.2 NCA

Half-cell plots for the PAM and NAM with combined artificial full cell dV/dQ versus normalized SoC (%) are presented for the NCA cell type in Figure 5.18. The full cell is termed "artificial" due to it being the mathematical sum of the PAM and NAM dV/dQ curves and not the actual full cell.

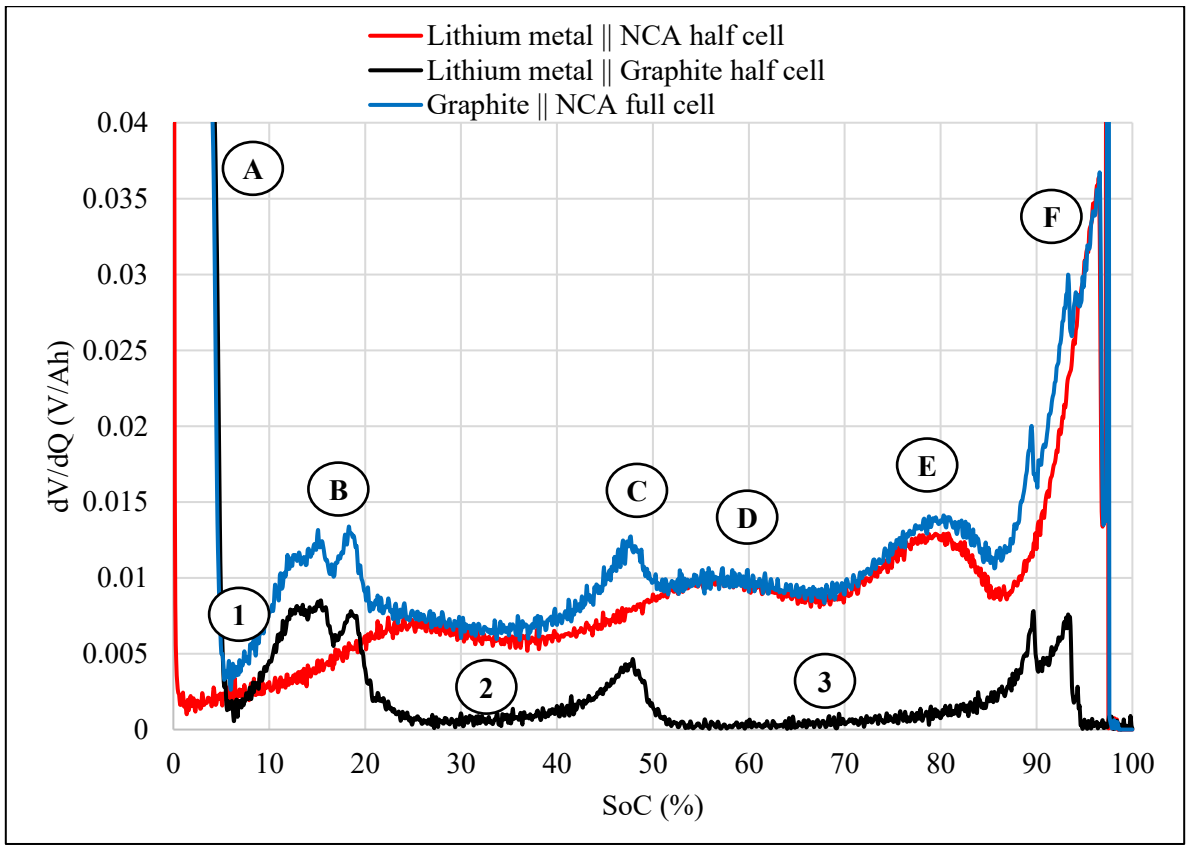

Figure 5.18 Half-cell and artificial full cell (0% NAM preloading) differential voltage over capacity (dV/dQ) with respect to percent SoC for the NCA cell type identifying dV/dQ peak A (NAM+PAM), peak B, C (NAM), peak D, E (PAM), peak F (NAM + PAM) and valley 1, 2, 3 (NAM)

In Figure 5.18, the letters represent "peaks" which visualize changes in lithium staging whereas numbers represent "valleys" that visualize homogenous lithium staging. From Figure 5.18 it is clear that the NAM individually contributes to peaks B and C while the PAM contributes to peaks D and E. Peak A and F represent a combination of both PAM and NAM contributions and respectively occur near the fully discharge and charged state. Using the peak identification in Figure 5.18 a comparison

between dV/dQ versus capacity curves for the actual BoL (i.e. uncycled with NAM preloading) NCA cell and NCA cells from the *temperature* and *vacuum* condition at EoL provide insight into the degradation occurring internally, see Figure 5.19.

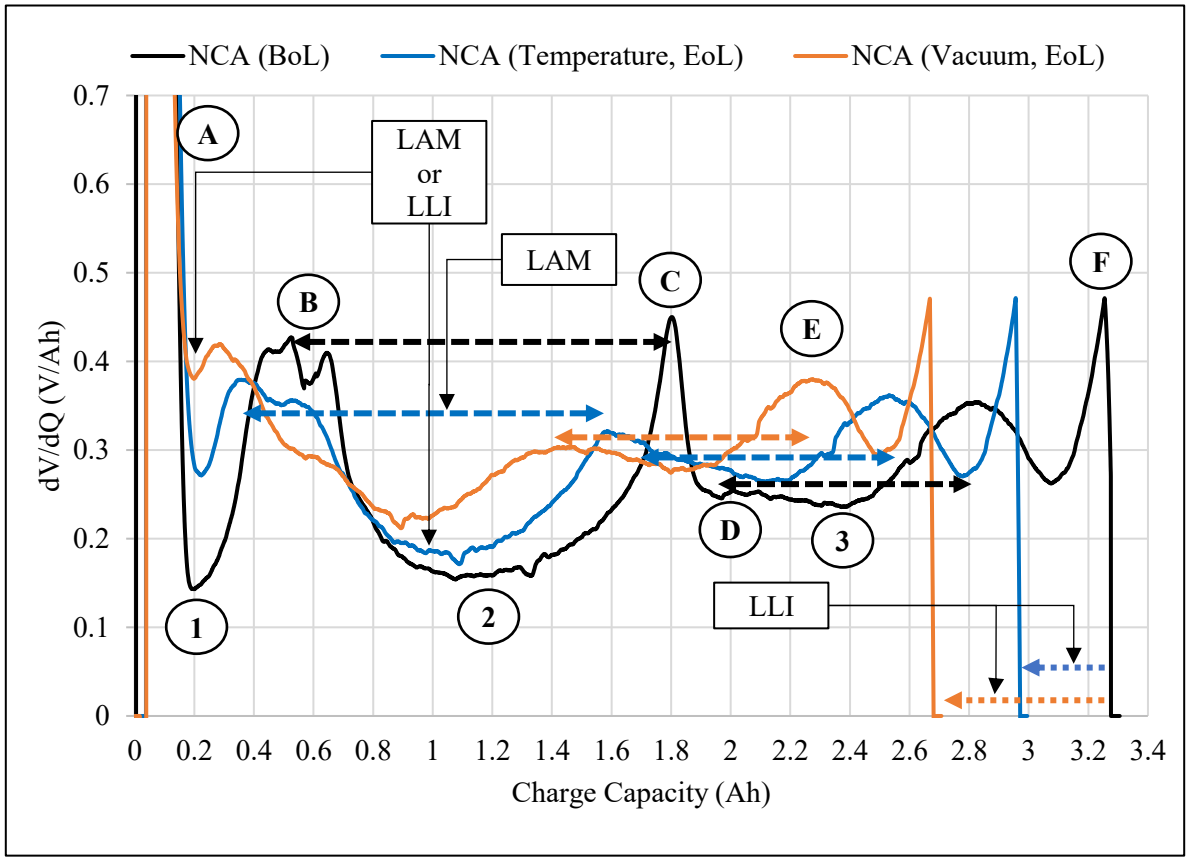

Figure 5.19 Full cell differential voltage over capacity (dV/dQ) with respect to discharge capacity for a BoL NCA cell contrasted with EoL NCA cells in the temperature and vacuum condition. NAM and PAM dV/dQ peaks labelled on BoL curve. Two sided arrows represent peak to peak distance (LAM) and one-sided arrows represent peak shift (LLI)

As dV/dQ cycling occurs after the initial three capacity reference cycles and single IR pulse cycle (Figure 4.20), SEI growth would have been formed prior to dV/dQ cycling. As a result of this SEI growth, lithium inventory has already been consumed and LAM on the negative electrode exists prior to dV/dQ cycling. In Figure 5.19 peaks C and D overlap, indicating approximately an additional 10% NAM preloading after the initial LAM on the negative electrode from initial SEI growth. Figure 5.19 reveals that both *temperature* and *vacuum* conditions experience LLI resulting in a respective 0.31

and 0.61 Ah capacity loss. This capacity loss is less than that described in Section 5.1.1 as the cells were cycled at a significantly slower rates during dV/dQ cycling.

The LAM on the negative electrode in the *temperature* condition is represented by the net decrease in peak B to C distance of 0.11 Ah relative to the BoL cell, representing 35% of total capacity loss in the full cell. There is no apparent LAM on the positive electrode as the peak D to E distance relative to BoL is unchanged. Thus, the entire loss in capacity in the *temperature* NCA cell can be attributed to at least 35% LAM on the negative electrode and the remainder is LLI which is likely from additional SEI growth and lithium plating (65%). With respect to the *vacuum* NCA cell, peak D to E distance has not decreased relative to BoL, thus there is no apparent LAM on the positive electrode. As peak C has completely disappeared, quantifying the LAM on the full negative electrode is not possible as it was the case with the *temperature* NCA group. Qualitatively, the combination of both LAM on the negative electrode and LLI in the full cell is illustrated for both the *temperature* and *vacuum* condition by valley 1, 2 and peak C losing intensity, which respectively identifies the lack of lithium-ion intercalation into the graphite NAM during stages I, II and III as shown in Figure 5.17.

5.1.6.3 NMC

Half-cell plots for the PAM and NAM with artificially produced full cell dV/dQ versus normalized SoC (%) are presented for the NMC cell type in Figure 5.20.

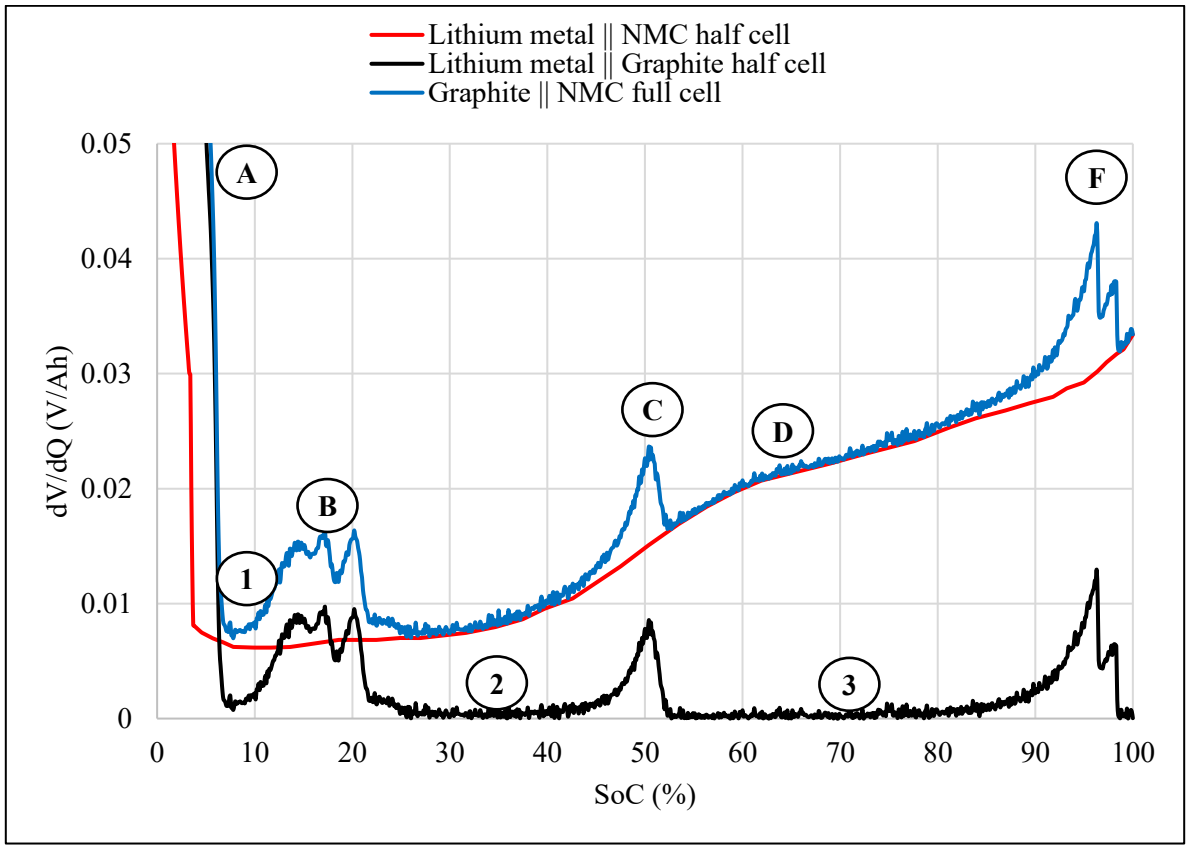

Figure 5.20 Half-cell and artificial full cell (0% NAM preloading) differential voltage over capacity (dV/dQ) with respect to percent SoC for the NMC cell type identifying dV/dQ peak A (NAM + PAM), peak B, C (NAM), peak D (PAM), peak F (NAM + PAM) and valley 1, 2, 3 (NAM)

In Figure 5.20 the numbering and lettering for change in lithium staging represented by "peaks" and homogenous lithium staging represented by "valleys" are kept consistent from the NCA analysis (Section 5.1.6.2). From Figure 5.20 it is clear that the NAM individually contributes to peaks B and C while the PAM does not contain very distinct features with a relatively low intensity peak D. Peaks A and F represent a combination of both PAM and NAM contributions and respectively occur near the fully discharged and charged state. A comparison between dV/dQ versus capacity from BoL to EoL provide insight into the degradation occurring internally, see Figure 5.21.

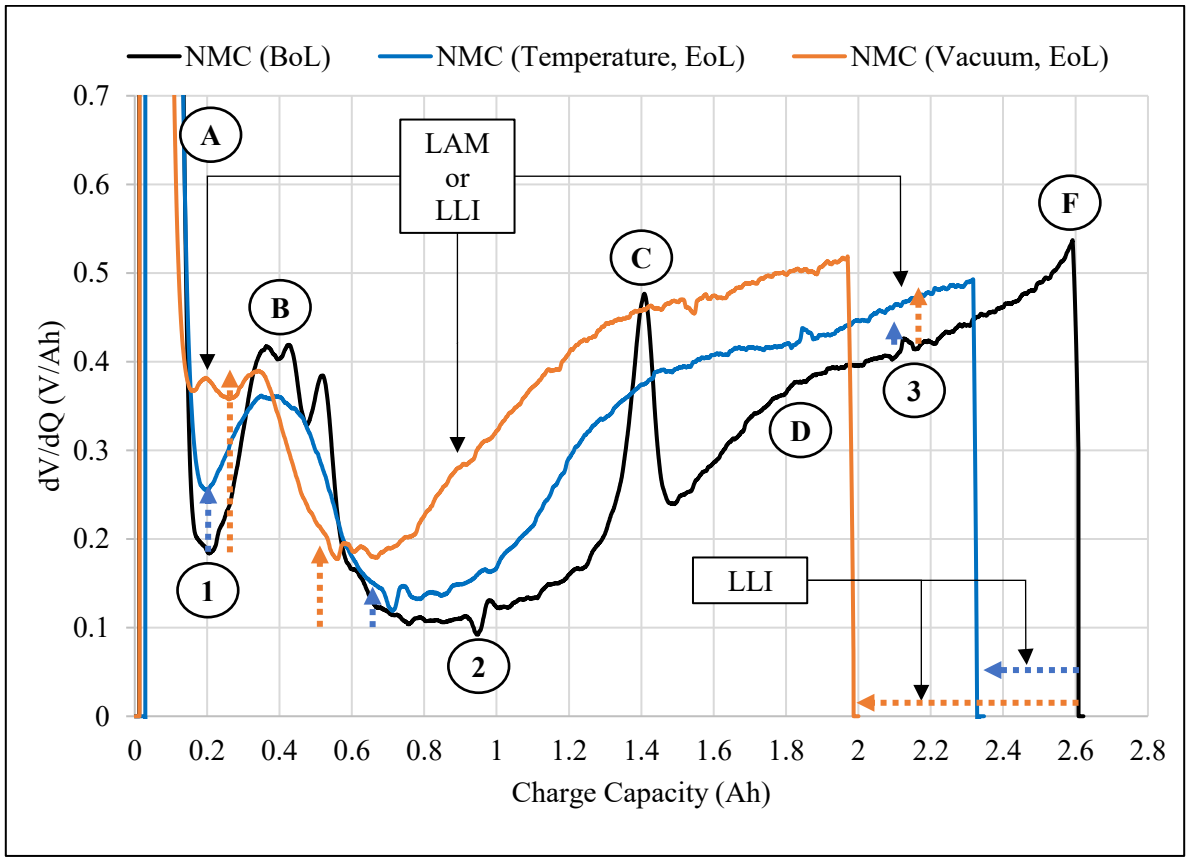

Figure 5.21 Full cell differential voltage over capacity (dV/dQ) with respect to discharge capacity for a BoL NMC cell contrasted with EoL NMC cells in the temperature and vacuum condition. NAM and PAM dV/dQ peaks labelled on BoL curve. Vertical arrows represent either LAM on negative electrode or LLI in full cell. Horizontal one-sided arrows represent peak shift (LLI) in full cell

In Figure 5.21 peak C appears at approximately 55% SoC whereas in Figure 5.20 it occurred at 51% Soc, thus there is a relatively low 4% NAM preloading remaining subsequent to the initial SEI growth. Figure 5.19 reveals that both *temperature* and *vacuum* conditions experience LLI yielding a respective 0.28 and 0.62 Ah capacity loss. As peak C has disappeared entirely in both cases, there is no peak to peak reference point to quantify loss of NAM. With regards to the PAM, peak D remains intact however there are no additional PAM reference peaks for a reference to quantify the total loss in PAM. However, from Figure 5.21, it is clear that in both the *temperature* and *vacuum* condition, valleys 1, 2, 3 and peak B are losing intensity, which respectively identify that a LAM in the negative

electrode or total cell LLI, preventing the intercalation of lithium ions into the graphite NAM during stage I, II and III as shown in Figure 5.17.

5.1.6.4 LFP

At the time of writing this thesis (July 2020), LFP cell groups did not achieve EoL and consequently did not undergo dV/dQ reference cycling as a result of the 4-month shutdown as a response to the COVID-19 pandemic. This 4-month shutdown resulted in shelf life capacity degradation in these degraded cells before a true EoL differential voltage analysis cycle could be completed.

In order to make this thesis as complete as possible, the LFP half-cells are analysed to determine peak contribution to the full cell dV/dQ curve, see Figure 5.22.

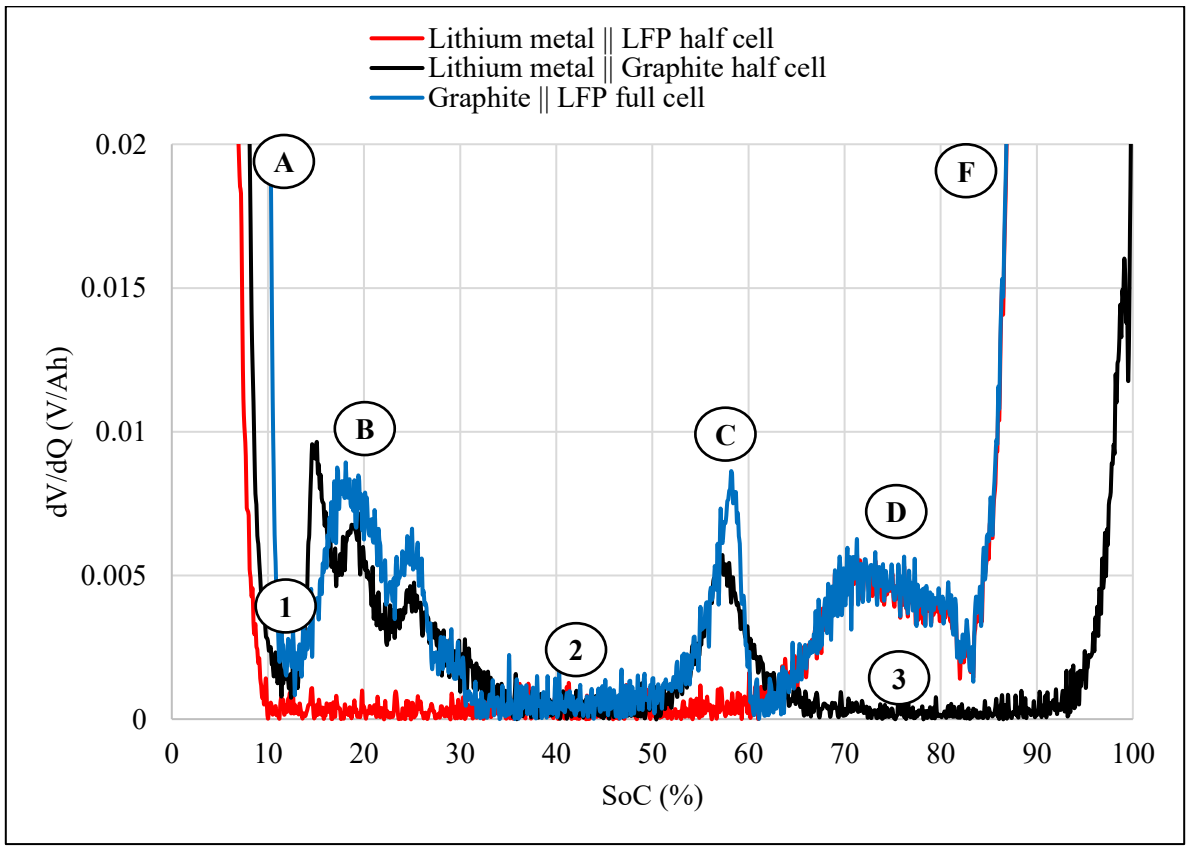

Figure 5.22 Half-cell and artificial full cell (0% NAM preloading) differential voltage over capacity (dV/dQ) with respect to percent SoC for the LFP cell type identifying dV/dQ peak A (NAM), peak B (NAM), peak C (PAM), peak D (PAM), peak F (NAM + PAM) and valley 1, 2, 3 (NAM)

From Figure 5.22 individual peaks A and B are features from the lithium staging occurring in the NAM whereas peak C is for the PAM. Similar to the NCA cell type, peak F represents the combination of lithium staging occurring in both PAM and NAM simultaneously. The actual full cell at BoL is shown in Figure 5.23.

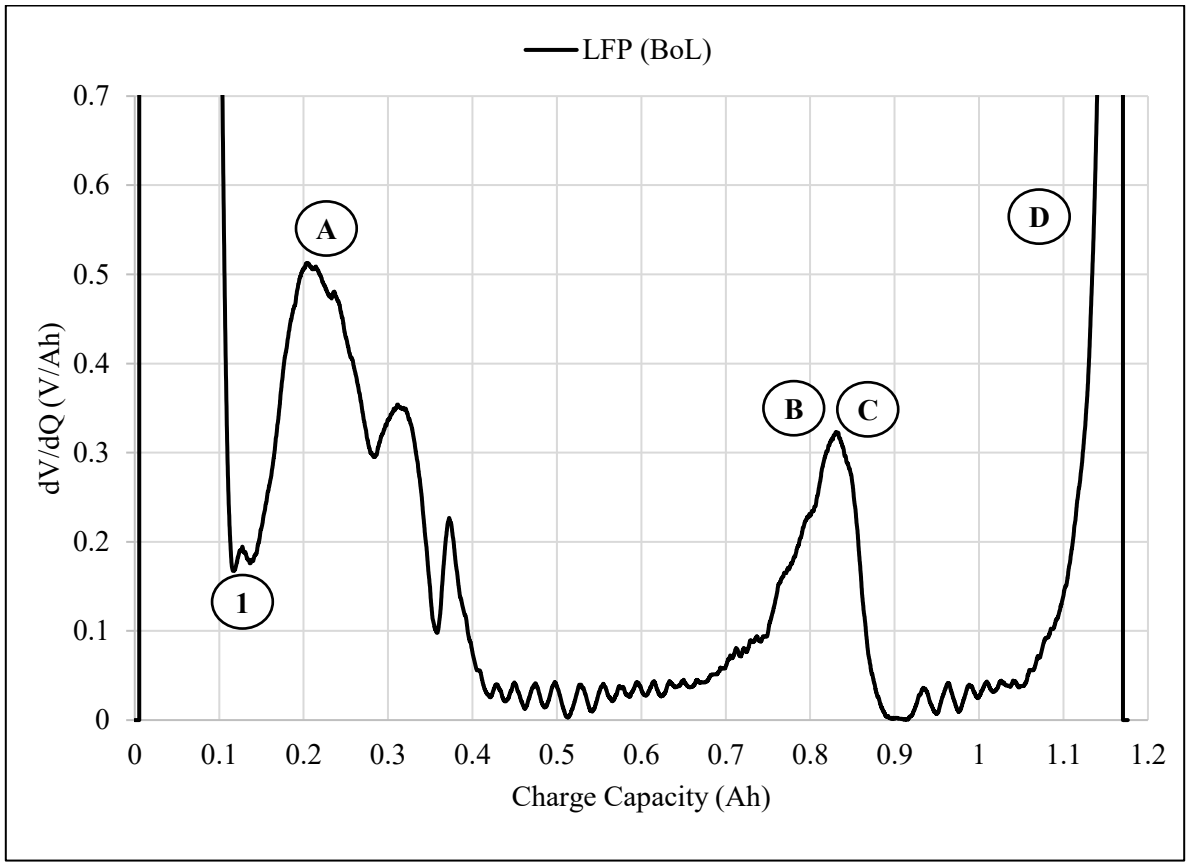

Figure 5.23 Full cell differential voltage over capacity (dV/dQ) with respect to discharge capacity for BoL LFP cell

From Figure 5.23 the actual full cell appears to have only one peak in place of peaks B and C as shown in Figure 5.22. This is attributed to a NAM preloading of ~15% shifting peak B to the right causing it to overlap with peak C. Interestingly, with disproportionate LAM between the NAM and PAM, peaks B and C would separate with cycling.

5.1.7 Shift in State of Energy for Low Earth Orbit Cycling

As cell capacity degrades during LEO cycling, the ΔSoE shifts from a high to low SoE. The CP discharge (33.6 W) for a precise time (700 s) yields a constant discharge energy on each 3P grouping

(6.534 Wh) and consequently each cell (2.178 Wh) in the group as a result of the parallel configuration. To exemplify how the change in ΔSoE is best be visualized, four instances are presented from this studies dataset. The examples include each cell type (NCA, NMC, LFP) in the *vacuum* condition and the NCA group in *temperature* condition. The ΔSoE shift for the *vacuum* condition NCA group is presented in Figure 5.24.

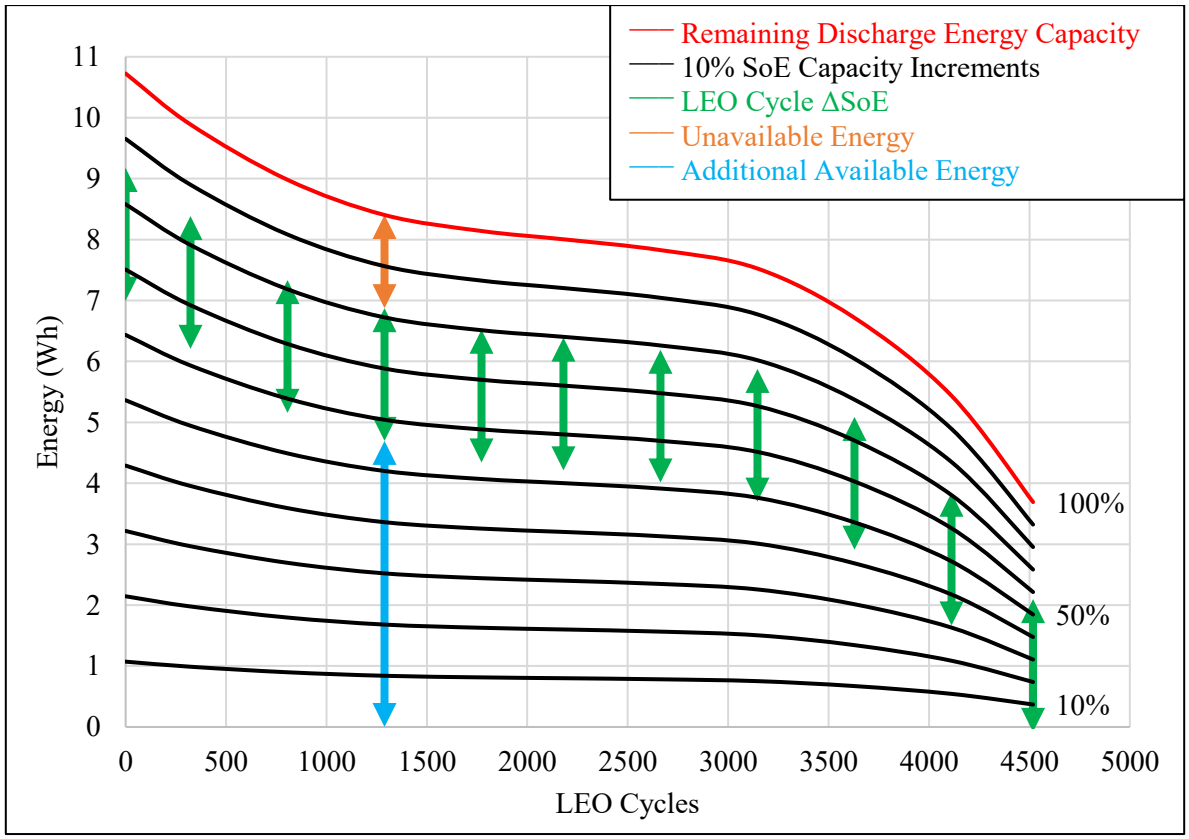

Figure 5.24 Remaining discharge energy capacity (red) with 10% ΔSoE increments (black) and required LEO cycle ΔSoE (green) with respect to LEO cycles completed for the NCA cell in vacuum condition (0.2 kPa, 10 °C) from BoL to EoL (4518 LEO Cycles). Unavailable (orange) and additional available (blue) energy shown at ~1300 LEO cycles

As the energy demand per LEO cycle on a cell is 2.178 Wh, this is the minimum available energy to successfully execute a LEO cycle. The upper bound of ΔSoE is a function of both the initial CC discharge to 90% SoC (1.20 – 1.26 Wh) and the additional decrease in ΔSoE from terminating charge early on the first LEO cycle (0.29 – 0.43 Wh) as a result of no CV charge. Without a CV charge, there is a significant portion of energy capacity that is unavailable during the LEO cycle (~1.6 Wh). The

unavailable energy (orange) is represented by the range above the ΔSoE range (green) while all energy below the ΔSoE range is additional available energy (blue). Hence, the total available energy for LEO cycling is measured from the upper ΔSoE bound to 0 Wh (green + blue).

At BoL, 1.6 Wh of unavailable energy accounts for approximately 15% of the entire cell discharge energy capacity, while at EoL this is increased to 43%. Parallel to the increase in unavailable energy, throughout LEO cycling, the ΔSoE required at BoL to EoL respectively increases from 20% to 57% of the entire cell discharge energy capacity. The increase in both unavailable energy (43%) and required energy (57%) at EoL sum to 100% of the full discharge capacity of the cell, exemplifying the point in which cell failure occurs due to lack of available energy. Interestingly, although most of the unavailable energy is a result of the initial CC discharge to 90% SoC, if the CC discharge were removed from the LEO cycle script (See Appendix B, ID 4), the contributions from IR would consist of the entire 1.6 Wh of unavailable energy due to a drop in SoE from ending sinusoidal charge early due to hitting the upper voltage limit. This could be eliminated with a CV charge however would not represent the ideal method for generating power on a LEO satellite as this would reduce the capacity factor of the solar photo-voltaic system.

As a point of contrast to IR growth failure, the *temperature* NCA group was found to have failed from disconnecting the CID in one cell of the 3P group (Section 5.1.5.1). As a result of failure from a disconnected CID, the ΔSoE never exceeded the total available energy in the *temperature* NCA group, see Figure 5.25.

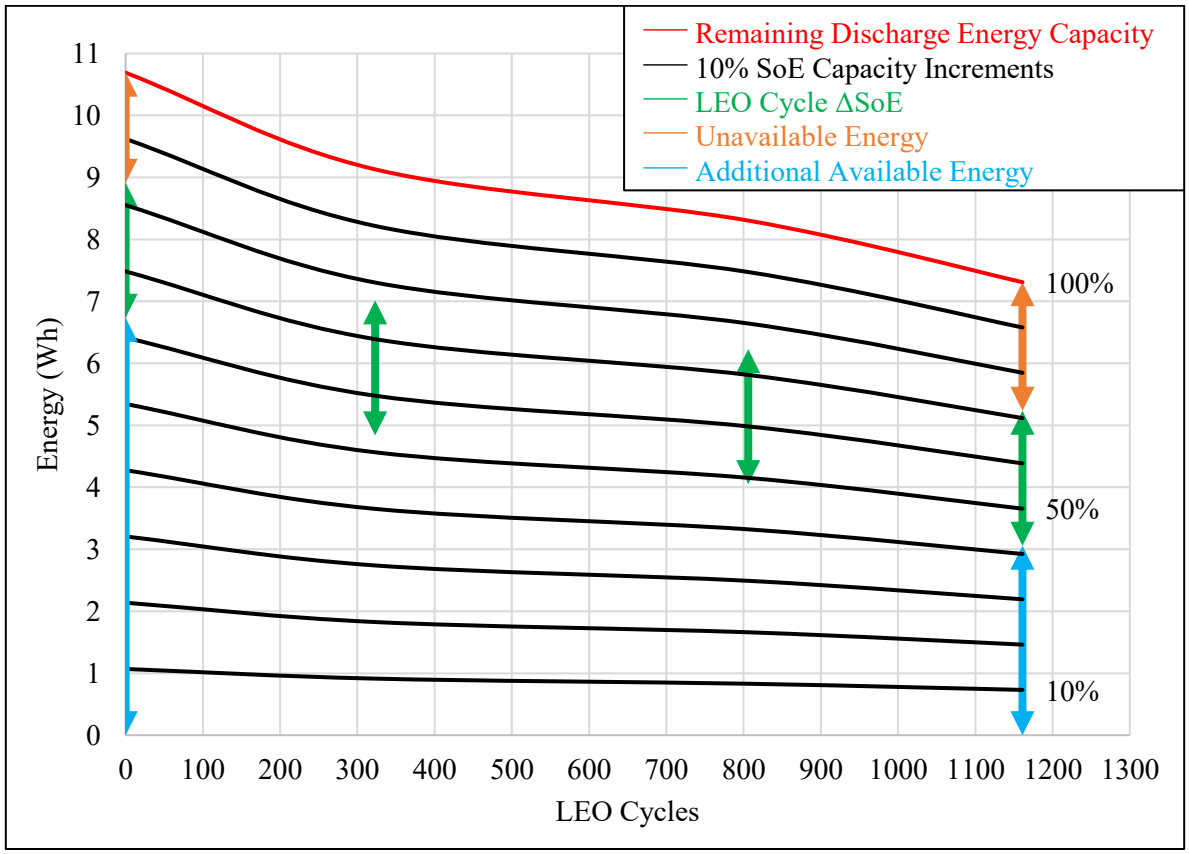

Figure 5.25 Remaining discharge energy capacity (red) with 10% ΔSoE increments (black) and required LEO cycle ΔSoE (green) with respect to LEO cycles completed for the NCA cell type in temperature condition (101 kPa, 10 °C) from BoL to EoL (1161 LEO Cycles). Unavailable (orange) and additional available (blue) energy shown at BoL and EoL

Figure 5.25 reveals there is over 3 Wh of unused additional available energy from the *temperature* NCA group at EoL as a consequence of its failure being a disconnected CID due to excessive gas generation.

Similar to the *vacuum* NCA group, the NMC group in *vacuum* experiences a depletion in available energy below the required LEO ΔSoE range, see Figure 5.26.

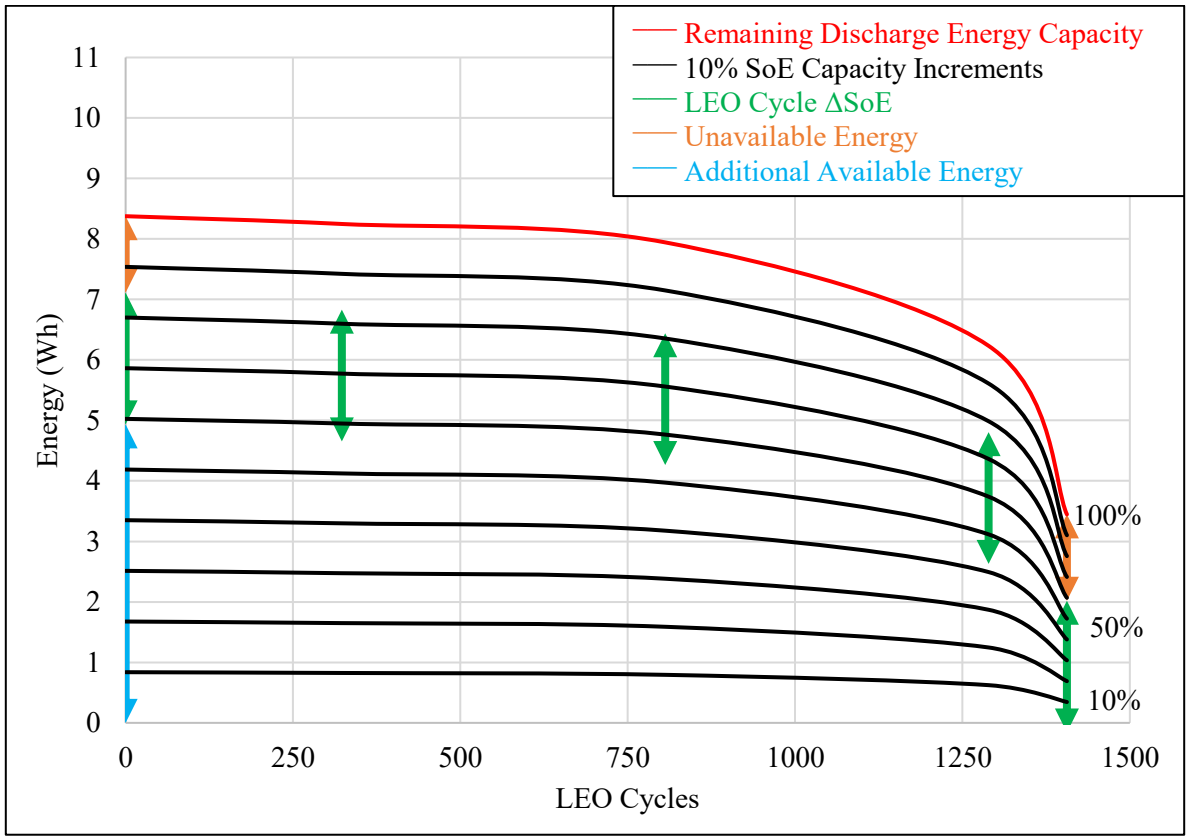

Figure 5.26 Remaining discharge energy capacity (red) with 10% ΔSoE increments (black) and required LEO cycle ΔSoE (green) with respect to LEO cycles completed for NMC cell type in vacuum condition (0.2 kPa, 10 °C) from BoL to EoL (1406 LEO Cycles). Additional available energy (blue) shown at BoL and unavailable energy (orange) shown at BoL and EoL

Figure 5.26 shows the unavailable energy and ΔSoE at EoL form 100% of the remaining discharge energy capacity in the cell and again exemplifies the point in which cell failure occurs due to lack of available energy as a result of IR growth, not the remaining discharge energy capacity.

The *vacuum* LFP group experiences a constant upper SoE bound as a result of its low IR growth and high power rating from BoL to EoL. Consequently, the unavailable energy (0.36 Wh) is determined entirely by the initial CC discharge to 90% SoC completed prior to the first LEO cycle. Plotting the shift in ΔSoE from BoL to EoL for the LFP group in *vacuum* reveals approximately 14% or 0.5 Wh of additional available energy required to complete the accelerated LEO cycle remains when LEO cycling was stopped, see Figure 5.27.

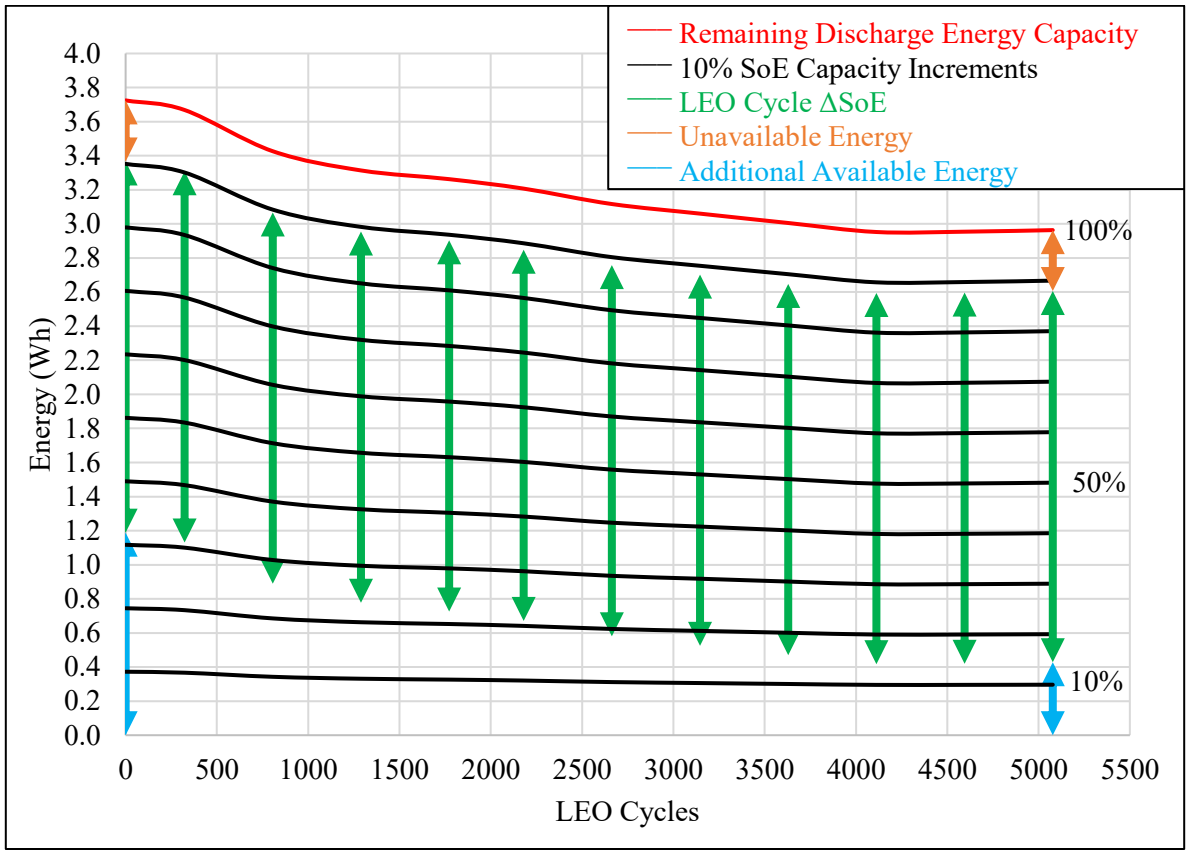

Figure 5.27 Remaining discharge energy capacity (red) with 10% ΔSoE increments (black) and required LEO cycle ΔSoE (green) with respect to LEO cycles completed for LFP cell type in vacuum condition (0.2 kPa, 10 °C) from BoL to EoL (5078 LEO Cycles). Unavailable (orange) and additional available (blue) energy shown at BoL and EoL

Unique to the LFP cell type, the unavailable energy is entirely formed from the initial CC discharge to 90% SoC, meaning a portion of the unavailable energy is artificially produced by the LEO cycling schedule. Although this is disadvantageous near EoL, operating away from the fully charged state reduces degradation (Section 3.4). Consequently, LEO satellites should cycle cells away from the upper cut-off potential at BoL to reduce degradation while additional available energy exists. If internal resistance growth has not consumed the entirety of unavailable energy once additionally available energy is depleted, the upper SoE should be raised to allow continued operation. It is recommended that this hypothesis be tested experimentally to quantify the benefit of cycling LFP cells in this manner.

By analyzing the shift in ΔSoE, the reduction in total LEO cycle count as a result of excessive IR growth and gas generation is illustrated. This highlights how CubeSat designs should consider cells with low initial IR and degradation rates (i.e. high cycle life) such as the LFP cell type which has significant advantages in maintaining operation in a LEO cycle due to the lack of a CV charge.

5.1.8 End of Test Summary

A summary of each cell group status, discharge coulombic capacity normalized by initial measurement, discharge energy throughput, equivalent cycles of initial measured coulombic capacity, and 100% ΔSoC energy efficiency are presented in Table 5.2.

Table 5.2 Summary of each cell type (NCA, NMC, LFP) by operational status and median single cell performance criteria at the last completed reference cycle. Cells marked "active" have yet to reach EoL condition in the LEO cycle

PAM	LEO Cycling Condition	Failed LEO Cycle	Discharge Coulombic Capacity Normalized by Initial Measurement	Discharge Energy Throughput (Wh)	Equivalent Cycles of Initial Measured Coulombic Capacity	100% ΔSoC Energy Efficiency
NCA	20 °C, 101 kPa	Active	54%	8300	741	84%
NCA	10 °C, 101 kPa	1161	71%	2700	247	82%
NCA	10 °C, 0.2 kPa	4518	37%	10,080	916	79%
NMC	20 °C, 101 kPa	3486	41%	7800	926	80%
NMC	10 °C, 101 kPa	854	66%	2000	240	83%
NMC	10 °C, 0.2 kPa	1406	43%	3000	380	81%
LFP	20 °C, 101 kPa	Active	80%	8300	2226	96%
LFP	10 °C, 101 kPa	Active	81%	10,380	3142	97%
LFP	10 °C, 0.2 kPa	Active	79%	10,380	3062	96%

5.2 Lithium-ion Cell Dissection, Scanning Electron Microscopy and Energy Dispersive X-ray Spectroscopy

Cell manufacturers do not provide detailed cell design or electrochemical material analysis. In fact, even the safety data sheets have a broad range of material proportions listed to protect from competitor reproduction. While principal active materials are known, their proportions are not disclosed by the manufacturer. Rather, manufacturer data sheets provide a wide range of possible elemental compositions for both PAM and NAM. For example, the LG Chem identifies that their cell has NMC material but will not quantify whether is it NMC 811 (i.e. 8/10th nickel, 1/10th manganese, 1/10th cobalt) or NMC 111, each of which cycle at a nominal 3.6 V. To verify the cell design and quantify the materials constituting each cell, a dissection, SEM and EDS analysis was performed.

In order to safely perform the dissection, lithium-ion cells were first discharged to 0 V in a flame retardant fume hood by connecting the positive and negative terminals through a resistor, see Figure 5.28.

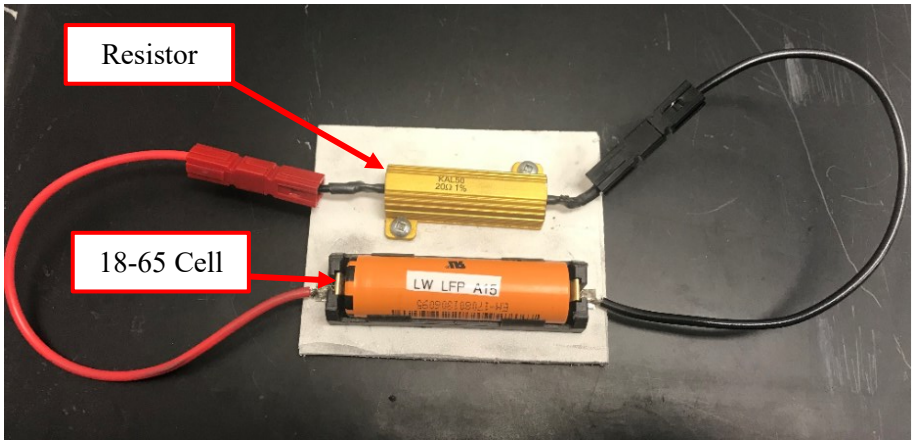

Figure 5.28 18-65 cell shorted through a resistor (20 Ω)

The NCA and NMC cells have a peak voltage of 4.2 V. As the 20 Ω resistor is applied, cell voltage will decrease non-linearly from 4.2 V to 0 V. Even at 4.2 V, the max discharge current is 0.21 A (0.88 W) making it safe for the resistor, wire, and the cell. After connecting the positive and negative terminals of each cell for 24+ hours through the resistor, the majority of capacity has been fully discharged. Subsequent to discharging each cell through a resistor, each cell was short circuited for an additional 24+ hours to remove any residual electrochemical energy, ensuring that no spark could be formed during dissection, see Figure 5.29.

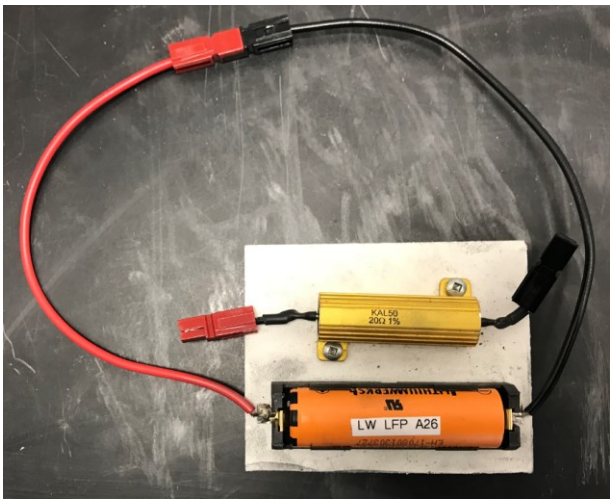

Figure 5.29 18650 cell externally shorted without resistor for final 24-hour full discharge to 0 V

It is important to note that there is still a material hazard when performing the dissection as both the electrolyte, separator and active materials are flammable. For safety, each cell was dissected in the fume hood with the positive and negative terminals shorted as shown in Figure 5.29. Tools used to perform the dissection are outlined in Table 5.3.

Table 5.3 Dissection and measurement tools

Tool	Description
Fine-toothed Hacksaw	Making an incision on the 18-65 cannister
Scalpel	Cutting away fine materials such as plastic shrink wrap
Scissors	Removing sections of electrode
Tape Measure	Measure jelly roll length, ± 0.5 mm
Mastercraft Digital Caliper	Measure jelly roll width, ± 0.03 mm
Mastercraft Digital Micrometer	Measure current collector and active material thickness, ± 0.005 mm

Upon removing the shrink wrap housing with the scalpel, a fine-toothed hacksaw was used to make the first incision along the circumference of the cannister adjacent to the crimp on the positive terminal side, exposing the cross-section of the jelly roll, see Figure 5.30.

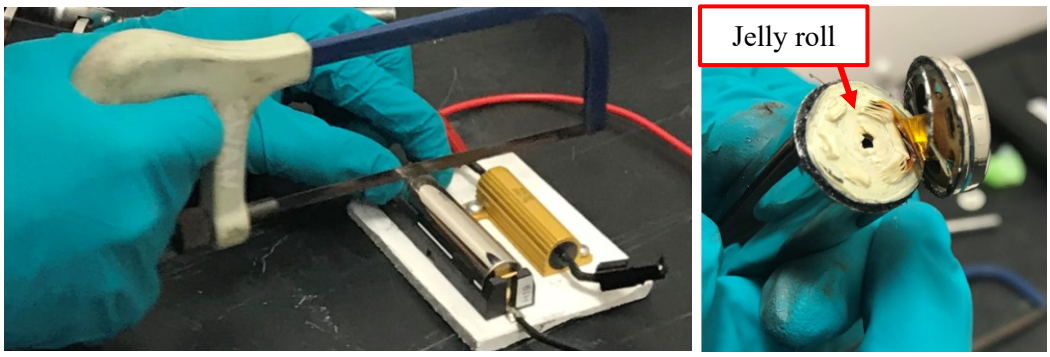

Figure 5.30 1st Cannister incision to 18-65 cell

The second cannister incision was made along the 65 mm length of the cannister using the fine-toothed hacksaw exposing the outer separator of the jelly roll, see Figure 5.31.

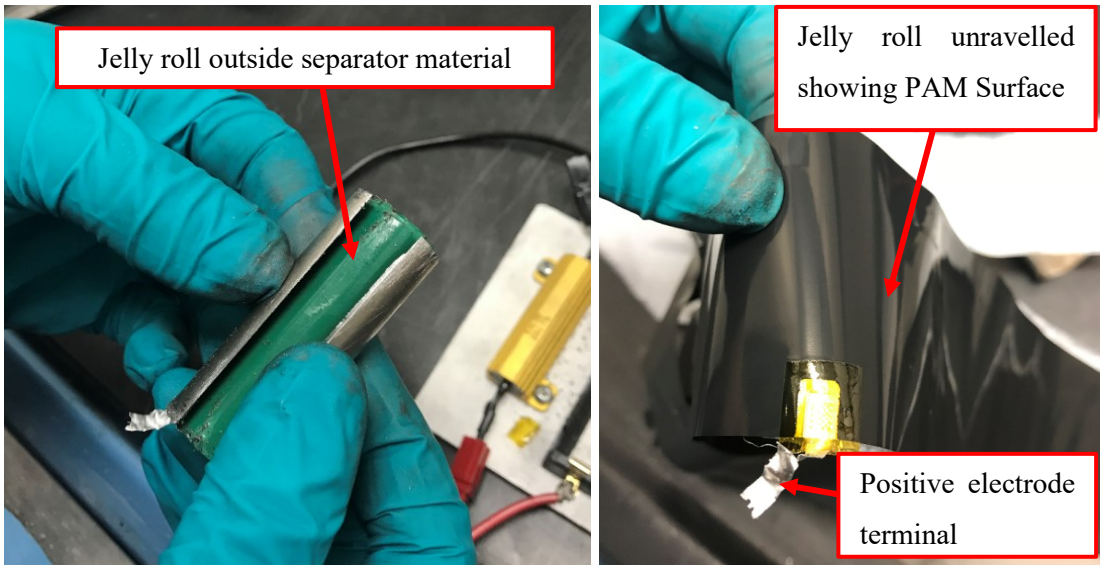

Figure 5.31 2nd Cannister incision to 18-65 cell

A micrometer was used to measure the jelly roll, PAM, NAM and separator thickness, a digital calliper was used to measure the width, while a tape measure was used to measure their respective lengths; see photo in Figure 5.32 and parameters in Table 5.4.

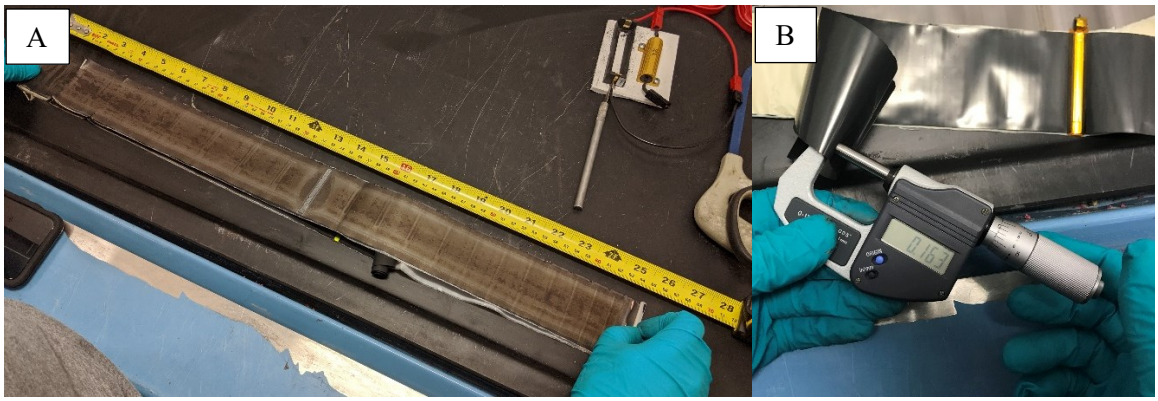

Figure 5.32 Cell dissection jelly roll measurements performed in fume hood at atmospheric pressure in ambient laboratory air. A: Jelly roll length, B: Jelly roll thickness

Table 5.4 Cell dissection parameters

Parameter (mm)	NCA	NMC	LFP
Jelly Roll Length	610	660	838
PAM Jelly Width	57.0	57.0	57.0
NAM Jelly Width	59.0	59.0	57.0
PAM Thickness	0.065	0.056	0.050
NAM Thickness	0.069	0.048	0.028
Aluminum Positive Current Collector Thickness	0.035	0.038	0.038
Copper Negative Current Collector Thickness	0.063	0.058	0.023
Separator Thickness	0.014	0.028	0.021
Shrink Wrap Thickness	0.065	0.080	0.095
Interior Rod Diameter	2.480	2.590	3.260
Interior Rod Thickness	0.150	0.140	0.190
Stack Thickness	0.394	0.360	0.259

The measurements in Table 5.4 show that LFP cell has a greater jelly roll length. The additional length in the same 18-65 cylindrical cannister size is achieved by reducing the jelly roll stack thickness. This additional length as a result of a thinner stack thickness gives the cell increased power capacity at the cost of energy density. The entire jelly roll thickness can be calculated using equation (5), with each parameter shown in Figure 5.33.

$$t_{stack} = 2\left(t_p + t_s + t_n\right) + t_{Al} + t_{Cu} \quad (5)$$

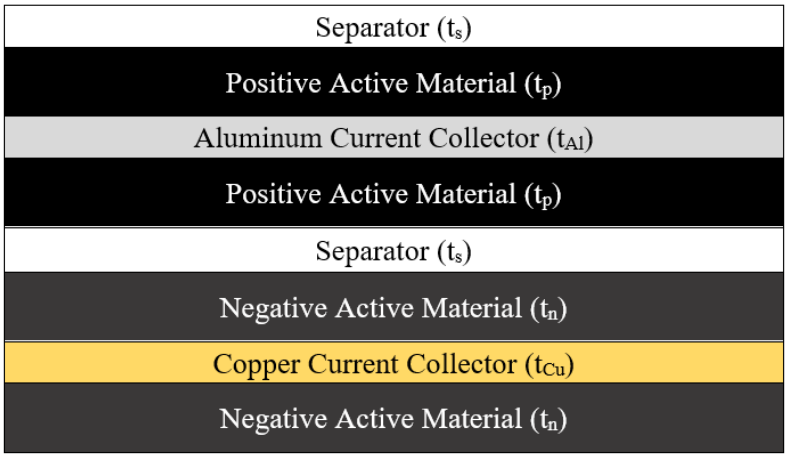

Figure 5.33 Lithium-ion 18-65 jelly roll stack (not to scale)

During the dissection process, a positive and negative electrode coated on both sides with active material was removed and sealed in a nitrogen glovebox. The samples were approximately 1 cm^2 and were taken from each cell type for SEM imaging and EDS analysis with the intent to further quantify the active material elemental composition.

SEM combined with EDS offer material researchers the capability of quantifying elements contained in a sample. SEM spectrum images were taken of both the PAM and NAM from each cell type at BoL in the fully discharged to 0 V state. The samples were placed on their individual specimen stubs and set in place on a common specimen holder (Figure 5.34A). The specimen holder containing all six samples (3 PAM, 3 NAM) was placed in the SEM analysis chamber and evacuated to $7x10^{-8}$ kPa (Figure 5.34B).

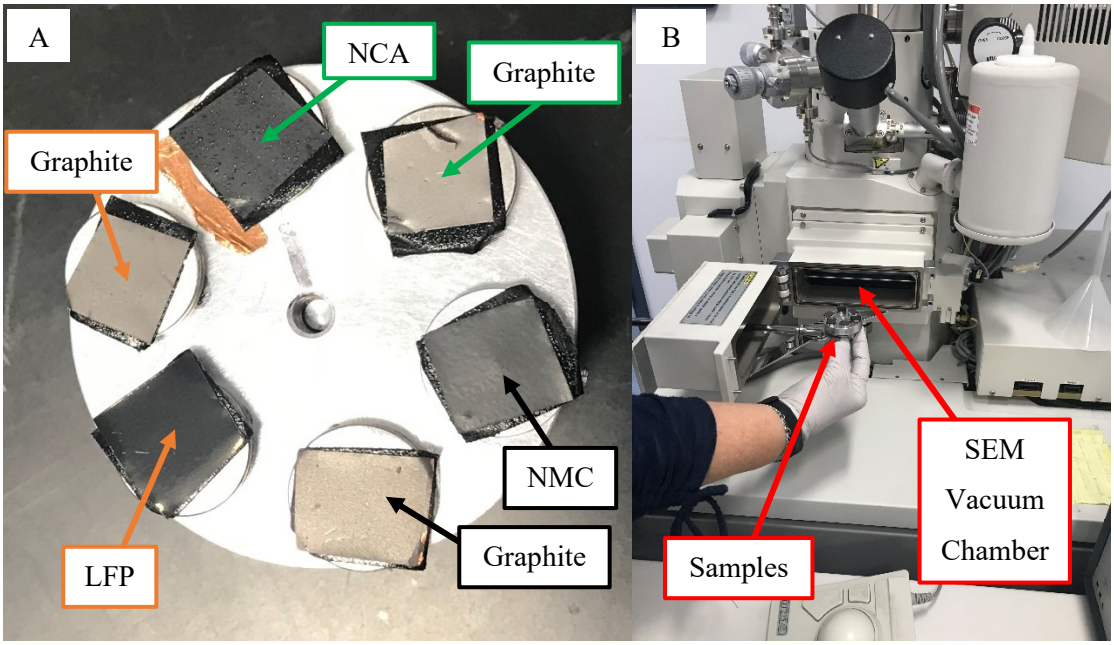

Figure 5.34 A: Six active material SEM samples with colour coded graphite materials, B: Hitachi S-4700

The main parameters involved in performing SEM include magnification, voltage and beam current and are to be adjusted accordingly depending on the material being scanned. In a lithium-ion cell, active materials are pasted to the current collector using a polyvinylidene fluoride binder [4], consequently it is recommended that SEM imaging be done at 10 kV [97]. All images were taken at the same 20 µA beam current in order to provide consistency between SEM images and EDS results. Magnification chosen for all samples were kept consistent in order to compare each active material visually. A 60k magnification was chosen as the final image to be used in EDS as this provided a count rate of approximately 5,000 counts per second to accurately perform EDS measurements. A low count rate results in insufficient data to accurately quantify element whereas a high count rate causes overlap between each data point and thus the data is rejected. Table 5.5 summarizes the various conditions used in each SEM spectrum.

Table 5.5 SEM experimental conditions

Electron image	Magnification	Voltage (kV)	Current (µA)	Lens (mm)	Images taken
1	x 1,000	10	20	3	1
2	x 10,000	10	20	3	1
3	x 20,000	10	20	3	1
4*	x 60,000	10	20	3	5

*Used as spectrum for EDS analysis

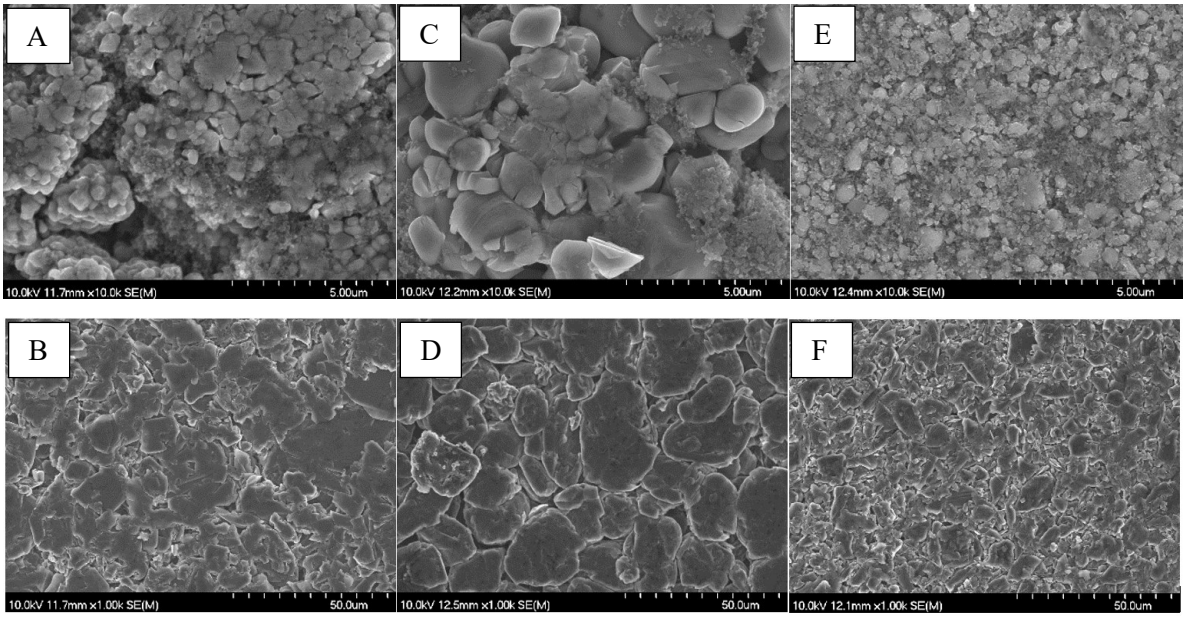

Figure 5.35 SEM images (A: Panasonic NCA PAM, B: Panasonic Graphite NAM, C: LG Chem NMC PAM, D: LG Chem Graphite NAM, E: Lithium Werks LFP PAM, F: Lithium Werks Graphite NAM). PAM setting (10.0 kV, x10,000 magnification). NAM Setting (10.0 kV, x1,000 magnification)

A total of five SEM images were taken of each active material and each analysed in the Inca EDS software. The elemental mass fractions of each material were obtained by creating a spectrum from the SEM electron image. The NAM for all three cells indicated mostly Carbon (98%) with trace amounts of fluorine and oxygen. Figure 5.35 shows that the graphite morphology in each cell type vary in particle size. Relatively speaking, the LFP has the smallest graphene (average ~2 µm), the NCA has a mixture of small and large graphene (average ~20 µm), the NMC has mostly large

graphene sheets (average ~30 μm). It should be noted that particle sizes were estimated visually. There are a multitude of factors that affect graphene properties such as precursor material, pyrolysis temperature, burn-off temperature thus it is no surprise that each manufacturer has slightly different graphite manufacturing processes that yield different graphite formations [17]. Dahn et al. [17] proposed a "falling cards method" to characterize different graphite formations and conclude that smaller pore sizes characterized by the radius of gyration 'R_g' are ideal for increasing LIB energy and power density. Thus, it is beneficial to the LFP cell to have the smallest graphite particles.

Each cell PAM varied in quantities of nickel, aluminium, cobalt, manganese, iron, phosphorous and oxygen. A summary of the elemental mole fraction for each PAM transition metal is presented in Table 5.6.

Table 5.6 Active material transition metal mass fraction EDS results

	Panasonic (NCA)			**LG Chem (NMC)**			**Lithium Werks (LFP)**	
Image	Ni	Co	Al	Ni	Mn	Co	Fe	P
1	0.85	0.14	0.01	0.48	0.35	0.17	0.69	0.31
2	0.85	0.13	0.01	0.50	0.32	0.18	0.70	0.30
3	0.82	0.17	0.01	0.50	0.33	0.17	0.70	0.30
4	0.84	0.14	0.01	0.50	0.32	0.18	0.68	0.32
5	0.85	0.13	0.01	0.49	0.33	0.18	0.69	0.31
Average	0.84	0.14	0.01	0.49	0.33	0.18	0.69	0.31

The results in Table 5.6 confirm the Panasonic, LG Chem and Lithium Werks cells respectively use NCA, NMC and LFP as their PAM. Using the mass fractions tabulated in Table 5.6 the mol fraction of each active material element can be calculated using equation (6).

$$n_f = \frac{m_f}{M} \tag{6}$$

The NCA, NMC and LFP transition metal component of its active material was found to respectively be $LiNi_{0.83}Co_{0.14}Al_{0.03}O_2$, $LiNi_{0.48}Mn_{0.34}Co_{0.18}O_2$ and $LiFePO_4$. As the LFP PAM is stoichiometric, it is not surprising to find that there is 1 mole of Fe for every mole of phosphorus. The NCA appears to be close to the NCA811 blend and the NMC is similar to a NMC532 blend. Since both NCA811 and NMC532 are commercially available blends [10], this improves the confidence in these EDS findings. It should be noted that other popular commercially available NMC blends exist such as NMC111,

NMC442, NMC622 and NMC811. For blends with more Ni content (i.e. NMC811) energy density is increased at the cost of thermal stability and cycle life [6], [10]. A summary of the main SEM and EDS findings are found in Table 5.7.

Table 5.7 Panasonic (NCA), LG Chem (NMC) and Lithium Werks (LFP) EDS results

Measured values	**NCA**	**NMC**	**LFP**
PAM Elemental Composition	$LiNi_{0.83}Co_{0.14}Al_{0.03}O_2$	$LiNi_{0.48}Mn_{0.34}Co_{0.18}O_2$	$LiFePO_4$
NAM Average Particle Diameter	Graphite, ~20 µm	Graphite, ~30 µm	Graphite, ~2 µm

5.3 Heat Transfer Model of 3P Cell Group

Heat is transferred by either convection, conduction, or radiation. In an attempt to better understand the contributions from each of these three modes of heat transfer, a model was developed which considers the three conditions (*laboratory*, *temperature*, *vacuum*) used in this degradation study. Each condition has a unique combination of ambient pressure, temperature, and convection mode (i.e. free or forced). The *laboratory* and *vacuum* condition use free convection while the *temperature* condition has forced air convection. The low gaseous density in *vacuum* condition results in a lower free convective heat transfer coefficient to that of the *laboratory* condition.

Conductive heat transfer relies on a solid interface between two bodies of varying temperatures and is independent of ambient pressure. Both convective and conductive heat transfer vary linearly with temperature gradient, see equation (7) and equation (8) respectively.

$$q_{conv} = hA_{conv}(T_s - T_{sur}) \tag{7}$$

$$q_{cond} = \frac{kA_{cond}(T_s - T_{Al})}{L_{cond}} \tag{8}$$

Radiative heat transfer is dependent on the emissivity constant and is proportional to the difference in temperatures, each to the fourth power as per equation (9).

$$q_{rad} = \varepsilon\sigma A_{rad}(T_s^4 - T_{sur}^4) \tag{9}$$

As each 3P grouping has a thermally complex design, a simplification is desirable in order to approximate the heat transfer in the system. The computer-aided design (CAD) model and the simplified thermal model are presented in Figure 5.36.

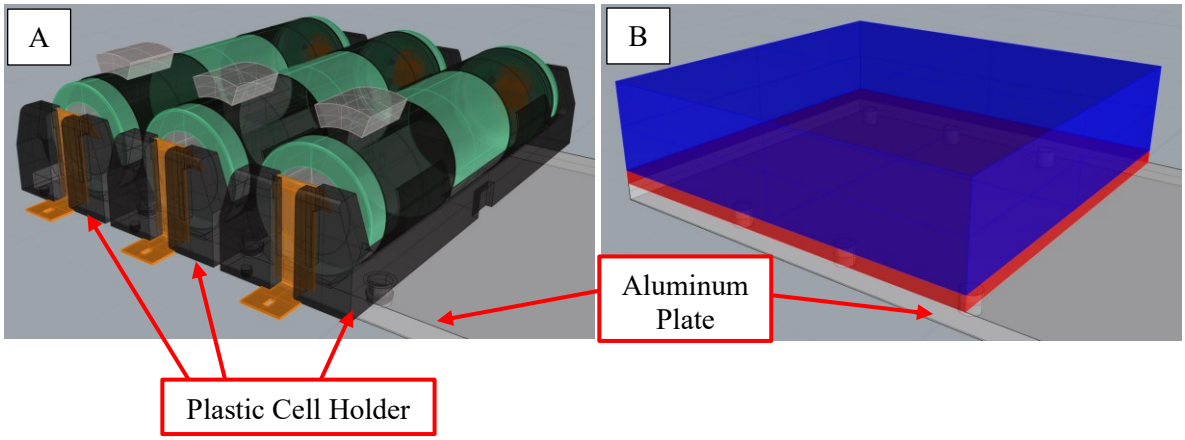

Figure 5.36 A: Original CAD drawing of 3P grouping. B: Simplified thermal model of 3P cell grouping with convection + radiation area (blue rectangle) and conduction thickness and area (red rectangle)

The conductive heat transfer model is represented by the red rectangle in Figure 5.36B. Heat will be conducted from each cell in the 3P group, through the plastic cell holders and into the aluminium plate. The convective and radiative heat transfer is represented by the blue square in Figure 5.36B. The convective and radiative heat transfer will occur on the 3P groupings exposed surfaces to ambient conditions. Physical parameters of the thermal model are summarized below:

- As each 18-65 cell has a length of 65 mm, the thermal model has a length of 65 mm.
- The width of the thermal model is 69 mm (18 mm x 3 cells + inter cell spacing).
- The thickness for both the red conductive and the blue convective/radiative portion of the thermal model are respectively 2.5 mm and 16 mm. A conduction model thickness of 2.5 mm was used for the thermal model as this is the average thickness of the bottom of each cell holder.
- Approximately 50% of the bottom surface of each cell holder does not contact the aluminium plate, thus a factor of 50% was multiplied by the total area of conductivity.
- Using the measurements stated in the above bullet points, A_{conv}, A_{cond} and L_{cond} are found to be 8770 mm^2, 2240 mm^2 and 2.5 mm respectively. Note that $A_{conv}=A_{rad}$.

- The cell holder is the main thermal conductor from each cell and is made of a low-density plastic. Thermal conductivity values of low-density plastics are found to be in the range of 0.1 – 0.3 [98], thus a conductivity of 0.2 W/mK was used.
- According to Hatchard et al. [99] emissivity constants for cells with their shrink wrap and black paint epoxy are 0.54 – 0.74 and 0.9 respectively. Considering 70% of the cell group is covered by black electrical tape and the black holders themselves, an emissivity constant of 0.8 is averaged for this model.

The total heat loss in the 3P grouping can be calculated as the sum of all three modes of heat transfer as shown in equation (10), where the temperature of the aluminum plate is simplified to be the same as the surroundings due the high thermal conductivity of aluminum (~200 W/mK).

$$q_{loss} = q_{conv} + q_{cond} + q_{rad} \\ = (T_s - T_{sur}) * \left(hA_{conv} + \frac{kA_{cond}}{L_{cond}}\right) + \varepsilon\sigma A_{rad}(T_s^4 - T_{sur}^4) \quad (10)$$

The heat generation changes throughout the LEO cycle and is dependant on SoC, cycling rate and cell temperature. As the LEO cycle operates over ΔSoC away from charge and discharge cut-off voltages, the IR will remain relatively constant over the LEO partial ΔSoC (Figure 5.16), hence negligible change in heat generation is expected as a result or varying SoC. During the LEO cycle the single cell charge and discharge power rates average from 6.73 to 11.2 W in the 3P grouping. This delta in cycling rate changes the ohmic losses (resistance for electron movement) by a squared effect as per equation (11).

$$q_{ohmic} = \left(\frac{P}{V_{cell}}\right)^2 R_{ohmic} \quad (11)$$

However, as the ohmic losses increase, the cell temperature increases and consequently a decrease in ionic losses (resistance for lithium-ion movement) occurs. The change in total heat generation from ionic resistivity is unknown and could potentially offset the contributions to decreased energy efficiency from ohmic resistance at the chosen LEO cycling rates.

In order to approximate how energy efficiency is impacted throughout the varying LEO cycle charge rates, a single cell from each type (NCA, NMC, LFP) was cycled using a low (CP charge of 6.73 W), median (standard sinusoidal charge of 6.73 – 11.2 W) and high charge rate (CP charge of 11.2 W) , all with a CP discharge of 11.2 W. Note that power rates are 1/3 that of the 3P group in the standard accelerated LEO cycle (Section 4.4 – Figure 4.19) due to the single cell configuration. Cells were

cycled in both *laboratory (*highest operating cell temperature) and *temperature* (lowest operating cell temperature) conditions. The effect of charge cycling rate on energy efficiency was linearly interpolated for the *vacuum* (median operating cell temperature).

As expected, the low, median, and high charge rates respectively achieved the high, median, and low cycle energy efficiencies. Table 5.8 summarizes the difference in energy efficiency between a CP charge of 6.73 and 11.2 W for each condition including the interpolated *vacuum* condition.

Table 5.8 Change in LEO cycle energy efficiency of each cell type (NCA, NMC, LFP) in each condition (laboratory, temperature, vacuum) at 6.73 and 11.2W CP single cell charge rates

Condition, Convection Type	Cell Type	$\eta_{6.73\,W}$	$\eta_{11.2\,W}$	$\Delta\eta$
Laboratory (20 °C, 101 kPa), Free Convection	NCA	92.43%	91.60%	0.83%
	NMC	90.94%	89.20%	1.74%
	LFP	93.06%	92.44%	0.62%
Temperature (10 °C, 101 kPa), Forced Convection	NCA	91.03%	89.53%	1.50%
	NMC	88.38%	86.06%	2.32%
	LFP	89.69%	88.19%	1.51%
Vacuum (10 °C, 0.2 kPa), Free Convection	NCA	91.73%	90.57%	1.16%
	NMC	89.66%	87.63%	2.03%
	LFP	91.37%	90.31%	1.06%

According to Table 5.8, the change in energy efficiency between CP charge at 6.73 and 11.2 W during the LEO cycle varies by less than 2.5% in each case with a maximum difference occurring in the *temperature* condition which has the smallest operating cell temperature delta from ambient temperature (Section 5.1.4). This finding highlights how the impact of power rate on energy efficiency is increased in conditions where the cell cannot compensate for increased ohmic losses by increasing the cell temperature (i.e. increasing ionic conductivity).

As a result of the findings from Table 5.8, the power loss at any point in time can be approximated using equation (12).

$$q_{gen} = q_{avg,loss}\left(\frac{P}{P_{avg}}\right)\eta_{factor} \tag{12}$$

Where the average power loss is calculated using the LEO cycle energy and time data as per equation (13).

$$q_{avg,loss} = \frac{E_{chg} - E_{dis}}{t_{chg} + t_{dis}} \tag{13}$$

The efficiency factor which adjusts the power losses to incorporate the change in energy efficiency presented in Table 5.8 is calculated using equation (14).

$$\eta_{factor} = \frac{100 - \eta}{100 - \eta_{LEO}} \tag{14}$$

Equation (14) determines the instantaneous efficiency $'\eta'$ by linearly interpolated from the standard LEO cycle efficiency $'\eta_{LEO}'$ (i.e. CP discharge, sinusoidal charge).

In addition to the calculations above, boundary conditions were applied to the thermal model convection coefficients based on literature research, see below:

- Using the free convection data by Wallenten [98], the *laboratory* condition convective heat transfer is approximated as 6 W/m^{2}K for the NCA and NMC cell groups and 4 W/m^{2}K for the LFP cell group based on the cell temperature delta from the ambient temperature. These heat transfer coefficients were made constant in the model.
- As per the findings of Saidi and Abardeh [96], the contributions from convection in the *vacuum* condition should be approximately 10% to that of the *laboratory* condition due to the reduction in air and temperature deltas. Consequently, the convective heat transfer coefficient in the *vacuum* condition was set to be 10% to that of the *laboratory* condition for each cell type.

After 3 LEO cycles, a consistent thermal profile is achieved, consequently the total heat loss from equation (10) and heat generation from equation (12) are equal. Applying the aforementioned physical model parameters, analytical calculations and boundary conditions, equation (10) and (12) were solved yielding the proportions of each of the three forms of heat transfer, see Table 5.9.

Table 5.9 Proportion of heat transfer (convection, conduction, radiation) for each cell type (NCA, NMC, LFP) in each condition (laboratory, temperature, vacuum) at MoL.

Condition, Convection Type	Cell Type	Convection	Conduction	Radiation
Laboratory (20 °C, 101 kPa), Free Convection	NCA	42%	49%	9%
	NMC	45%	47%	8%
	LFP	31%	59%	10%
Temperature (10 °C, 101 kPa), Forced Convection	NCA	73%	24%	4%
	NMC	74%	22%	3%
	LFP	71%	25%	4%
Vacuum (10 °C, 0.2 kPa), Free Convection	NCA	4%	83%	13%
	NMC	4%	82%	13%
	LFP	3%	84%	13%

Table 5.9 shows that due to the forced convection fan in the thermal chamber, the *temperature* condition heat transfer is dominated by convection. In the *laboratory* and *vacuum* condition, the majority of heat transfer is conductive. This finding highlights the importance conductive heat transfer in battery pack design as convection is reduced. Since LEO satellites can only expel heat from the outer chassis via radiation [99], conduction is the primary mover of heat for the enclosed battery pack and must be considered when designing the satellite.

As cells degrade, the values in Table 5.9 will change. A list of assumptions made to perform this analysis and simplify the thermal model are summarized in Table 5.10.

Table 5.10 List of assumptions for developing thermal model of 3P groupings in all conditions

List of Assumptions
• As only one surface temperature was recorded on the middle cell of each 3P grouping, this surface temperature was as an approximate for the surface temperature of the entire thermal model.
• An estimated average emissivity constant for the entire cell grouping is reasonable to represent the radiative heat transfer.
• Although each cell type has different colour shrink wrap, the results do not depend on cell shrink wrap colour and can be applied to all cell types. This is supported by the research findings from Section 5.4.
• 3P groupings operating near other 3P groupings provide negligible heating to one another in all three conditions. This is supported by the findings that radiation plays a minor role in total heat transfer as shown in Table 5.9.
• Thermal conductivity and emissivity values chosen in the analysis are correct.
• The aluminum plate temperature remains at ambient temperature due to its high thermal conductivity.
• The acrylic vacuum chamber does not significantly reflect heat to the 3P groupings and has a similar emissivity constant to that of the cell groups (~0.8) [100].
• The difference in IR on charge and discharge for the same power rate and cell condition is negligible.

5.4 Effect of Sleeves on Cell Temperature in Vacuum

Prior to being cleared for boarding the international space station, manufacturer shrink wrap sleeves must be removed from cells due to stringent outgassing regulations outlined in Nanoracks guidelines [72]. Cells are typically re-sleeved in an approved material which does not outgas in LEO vacuum (~10^{-9} kPa). However, for safety and cell identity in the laboratory, the cell sleeve was left on.

The operating cell temperature is a function of its energy efficiency, ΔSoC, current direction (charge or discharge), cycling rates, ambient temperature, battery design and heat transfer characteristics (convection, conduction, radiation). In the case of the *vacuum* condition, convection is reduced due

to the near absence of air, however material properties that establish conductive (i.e. battery holder size and thermal conductivity) and radiative (i.e. emissivity) heat transfer are unchanged. Consequently, the heat transfer contributions from radiation are the greatest in the *vacuum* condition (Section 5.3). The increase in radiative heat transfer significance can cause surface emissivity to play a significant role in cell operating temperature. Hatchard et. al [101] proved that surface emissivity should be considered for improving the thermal abuse tolerance of lithium-ion batteries to help mitigate thermal runaway. Hatchard et. al [101] show the difference in thermal response of an 18-65 lithium-ion cell being heated in an oven at 140 °C with the sleeve on warmed faster and then rejected heat at a greater rate once 140 °C was achieved due to the higher emissivity. In one case, the higher emissivity on the sleeved cell prevented thermal runaway. These findings prompted the question, "How does the sleeve affect cell thermal characteristics in the *vacuum* condition?". To answer this, one LFP and NCA cell were tested in the *vacuum* condition with the manufacturer sleeve on and off. It was hypothesized that the sleeve would have negligible affects as only approximately 50% of the cell surface is exposed for radiative heat transfer due to the cell holder, of which only 33% of this surface is not covered in black electrical tape, thus limiting available area for change in surface emissivity. The change in emissivity by removing the sleeve is dictated by the visible green manufacturer sleeve show in Figure 5.37.

Figure 5.37 3P NCA cell group with manufacturer shrink wrap sleeve (green) on

A detached thermocouple constitutes a major safety concern in LIB experimental testing as the cycler will not be able to trigger shutdown due to high temperature readings which could lead to thermal runaway. The black electrical tape is a safety precaution used to ensure the thermocouple does not strip off the cell during testing. This experiment could have been improved by eliminating the need for electrical tape by micro welding the thermocouple to the cell, consequently maximizing the impact

to surface emissivity by removing the sleeve. The thermal response for both LFP and NCA cell for the reference cycle (Section 4.5.1) is depicted in Figure 5.38.

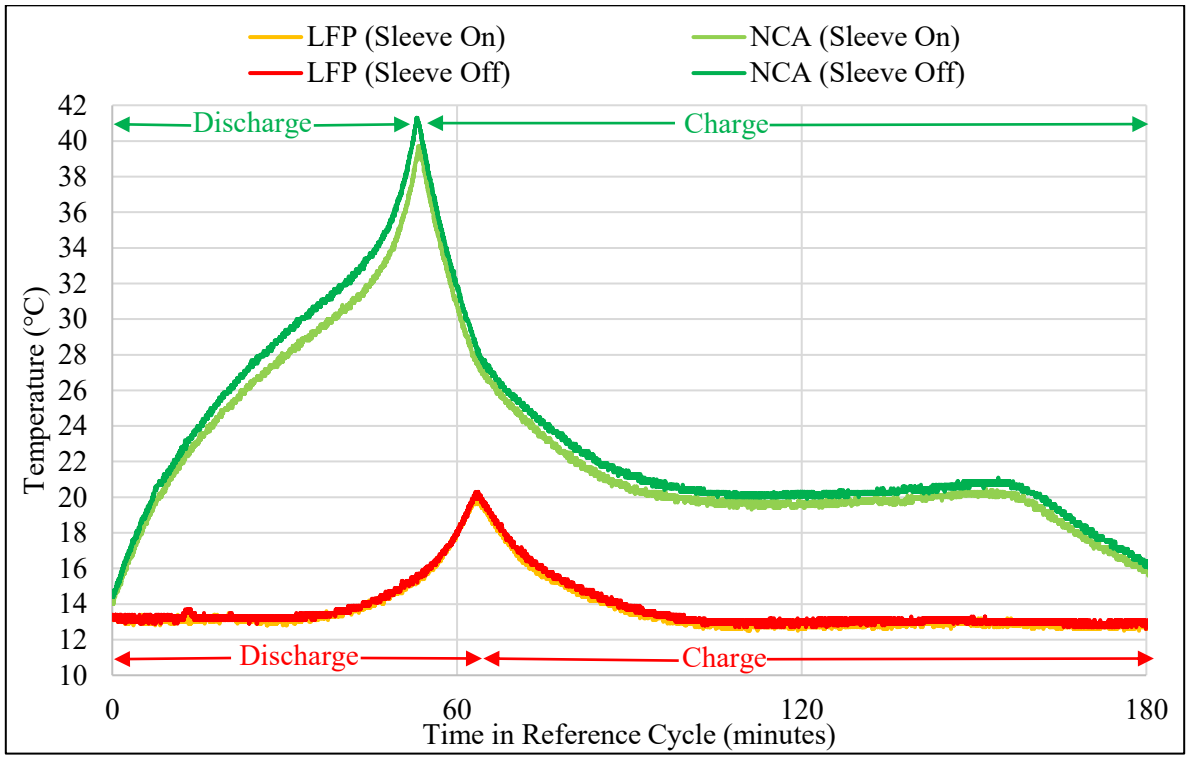

Figure 5.38 NCA and LFP cell temperature in vacuum condition (0.2 kPa, 10 °C) during capacity and energy efficiency reference cycling

As shown in Figure 5.38, the LFP cells experience near identical temperature profiles with the sleeve on and off. However, there is some visible (~ 1 °C) temperature difference for the NCA cell during discharge. The temperature difference exhibits traits of a decreased surface emissivity on the sleeveless cell as it is not able to dissipate heat as quickly. This result agrees with Hatchard et al. [101] that removing the sleeve does reduce radiative emissivity.

As lithium-ion cells are capable of operating over temperature ranges from -20 to 60 °C, an operating difference of less than ±1 °C suggests that there is likely no change in performance (capacity and energy efficiency) with the sleeve on and off. To quantify this, the average percent difference of temperature, capacity, and energy efficiency is depicted in Figure 5.39.

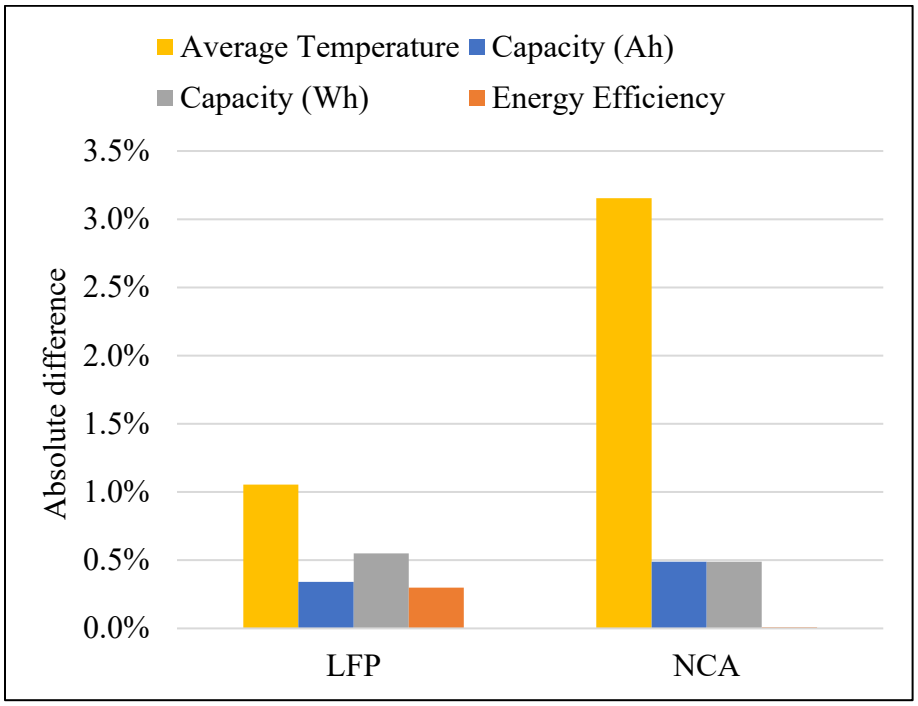

Figure 5.39 Absolute difference of LFP and NCA cells with sleeve on/off in vacuum (0.2 kPa, 10 °C) during discharge capacity and energy efficiency reference cycling

Note that in Figure 5.39 there is no difference in energy efficiency between the NCA with and without the sleeve. While temperature differences are 1 – 3%, capacity differences are less than 0.5% for both LFP and NCA cell types which suggest that there is not a significant difference in performance achieved by removing the cell sleeves.

In addition to performing the experiment discussed above, an analytical analysis was completed. The analysis models conduction heat transfer through the sleeve wall to determine the change in surface temperature across the sleeve as per equation (8). Similar to the heat transfer analysis performed in Section 5.3, the energy efficiency throughout the cycle is unknown, however it is well known that the energy efficiency of a LIB decreases rapidly near the end of discharge due to the increase in IR (Figure 5.16) and temperature (Figure 5.8). That being said, a minimum energy efficiency 'η_{min}' range from 0% to 100% was modelled, see results in Table 5.11.

Table 5.11 Inner and outer sleeve temperature analytical calculation summary for both LFP and NCA cell types in vacuum (0.2 kPa, 10 °C) during capacity and energy efficiency reference cycling

Sleeve Parameter	LFP	NCA
Thickness (Measured with micrometer, see Table 5.3)	0.095 mm	0.065 mm
Conductive Area (56.5 mm circumference x 65 mm length)	3676 mm^2	3676 mm^2
Thermal Conductivity of Plastic Sleeve (Section 5.3)	0.2 W/m^2K	0.2 W/m^2K
Peak ΔT between T_i and T_o ($\eta_{min} = 0\%$)	0.50	1.17
Peak ΔT between T_i and T_o ($\eta_{min} = 20\%$)	0.40	0.93
Peak ΔT between T_i and T_o ($\eta_{min} = 40\%$)	0.30	0.70
Peak ΔT between T_i and T_o ($\eta_{min} = 60\%$)	0.20	0.47
Peak ΔT between T_i and T_o ($\eta_{min} = 80\%$)	0.10	0.23
Peak ΔT between T_i and T_o ($\eta_{min} = 100\%$)	0.00	0.00

The findings from Table 5.11 suggest that even if the cell were 0% energy efficient during the end of discharge, the difference across the cell sleeve would be 0.50 and 1.17 °C for the LFP and NCA cell respectively. As the measured difference in cell temperature between the sleeved and non-sleeved cell was found to be 0.2 and 0.7 °C for the LFP and NCA cell respectively, Table 5.11 suggests that the minimum energy efficiency occurring at the end of discharge is in the range of 40 to 60%.

5.5 Effect of Vacuum Rating on Cell Temperature

The thermal profile of a lithium-ion cell throughout cycling greatly affects performance characteristics (Section 3.4). Consequently, it is important that when testing a lithium-ion cell for an application, the thermal characteristics of the cell are similar to what would occur in the application. In LEO, the average ambient temperature and pressure is approximately 10 °C and 1.24 x 10^{-9} kPa at a 400 km altitude (Section 2.3). As the *vacuum* condition (0.2 kPa, 10 °C) is designed to emulate LEO, it is important to verify if the pressure difference between *vacuum* and true LEO pressure will not lead to significant differences in cell performance due to a decrease in convective heat transfer coefficient. Saidi and Abardeh [96] show that the convective heat transfer coefficient changes non-linearly with temperature and pressure, see Figure 5.40.

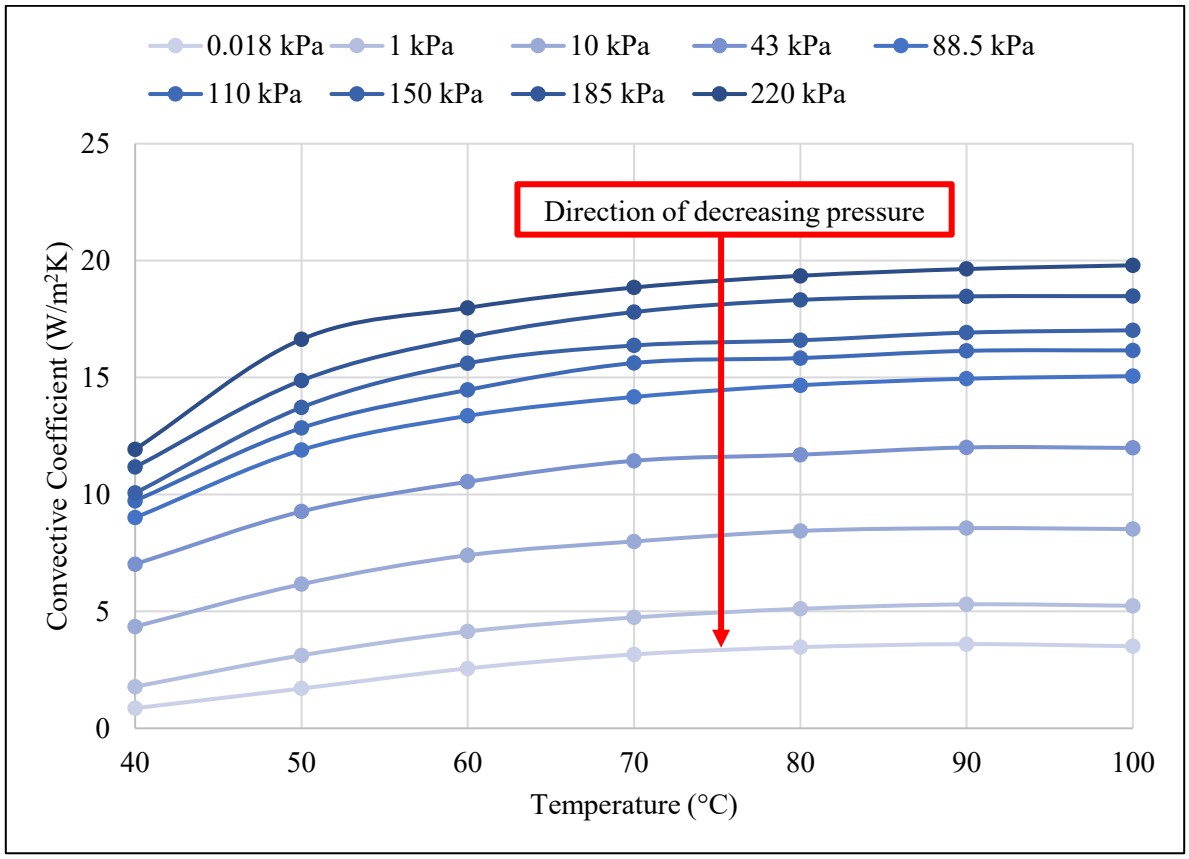

Figure 5.40 Convective heat transfer coefficient versus ambient temperature based upon [96]

Due to the near zero LEO pressure, the convective heat transfer coefficient would be zero at all temperatures due to the lack of air. As the vacuum pump and chamber apparatus can only attain a 0.2 kPa vacuum, it poses the question "Would there be significant differences in cell operating temperature if cells were cycled in the true LEO pressure compared to 0.2 kPa?". Since a vacuum pressure of 1.24×10^{-9} kPa cannot be achieved with the available vacuum chamber and pump, an alternative approach to answer this question was determined using Figure 5.41.

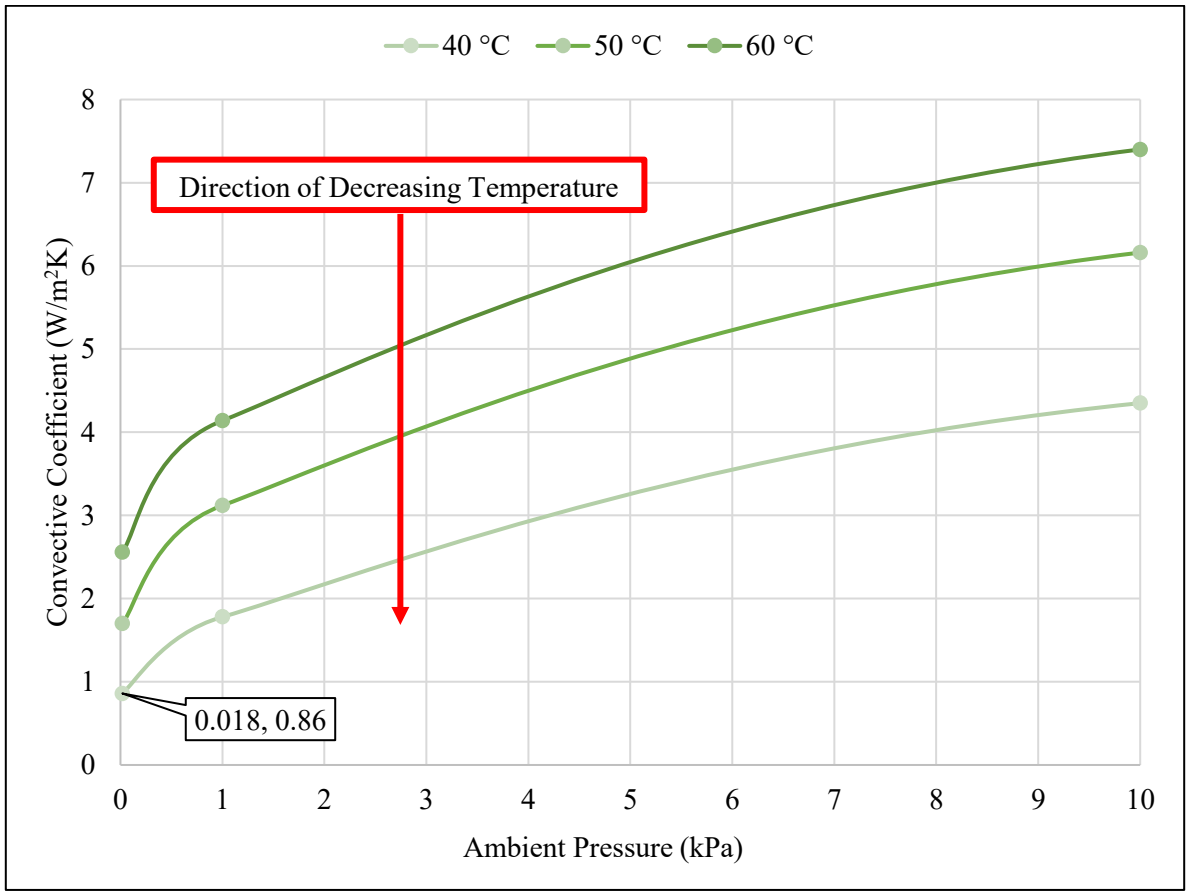

Figure 5.41 Convective heat transfer coefficient versus ambient pressure for 40, 50 and 60 °C ambient temperature based upon [96]

From Figure 5.41 the convective heat transfer coefficient at 0.2 kPa can be estimated for the 40, 50 and 60 °C ambient conditions. Additionally, the ambient pressure at which the convective heat transfer coefficient would be double that of the 0.2 kPa pressure can be estimated for each temperature condition, see Table 5.12.

Table 5.12 Convective heat transfer coefficient at 0.2 kPa and pressure at which the heat transfer coefficient doubles for the 40, 50 and 60 °C temperature conditions

Temperature (°C)	0.2 kPa Convective Heat Transfer Coefficient (W/m^2K)	Pressure at which the convective heat transfer coefficient is twice that of the 0.2 kPa condition
40	1.15	2.00
50	2.15	3.25
60	2.95	4.75

From Table 5.12 it is apparent that as temperature decreases, the pressure at which the convective heat transfer coefficient is doubled also decreases. This suggests that at 10 °C, the pressure in which the heat transfer coefficient is double that of the 0.2 kPa condition would be less than 2 kPa. However, as 40 °C is the closest temperature available from the dataset, this will serve as the conservative approximate to what would occur at 10 °C.

The convective heat transfer coefficient in a true LEO is 0 W/m^2K due to the lack of convection [99]. Therefore, the increase in convective heat transfer from ~0 kPa to 0.2 kPa would be identical to the increase in pressure from 0.2 to 2 kPa (i.e. $+\Delta 1.15$ W/m^2K) as per the findings in Table 5.12. As the difference in convective heat transfer coefficients would be the same, the latter will be used as a proxy for determining the affect on cell temperature between the true LEO pressure and 0.2 kPa *vacuum* condition.

A 3P group of NMC cells (Cell A, B, C) were cycled first at 0.2 kPa, then 2 kPa, and then a second time at 0.2 kPa in 10 °C using the accelerated LEO cycle (Section 4.3). Vacuum pressure was controlled using a mechanical cash valve. The thermal response for each cell in the 3P group for the 0.2 kPa and 2 kPa pressure conditions are plotted in Figure 5.42.

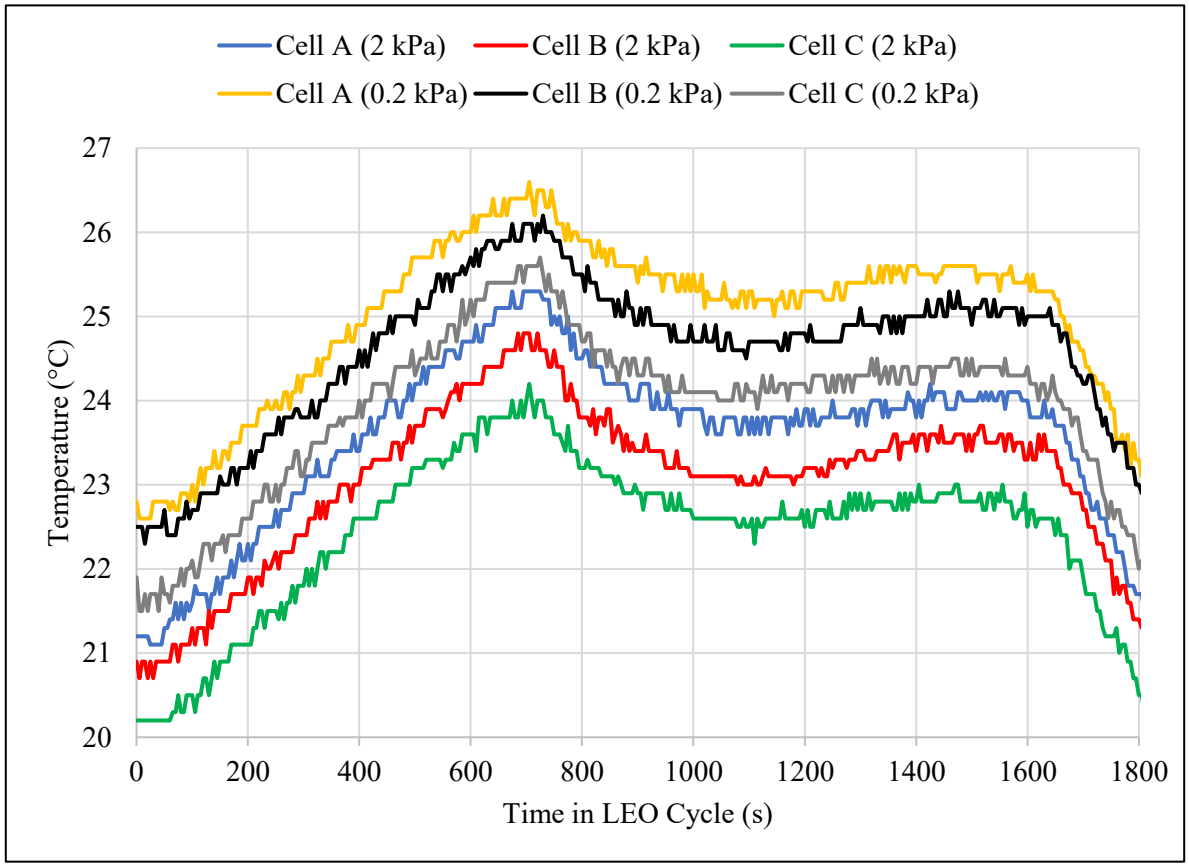

Figure 5.42 Thermal response of NMC cell A, B and C at 10 °C under the accelerated LEO cycle at 0.2 and 2 kPa vacuum pressures for the 10th LEO cycle completed in each set

Figure 5.42 reveals that in each condition, there is a 1 °C delta across the 3P group and a decrease in temperature when the pressure is increased from 0.2 kPa to 2 kPa as a result of the increased convective heat transfer. For better resolution, the difference in cell temperature between 0.2 and 2 kPa pressure conditions are presented Figure 5.43.

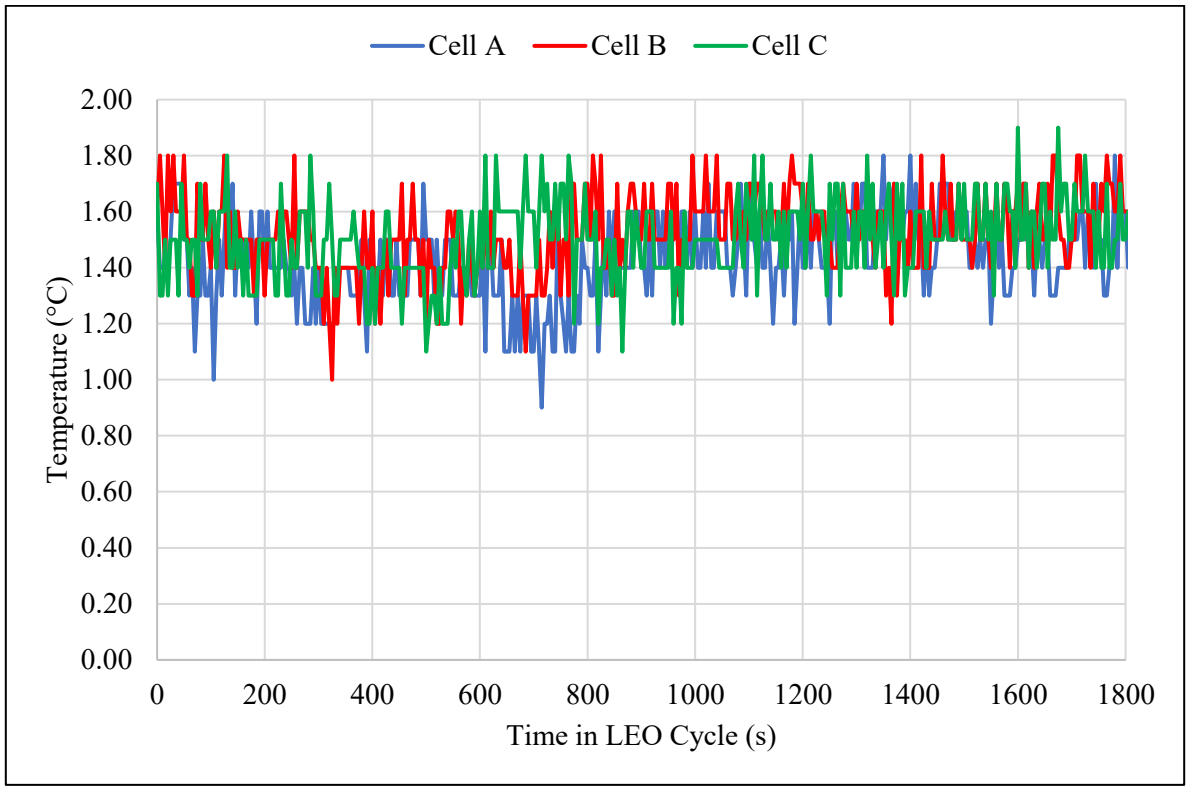

Figure 5.43 Thermal profile difference between NMC cell A, B and C at 10 °C under the accelerated LEO cycle at 0.2 and 2 kPa vacuum pressures for the 10th LEO cycle completed in each set

Figure 5.43 shows that the average temperature difference between the two pressure conditions is ~1.5 °C, however, this is not entirely due to a change in pressure as a temperature increase of ~0.5 °C was observed between the two identical 0.2 kPa experiments. This is not surprising as an increase in temperature is expected with each cycle, due to IR increases as a result of SEI formation and lithium plating, which the NMC cell type is prone to in the *vacuum* condition. This finding indicates that the difference in temperature between cells operating in the second 0.2 kPa and 2 kPa experiment shown in Figure 5.43 is partially attributed to IR growth. Thus, the true difference in temperature between cells in 0.2 and 2 kPa is likely closer to ~1 °C. As the LIB in this experiment are design to operate between -20 and +60 °C (see Table 4.1), a temperature delta of ~1°C is not expected to significantly impact performance and is supported by the findings of Section 5.4.

To summarize, increasing the pressure from 0.2 to 2 kPa caused a decrease in operating temperature of ~1 °C by doubling the heat transfer coefficient (+Δ1.15 W/m^{2}K). Decreasing the pressure from 0.2

kPa to the true LEO pressure would cause the same delta in heat transfer coefficient, consequently an increase in operating temperature of ~1 °C is expected, however this is not expected to effect performance or degradation. This finding is supported by the heat transfer analysis completed in Section 5.3 which showed that in the *vacuum* condition, conduction and radiation contribute ~95% of the total heat transfer from the 3P group and are unaffected by ambient pressure.

Chapter 6 : Conclusions and Recommendations

Three high quality, commercially available 18-65 lithium-ion cells (NCA, NMC, LFP) with different PAM, NAM and electrode designs were tested in an accelerated LEO cycle for ~1 year of equivalent LEO cycles in *laboratory* (101 kPa, 20 °C), *temperature* (101 kPa, 10 °C), and *vacuum* (0.2 kPa, 10 °C) test conditions. Conclusions and recommendations pertaining to this degradation experiment are numerically presented below. Note that I through VIII are related to research objectives presented in Section 1.1. Recommendations IX through XI are additional suggestions for future LEO battery testing.

I. The results show that while the LFP ΔSoE and ΔSoC operating window is much greater, its degradation rate, especially at lower temperatures, is much less than the other chemistries and it outperforms them in both application cycle life and energy efficiency. These results clearly identify there is potential to utilize the high power LFP chemistry in lengthier satellite applications to both lower battery pack volume and mass, while reducing total required photovoltaic sizing. It is recommended that the LFP chemistry be considered in future satellite missions and experimental research.

II. The three different conditions (*laboratory*, *temperature*, *vacuum*) result in a different thermal response for each cell type (NCA, NMC, LFP). By observing discharge capacity trends, it is evident that both NCA and NMC cell types perform differently in each condition. The LFP discharge capacity is similar in all three conditions. On further inspection, via end of discharge voltage analysis, differences between LFP cell groups were evident, showing that the warmer cell groups (*vacuum* and *laboratory*) will likely outlast the colder cell groups regardless of capacity degradation rates. It is recommended that the three cell types be cycled in the *vacuum* condition to best analyze how they would perform in the true LEO environment.

III. Failure mode analysis reveals that NCA cells failed from disconnecting the CID due to excessive gas generation in the *temperature* condition, whereas in the *vacuum* condition they failed from IR growth. These results indicate that the NCA cell type is more prone to degradation that causes gassing such as electrolyte decomposition and SEI growth. Hence focus towards improving the NCA cell type should be in the electrolyte and/or the graphitic NAM cycle life stability at lower temperatures. NMC groups all failed from IR growth with no CID components being disconnected, consequently it is likely that lithium plating played a larger role in degradation

compared to the NCA cell type. It is recommended that focus of the NMC cell type should be on improving the power capability of the NAM to prevent lithium plating.

IV. dV/dQ cycling revealed that the *temperature* NCA group experienced LAM on the negative electrode while no LAM on the positive electrode was present. These findings once again exemplify the graphitic NAM is the main cause of capacity loss in the NCA cell type. In the more degraded *vacuum* NCA group this distinction was not possible. Likewise, due to the high degradation in the NMC groups at EoL, the difference between LAM and LLI was ambiguous. These findings highlight the importance of performing dV/dQ slow cycling (i.e. C/24 or slower) at a higher resolution than BoL and EoL if the primary focus is to differentiate between LAM and LLI contributions.

V. An alternative method for viewing cell performance from BoL to EoL using the change in ΔSoE throughout LEO cycling is presented, highlighting the distinction between total discharge capacity energy, unavailable energy, and additional available energy. Section 5.1.7 reveals how a disconnected CID induces failure although additional available energy is present whereas IR growth depletes the available energy entirely. This methodology in analyzing battery performance is ideal when comparing cell performance from different applications or power ratings, as it illustrates how power capability improves available energy and exemplifies that LEO CubeSat designs should consider cells with low initial IR and degradation rates (i.e. high cycle life) such as the LFP cell type. It is recommended that this technique be used in future battery degradation experimentation as it provides the best visual of cell operational status and its ability to perform in the application.

VI. A heat transfer model was developed with contributions from convection, conduction and radiation analytically solved for each condition and cell type. Findings highlight the importance conductive heat transfer has in battery pack design in conditions with poor convection such as the *vacuum* condition. Although radiation is the only mode of external heat transfer in a LEO Satellite, internally, conduction is the primary mover of heat for the enclosed battery pack. Consequently, CubeSat designs should consider conductive heat transfer in order to optimize cell performance in the LEO environment.

VII. Experimental validation was completed to determine if the cell sleeve played a significant role in performance due to the change in heat transfer characteristics. Results indicate that cell sleeves insignificantly effect cell operating temperature and cell performance in the *vacuum* condition. This finding gives confidence that battery performance testing may retain cell sleeves for this research. Additionally, these findings suggest that replacing the cell sleeve with a non-outgassing

sleeve of similar size (i.e. thickness, length) would not alter cell performance in a LEO environment, however additional testing of industry leading non-outgassing sleeves may prove useful in validating this hypothesis.

VIII. Experimental comparison between cells in the *vacuum* condition (0.2 kPa, 10 °C) and higher-pressure condition (2 kPa, 10 °C) was completed, indicating negligible difference in performance between the two conditions. This finding suggests that changes in performance as a result in reduced heat transfer convection coefficients between the *vacuum* condition and true LEO condition are also negligible. It is recommended that this be confirmed with a vacuum system that can achieve true LEO pressure.

IX. The lowest absolute pressure obtainable using the vacuum equipment was ~0.2 kPa due to an imperfect seal between the acrylic block and the stainless-steel plate. The Leybold D4B vacuum pump can achieve a 0.006 kPa absolute pressure when leaks are mitigated. It is recommended that subsequent vacuum chambers be designed to reduce leaks so that lower operating pressure, that is closer to true LEO ambient pressure, can be achieved ($\sim 10^{-9}$ kPa). A potential vacuum chamber design to achieve a better seal would use stainless-steel walls welded to the 1/2" plate, with a flat clear glass cover and rubber seal.

X. Degradation was found to be a predominantly a function of NAM power capability, electrolyte gas evolution, and electrode design. It is recommended that future LEO cell testing use custom 18-65 cells with similar material particle sizes, electrolytes and electrode designs (power or energy) for each PAM variant to achieve new insight into longer lasting and more energy efficient LIB designs for LEO cycling.

XI. Testing cells without manufacturer sleeves should be considered for future LEO cycle testing as this would enable the thermocouple sensor to be micro welded directly to the cell cannister. This removes the need for electrical tape, while more securely attaching the thermocouple. In order to safely remove cell sleeves, it is recommended that the paper disk on the positive terminal be secured using adhesive and a custom-built battery holder designed with the intent to reduce the risk of an external electrical short. Additionally, both current and voltage taps should be spot welded to the appropriate cell terminals to reduce contact resistance and emulate final pack connections.

References

[1] S. Gao *et al.*, “Antennas for modern small satellites,” *IEEE Antennas Propag. Mag.*, vol. 51, no. 4, pp. 40–56, 2009.

[2] Nanosats, “NanoSatellite Database.” [Online]. Available: https://www.nanosats.eu/. [Accessed: 03-Mar-2019].

[3] D. Deng, “Review: Li-ion batteries: Basics, progress, and challenges,” *Energy Sci. Eng.*, vol. 3, no. 5, pp. 385–418, 2015.

[4] G. . Ehrlich, J.R. Dahn, “Linden’s Handbook of Batteries. Chapter 17: Lithium-Ion Batteries,” Mcgraw-Hill Education, pp. 1–131.

[5] D. Deng, M. G. Kim, J. Y. Lee, and J. Cho, “Green energy storage materials: Nanostructured TiO2 and Sn-based anodes for lithium-ion batteries,” *Energy Environ. Sci.*, vol. 2, no. 8, pp. 818–837, 2009.

[6] C. Pillot, “The Rechargeable Battery Market and Main Trends 2016-2025.” http://www.avicenne.com/pdf/The%20Rechargeable%20Battery%20Market%20and%20Main%20Trends%202016-2025_C%20Pillot_M%20Sanders_September%202017.pdf; Unpublished results, 2017.

[7] C. Pillot, “Avicenne Energy - Batteries Event 2020.” http://www.avicenne.com/batteries_event.php; Unpublished results, Lyon, France, 2020.

[8] The International Council on Clean Transportation, “Global and U.S. electric vehicle trends,” *The International Council on Clean Transportation*. https://theicct.org/sites/default/files/Drew%20Kodjak_Canada%20global%20EV_12June2019_0.pdf; Unpublished results, pp. 1–22, 2019.

[9] K. Chen, F. Zhao, H. Hao, and Z. Liu, “ScienceDirect ScienceDirect ScienceDirect Selection of Lithium-ion Battery Technologies for Electric Vehicles Cooling Vehicles Selection of Battery Technologies for and Electric under China ’ s New Energy Vehicle Credit Regulation under China ’ s New Ener,” *Energy Procedia*, vol. 158, pp. 3038–3044, 2019.

[10] X. Zeng *et al.*, “Commercialization of Lithium Battery Technologies for Electric Vehicles,” *Adv. Energy Mater.*, vol. 9, no. 27, pp. 1–25, 2019.

[11] J. J. Kim and S. H. Ahn, “LG Chem ICR18650B4 Data Sheet,” vol. 21, no. 1. https://www.batteryspace.com/prod-specs/5457_B4.pdf; Unpublished Results, 2011.

[12] Panasonic, “NCR18650B Data Sheet.” https://www.batteryspace.com/prod-specs/NCR18650B.pdf; Unpublished Results.

[13] LithiumWerks, “APR18650M1B Data Sheet.” https://www.batteryspace.com/prod-specs/6612-APR18650M1B.pdf; Unpublished results, pp. 1–2.

[14] N. Nitta.pdf, “Li-ion battery materials: present and future,” *Materials (Basel).*, vol. 18, pp. 252–264, 2015.

[15] S. Yang, X. Zhou, J. Zhang, and Z. Liu, “Morphology-controlled solvothermal synthesis of LiFePO4 as a cathode material for lithium-ion batteries,” *J. Mater. Chem.*, vol. 20, no. 37, pp. 8086–8091, 2010.

[16] A. Ulvestad, “A Brief Review of Current Lithium Ion Battery Technology and Potential Solid State Battery Technologies.” https://arxiv.org/abs/1803.04317; Unpublished results, 2018.

[17] Y. G. J.R. Dahn, W. Xing, “The “Falling Cards Model" for the Structure of Microporous Carbons,” *Pergamon*, vol. 35, no. 6, pp. 825–830, 1997.

[18] L. O. Valøen and J. N. Reimers, “Transport Properties of LiPF_6 Based Li-Ion Battery Electrolytes,” *J. Electrochem. Soc.*, vol. 152, no. 5, p. A882, 2005.

[19] D. Moosbauer, S. Zugmann, M. Amereller, and H. J. Gores, “Effect of ionic liquids as additives on lithium electrolytes: Conductivity, electrochemical stability, and aluminum corrosion,” *J. Chem. Eng. Data*, vol. 55, no. 5, pp. 1794–1798, 2010.

[20] P. Mozur, “Galaxy Note 7 Fires Caused by Battery and Design Flaws, Samsung Says,” *The New York Times*, 2017. [Online]. Available: https://www.nytimes.com/2017/01/22/business/samsung-galaxy-note-7-battery-fires-report.html; Unpublished results. [Accessed: 10-Apr-2020].

[21] T. R. Ashwin, A. Barai, K. Uddin, L. Somerville, A. McGordon, and J. Marco, “Prediction of battery storage ageing and solid electrolyte interphase property estimation using an electrochemical model,” *Journal of Power Sources*, vol. 385. pp. 141–147, 2018.

[22] GT-Suite, “GT-AutoLion.” [Online]. Available: https://www.gtisoft.com/gt-autolion/. [Accessed: 14-May-2019].

[23] K. Smith, Y. Shi, and S. Santhanagopalan, “Degradation mechanisms and lifetime prediction for lithium-ion batteries - A control perspective,” *Proc. Am. Control Conf.*, vol. 2015-July, pp. 728–730, 2015.

[24] M. Dubarry, A. Devie, and B. Liaw, “The value of battery diagnostics and prognostics,” *J. Energy Power Sources*, vol. 1, no. 5, pp. 242–249, 2014.

[25] M. C. Smart, “Irreversible Capacities of Graphite in Low-Temperature Electrolytes for Lithium-Ion Batteries,” *J. Electrochem. Soc.*, vol. 146, no. 11, p. 3963, 1999.

[26] M. Dubarry, C. Truchot, and B. Y. Liaw, “Synthesize battery degradation modes via a diagnostic and prognostic model,” *J. Power Sources*, vol. 219, pp. 204–216, 2012.

[27] X. G. Yang, Y. Leng, G. Zhang, S. Ge, and C. Y. Wang, “Modeling of lithium plating induced aging of lithium-ion batteries: Transition from linear to nonlinear aging,” *J. Power Sources*, vol. 360, pp. 28–40, 2017.

[28] J. Groot, “State-of-health estimation of Li-ion batteries: cycle life test methods,” *PhD, CHALMERS Univ. Technol.*, p. 138, 2012.

[29] M. Dubarry *et al.*, “Identifying battery aging mechanisms in large format Li ion cells,” *J. Power Sources*, vol. 196, no. 7, pp. 3420–3425, 2011.

[30] B. Michalak, H. Sommer, D. Mannes, A. Kaestner, T. Brezesinski, and J. Janek, “Gas Evolution in Operating Lithium-Ion Batteries Studied in Situ by Neutron Imaging,” *Sci. Rep.*, vol. 5, pp. 1–9, 2015.

[31] N. Galushkin, N. N. Yazvinskaya, and D. N. Galushkin, “Mechanism of gases generation during lithium-ion batteries cycling,” *J. Electrochem. Soc.*, vol. 166, no. 6, pp. A897–A908, 2019.

[32] M. Metzger, B. Strehle, S. Solchenbach, and H. A. Gasteiger, “Origin of H2 evolution in LIBs: H2O Reduction vs. Electrolyte oxidation,” *J. Electrochem. Soc.*, vol. 163, no. 5, pp. A798–A809, 2016.

[33] B. Bro, “Battery Safety 101: Anatomy - PTC vs PCB vs CID.” [Online]. Available: https://batterybro.com/blogs/18650-wholesale-battery-reviews/18306003-battery-safety-101-anatomy-ptc-vs-pcb-vs-cid%0A. [Accessed: 04-Apr-2019].

[34] Isidor Buchmann, “Battery Univerisity,” 2019. [Online]. Available: https://batteryuniversity.com/index.php/learn/; Unpublished results. [Accessed: 11-Nov-2018].

[35] C. Mikolajczak, P. Michael Kahn, K. White, and R. Thomas Long, “Lithium-Ion Batteries Hazard and Use Assessment Final Report,” no. July. https://www.prba.org/wp-content/uploads/Exponent_Report_for_NFPA_-_20111.pdf; Unpublished results, 2011.

[36] NASA, “Limitations of Internal Protective Devices in High-Voltage/High- Capacity Batteries Using Lithium-Ion Cylindrical Commercial Cells,” *NASA Eng. Saf. Cent. Tech. Bull. Limitations*, no. No. 09-02, p. 1, 1998.

[37] B. McKissock, P. Loyselle, and E. Vogel, “Guidelines on Lithium-ion battery use in space applications,” *NASA Eng. Saf. Cent. Tech. Rep.*, no. May, p. 54, 2009.

[38] J. Bouwmeester and J. Guo, “Survey of worldwide pico- and nanosatellite missions, distributions and subsystem technology,” *Acta Astronaut.*, vol. 67, no. 7–8, pp. 854–862, 2010.

[39] Yannick Borthomieu, *Satellite Lithium-Ion Batteries - Chapter 14: Advances and Applications*. France: Elsevier, http://dx.doi.org/10.1016/B978-0-444-59513-3.00014-5 (book), 2014.

[40] P. Bugryniec, “CubeSat : The Need for More Power to Realise Telecommunications Overview of CubeSats Aims & Objectives,” no. June. https://static1.squarespace.com/static/53ce14b9e4b03fc272f43709/t/586e5e95e4fcb57853a2947b/1483628182901/Bugryniec+mini+project+report.pdf; Unpublished results, pp. 1–10, 2016.

[41] K. Woellert, P. Ehrenfreund, A. J. Ricco, and H. Hertzfeld, “Cubesats: Cost-effective science and technology platforms for emerging and developing nations,” *Adv. Sp. Res.*, vol. 47, no. 4, pp. 663–684, 2011.

[42] NASA, *US Standard Atmosphere, 1976*. United States, NASA Technical Reports Server, Book (https://ntrs.nasa.gov/archive/nasa/casi.ntrs.nasa.gov/19770009539.pdf), 1976.

[43] O. Popescu, "Power Budgets for CubeSat Radios to Support Ground Communications and Inter-Satellite Links," *IEEE Access*, vol. 5, pp. 12618–12625, 2017.

[44] Z. Cameron, C. S. Kulkarni, A. G. Luna, K. Goebel, and S. Poll, "A battery certification testbed for small satellite missions," *AUTOTESTCON (Proceedings)*, vol. 2015-Decem, pp. 162–168, 2015.

[45] R. A. Minzner, "The 1976 Standard Atmosphere and its Relationship to Earlier Standards," *Rev. Geophys. Sp. Phys.*, vol. 15, no. 3, pp. 375–386, 1977.

[46] J. R. Dennison, K. Hartley, L. Phillipps, J. Dekany, R. H. Johnson, and J. S. Dyer, "SSC14-P1-6 Small Satellite Space Environments Effects Test Facility," *Proc. AIAA/USU Conf. Small Satell.*, no. 435, pp. 1–10, 2014.

[47] N. Navarathinam, R. Lee, and H. Chesser, "Characterization of Lithium-Polymer batteries for CubeSat applications," *Acta Astronaut.*, vol. 68, no. 11–12, pp. 1752–1760, 2011.

[48] R. Thirsk, A. Kuipers, C. Mukai, and D. Williams, "The space-flight environment: The international space station and beyond," *Cmaj*, vol. 180, no. 12, pp. 1216–1220, 2009.

[49] M. M. Finckenor and K. K. de Groh, "Space Environmental Effects." https://www.nasa.gov/sites/default/files/files/NP-2015-03-015-JSC_Space_Environment-ISS-Mini-Book-2015-508.pdf, pp. 521–527, 2009.

[50] G. A. Harvey and W. H. Kinard, "NASA Langley Research Center - MISSE 1 & 2 Tray Temperature Measurements (Post-Retrieval Conference)." MISSE Post-Retrieval Conference, NASA, 2006.

[51] C. S. Clark and E. Simon, "Evaluation of Lithium Polymer Technology for Small Satellite Applications," *21st Annual AIAA/USU Conference on Small Satellites*. https://digitalcommons.usu.edu/smallsat/2007/all2007/66/, Unpublished results, pp. 1–11, 2007.

[52] J. Jeevarajan, “NASA (JSC) - Tolerance of Li-ion Pouch Cells to Varied Space Environment Pressures Lithium Power 2012,” *Nasa-jsc*. https://ntrs.nasa.gov/archive/nasa/casi.ntrs.nasa.gov/20130000451.pdf, Unpublished results, 2012.

[53] J. A. Jeevarajan and T. Inoue, “NASA (JSC) - A Novel Lithium-ion Laminated Pouch Cell Tested For Performance And Safety,” no. 281. https://ntrs.nasa.gov/search.jsp?R=20060020764, Unpublished results, pp. 2–5, 2000.

[54] X. Wang, Y. Sone, and S. Kuwajima, “Effect of operation conditions on simulated low-earth orbit cycle-life testing of commercial lithium-ion polymer cells,” *J. Power Sources*, vol. 142, no. 1–2, pp. 313–322, 2005.

[55] J. A. Jeevarajan and B. E. Duffield, “NASA (JSC) - Performance and Safety of Lithium-Ion Polymer Pouch Cells,” *J. Sp. Saf. Eng.*, vol. 1, no. 1, pp. 10–16, 2014.

[56] J. Jeevarajan, “NASA (JSC) - Safety and Long-Term Performance of Lithium- ion Pouch Cells.” https://ntrs.nasa.gov/archive/nasa/casi.ntrs.nasa.gov/20120016551.pdf, Unpublished results, 2017.

[57] Joshua Su, “Assessment of Performance and Safety on Lithium Ion Pouch Battery Under Various Test Conditions | Battery Power Magazine,” vol. 1. https://www.batterypoweronline.com/articles/assessment-of-performance-and-safety-on-lithium-ion-pouch-battery-under-various-test-conditions/; Unpublished results, pp. 1–6, 2015.

[58] R. Bugga *et al.*, “NASA (JPL) - Performance of Commercial High Energy and High Power Li-Ion Cells in Jovian Missions Encountering High Radiation Environments.” https://www.nasa.gov/sites/default/files/atoms/files/3-nasa_battery_workshop_nov_2019_high_power_li-ion_cells_final.pdf, Unpublished results, 2019.

[59] Université de Sherbrooke QMSat Team, “Preliminary Design Review QMSat Team Mission objective of QMSat,” *CSA-CCP-PDA-0002*. Unpublished results, Not publically available, pp. 1–111, 2019.

[60] New Brunswick Community College, Université de Moncton, and University of New Brunswick, “Preliminary Design Review CubeSat NB Team New Brunswick Community College Université de Moncton University of New Brunswick CCP-CNB-00040-COM-RP-P2 Mission Overview & Payload,” *CCP-CNB-00040-COM-RP-P2*. Unpublished results, Not publically available, 2019.

[61] D. Muthulingam, “NASA (JPL) - Power Subsystem Options for CubeSat OpComm.” https://www.kiss.caltech.edu/workshops/optcomm/presentations/Muthulingam.pdf, Unpublished results, pp. 1–12.

[62] F. C. Krause, J. A. Loveland, M. C. Smart, E. J. Brandon, and R. V. Bugga, “Implementation of commercial Li-ion cells on the MarCO deep space CubeSats,” *Journal of Power Sources*, vol. 449. DOI: 10.1016/j.jpowsour.2019.227544, pp. 1–9, 2020.

[63] M. Dubarry and A. Devie, “Battery durability and reliability under electric utility grid operations: Representative usage aging and calendar aging,” *J. Energy Storage*, vol. 18, no. December 2017, pp. 185–195, 2018.

[64] M. Driedger, M. Taverner, and V. Platero, “University of Manitoba - SSC18-PI-23 TSAT4 : A Modular 3U CubeSat Characterizing Anabaena Cylindrica in Low Earth Orbit.” https://digitalcommons.usu.edu/cgi/viewcontent.cgi?article=4181&context=smallsat, Unpublished results, 2018.

[65] D. Choi, A. Crawford, Q. Huang, V. V Viswanathan, M. C. Kintner-Meyer, and V. L. Sprenkle, “Pacific Northwest National Laboratory - Li-ion Battery Chemistries under Grid Duty Cycles.” https://www.sandia.gov/ess-ssl/docs/pr_conferences/2016/Monday_Presentations/27_Daiwon_Choi.pdf, Unpublished results, pp. 1–15, 2016.

[66] A. J. Crawford *et al.*, “Lifecycle comparison of selected Li-ion battery chemistries under grid and electric vehicle duty cycle combinations,” *Journal of Power Sources*, vol. 380. DOI: 10.1016/j.jpowsour.2018.01.080, pp. 185–193, 2017.

[67] N. Omar *et al.*, "Assessment of performance of lithium iron phosphate oxide, nickel manganese cobalt oxide and nickel cobalt aluminum oxide based cells for using in plug-in battery electric vehicle applications," *2011 IEEE Vehicle Power and Propulsion Conference, VPPC 2011*. https://ieeexplore.ieee.org/document/6043017, Unpublished results, pp. 1–7, 2011.

[68] W. Alpha, "Circle Packing." [Online]. Available: http://mathworld.wolfram.com/CirclePacking.html. [Accessed: 04-Nov-2019].

[69] Battery Space, "Pouch Cell Energy Density Data." [Online]. Available: https://www.batteryspace.com/1-2cratepolymerli-ioncellspacks.aspx. [Accessed: 04-Nov-2019].

[70] Panasonic, "Panasonic Prismatic Cell Data." [Online]. Available: https://industrial.panasonic.com/ww/products/batteries/secondary-batteries/lithium-ion/prismatic-type. [Accessed: 23-Oct-2019].

[71] A123 Systems, "26Ah Prismatic Pouch Cell NMC Lithium-Ion." https://www.altertek.com/new/wp-content/uploads/2017/02/26Ah_2016.pdf, p. 1, 2016.

[72] T. Prejean, "NanoRacks CubeSat Deployer (NRCSD) Interface Definition Document (IDD)," no. NR-NRCSD-S0003. http://nanoracks.com/wp-content/uploads/NanoRacks-CubeSat-Interface-Control-Document-CubeSat-Gu, pp. 1–53, 2018.

[73] F. Yang, D. Wang, Y. Zhao, K. L. Tsui, and S. J. Bae, "A study of the relationship between coulombic efficiency and capacity degradation of commercial lithium-ion batteries," *Energy*, vol. 145, pp. 486–495, 2018.

[74] M. Dubarry, A. Devie, and K. McKenzie, "Durability and reliability of electric vehicle batteries under electric utility grid operations: Bidirectional charging impact analysis," *J. Power Sources*, vol. 358, pp. 39–49, 2017.

[75] S. Ma *et al.*, "Temperature effect and thermal impact in lithium-ion batteries: A review," *Prog. Nat. Sci. Mater. Int.*, vol. 28, no. 6, pp. 653–666, 2018.

[76] J. Xia, M. Nie, L. Ma, and J. R. Dahn, "Variation of Coulombic Efficiency versus Upper Cutoff Potential of Li-ion Cells Tested With Aggressive Protocols," *J. Power Sources*, vol. 306, no. December, pp. 233–240, 2015.

[77] P. Keil, S. F. Schuster, J. Travi, A. Hauser, R. C. Karl, and A. Jossen, “Calendar Aging of Lithium-Ion Batteries I. Impact of the Graphite Anode on Capacity Fade,” *J. Electrochem. Soc.*, vol. 163, no. July, pp. A1872–A1880, 2016.

[78] J. Taylor, A. Barai, T. R. Ashwin, Y. Guo, M. Amor-Segan, and J. Marco, “An insight into the errors and uncertainty of the lithium-ion battery characterisation experiments,” *J. Energy Storage*, vol. 24, no. January, p. 100761, 2019.

[79] Y. Song, D. Liu, C. Yang, and Y. Peng, “Data-driven hybrid remaining useful life estimation approach for spacecraft lithium-ion battery,” *Microelectron. Reliab.*, vol. 75, pp. 142–153, 2017.

[80] P. Fermín-Cueto *et al.*, “Identification and machine learning prediction of knee-point and knee-onset in capacity degradation curves of lithium-ion cells,” *Energy AI*, vol. 1, p. 100006, 2020.

[81] K. A. Severson *et al.*, “Data-driven prediction of battery cycle life before capacity degradation,” *Nat. Energy*, vol. 4, no. 5, pp. 383–391, 2019.

[82] Fluke, “Fluke 289 - Multimeter.” https://www.fluke.com/en-ca/product/electrical-testing/digital-multimeters/fluke-289.

[83] Arbin, “Arbin-002 MITS Pro 3.0-BT2000 User Manual,” no. July. https://manualzz.com/doc/6665748/table-of-contents---arbin-instruments, 2002.

[84] Neware, “Neware BTS-5V50A (8Ch) Technical Specification Document,” no. 128. https://newarebattery.com/wp-content/uploads/2019/05/BTS4000-User-Manual.pdf, 2018.

[85] I. Cincinnati Sub-Zero Products, “CSZ-Z series thermal chamber- operator manual 56276 REV F.pdf.” https://www.atecorp.com/atecorp/media/pdfs/data-sheets/csz-zh-h-ac-manual.pdf?ext=.pdf.

[86] Sartorius, “Sartorius ELT-103 Milligram Scale.” http://www.scalenet.com/pdf/Sartorius_ELT_manual.pdf.

[87] Fluke, “Fluke 500 Series Battery Analyzer Data Sheet.” https://www.myflukestore.ca/pdfs/cache/www.myflukestore.ca/bt510/datasheet/bt510-datasheet.pdf, pp. 1–5.

[88] Hitachi, “Hitachi S-4700 SEM Technical Data Sheet.” https://hitachi-hta.com/sites/default/files/technotes/Hitachi_4700_cryo.pdf.

[89] LeyBold, “Trivac B D8B Rotary Vane Vacuum Pump,” no. 112. https://www.idealvac.com/files/manuals/Leybold_d4_8B_InstructionManual.pdf, pp. 1–30.

[90] MatWeb, “MatWeb Material Property Data on Cast Acrylic.” [Online]. Available: http://www.matweb.com/search/datasheet.aspx?bassnum=O1303&ckck=1. [Accessed: 06-Jun-2019].

[91] M. Doms, A. Bekesch, and J. Mueller, “A microfabricated Pirani pressure sensor operating near atmospheric pressure,” *J. Micromechanics Microengineering*, vol. 15, no. 8, pp. 1504–1510, 2005.

[92] K. K. de Groh, B. A. Banks, and D. C. Smith, “NASA Lewis Research Center - Environmental durability issues for solar power systems in low earth orbit.” https://ntrs.nasa.gov/search.jsp?R=19950009355, Technical Memorandum; Unpublished results, Cleveland, pp. 1–14, 1995.

[93] M. B. Elliott, “Degradation of Electric Vehicle Lithium-ion Batteries in Electricity Grid Services,” Dalhousie University, 2020.

[94] R. W. Cook, L. G. Swan, and K. P. Plucknett, “Failure mode analysis of lithium ion batteries operated for low Earth orbit CubeSat applications,” *J. Energy Storage*, vol. 31, no. February, pp. 1–10, 2020.

[95] J. Self, C. P. Aiken, R. Petibon, and J. R. Dahn, “Survey of gas expansion in Li-Ion NMC pouch cells,” *J. Electrochem. Soc.*, vol. 162, no. 6, pp. A796–A802, 2015.

[96] M. Saidi and R. H. Abardeh, “Air pressure dependence of natural-convection heat transfer,” *WCE 2010 - World Congress on Engineering 2010*, vol. 2. http://www.iaeng.org/publication/WCE2010/WCE2010_pp1444-1447.pdf, Unpublished results, pp. 1444–1447, 2010.

[97] S. Freitag, C. Berger, J. Gelb, C. Weisenberger, and T. Bernthaler, “Li-Ion Battery Components – Cathode , Anode , Binder , Separator – Imaged at Low Accelerating Voltages With ZEISS FE-SEMs.” https://blogs.zeiss.com/microscopy/en/scanning-electron-microscopy-of-li-ion-battery-components/, 2016.

[98] P. Wallenten, “Heat transfer coefficiant in room with and without furniture,” *Dep. Build. Sci. Lund Inst. Technol.*, pp. 1–8, 2018.

[99] A. Poghosyan and A. Golkar, “CubeSat evolution: Analyzing CubeSat capabilities for conducting science missions,” *Prog. Aerosp. Sci.*, vol. 88, no. September 2016, pp. 59–83, 2017.

[100] R. G. Belliveau *et al.*, “Mid-infrared emissivity of nylon, cotton, acrylic, and polyester fabrics as a function of moisture content,” *Text. Res. J.*, vol. 90, no. 13–14, pp. 1431–1445, 2020.

[101] T. D. Hatchard, D. D. MacNeil, D. A. Stevens, L. Christensen, and J. R. Dahn, “Importance of heat transfer by radiation in Li-ion batteries during thermal abuse,” *Electrochem. Solid-State Lett.*, vol. 3, no. 7, pp. 305–308, 2000.

Appendix A : Construction Drawings

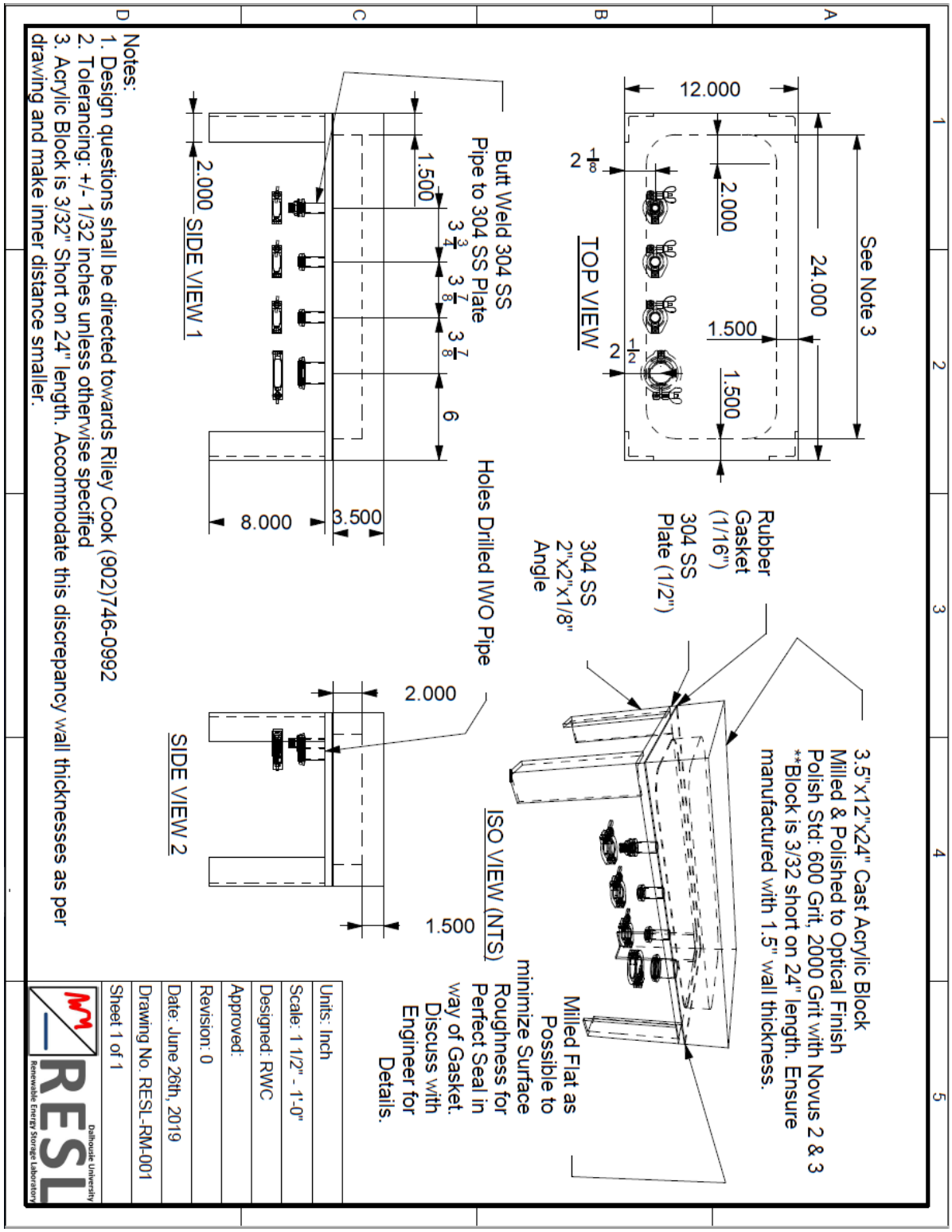

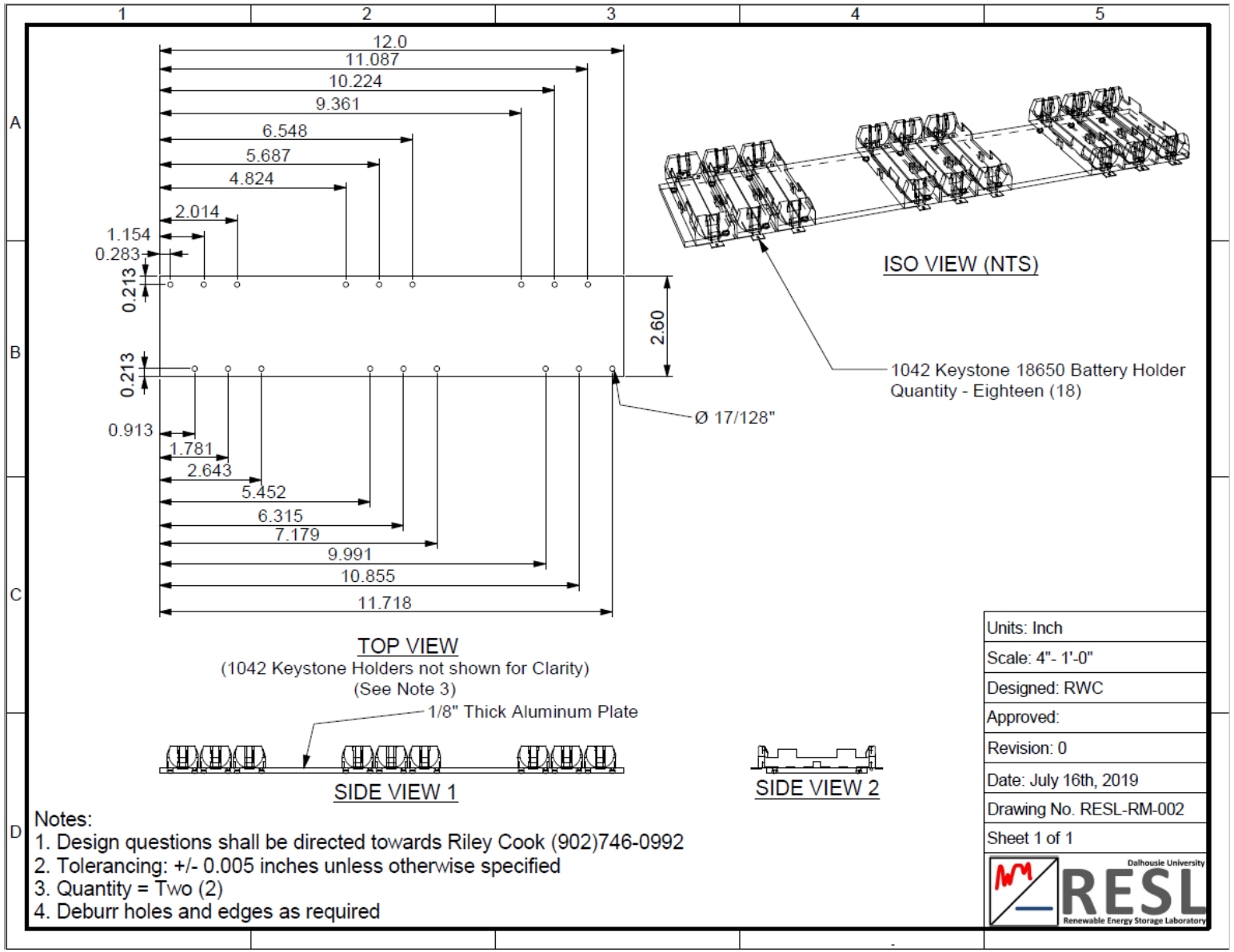
12.0
11.087
10.224
9.361
6.548
5.687
4.824
2.014
1.154
0.283
0.213
0.213
2.60
0.913
1.781
2.643
5.452
6.315
7.179
9.991
10.855
11.718
Ø 17/128"
ISO VIEW (NTS)
1042 Keystone 18650 Battery Holder
Quantity - Eighteen (18)
TOP VIEW
(1042 Keystone Holders not shown for Clarity)
(See Note 3)
1/8" Thick Aluminum Plate
SIDE VIEW 1
SIDE VIEW 2
Notes:
1. Design questions shall be directed towards Riley Cook (902)746-0992
2. Tolerancing: +/- 0.005 inches unless otherwise specified
3. Quantity = Two (2)
4. Deburr holes and edges as required
Units: Inch
Scale: 4"- 1'-0"
Designed: RWC
Approved:
Revision: 0
Date: July 16th, 2019
Drawing No. RESL-RM-002
Sheet 1 of 1
Dalhousie University
RESL
Renewable Energy Storage Laboratory

Appendix B : Cycling Scripts

Capacity and Energy Efficiency Reference Cycle Script (Neware BTS-5V50A)

Standard Settings | Professional Settings

ID	Step name	StepTime(hh:mm:ss)	Rate(C)	Volt.(V)	Cur.(A)	Cap.(Ah)	Stop Rate(C)	Stop Cur.(A)
1	Rest	00:00:30						
2	Rest	1000:00:00						
	IF		AuxTMax	<	28.000000	Goto:3		
3	CC_Dchg			2.7500	2.6000			
	IF		StepTime	>=	4800sec	Goto:chnl. protect		
4	Rest	00:00:30						
5	Rest	1000:00:00						
	IF		AuxTMax	<	28.000000	Goto:6		
6	CC_Chg			4.2000	1.3000			
	IF		StepTime	>=	8400sec	Goto:chnl. protect		
7	CCCV_Chg			4.2000	1.3000			0.2500
8	Rest	00:00:30						
9	Rest	1000:00:00						
	IF		AuxTMax	<	28.000000	Goto:10		
10	Cycle	Begin ID: 3	Times: 3					
11	Rest	00:00:01						
12	Cycle	Begin ID: 11	Times: 2					
13	SIM	File path	Js-Lines-64.txt	Cur mode	Multiplicator: 1			
	IF		Volt.	<=	2.7500V	Goto:14		
	IF		StepTime	>=	4800sec	Goto:chnl. protect		
14	Rest	00:00:30						
15	Rest	1000:00:00						
	IF		AuxTMax	<	28.000000	Goto:16		
16	SIM	File path	Js-Lines-64.txt	Cur mode	Multiplicator: 1			
	IF		Volt.	>=	4.2000V	Goto:17		
	IF		StepTime	>=	8400sec	Goto:chnl. protect		

17	CCCV_Chg			4.2000	1.3000			0.2500
18	Rest	00:00:30						
19	Rest	1000:00:00						
	IF		AuxTMax	<	28.000000	Goto:Finished		
20	End							

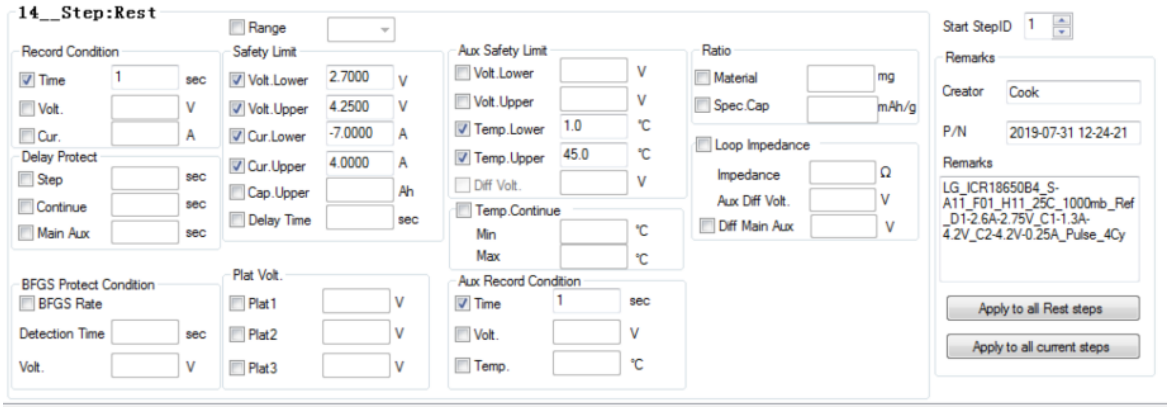

Differential Voltage Reference Cycle Script (Arbin BT2000)

		Step Label	Number Of Limits	Control Type	Control Value	Extra Control Value 1	Extra Control Value 2	Current Range	Extended Definition	Extended Definition 1
1		RestBegin	2	Rest						
		Log Limit	Step Limit	Goto Step	Variable1	Operator1	Value1	Variable2	Operator2	Value2
	1	☑	☑	Next Step	PV_CHAN_Ste	>=	00:00:30	AV_T[2]	<=	28
	2	☑	☐		DV_Time	>=	00:00:10			
2		Dis1	4	Current(A)	-0.14			Medium		
		Log Limit	Step Limit	Goto Step	Variable1	Operator1	Value1	Variable2	Operator2	Value2
	1	☑	☑	Next Step	PV_CHAN_Vol	<	2.5			
	2	☑	☑	Unsafe	PV_CHAN_Ste	>=	1:06:00:00			
	3	☑	☑	Unsafe	PV_CHAN_Cur	>=	-0.12	PV_CHAN_Ste	>=	00:00:01
	4	☑	☐		DV_Time	>=	00:00:10			
3		RestDis1	2	Rest						
		Log Limit	Step Limit	Goto Step	Variable1	Operator1	Value1	Variable2	Operator2	Value2
	1	☑	☑	Next Step	PV_CHAN_Ste	>=	00:10:00	AV_T[2]	<=	28
	2	☑	☐		DV_Time	>=	00:00:10			
4		Chg1	4	Current(A)	0.14			Medium		
		Log Limit	Step Limit	Goto Step	Variable1	Operator1	Value1	Variable2	Operator2	Value2
	1	☑	☑	Next Step	PV_CHAN_Vol	>	4.2			
	2	☑	☑	Unsafe	PV_CHAN_Ste	>=	1:06:00:00			
	3	☑	☑	Unsafe	PV_CHAN_Cur	<=	0.12	PV_CHAN_Ste	>=	00:00:01
	4	☑	☐		DV_Time	>=	00:00:10			
5		RestChg1	2	Rest						
		Log Limit	Step Limit	Goto Step	Variable1	Operator1	Value1	Variable2	Operator2	Value2
	1	☑	☑	Next Step	PV_CHAN_Ste	>=	00:10:00	AV_T[2]	<=	28
	2	☑	☐		DV_Time	>=	00:00:10			
6		Dis2	4	Current(A)	-0.14			Medium		
		Log Limit	Step Limit	Goto Step	Variable1	Operator1	Value1	Variable2	Operator2	Value2
	1	☑	☑	Next Step	PV_CHAN_Vol	<	2.5			
	2	☑	☑	Unsafe	PV_CHAN_Ste	>=	1:06:00:00			
	3	☑	☑	Unsafe	PV_CHAN_Cur	>=	-0.12	PV_CHAN_Ste	>=	00:00:01
	4	☑	☐		DV_Time	>=	00:00:10			
7		RestDis2	2	Rest						
		Log Limit	Step Limit	Goto Step	Variable1	Operator1	Value1	Variable2	Operator2	Value2
	1	☑	☑	Next Step	PV_CHAN_Ste	>=	00:10:00	AV_T[2]	<=	28
	2	☑	☐		DV_Time	>=	00:00:10			
8		Chg2	3	CCCV	CC(A):1.675	CV(V):4.2		Medium		
		Log Limit	Step Limit	Goto Step	Variable1	Operator1	Value1	Variable2	Operator2	Value2
	1	☑	☑	Next Step	PV_CHAN_Cur	<=	0.25			
	2	☑	☑	Unsafe	PV_CHAN_Ste	>=	04:00:00			
	3	☑	☐		DV_Time	>=	00:00:10			
9		RestEnd	2	Rest						
		Log Limit	Step Limit	Goto Step	Variable1	Operator1	Value1	Variable2	Operator2	Value2
	1	☑	☑	Next Step	PV_CHAN_Ste	>=	00:00:30	AV_T[2]	<=	28
	2	☑	☐		DV_Time	>=	00:00:10			

Accelerated LEO Cycle Script (Neware BTS-5V50A)

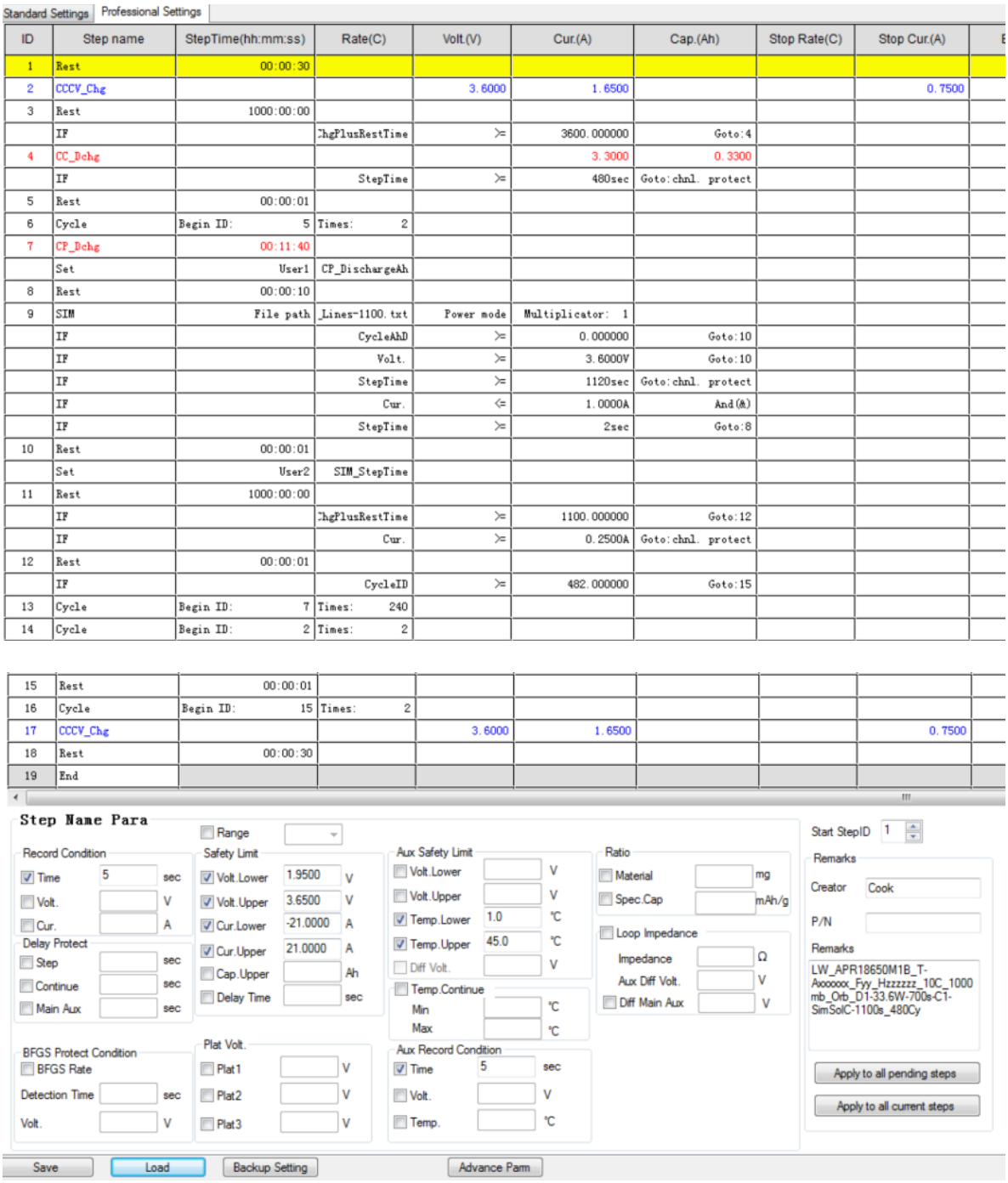

Standard Settings | Professional Settings

ID	Step name	StepTime(hh:mm:ss)	Rate(C)	Volt.(V)	Cur.(A)	Cap.(Ah)	Stop Rate(C)	Stop Cur.(A)
1	Rest	00:00:30						
2	CCCV_Chg			3.6000	1.6500			0.7500
3	Rest	1000:00:00						
	IF		ChgPlusRestTime	>=	3600.000000	Goto:4		
4	CC_Dchg				3.3000	0.3300		
	IF		StepTime	>=	480sec	Goto:chnl. protect		
5	Rest	00:00:01						
6	Cycle	Begin ID: 5	Times: 2					
7	CP_Dchg	00:11:40						
	Set	User1	CP_DischargeAh					
8	Rest	00:00:10						
9	SIM	File path	_Lines-1100.txt	Power mode	Multiplicator: 1			
	IF		CycleAhD	>=	0.000000	Goto:10		
	IF		Volt.	>=	3.6000V	Goto:10		
	IF		StepTime	>=	1120sec	Goto:chnl. protect		
	IF		Cur.	<=	1.0000A	And(&)		
	IF		StepTime	>=	2sec	Goto:8		
10	Rest	00:00:01						
	Set	User2	SIM_StepTime					
11	Rest	1000:00:00						
	IF		ChgPlusRestTime	>=	1100.000000	Goto:12		
	IF		Cur.	>=	0.2500A	Goto:chnl. protect		
12	Rest	00:00:01						
	IF		CycleID	>=	482.000000	Goto:15		
13	Cycle	Begin ID: 7	Times: 240					
14	Cycle	Begin ID: 2	Times: 2					
15	Rest	00:00:01						
16	Cycle	Begin ID: 15	Times: 2					
17	CCCV_Chg			3.6000	1.6500			0.7500
18	Rest	00:00:30						
19	End							

Step Name Para

Range

Record Condition: Time 5 sec; Volt. V; Cur. A

Delay Protect: Step sec; Continue sec; Main Aux sec

Safety Limit: Volt.Lower 1.9500 V; Volt.Upper 3.6500 V; Cur.Lower -21.0000 A; Cur.Upper 21.0000 A; Cap.Upper Ah; Delay Time sec

Aux Safety Limit: Volt.Lower V; Volt.Upper V; Temp.Lower 1.0 ℃; Temp.Upper 45.0 ℃; Diff Volt. V

Temp.Continue: Min ℃; Max ℃

Ratio: Material mg; Spec.Cap mAh/g

Loop Impedance: Impedance Ω; Aux Diff Volt. V; Diff Main Aux V

BFGS Protect Condition: BFGS Rate; Detection Time sec; Volt. V

Plat Volt.: Plat1 V; Plat2 V; Plat3 V

Aux Record Condition: Time 5 sec; Volt. V; Temp. ℃

Start StepID 1

Remarks

Creator Cook

P/N

Remarks

LW_APR18650M1B_T-Axxxxxx_Fyy_Hzzzzzz_10C_1000mb_Orb_D1-33.6W-700s-C1-SimSolC-1100s_480Cy

Apply to all pending steps

Apply to all current steps

Save | Load | Backup Setting | Advance Parm

Appendix C : Data Processing Matlab code

The Matlab code below was used to extract data from discharge capacity and energy efficiency reference cycles from multiple excel spreadsheets autogenerated by Neware BTS-5V50A software. This code vastly reduced manual data processing time while reducing the likelihood of human error.

```
%Pulls cycle data from excel files and makes a copy and paste table
%Step 0: To run again, type clearvars then filepath="" in command window
%Step 1: You must copy below to command window first before running
% filepath="";
%Step 2: Copy all file paths from neware xls to the filepath string array
%Step 3: Click Run and copyandpaste final product
filepath=strrep(filepath(:,1),"","");
x=array2table(filepath);
y=height(x);
warning('OFF', 'MATLAB:table:ModifiedAndSavedVarnames');
for i=1:y
   if i==1
      Cycledata = readtable(filepath(i,1), 'Sheet', 4,'Range','A:K');
      n(i,1)=height(Cycledata);
   end
   if i>1
      Cycledata_new=readtable(filepath(i,1), 'Sheet', 4,'Range','A:K');
      Cycledata=[Cycledata; Cycledata_new];
      n(i,1)=height(Cycledata_new);
   end
end
m=1;
j=1;
for k=1:y
   for j= 1:n(k,1)
      file=filepath(k,1);
      ST_ID=strfind(file,'_T-');
```

```
type=isempty(ST_ID);
if type==1
    cellID=strfind(file,'-A');
    cellID = extractBetween(file,cellID+1,cellID+3);
    fileID=strfind(file,'_F');
    fileID = extractBetween(file,fileID+1,fileID+3);
    holdID=strfind(file,'_H');
    holdID = extractBetween(file,holdID+1,holdID+3);
    chemID=strfind(file,'XLS\');
    chemID = extractBetween(file,chemID+4,chemID+5);
    typeID=strfind(file,'mb_');
    typeID = extractBetween(file,typeID+3,typeID+5);
    manuID=strfind(file,'XLS\');
    manuID = extractBetween(file,manuID+4,manuID+5);
end
if type==0
    cellID=strfind(file,'-A');
    cellID = extractBetween(file,cellID+1,cellID+7);
    fileID=strfind(file,'_F');
    fileID = extractBetween(file,fileID+1,fileID+3);
    holdID=strfind(file,'_H');
    holdID = extractBetween(file,holdID+1,holdID+7);
    chemID=strfind(file,'XLS\');
    chemID = extractBetween(file,chemID+4,chemID+5);
    typeID=strfind(file,'mb_');
    typeID = extractBetween(file,typeID+3,typeID+5);
    manuID=strfind(file,'XLS\');
    manuID = extractBetween(file,manuID+4,manuID+5);
end
if chemID=='PS'
   chemID='NCA';
elseif chemID=='LG'
   chemID='NMC';
```

```
    elseif chemID=='LW'
        chemID='LFP';
    end
    filterdata(m,1:6)=[cellID,chemID,fileID,holdID,typeID,manuID];
    m=m+1;
  end
end
filterdata=array2table(filterdata(:,:));
filterdata.Properties.VariableNames = {'Cell' 'Chemistry' 'File' 'Holder' 'Type' 'Manufacturer'};
%Step 4: FINAL PRODUCT copy and paste table to master sheet
FinalProduct=[filterdata Cycledata];
%Last line of code
```

The Matlab code below was used to extract IR measurements from multiple excel spreadsheets autogenerated by Neware BTS-5V50A software. This code vastly reduced manual data processing time while reducing the likelihood of human error.

```
%Pulls a partial amount of record data from excel files for IR analysis
%IF you want to run more than A01 through A12 for PS, LG and LW you must
%add additional cells in the 's' variable for loop at approx. line 104
%Step 0: To run again, type clearvars then filepath="" in command window
%Step 1: Right Click and "Copy as Path" Pulse RefCycle xls' to filepath
%Step 2: Choose how many seconds into the pulse you want V and Current
%Note: p=29 pulls the 30th pulse datapoint.
p=28;
%Step 3: Choose Cell manufactuer, Cell ID, and Cycle ID
%Step 4: Copy and Paste Final Product to xls sheet as desired
filepath=strrep(filepath(:,1),"","");
x=array2table(filepath);
y=height(x);
warning('OFF', 'MATLAB:table:ModifiedAndSavedVarnames');
for i=1:y
  if i==1
    recorddata = readtable(filepath(i,1), 'Sheet', 5,'Range','A:G');
```

```
        n(i,1)=height(recorddata);
    end
    if i>1
        recorddata_new=readtable(filepath(i,1), 'Sheet', 5,'Range','A:G');
        recorddata=[recorddata; recorddata_new];
        n(i,1)=height(recorddata_new);
    end
end
m=1;
j=1;
for k=1:y
    for j= 1:n(k,1)
        file=filepath(k,1);
        ST_ID=strfind(file,'_T-');
        type=isempty(ST_ID);
        if type==1
            cellID=strfind(file,'-A');
            cellID = extractBetween(file,cellID+1,cellID+3);
            fileID=strfind(file,'_F');
            fileID = extractBetween(file,fileID+1,fileID+3);
            holdID=strfind(file,'_H');
            holdID = extractBetween(file,holdID+1,holdID+3);
            chemID=strfind(file,'XLS\');
            chemID = extractBetween(file,chemID+4,chemID+5);
            typeID=strfind(file,'mb_');
            typeID = extractBetween(file,typeID+3,typeID+5);
            manuID=strfind(file,'XLS\');
            manuID = extractBetween(file,manuID+4,manuID+5);
        end
        if type==0
            cellID=strfind(file,'-A');
            cellID = extractBetween(file,cellID+1,cellID+7);
            fileID=strfind(file,'_F');
```

```
        fileID = extractBetween(file,fileID+1,fileID+3);
        holdID=strfind(file,'_H');
        holdID = extractBetween(file,holdID+1,holdID+7);
        chemID=strfind(file,'XLS\');
        chemID = extractBetween(file,chemID+4,chemID+5);
        typeID=strfind(file,'mb_');
        typeID = extractBetween(file,typeID+3,typeID+5);
        manuID=strfind(file,'XLS\');
        manuID = extractBetween(file,manuID+4,manuID+5);
      end
      if chemID=='PS'
        chemID='NCA';
      elseif chemID=='LG'
        chemID='LCO';
      elseif chemID=='LW'
        chemID='LFP';
      end
      filterdata(m,1:6)=[cellID,chemID,fileID,holdID,typeID,manuID];
      m=m+1;
    end
end
filterdata=array2table(filterdata(:,:));
stampeddata=[filterdata recorddata];
SIMlines=find(strcmp('SIM',stampeddata{:,9}));
h=length(SIMlines);
Pulsedata(:,1)=stampeddata(SIMlines,1);
Pulsedata(:,2)=stampeddata(SIMlines,2);
Pulsedata(:,3)=stampeddata(SIMlines,3);
Pulsedata(:,4)=stampeddata(SIMlines,4);
Pulsedata(:,5)=stampeddata(SIMlines,5);
Pulsedata(:,6)=stampeddata(SIMlines,6);
Pulsedata(:,7)=stampeddata(SIMlines,7);
Pulsedata(:,8)=stampeddata(SIMlines,13);
```

```
Pulsedata(:,9)=stampeddata(SIMlines,12);
Pulsedata.Properties.VariableNames = {'Cell' 'Chemistry' 'File' 'Holder' 'Type' 'Manufacturer' 'Cycle'
'Current' 'Voltage'};
x=1;
for i = 2:(h-30)
   a=Pulsedata(i,8);
   b=Pulsedata(i-1,8);
   a=table2array(a);
   b=table2array(b);
   if (a/b)>1.9
      if x==1
         IRpoints_first=[Pulsedata(i-1,1:9)];
         IRpoints_second=[Pulsedata(i+p,1:9)];
         IRpoints=[IRpoints_first; IRpoints_second];
         x=2;
      elseif x==2
         IRpoints_first=[Pulsedata(i-1,1:9)];
         IRpoints_second=[Pulsedata(i+p,1:9)];
         IRpoints=[IRpoints; IRpoints_first; IRpoints_second];
      end
   end
end

vars = {'FinalProduct'};
clear(vars{:});
%ADD MORE CELLS HERE
z=0;
for s = 1:36
   vars = {'dVdI','d','Pulselines1','Pulselines2','Pulselines3','Matchedlines','IRspecificpoints'};
   clear(vars{:});
   if s == 1
      ManuID='PS';
      CellID='A01';
```

```
elseif s == 2
    ManuID='PS';
    CellID='A02';
elseif s == 3
    ManuID='PS';
    CellID='A03';
elseif s == 4
    ManuID='PS';
    CellID='A04';
elseif s == 5
    ManuID='PS';
    CellID='A05';
elseif s == 6
    ManuID='PS';
    CellID='A06';
elseif s == 7
    ManuID='PS';
    CellID='A07';
elseif s == 8
    ManuID='PS';
    CellID='A08';
elseif s == 9
    ManuID='PS';
    CellID='A09';
elseif s == 10
    ManuID='PS';
    CellID='A10';
elseif s == 11
    ManuID='PS';
    CellID='A11';
elseif s == 12
    ManuID='PS';
    CellID='A12';
```

```
elseif s == 13
    ManuID='LG';
    CellID='A01';
elseif s == 14
    ManuID='LG';
    CellID='A02';
elseif s == 15
    ManuID='LG';
    CellID='A03';
elseif s == 16
    ManuID='LG';
    CellID='A04';
elseif s == 17
    ManuID='LG';
    CellID='A05';
elseif s == 18
    ManuID='LG';
    CellID='A06';
elseif s == 19
    ManuID='LG';
    CellID='A07';
elseif s == 20
    ManuID='LG';
    CellID='A08';
elseif s == 21
    ManuID='LG';
    CellID='A09';
elseif s == 22
    ManuID='LG';
    CellID='A10';
elseif s == 23
    ManuID='LG';
    CellID='A11';
```

```
elseif s == 24
    ManuID='LG';
    CellID='A12';
elseif s == 25
    ManuID='LW';
    CellID='A01';
elseif s == 26
    ManuID='LW';
    CellID='A02';
elseif s == 27
    ManuID='LW';
    CellID='A03';
elseif s == 28
    ManuID='LW';
    CellID='A04';
elseif s == 29
    ManuID='LW';
    CellID='A05';
elseif s == 30
    ManuID='LW';
    CellID='A06';
elseif s == 31
    ManuID='LW';
    CellID='A07';
elseif s == 32
    ManuID='LW';
    CellID='A08';
elseif s == 33
    ManuID='LW';
    CellID='A09';
elseif s == 34
    ManuID='LW';
    CellID='A10';
```

```
elseif s == 35
   ManuID='LW';
   CellID='A11';
elseif s == 36
   ManuID='LW';
   CellID='A12';
end
%Cell Manufacturer
Pulselines1=find(strcmp(ManuID,IRpoints{:,6}));
if isempty(Pulselines1), continue, end
%Cell ID
Pulselines2=find(strcmp(CellID,IRpoints{:,1}));
if isempty(Pulselines2), continue, end

%Check to make sure there are matches before proceeding
w=0;
for i = 1:length(Pulselines1)
   for j = 1:length(Pulselines2)
      if Pulselines1(i,1)==Pulselines2(j,1)
         w=1;
      end
   end
end
if w==0, continue, end
%Cycle ID(Typically Cycle 4)
Pulselines3=find(IRpoints{:,7}==4);
z=z+1;
warning ('off','all');
d=height(IRpoints);
dVdI(1:15,1)="Discharge";
dVdI(16:45,1)="Charge";
dVdI(1:15,2)=1:15;
dVdI(16:45,2)=1:30;
```

```
dVdI=array2table(dVdI);
k=1;
for i = 1:length(Pulselines1)
    for j = 1:length(Pulselines2)
        if Pulselines1(i,1)==Pulselines2(j,1)
            for l=1:length(Pulselines3)
                if Pulselines1(i,1)==Pulselines3(l,1)
                    Matchedlines(k,1)=Pulselines1(i,1);
                    k=k+1;
                end
            end
        end
    end
end
IRspecificpoints=IRpoints(Matchedlines(:,1),:);
k=1;
for i = 2:1:height(IRspecificpoints)
    if IRspecificpoints{i,8}<0 andand (IRspecificpoints{i,8}/IRspecificpoints{i-1,8})>1.9
        dVdI{k,3}=(IRspecificpoints{i,9}-IRspecificpoints{i-1,9})/(IRspecificpoints{i,8}-
IRspecificpoints{i-1,8});
        k=k+1;
    elseif IRspecificpoints{i,8}>0
        i=height(IRspecificpoints);
    end
end
k=16;
for i = 2:1:height(IRspecificpoints)
    if IRspecificpoints{i-1,8}>0 andand (IRspecificpoints{i,8}/IRspecificpoints{i-1,8})>1.9
        dVdI{k,3}=(IRspecificpoints{i,9}-IRspecificpoints{i-1,9})/(IRspecificpoints{i,8}-
IRspecificpoints{i-1,8});
        k=k+1;
    end
end
```

```
    dVdI.Properties.VariableNames = {'Mode' 'PulseNumber' 'dV_dI'};
    for i = 1:height(dVdI)
        if dVdI{i,3}==0
            dVdI{i,3}="";
        end
    end
    newdataset=dVdI{:,3}*1000; %Ohms to Milliohms
    if z==1
        FinalProduct=newdataset;
    elseif z>1
        FinalProduct=[FinalProduct newdataset];
    end
end
%Last line of code
```

Appendix D : Copyright Permissions

Figure 2.1 LIB electrochemical process showing charge and discharge – The creative commons attribution 4.0 international license allows reproduction of this figure. Reproduced with permission from the Author. See Below.

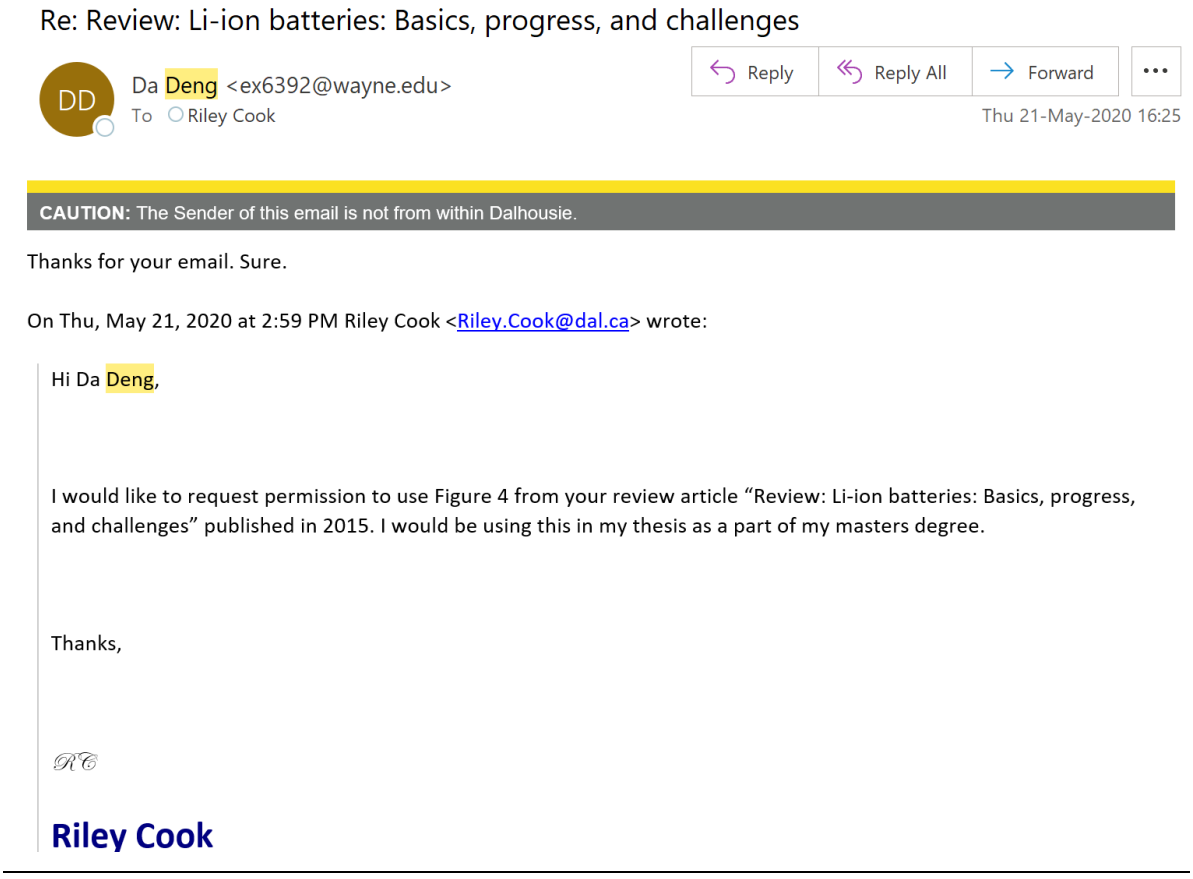

Re: Review: Li-ion batteries: Basics, progress, and challenges

DD

Da Deng <ex6392@wayne.edu>

To Riley Cook

Reply | Reply All | Forward | ...

Thu 21-May-2020 16:25

CAUTION: The Sender of this email is not from within Dalhousie.

Thanks for your email. Sure.

On Thu, May 21, 2020 at 2:59 PM Riley Cook <Riley.Cook@dal.ca> wrote:

> Hi Da Deng,
>
> I would like to request permission to use Figure 4 from your review article "Review: Li-ion batteries: Basics, progress, and challenges" published in 2015. I would be using this in my thesis as a part of my masters degree.
>
> Thanks,
>
> *RC*
>
> **Riley Cook**

Figure 2.2 Use of PAM in commercialized LIB as of 2016 [6] and 2019 [7] – Reproduced with permission from the Author. See Below.

RE: The Rechargeable Battery Market and Main Trends 2016-2025 Plot Permission in Publication

PC PILLOT Christophe <c.pillot@avicenne.com>
To Riley Cook

CAUTION: The Sender of this email is not from within Dalhousie.

Reference:

Christophe Pillot, AVICENNE Energy 2020

Christophe

avicenne ENERGY

Christophe PILLOT
AVICENNE Energy Director
00 33 (1) 44 55 19 90

BATTERIES EVENT 2020

SAVE THE DATE
7TH > 9TH OCT.
LYON - FRANCE

De : Riley Cook <Riley.Cook@Dal.Ca>
Envoyé : vendredi 12 juin 2020 15:06
À : PILLOT Christophe <c.pillot@avicenne.com>
Objet : RE: The Rechargeable Battery Market and Main Trends 2016-2025 Plot Permission in Publication

This is great Christophe. Would you mind me using this in my Masters Thesis? If this is okay, how would you like me to reference the Data?

Thanks,

Riley

Figure 2.3 Anode material share of commercial LIB in 2016 [6] – Reproduced with permission from the Author. See Below.

Re: The Rechargeable Battery Market and Main Trends 2016-2025 Plot Permission in Pu...

PC PILLOT Christophe <c.pillot@avicenne.com>
To Riley Cook

Reply | Reply All | Forward | ...

Fri 22-May-2020 04:03

CAUTION: The Sender of this email is not from within Dalhousie.

Ok, no problem

Envoyé de mon iPhone

Le 21 mai 2020 à 21:55, Riley Cook <Riley.Cook@dal.ca> a écrit :

Hi Christophe Pillot,

I would like to request permission to use the figure below from your battery seminar exhibit "The Rechargeable Battery Market and Main Trends 2016-2025" . I would be using this in my thesis as a part of my masters degree and would certainly reference the pie chart.

Thanks,

RC

Riley Cook

Figure 2.4 Graphene planar sheets (A, B, C) in both hexagonal 2H and rhombohedral (3R) structure of graphite [4] – Reproduced with permission from the Author and Publisher Copyright. See Below.

From: Jeff Dahn <Jeff.Dahn@Dal.Ca>
Sent: May 21, 2020 17:00
To: Riley Cook <Riley.Cook@Dal.Ca>
Subject: Re: Chapter 17 - Lithium Ion Batteries request for permission to use Fig. 19

fine with me. I do not know if you need to contact the publisher or not.

Jeff Dahn, FRSC
Professor of Physics and Atmospheric Science
NSERC/Tesla Canada Industrial Research Chair
Canada Research Chair
Room 218, Sir James Dunn Science Building
6300 Coburg Road
Dalhousie University
Halifax, N.S. B3H4R2
Canada
e-mail: jeff.dahn@dal.ca
voice: 902-494-2991
website: https://www.dal.ca/diff/dahn.html

From: Riley Cook <Riley.Cook@Dal.Ca>
Sent: Thursday, May 21, 2020 4:58 PM
To: Jeff Dahn <Jeff.Dahn@Dal.Ca>
Subject: Chapter 17 - Lithium Ion Batteries request for permission to use Fig. 19

Hi Jeff,

I'm emailing to request permission to use the below figure from Chapter 17 - Lithium Ion Batteries Written by yourself and Grant M. Ehrlich. I would be using this figure in my Masters Thesis.

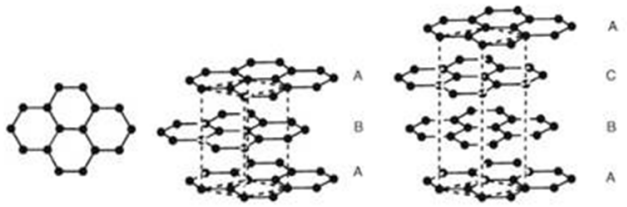

Figure 19. The hexagonal structure of graphene, i.e., a layer of carbon, and the structures of hexagonal (2H) and rhombohedral (3R) graphite.

Copyright Clearance Center Marketplace™

McGraw Hill LLC - License Terms and Conditions

This is a License Agreement between Riley Cook ("You") and McGraw Hill LLC ("Publisher") provided by Copyright Clearance Center ("CCC"). The license consists of your order details, the terms and conditions provided by McGraw Hill LLC, and the CCC terms and conditions.

All payments must be made in full to CCC.

Order Date	12-Jun-2020	**Type of Use**	Republish in a thesis/dissertation
Order license ID	1041327-1		
ISBN-13	9781260115925	**Publisher**	McGraw Hill Education
		Portion	Image/photo/illustration

LICENSED CONTENT

Publication Title	Linden's Handbook of Batteries, 5/E	**Country**	United States of America
		Rightsholder	McGraw Hill LLC
Author/Editor	Beard	**Publication Type**	Book
Date	01/01/2019		

REQUEST DETAILS

Portion Type	Image/photo/illustration	**Distribution**	Worldwide
Number of images / photos / illustrations	2	**Translation**	Original language of publication
Format (select all that apply)	Electronic	**Copies for the disabled?**	No
		Minor editing privileges?	No
Who will republish the content?	Academic institution	**Incidental promotional use?**	No
Duration of Use	Current edition and up to 5 years	**Currency**	CAD
Lifetime Unit Quantity	Up to 499		
Rights Requested	Main product		

NEW WORK DETAILS

Title	ANALYSIS OF CAPACITY DEGRADATION AND FAILURE MECHANISMS IN LITHIUM-ION BATTERIES FOR LOW EARTH ORBIT SATELLITE APPLICATIONS	**Institution name**	Dalhousie University
		Expected presentation date	2020-08-20
Instructor name	Riley Cook		

REUSE CONTENT DETAILS

Title, description or numeric reference of the portion(s)	Figure 19 & Figure 37	**Title of the article/chapter the portion is from**	Linden's Handbook of Batteries. Chapter 17: Lithium-Ion Batteries
Editor of portion(s)	N/A	**Author of portion(s)**	Beard
Volume of serial or monograph	Chapter 17	**Issue, if republishing an article from a serial**	N/A
Page or page range of portion	1-131	**Publication date of portion**	2019-01-01

Figure 2.5 Electrolyte conductivity versus concentration at various temperatures [19] – Reproduced with permission from the Publisher Copyright. See Below.

REUSE CONTENT DETAILS

Title, description or numeric reference of the portion(s)	Figure 14	Title of the article/chapter the portion is from	Transport Properties of LiPF[sub 6]-Based Li-Ion Battery Electrolytes, Journal of The Electrochemical Society
Editor of portion(s)	N/A	Author of portion(s)	ELECTROCHEMICAL SOCIETY.
Volume of serial or monograph	152	Issue, if republishing an article from a serial	5
Page or page range of portion	A882	Publication date of portion	1948-01-01

Figure 2.6 Conductivity versus temperature of 1 M $LiPF_6$ electrolyte with EC mixed with various other solvents [4] – Reproduced with permission from the Author and Publisher Copyright. See Below.

Re: Chapter 17 - Lithium Ion Batteries request for permission to use Fig. 19

Reply | Reply All | Forward | ...

JD

Jeff Dahn
To Riley Cook

Thu 21-May-2020 20:39

This is fine

Jeff Dahn, FRSC
Professor of Physics and Atmospheric Science
NSERC/Tesla Canada Industrial Research Chair
Canada Research Chair
Room 218, Sir James Dunn Science Building
6300 Coburg Road
Dalhousie University
Halifax, N.S. B3H4R2
Canada
e-mail: jeff.dahn@dal.ca
voice: 902-494-2991
website: https://www.dal.ca/diff/dahn.html

From: Riley Cook <Riley.Cook@Dal.Ca>
Sent: Thursday, May 21, 2020 8:01 PM
To: Jeff Dahn <Jeff.Dahn@Dal.Ca>
Subject: RE: Chapter 17 - Lithium Ion Batteries request for permission to use Fig. 19

Hi Jeff,

One more I would like to use from the same chapter 17 is Fig. 38. I've included below. Let me know if this is fine with you.

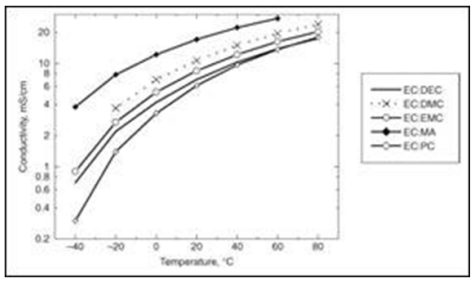

Thanks,

Riley

Copyright Clearance Center Marketplace™

McGraw Hill LLC - License Terms and Conditions

This is a License Agreement between Riley Cook ("You") and McGraw Hill LLC ("Publisher") provided by Copyright Clearance Center ("CCC"). The license consists of your order details, the terms and conditions provided by McGraw Hill LLC, and the CCC terms and conditions.

All payments must be made in full to CCC.

Order Date	12-Jun-2020	**Type of Use**	Republish in a thesis/dissertation
Order license ID	1041327-1		
ISBN-13	9781260115925	**Publisher**	McGraw Hill Education
		Portion	Image/photo/illustration

LICENSED CONTENT

Publication Title	Linden's Handbook of Batteries, 5/E	**Country**	United States of America
		Rightsholder	McGraw Hill LLC
Author/Editor	Beard	**Publication Type**	Book
Date	01/01/2019		

REQUEST DETAILS

Portion Type	Image/photo/illustration	**Distribution**	Worldwide
Number of images / photos / illustrations	2	**Translation**	Original language of publication
Format (select all that apply)	Electronic	**Copies for the disabled?**	No
		Minor editing privileges?	No
Who will republish the content?	Academic institution	**Incidental promotional use?**	No
Duration of Use	Current edition and up to 5 years	**Currency**	CAD
Lifetime Unit Quantity	Up to 499		
Rights Requested	Main product		

NEW WORK DETAILS

Title	ANALYSIS OF CAPACITY DEGRADATION AND FAILURE MECHANISMS IN LITHIUM-ION BATTERIES FOR LOW EARTH ORBIT SATELLITE APPLICATIONS	**Institution name**	Dalhousie University
		Expected presentation date	2020-08-20
Instructor name	Riley Cook		

REUSE CONTENT DETAILS

Title, description or numeric reference of the portion(s)	Figure 19 & Figure 37	Title of the article/chapter the portion is from	Linden's Handbook of Batteries. Chapter 17: Lithium-Ion Batteries
Editor of portion(s)	N/A	Author of portion(s)	Beard
Volume of serial or monograph	Chapter 17	Issue, if republishing an article from a serial	N/A
Page or page range of portion	1-131	Publication date of portion	2019-01-01

Figure 2.7 Graphite||LNMO (lithium nickel manganese oxygen) cell voltage and gassing response of first two cycles versus time - cycle 1 (C/10), cycle 2 (C/2) [30] – The creative commons attribution 4.0 international license allows reproduction of this figure.

Figure 2.8 Gas generation as a result of operating voltage range A: 2.6 to 4.2 Volts, B: 2.6 to 4.8 Volts for SLP30 graphite||NMC cells [31] – Open access permits reproduction of this figure.

Figure 2.9 First 2 cycles of NMC cell gas generation results for SLP30 graphite||NMC cells [32] – Open access permits reproduction of this figure.

Figure 2.11 Cylindrical cell positive terminal cross-section showing protective devices *[36]*

Figure 2.12 Kinetic temperature as a function of geometric altitude [42]

Figure 2.13 Number density of individual and total species as a function of geometric altitude [42]

Figure 2.14 Total pressure and mass density as a function of geometric altitude [42]

No Copyright (Figure 2.11, Figure 2.12, Figure 2.13, Figure 2.14). "NASA material is not protected by copyright unless noted. If copyrighted, permission should be obtained from the copyright owner prior to use. If not copyrighted, NASA material may be reproduced and distributed without further permission from NASA" – https://www.nasa.gov/multimedia/guidelines/index.html

---

Appendix E : Statistical Inference

Performance (i.e. discharge capacity, energy efficiency, etc…) varies with each cell type (NCA, NMC, LFP) and condition (*laboratory*, *temperature*, *vacuum*) when cycled as per the accelerated LEO cycle. When performance metrics are plotted for various cell group, a comparison between each cell group degradation, energy efficiency and other performance metrics can either be drastically different or visibly indistinguishable. This research has utilized high quality commercially available cells with low probability of manufacturer error due to tight tolerancing (Section 4.1) and each test condition utilized 3P cell groupings (Section 4.3). Thus, when results appear to be radically different (i.e. cell group "A" completed twice as many accelerated LEO cycles compared to cell group "B") conclusions can be made without using the statistical approach with a high qualitative level of confidence. However, when experimental testing yields two cell groups that achieve very similar performance (i.e. cell group A completed 2% more accelerated LEO cycles compared to cell group B), a more quantitative statistical approach is required to determine if as a population cell group A is better suited for the condition and accelerated LEO cycle compared to cell group B.

As true variance for each cell type is unknown, a mean comparison t-test was used to make a quantitative judgment on cell groups of similar performance. Hypothetical cell group 'A' and 'B' were used for the statistical pseudo calculations presented in equations (15) through (23). A two-sided t-test will be used with the null hypothesis as shown in equation (15).

$$H_o: \mu_A = \mu_B \tag{15}$$
$$H_1: \mu_A \neq \mu_B$$

The variance of cell group 'A' and 'B' are calculated using equation (16).

$$S_A^2 = \sum_{i=1}^{n_A} \frac{\left(X_{A,i} - \overline{X_A}\right)^2}{n_A - 1} \tag{16}$$
$$S_B^2 = \sum_{i=1}^{n_B} \frac{\left(X_{B,i} - \overline{X_B}\right)^2}{n_B - 1}$$

Where: $n_A \; and \; n_B = 3$

The sample size for each cell group is represented by $'n'$ and is equal to 3 as cell groups were cycled 3 in parallel. When cells groups of the same population (i.e. cell type) are compared, it can be assumed that the population variance is the same for each cell type. In this case, the degree of freedom is calculated as per equation (17).

$$v = n_A + n_B - 2 = 3 + 3 - 2 = 4 \tag{17}$$

However, when comparing cell groups from different populations it should be assumed that the population variance is different for each cell group. In this case, the degree of freedom is calculated using equation (18).

$$v = \frac{\left(\frac{S_A^2}{n_A} + \frac{S_B^2}{n_B}\right)^2}{\frac{\left(\frac{S_A^2}{n_A}\right)^2}{n_A - 1} + \frac{\left(\frac{S_B^2}{n_B}\right)^2}{n_B - 1}} \tag{18}$$

The paired variance for both cell groups 'A' and 'B' are calculated as per equation (19).

$$S_p^2 = \frac{(n_A - 1)S_A^2 + (n_B - 1)S_B^2}{n_A + n_B - 2} \tag{19}$$

The null hypothesis t-value is then determined using equation (20) and compared to the two sided critical t-value in equation (21).

$$t_o = \frac{(\bar{X}_A - \bar{X}_B) - (\mu_A - \mu_B)}{S_p\sqrt{\frac{1}{n_A} + \frac{1}{n_B}}} \tag{20}$$

$$t_{crit} = t_{1-\frac{\alpha}{2},v} = t_{0.975,v} \tag{21}$$

Where: $1 - \alpha = 0.95$ (significance $'\alpha'$ of 0.05 for two-sided t-test with a confidence interval of 95%)

The critical t-value is determined using t-distribution table. If equation (22) is true, there is not sufficient evidence to reject the null hypothesis and there is insignificant evidence to prove H_1 from equation (15) is correct. Concluding there is no significant difference in performance between cell groups 'A' and 'B' with a 95% confidence.

$$|t_o| < t_{crit} \tag{22}$$

If equation (23) is true, there is sufficient evidence to reject the null hypothesis. Thus, there is a significant difference in performance between cell groups 'A' and 'B' with a 95% confidence.

$$|t_o| > t_{crit} \tag{23}$$